Technological development and system integration of VCSELs and SiGe HPT receivers for 60 GHz low cost Radio-over-Fiber applications

Carlos Araujo Viana

UNIVERSITÉ PARIS-EST
École Doctorale MSTIC
Mathématiques, sciences et Technologies de lôInformation
et de la Communication

THÈSE

Pour obtenir le grade de

Docteur de lôUniversité Paris-Est

Spécialité: Electronique, Optronique et Systèmes

Présentée et Soutenue publiquement le 5 May 2014 par

Carlos Alberto Araújo VIANA

Développement technologique et lôintégration système de VCSEL et HPT SiGe pour des applications Radio-sur-Fibre bas cout

Directeur de thèse: Prof. Catherine ALGANI
Encadrant de thèse: Dr. Jean-Luc POLLEUX

JURY:

Rapporteurs	Béatrice CABON, Pr.	IMEP - LaHC, Grenoble INP (France)
	Stavros IEZEKIEL, Pr.	Université de Chypre (Chypre)
Encadrants	Catherine ALGANI, Pr.	ESYCOM - Le Cnam (France)
	Jean-Luc POLLEUX, Dr.	ESYCOM - ESIEE-Paris (France)
Examinateurs	Anna PIZZINAT, Dr.	ORANGE, Lannion (France)
	Henrique SALGADO, Pr.	FEUP, Université de Porto (Portugal)
	Jean-Marc Laheurte, Pr.	ESYCOM - UPEM (France)

Abstract

This work is based on the frame of the French ORIGIN project and intended to explore the Home Area Network using the most recent Wi-Fi standard at 60 GHz with the goal to present a solution for the upcoming days where MultiGbit/s wireless communication will be required. The ORIGIN solution is characterized by the complementary action of two technologies: 60 GHz Wireless communication and Radio-over-Fiber (RoF) infrastructure. The project pretends to propose a real prototype based on RoF transducers and a Multipoint-to-Multipoint architecture to cover the entire house. This thesis covers from the single optoelectronic chip devices until the system implementation and the final demonstrator. The light source and the photodetector choice were very important since it dictated the RoF transducer architecture. Our choice was on 850 nm multimode devices (GaAs VCSEL and SiGe HPT) which allow relaxed constraints on the optical packaging and, therefore, low cost solutions. In terms of performances those devices are limited in a few tens of Gigahertz of bandwidth which was the reason for the intermediate frequency (IF) architecture. This thesis work addressed the electrical and optical interconnection of the optoelectronic chip devices. It explored the integration of hybrid amplification stages and passive networks within optoelectronic receivers and emitters. The optical packaging issues were addressed through a conventional coupling technique using a ball lens first. The die device performances were evaluated and compared with a packaged module in terms of frequency response, noise and nonlinearities. Since performances are usually measured as link performances we proposed a definition of the Opto-microwave figures of merit, such as Opto-microwave gain, noise, nonlinearities and EVM. They are presented and integrated into behavioral models, allowing both the individual performances extraction and system design. The integration of the RoF module in the system is the final part of this thesis. The performances were measured and simulated at each integration step. The final demonstrator based on the multipoint-to-multipoint architecture was implemented using an optoelectronic central node for the signal repartition and the Green Box for signal controlling. Real-time bidirectional transmission between two commercial WirelessHD devices at ~3 Gbit/s was validated. In a final section directions to improve VCSEL and SiGe HPT are explored. 25 GHz analogue VCSELs are explored with a focus on their dimensions, improved access and the potential of a suited matching approach. A novel collective and passive optical coupling technology is also proposed for both VCSEL and top illuminated detectors that couple smaller and faster devices.

Keywords: Radio-over-Fiber, VCSEL, HPT, Optical Interconections, Opto-Microwave Modelling, 60 GHz wireless comunication.

Résumé

Cette thèse s'inscrit dans le cadre du projet français FUI8-ORIGIN qui vise à développer les performances des réseaux domestiques en apportant des solutions sans multi-Gigabits faiblement radiatives, économes et pérennes. La solution ORIGIN est caractérisée par l'action complémentaire de deux technologies: les communications sans fil 60 GHz et la mise en place d'une infrastructure Radio-sur-Fibre (RoF). Cette thèse porte sur le développement des composants et modules optoélectroniques (GaAs VCSEL et SiGe HPT) bas couts. Le travail implique de couvrir de la puce semi-conducteur au modules et jusqu'au système intégré dans le démonstrateur. Les puces sélectionnées sont caractérisées de manière précise en développant des bancs de mesures adaptées aux applications analogiques RoF. Des substrats d'interconnexions sont développés pour permettre le couplage optique et l'interconnexion électrique des puces et ainsi la création de modules. Ce développement est poussé de façon à intégrer de façon hybride des étages d'amplification en aval et amont des composants optiques, ainsi que des étages d'adaptations passifs. Les performances RoF ont été évaluées et comparées en termes de réponse en fréquence, de bruit et de nonlinéarités. Nous avons poursuivi l'approche actuelle des grandeurs optique-microondes qui chacune permette d'isoler et caractériser la performance individuelle des composants optiques ou optoélectroniques pris individuellement. Ces grandeurs sont présentées puis exploitées dans un développement de modèle comportemental, permettant à la fois l'extraction des performances individuelles des composants et le design de l'ensemble du système. Un dimensionnement complet de l'infrastructure RoF pour le démonstrateur est ensuite mené, intégrant et dimensionnant le bilan de liaison global à partir modules et cartes réalisés et développés par les partenaires du projet. Le module transmetteur Radio-sur-Fibre (TRoF) est ainsi conçu, assemblé et testé. Le démonstrateur final basé sur l'architecture multipoint-à-multipoint a été réalisée à l'aide d'un nœud central optoélectronique pour la répartition du signal et d'une Green Box permettant le contrôle de l'allumage des différentes pièces, et ainsi la rationalisation du rayonnement et de la consommation du système. Une transmission bidirectionnelle en temps réel entre deux dispositifs de WirelessHD commerciaux à ~3 Gbit/s a été démontrée. Dans une dernière section de cette thèse, des directions pour améliorer les lasers à cavité émettant par la surface (VCSEL) et les phototransistors SiGe sont explorées. Des VCSEL analogiques avec une bande passante de plus de 25 GHz sont développés avec la société Philips ULM Photonics et mesurés. Une nouvelle technologie de couplage optique collective et passive est enfin proposée.

Mots clés : Radio-sur-Fibre, VCSEL, HPT, Interconnexions optiques, Modélisation optique microonde, Communications sans fil 60 GHz.

Acknowledgements

This research project would not have been possible without the support of many people.

I would like to express my deepest gratitude to my thesis director, Prof. Catherine Algani and thesis adviser, Dr. Jean-Luc Polleux. Both were abundantly helpful and offered invaluable assistance, support and guidance.

My sincere gratitude also to the committee members: the reviewers, Prof. Béatrice Cabon, Prof. Stavros Iezekiel, and the examiners, Dr. Anna Pizzinat, Prof. Henrique Salgado and Prof. Jean-marc Laheurte.

Special thanks also to all my dear PhD student friends that I had luck to cross paths along the last 4 years at the ESYCOM laboratory (ESIEE-Paris, Le CNAM and UPEM), for the support, the enoumerous stimulating discussions and invaluable support. Thanks, also, to all the professors and staff members of ESIEE-Paris that accompanied me along the way.

I would also like to convey thanks to the sponsors, partners and members of the ORIGIN project for the opportunity and the support to success of the project.

I would also like to thank my parents, two older sisters, and two older brothers. They were always supporting me and encouraging me with their best wishes.

Contents

List of Figures

List of Tables

Nomenclature

ADS	Advanced Design Software from Agilent
AGC	Automatic Gain Control
ADC	Analog-to-Digital Converter
CCK	Complementary Code Keying
DBR	Distributed Bragg Reflectors
DH	Doubled Heterojunction
DC2OP	Directly Coupled to Optical Probe
DAC	Digital-to-Analog Converter
DC2PM	Directly Coupled to Power Meter
DSSS	Direct Sequence Spread Spectrum
E/O	Electrical-to-Optical
eO	Etched Oxide
EVM	Error-Vector-Magnitude
EIRP	Equivalent Isotropically Radiated Power
EEL	Edge Emitting Laser
ESYCOM	Electronique, SYstèmes de COmmunications et Microsystèmes
FDM	Frequency Division Multiplexing
F	Noise Factor
FCC	Federal Communications Commission
FTTH	Fiber-To-The-Home
FTTB	Fiber-To-The-Building
FWHM	Full Width at Half Maximum
GaAs	Gallium Arsenide
HAN	Home Area Network
HD	High Definition
HPT	Heterojunction Bipolar Phototransistor
ISM	Industrial, Scientific and Medical
IC	Integrated Circuits
IR-OFDM	Impulse Radio ODFM
IF	Intermediate Frequency

IV	Current-voltage
ITU	International Telecommunication Union
ISI	Inter-Symbol Interferences
ISM bands	The Industrial, scientific and Mediacal radio bands
InGaAs	Indium Gallium Arsenide
LNA	Low Noise Amplifier
LAN	Local Area Network
LI	Light-Current
LIV	Light-Current-Voltage
LED	Light Emitting Diode
LD	Laser Diode
MAC	Media Access Control
M2M	Multipoint-to-Multipoint
MQW	Multiple Quantum Well
MM	Multi-Mode
MB-OFDM	Multiband OFDM
MME	Optical Multipoint-to-Multipoint architecture with electrical multiplexing
MMO	Optical Multipoint-to-Multipoint architecture with optical multiplexing
MIMO	Multiple-Input Multiple-Output
MCEF	Modulation Current Efficiency Factor
NFPD	New Focus Photodiode
NF	Noise Figure
NEP	Noise Equivalent Power
Nq	Shot Noise
Nth	Thermal Noise
O/E	Optical-to-Electrical
OFDM	Orthogonal Frequency Division Multiplexing
ORIGIN	Optical Radio Infrastructure for Gbit/s Indoor Network
PA	Power Amplifier
PoE	Power over Ethernet
PAPR	Peak-to-Average Power Ratio
PD	Photodiode
PCB	Printed Circuit Board
PSK	Phased-shift Keying
PHY	Physical Layer
P2P	Point-to-Point
QAM	Quadrature Amplitude Modulation
RF	Radio Frequency
RoF	Radio-over-Fiber
RIN	Relative Intensity Noise
ROSA	Receiver Optical Sub-Assembly

SMT	Surface Mounted Technology
SDD	Symbolically Defined Device
SQ	Squared layout
SFDR	Spurious Free Dynamic Range
SM	Single-Mode
SP	Sub-Projects
SiGe	Silicon Germanium
SIC	Selective Implanted Collector
TIA	Trans-Impedance amplifier
TOSA	Transmitter Optical Sub-Assembly
TRoF	Transducer RoF
TEM	Transverse Electromagnetic Mode
TE	Transverse Electric Mode
TM	Transverse Magnetic Mode
UWB	Ultra-Wideband
VCSEL	Vertical Cavity Surface Emitting Laser
Wi-Fi	Wireless Fidelity
WLAN	Wireless Local Area Network
xEBC	extended Emitter, Base and Collector

Chapter I - **Introduction**

This chapter intends to present an overview of the work for this dissertation, exposing the subject, describing its objectives and finally gives the presentation of the manuscript structure.

I.A. Subject and Context

MultiGbit/s wireless technology and Home Area Network (HAN) will be part of our days in the future. The increasing of new services and wireless technologies leads us towards more and more data rates reaching Gbit/s. Home services using High Definition (HD) becomes reality in our days and one example where multiGbit/s are required. Domestic cloud approach needs to be considered with the using of all the services and wireless devices in anyplace in the house simultaneously in a ubiquitous manner.

The conventional, and most popular, Wi-Fi (Wireless Fidelity) based on the standard IEEE 802.11 using centimetric-wave frequency band range allows data rates up to 600 Mbit/s. Consequently the new solution reaching higher data rates is essential to develop for the future. One solution is the use of millimeter-wave frequency band, from 57 to 66 GHz. Different radio standards in the millimeter-wave band were already developed and most recently in January 2013 the IEEE 802.11ad Wi-Fi technology. Higher bandwidth channels are available getting data rates up to 7 Gbit/s [16]. At this frequency band, high oxygen absorption leads to short range communication of a few meters. This characteristic is very attractive for indoor networks in terms of privacy since the signal does not cross walls. Because of the single room coverage, an additional network is required to transpose multiGbit/s signal to different rooms. Introducing the Radio-over-Fiber (RoF) technology appears very promising for such high data rates. Optical fiber has become the most interesting communication channel mainly for the low attenuation and its very high frequency bandwidth. The challenge is here on the optoelectronic devices where high performances and low costs are fundamental requirements.

At the end a Wi-Fi 60 GHz for multiGbit/s wireless indoor network based on the RoF technology is believed to be one of the future solutions for people's needs. In 2016 more than 40 % of the total Wi-Fi market should be using the 60 GHz band frequency [17]. Development of a RoF infrastructure is then considered to be crucial in the few upcoming years.

I.B. Objectives of the thesis

This PhD subject is proposed in the frame of a national project dedicated to the development of optoelectronics and photonics within the RoF infrastructure domain for Ultra-WideBand (UWB) and 60 GHz wireless communications. The project name is ORIGIN (Optical Radio Infrastructure for Gbit/s Indoor Network). The main objective of our work is the technology development of a low cost RoF transceiver for wireless home network at high data rates (10 Gbit/s) and the contribution to the whole system design. As we can see in Figure I-1, a generic RoF transceiver is composed of simple modules which help us to define our work objectives.

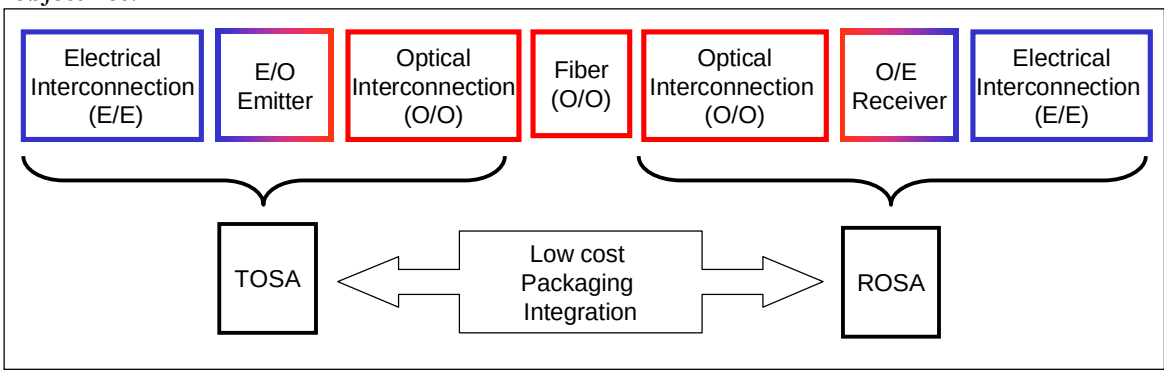

Figure I-1 - Radio-over-Fiber transceiver modules

The core of the RoF transceiver is composed of active devices in the Electrical-to-Optical (E/O) emitter and the Optical-to-Electrical (O/E) receiver. The objectives of this PhD work on these modules are:

- E/O emitter characterization and performance optimization. GaAs-based multimode 850 nm Vertical Cavity Surface Emitting Laser (VCSEL) is considered for its low cost and performances. Some degrees of freedom in their optimization are the layout design in the optical window aperture diameter and the bias operation conditions. Their measurement results will feed a behavior model that we developed to include their frequency response, nonlinearities and noise behavior.
- O/E receiver characterization and performance optimization. Three photodetectors are considered: New Focus InGaAs-based PiN Photodiode used as the reference for E/O emitters characterizations; a photo receiver from Finisar with integrated Trans-Impedance Amplifier (TIA); and finally a home-made SiGe-based 850 nm Heterojunction Bipolar Phototransistor (HPT) receiver. The last one will be explored by varying the physical layout design, the technology configuration, the optical window aperture diameter and the bias operation condition.

Both E/O and O/E devices have an important impact on the optical link system performance where a simulation tool was used to identify their individual influence. A model that is compatible with typical microwave system simulator (ADS Agilent for instance) was developed together with a new definition of Opto-microwave figures of merit. This model is helpful to understand the individual impact of the devices on the system link measurements. An experimental setup was developed that produced accurate data measurements of static characteristic, dynamic response and noise behavior. All these data was used to model each device. Then system measurement (Error-Vector-Magnitude (EVM) for instance) was performed that validated system simulation predictions. Models even allowed further device parameter extraction.

Development of the electrical interfaces was considered for dies integration and was optimized in terms of device performances. Passive reactive matching networks were developed to reduce the reflection losses and improve the system bandwidth, its gain and noise. SiGe Integrated Circuits (IC) design for both sides of the link such as a Power Amplifier (PA) and Low Noise Amplifier (LNA) were designed and integrated.

Optical interface, which provides the light coupling between the E/O emitter and the fiber as between the fiber and the O/E detector, was adressed on two fronts: mechanical receptacle using a ball lens; optical waveguide based in polymer. The optical waveguide structure design and simulations was considered as the integration method.

Packaging and Integration of the multimode optoelectronic devices are the next objectives: from the simple VCSEL die to a Transmitter Optical Sub-Assembly (TOSA) module; from the HPT die to a Receiver Optical Sub-Assembly (ROSA) module. Here again, both characterizations and simulations were taken into account comparing with die performances and reference commercial devices. The final step is the integration of those modules in the RoF transducer (TRoF) to be used in the multiGbit/s wireless communication system. The integration and system performance characterization of the full system at the scale of a four room house were the final objectives in order to do a final demonstrator using real data communications.

I.C. Dissertation Structure

This manuscript is organized according to the following structure. The current chapter is an introduction to this dissertation manuscript.

Chapter II exposes the problematic of the multiGbit/s wireless communication system within the Home Area Network context. The state-of-the-art found nowadays will be presented, including the general solution proposed by the ORIGIN project using the 60 GHz wireless communication through the RoF technology infrastructure. The ORIGIN architecture concept is considered exploring the Optical Multipoint-to-Multipoint architecture with either an Electrical multiplexing (MME) or Optical multiplexing (MMO) and comparing their advantages and drawbacks of the RoF system. Optoelectronic devices will be given a special focus since it is the main context of our work with the target of low cost solutions. Basic principles will be considered, including the state-of-the-art of such GaAs-based VCSEL and SiGe-based Heterojunction Phototransistors technologies. The last point will be the presentation of the three Radio-over-Fiber Transducer generations which are predicted by the evolution on the optoelectronic device solutions.

Chapter III considers the on wafer VCSEL characterization and the careful preparation of experimental setups. A reference photodetector that has a flat frequency and very linear behavior is used in order to extract the laser performances. A complete link characterization will be considered including static performance, dynamic response, noise behavior and the nonlinearities. System performance assessment such as the Spurious Free Dynamic Range (SFDR) and EVM with in the context of 60 GHz standards will be considered too. Each experimental setup will be presented as the eventual calibration procedures regarding the measurement accuracy.

In Chapter IV, the impact of individual optoelectronic devices on the optical link system performance will be explored. The extraction of the device parameters is important which allows the system modeling and optimization. Here the optoelectronic device parameters modeling will require the definition of Opto-microwave Figures of Merit that will be presented and developed further in this section. A behavioral model for each of the link devices will be created using the Symbolically Defined Device (SDD) tool from the ADS software. The model simulation will be compared and validated with measurements operated in the previous chapter.

Chapter V is dedicated to the final demonstrator developed within the ORIGIN project. The first section focuses on the Optical Sub-Assembly modules (TOSA and ROSA) development in terms of electrical and optical interconnections. VCSEL and SiGe HPT dies are assembled on an interconnecting substrate. RF access and transmission lines are optimized. Passive reactive matching networks are prepared and ICs are associated to SiGe HPT to build up a complete SiGe based ROSA. The complete VCSEL based TOSA and SiGe based ROSA modules performance, are compared to the single die performance. The second section intends to evaluate and design the TRoF in terms of the dynamic power budget using 2 configurations – SiGe HPT link and Finisar ROSA link. A system link budget is computed and studied to achieve the system performance required for different scenarios and architecture topologies. Last section presents the final and complete system, including the centimeter-wave Printed Circuit Board (PCB), Local Oscillator PCB, power supply boards PCB and the millimeter-wave PCB fabricated and assembled with the ORIGIN project partners. A point-to-point link communication using 2 TRoFs will be evaluated, optimized and validated by using real live multiGbit/s communication data communications. The final step includes the multipoint-to-multipoint concept using a central node and green box, responsible for the signal distribution and energy/radiation saving, respectively.

Chapter VI presents the future developments on the RoF transducers. Two directions are pointed: system operating frequency and optical coupling efficiency. The first point explores analogue VCSELs performance toward 20 GHz. Through the modification of the layout in terms of optical aperture diameter and RF access lines together with the improved vertical stack of layers provided by Philips-ULM Photonics. The goal is to study different sizes and be able to choose one device to be the candidate for the next generation of TOSA module. The second point is optical coupling where the ball lens optical coupling technique will be simulated in order to compare with measurements. A proposition of a novel optical coupling technique to improve the efficiency results in a collective and passive process will be exposed. Both optical coupling techniques are compared.

Last chapter summarizes all the work providing conclusions. It presents, also, the main contribution of this work and perspectives addressed for future directions.

Chapter II - **RoF in Domestic Wireless Networks: the ORIGIN Project**

This chapter presents an overview on the evolution of the wireless network systems with a focus on the Wi-Fi technology and the arrival of the last standard based on the 60 GHz. It introduces the Radio-over-Fiber (RoF) technology, which can complement the 60 GHz wireless communication to overcome the short range communication. Both technologies are exposed since they are the core of the ORIGIN project.

The first section presents the evolution of the broadband wireless network systems with special attention on the Ultra-Wideband (UWB) wireless system communication and the 60 GHz wireless system communication.

The second section introduces the RoF technology covering both optical transmitters and receivers. Fundamental of optical sources and detectors suited for the RoF low cost applications are covered with a state-of-the-art analysis of VCSELs and specific SiGe phototransistors that could potentially replace standard detectors.

The last section presents the ORIGIN project in terms of objectives, architecture and describes the different RoF generation evolutions that are developed.

II.A. Broadband Wireless Networks Evolution

Wireless communication technology is becoming a very hot topic today. Massive utilization is applied in different areas worldwide. Mobile communication is one of the best examples since by the end of 2013 the number of mobile subscriptions is expected to be the same as the total world population of seven billions people [18]. Wireless data communications for internet access is another example where we get a tremendous increase to 39 % of the world population connected by the end of 2013 [18]. Wireless Local Area Networks (WLAN) become very popular, moving more and more into Home Area Networks (HAN) with the increase of connected wireless devices and services.

Table II.1 - Evolution of the WLAN (IEEE 802.11) Standard at the physical layer (PHY) [19]

Year	Standard	Frequency	Indoor Range	Data rate	No. channels	Modulation Scheme	Channel Bandwidth
2013	802.11ad	57-66 GHz	10 m	7 Gbit/s	4	16-QAM*	2 GHz
2012	802.11ac	5GHz	30 m	1.3 Gbit/s	5	256-QAM*	80 MHz
2006	802.11n	2.4/5 GHz	70 m	600 Mbit/s	22	64-QAM*	20/40 MHz
2003	802.11g	2.4 GHz	38 m	54 Mbit/s	11	CCK and 64-QAM*	20 MHz
1999	802.11a	5 GHz	35 m	54 Mbit/s		64-QAM*	20 MHz
1999	802.11b	2.4 GHz	35 m	11 Mbit/s	11	CCK	20 MHz
1997	802.11	2.4 GHz	20 m	2 Mbit/s		DSSS	20 MHz

*OFDM signals

The most popular and used wireless protocol technology for WLAN products is the Wi-Fi (Wireless Fidelity) based on the standard IEEE 802.11. Most of the wireless products available on the market are based on this technology and are commonly integrated in laptops and Smartphone. High data rates are needed to face the tremendous increase of the connected wireless devices and applications such as wireless sensor networks, domotics, teleconferences, telemedicine, HD-TV, etc. The IEEE 802.11 standard is continuously being updated since it was born in 1997, to satisfy the user data rate demand which increases every year. Table II.1 shows the standard evolution in terms of frequency, bandwidth, range distance and data rates. The IEEE 802.11n standard is currently widely used based on the 2.4 GHz and 5 GHz unlicensed ISM band. Theoretically date rates up to 600 Mbit/s over a 40 MHz bandwidth can be achieved. But the users demand for the future HAN, where large increase of wireless devices connected to numerous services requires multiGigabit/s to permit a high number of high data rate connections simultaneously. The new 802.11ad, 60 GHz Wi-Fi standard that was successfully published in January 2013 [20] answers such needs. This standard is based on the combination of Multiple-input Multiple-Output (MIMO) technology and of the Orthogonal Frequency-Division Multiplexing (OFDM) modulation scheme.

The MIMO technique is a wireless technology based on multiple transmitters and receivers, working simultaneously to increase the data transfer at the same time. It is used in modern wireless standards, including in IEEE 802.11 (n, ad), 3GPP LTE, and mobile WiMAX systems [21]-[23]. MIMO takes advantage of multipath to combine the information from multiple signals improving both speed and data integrity.

The OFDM is the main modulation currently used in recent standards. It is based on the Frequency Division Multiplexing (FDM) and it includes a large number of orthogonal subcarriers, each of them uses Quadrature Amplitude Modulation (QAM) or Phased-shift Keying (PSK) modulation schemes. Low multipath distortion, high spectral efficiency and resiliency to RF interference are the main benefits of OFDM signals. We get high spectral efficiency since the spectral spacing between adjacent subcarriers is minimized by using a base of orthogonal functions. In other hand, it is more sensitive to time and frequency synchronization errors [24]. Another important disadvantage is the high Peak-to-Average Power Ratio (PAPR) which is proportional to the number of subcarriers used for OFDM systems. Large PAPR of a system makes the implementation of Digital-to-Analog Converter (DAC) and Analog-to-Digital Converter (ADC) extremely difficult. The design of RF amplifier also becomes increasingly difficult as the PAPR increases.

Next subsection introduces the Ultra-Wideband and the 60 GHz wireless communications, providing an overview of the fundamentals and state-of-the-art.

II.A.1. Ultra-Wideband (UWB) wireless communications

Ultra-wideband (UWB) communication is a very attractive technique with interest in both academia and industry in the past few years. It has a high bandwidth and was potentially intended for indoor short range and high data rates wireless system applications. In 2002, the U.S Federal Communications Commission (FCC) amended the Part 15 rules to allow operation of devices incorporating UWB technology with 7.5 GHz unlicensed band in the frequency band of 3.1-10.6 GHz [25]-[27]. Two main types of UWB technology exist [28]: the UWB multiband OFDM (MB-OFDM) and the UWB impulse radio (IR-UWB). The impulse radio UWB is characterized by transmitting ultra low power radio signal with very short electrical pulses on the order of one nanosecond. The total emitted power over several Gigahertz of bandwidth is a fraction of a milliwatt, due to its low Equivalent Isotropically Radiated Power (EIRP) emission limit (the power spectral density emission to -41.3 dBm/MHz, means -14 dBm in a band of 528MHz), an UWB signal “behaves as noise” to other radio systems, which results in a low probability of interception and detection. Besides, an UWB signal has excellent multipath immunity and less susceptibility to interferences from other radios, due to its wide bandwidth nature. Since the information is encoded as short pulses the up and down conversions can be omitted. This results in substantial reduction in the use of power consumption and possibility of simplifying the complexity of the transceiver architectures. The UWB multiband OFDM is characterized by transmitting OFDM symbols successively over several radio bands in order to reduce Inter-Symbol Interferences (ISI) and to exploit diversity. Nevertheless, this technique is complex and costly compared to IR-UWB.

Summary of UWB communication advantages is as follows:

- High Data Rates: up to 500 Mbit/s;
- Low Power Consumption;
- Low interference, immunity to multipath propagation;
- Less complex transceiver hardware and low cost.
- Summary of Disadvantages:
- Short range communication, up to 10 m;
- The spectrum mask is not harmonized worldwide;
- Constraints on the emitted power.

II.A.2. 60 GHz Wireless communications

Recently the millimeter-wave band for wireless communication technology got a strong interest as a solution for the requirements of bandwidth demands which move quickly towards the multiGigabit/s wireless communications. Lately different consortiums moved towards the 60 GHz wireless systems since it is believed to be the future of the broadband wireless network exceeding the Gigabit/s. 60 GHz wireless standards have been developed with the dedicated ISM band for high data rate Wireless Personal Area Networks (WPANs) like the ECMA-387 [29] in 2008 and 802.15.3c [30] in 2009. The 802.15.3c standard was supported by the Wireless Gigabit Alliance (WiGig) consortium [31] based on the 60 GHz unlicensed spectrum. The internationally available unlicensed spectrum surrounding the 60 GHz carrier frequency got particular interest due to its propagation characteristics and the 9 GHz available bandwidth. This spectrum is divided into 4 channels of 2.16 GHz as seen in Figure II-1, enabling up to 5-6 Gbps per channel.

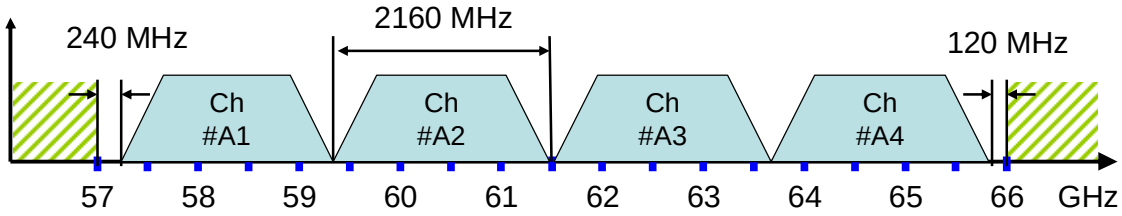

Figure II-1 – IEEE 802.11ad standard Millimeter-wave band spectrum allocation in Europe (ISM 60 GHz mm-wave band)

The standard IEEE 802.11ad announced by WiGig consortium in 2012 came in this direction, presenting a maximum throughput of up to 7 Gbit/s [16]. This new generation of 60 GHz Wi-Fi systems are intended to be massively introduced in the next years, keeping the compatibility with the current 2.4 and 5 GHz Wi-Fi solutions. The performance characteristics of the all three 60 GHz standards are gathered in Table II.2 below.

At 60 GHz, signal attenuation is high because of the oxygen absorption peak, which leads to a short covered range. Nevertheless, this high attenuation reduces the signal to a level that will not interfere with other 60 GHz links operating in the same geographic vicinity. Therefore, signals cannot travel far beyond their intended range, which gives another important characteristic: high security level communication. Another important parameter is the antenna directivity. At such high frequency, highly directional antennas with narrow beam associated to low interferences and high security are easily enabled as compared to other frequency signals in cm-waveband (2.4 and 5 GHz). Moreover, the small size of the antennas at this frequency leads to more compact radio systems that could be integrated in Smartphones or laptops. These radio systems are based on OFDM modulation and MIMO antenna systems.

Table II.2 - Millimeter-wave band standard parameters

Parameter	IEEE 802.15.3c HSI mode	ECMA-387 Type A	IEEE 802.11ad OFDM PHY
Occupied bandwidth	1.815 GHz	~1.904 GHz	1.815 GHz
Sampling rate	2.640 GSa/s	2.592 GSa/s	2.640 GSa/s
Number of subcarriers	512		
FFT period	193.9 ns	197.53 ns	193.9 ns
Cyclic Prefix duration	24.24 ns	24.70 ns	48.5 ns
Cyclic Prefix length	64	64	128
OFDM symbol duration	218.18 ns	222.23 ns	242.4 ns
Number of data subcarriers	336	360	336
Number of pilots subcarriers	16		
Number of DC subcarriers	3		
Number of null subcarriers	141	133	0
Number of unused subcarriers	16	0	157
Modulation	QPSK; 16/64-QAM,	QPSK, 16-QAM	SQPSK, QPSK, 16/64-QAM

Beamforming is one technique to provide the best wireless transmission channel between the emitter and the receiver. It is important to adjust automatically the radiated beam pattern from the emitter according to the receiver position and its environment. Even with a promising future on short range wireless application, satisfying the requirements of bandwidth demands, there is still a lot of work to do and many challenges to overcome. The high attenuation and directional nature of the 60 GHz signal propagation can become a difficulty for some applications. Yet beamforming is restricted to fixed equipments due to the size of the antenna array and to the transceivers consumption.

The millimeter-wave band power regulations and available spectrum of different regions of the world is given in Table II.3.

Table II.3 - Worldwide power regulation on the millimeter-wave band [32]-[34]

Region	Unlicensed band	Max TX power	EIRP (dBm)	Antenna Gain
USA	57.05-64 GHz	27 dBm	40/43 (average)/(peak)	-
Canada				
South Korea	57-64 GHz	10 dBm	27	-
Europe	57-66 GHz	13 dBm	57 (peak)	37 dBi
Australia	59.04-62.9 GHz	10 dBm	57	-
Japan	59-66 GHz			47dBi (max)

The power regulations are given as the conventional Equivalent Isotropically Radiated Power (EIRP). It corresponds to the product (in linear) of transmitter power and the antenna gain in a given direction relative to an isotropic antenna of a radio transmitter. The losses between the power transmitter and the antenna can be added as well.

$$EIRP(dBi) = P_{TX}^{OUT} - (Losses) + Gain_{antenna}$$ Equation Section 2(2.1)

On this thesis EIRP of 27 dBm is considered as a low level limit since it is the most restrictive value founded (South Korean) around the world. Also, we consider the IEEE 802.11ad standard in characterization and modeling.

II.B. Radio-over-Fiber technology

Optical fiber communication systems, which include optical fiber transmission channels and optoelectronic devices, have been developed worldwide since 1980. The use of optical fiber as a transmission channel becomes the solution with the increase of data rates for long and short distances. The traditional copper pair cables are still used on the front-end for short distances and low data rates, which becomes obsolete for the multiGbit/s operation. Optical Fiber can be considered for the future because of its several advantages:

- Abundant material: Silica is the main material used on the optical fiber and it is abundant on Earth and not expensive. The cost mainly comes from the manufacturing since it is very small and the refractive index value of the different layer needs to be very precise. Also the need to control the purity of silica avoiding contaminants, such as OH+ ion.
- Low transmission attenuation and wide bandwidth: Optical Fiber has a very low transmission attenuation, less than 3 dB/Km at 850 nm and 0.2 dB/km at 1550 nm compared to 200-500 dB/km for copper and coaxial cables (depending on the electrical carrier frequency), and also extremely high bandwidth.
- Size and weight: because of its few hundreds of microns in diameter (hair-sized), the weight is low. This is important compared to the conventional copper cables becoming very heavy for certain applications used in aircraft, satellites, ships, etc.
- Electromagnetic interferences: The optical fiber is immune to electromagnetic interference. This characteristic eliminates the crosstalk between transmission lines. Hence, it has particular interest in electrically noisy environment.
- Signal security: Since the signal is well confined within the waveguide core, the signal is protected by the optical fiber itself. This makes it very attractive in military and governmental applications as well.

Optical fiber is already massively used for transmission of data from high distances intercities or even transatlantic communications. The future is going towards the individual home with fiber-to-the-home (FTTH) or fiber-to-the-building (FTTB) topologies. The high bandwidth provided by the optical fiber makes it a good choice for:

-Transmitting broadband signals such as television and radio high-definition broadcasting.

-Mobile cellular network with Pico-cell approach [35]

-Aerospace and military applications

-The more recent wireless LANs exceeding multigigabit/s data rates.

In a Radio-over-Fiber (RoF) system, the transmitted signal is directly the radio signal, including its RF modulated carrier frequency. Both microelectronics and photonics circuits are part of the microwave photonics systems. The structure of a RoF system is illustrated in Figure II-2.

RoF can be sub-divided in three categories:

- RF-over-Fiber: the radio frequency signal (typically higher than 10 GHz) directly modulates the optical carrier transmitted over the fiber. Up/down electrical conversion circuits are not required, but high speed optoelectronic devices are needed (ex: external modulators or directly modulated lasers), which could be a challenge in terms of cost and availability at very high frequency. The major advantages are the design simplicity and low consumption.
- IF-over-Fiber: the RF signal is transposed to an Intermediate Frequency (typically lower than 10 GHz) before modulating the light. The system becomes more relaxed

in terms of the speed of optoelectronic devices and therefore its cost. However, the system is more complex with up/down conversion steps, adding extra losses, noise, nonlinearities and consumption which can be a challenge.

- Baseband-over-fiber: the radio baseband IQ modulated signal is kept baseband and directly transmitted through the fiber. At the receiver end, the signal is upconverted to the RF carrier frequency.

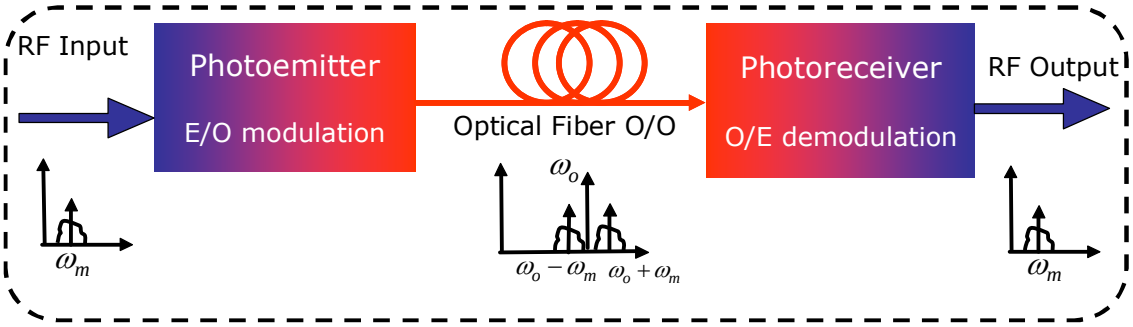

Figure II-2 - Radio-over-Fiber technology link. Negative frequencies are not shown.

The 60 GHz Wi-Fi has a great potential for short distance multiGbit/s wireless communications using the concept of micro-cells or Pico-cells inside home. The RoF technology can be a solution for connecting all the rooms each other with multiGbit/s data rate operation. In this way, RF signals are propagated from different remote radio cells to the different rooms of the whole building, using optical links as presented in Figure II-19.

The following sections are dedicated to the VCSEL and SiGe photodetector. The first subsection presents the VCSEL as a low cost optical transmitter source to be integrated into the RoF system. It covers the basic principles, state-of-the-art, speed limitations and technology selected for further study.

The second subsection introduces the SiGe Heterojunction Phototransistor (HPT) as a detector to be integrated into the RoF system. It covers the basic principles, state-of-the-art and the technology.

II.B.1. VCSEL: a low cost optical transmitter

Differences between VCSELs and the Edge Emitting lasers (EEL) are shown in Figure II-3. The main difference is the optical aperture which is on the top for a VCSEL and on the side edge for an EEL. Also an EEL has a longer active layer generating higher optical power. Nevertheless, the reduced active layer of the VCSELs induces a lower threshold current and higher speed operation. The small lasing cavity of the VCSEL, shown in Figure II-3 a), requires mirrors with very high reflectivity (more than 99 %).

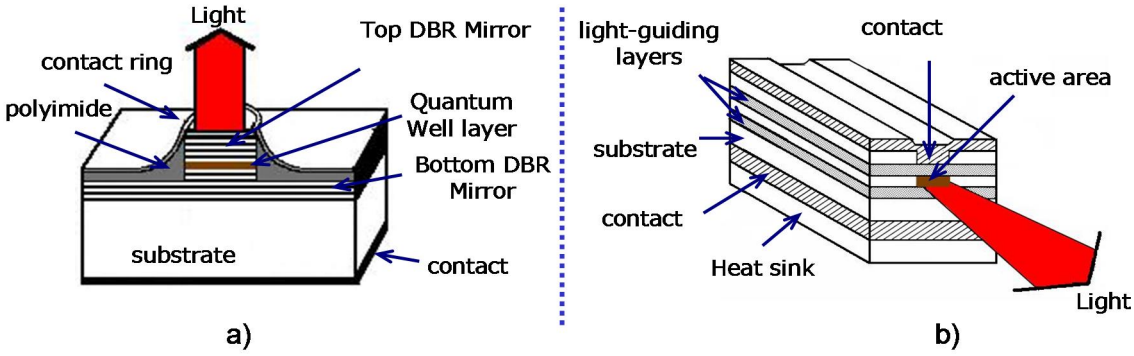

Figure II-3 – Physical structure differences between VCSEL and EEL

It is clear that VCSELs are more efficient given: low power consumption, single mode operation (SM), and high optical efficiency. The main advantage of the EELs is their high optical power.

The VCSELs are more complex semiconductor laser devices than the EEL, however, numerous advantages made it the first choice in many applications. As a vertical emission laser, it gives the capability of on wafer level testability and 2-D array production which reduces the cost. Circular and low divergent optical beam facilitates the alignment and packaging into the optical fiber. The low volume of the optical cavity reached also allows a single mode operation and high speed operation.

The following parts of the subsection consider the VCSEL: theory and fundamentals of operation; lasing conditions, radiation efficiency definition, state-of-the-art, speed limitations; selected technology for further investigation. This VCSEL principle work is based on the following literature: [37]-[97].

II.B.1.1 Theoretical fundamentals

The conventional structure is detailed further in Figure II-4. Three sections: Top Distributed Bragg Reflector (DBR), Bottom DBR and the lasing cavity placed between the 2 mirrors. The typical DBR consists of an alternating sequence of high and low refractive layer's index of a quarter wavelength thickness. These mirrors provide optical feedback for the standing wave, which is amplified inside the active layer along the longitudinal direction.

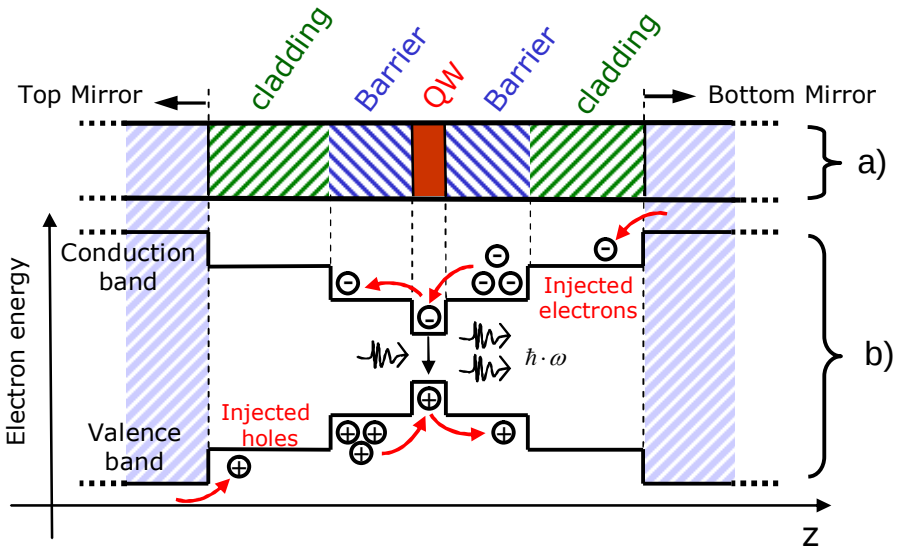

Figure II-4 – VCSEL lasing cavity details: a) material layer structure; b) Energy band diagram

Looking in detail inside the lasing cavity, we distinguish two regions: cladding layers and the active layer. In conventional VCSELs a barrier layer is added to the cladding layer as we can see in Figure II-4. It is sometimes called as separate-confinement heterostructure layer. The cladding and barrier layers achieve electrical and optical confinement as is illustrated in electron energy diagram Figure II-4 b). They are both fabricated in the same material, only doping is different introducing a difference refractive index. For the active layer different configurations can be used. In order to minimize the threshold current density a QW structure is used as the active layer instead of a bulk active layer. The advantage is the huge enhancement in differential gain, which is directly related to the threshold current density. The drawback is the reduction of the longitudinal confinement factor because of the use of Multiple Quantum Wells (MQW). To simplify the understanding, the illustration is made with single QW. The choice of the different materials of the lasing cavity is very important. A special attention is given to the lattice matching and the band gap energy for the reliability and wavelength operation, respectively. Common laser materials are GaAs, AlGaAs, InGaAs and InGaAsP depending upon the desired lasing wavelength. For operation in the 800 to 900 nm spectrum the principal material used is the ternary alloy $Ga_{1-x}Al_xAs$. The ratio x of aluminum arsenide to gallium arsenide determines the band gap of the alloy, and so the wavelength of the peak emitted radiation. InGaP, AlGaAs, GaAs, InGaAs, and InGaAsP are appropriate materials for lasers emitting at 650, 780, 850, 980, and 1300 nm, respectively. The stimulated emission in the QW occurs after the population inversion occurs, which is made possible by the carrier injection with an external pumping as we can see in the electron diagram.

II.B.1.2 Lasing Conditions

The Lasing threshold is the condition at which light amplification equals the total losses within the laser cavity. In a Fabry-Perot laser, at the lasing threshold a steady-state oscillation takes place and the magnitude and phase of the returned wave must be equal to those of the original wave which gives the follow round trip condition [37]:

$$1 = R_t \cdot R_b \cdot e^{2 \cdot L \cdot (\Gamma_z \cdot g_{th} - \alpha_{in})} \cdot e^{(-j \cdot 2 \cdot \beta \cdot L)} \qquad (2.2)$$

where Γ_z is the longitudinal confinement, g_{th} is the threshold gain, α_{in} is the cavity internal loss, L is the total cavity length and $\beta = 2\pi n/\lambda$ the phase propagation constant. R_t and R_b are the top and bottom mirror reflection coefficients, respectively. From the lasing threshold state Eq. (2.2) we extract the lasing condition in terms of the amplitude and the phase. The lasing amplitude condition can be written as:

$$\Gamma_z \cdot g_{th} \geq \alpha_T = \alpha_{in} - \frac{1}{2 \cdot L} \ln\left(\frac{1}{R_t \cdot R_b}\right) \tag{2.3}$$

where it gives the minimum cavity gain coefficient, necessary to overcome the total cavity losses. The mode which satisfies the Eq. (2.3) reaches threshold first where more than one mode can be excited. The round-trip phase condition of longitudinal mode wavelength can be obtained from the imaginary part of Eq. (2.2) given by:

$$2 \cdot \beta \cdot L = 2 \cdot \pi \cdot m \quad or \quad \upsilon = \upsilon_m = \frac{m \cdot c}{2 \cdot n \cdot L} \tag{2.4}$$

where m is an integer and n is the effective refractive index. The longitudinal cavity modes can be seen as different optical frequencies in which the light beam forms a standing wave. Figure II-5 shows two longitudinal modes corresponding to two standing waves at different frequencies. The output beam signal is given by 2 modes travelling in the same direction.

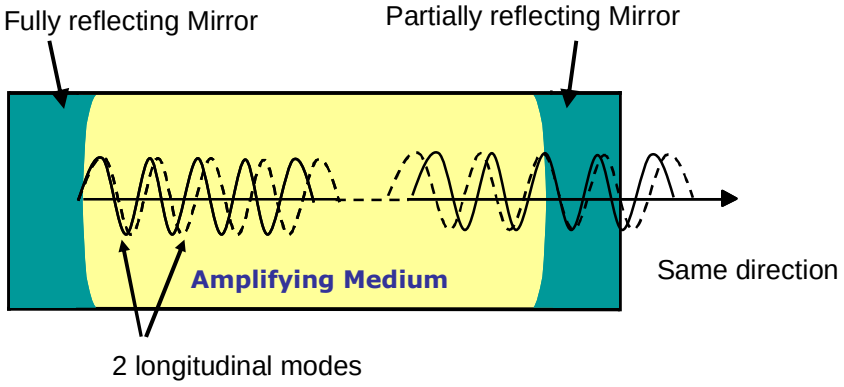

Figure II-5 – Illustration of two longitudinal operation modes propagating inside the cavity

The Fabry-Perot type face emitting laser uses cleaved facets as partial reflecting mirrors which can be assumed to be wavelength independent. As such resonance wavelength is only determined by the refractive index of laser cavity.

However on VCSELs, the phase of the DBRs influences the resonance wavelength too. A simple expression to estimate the longitudinal mode spacing of the VCSELs (assuming that the phase of the mirrors is independent of wavelength) is:

$$\Delta\lambda_m = \frac{\lambda^2}{2 \cdot n \cdot L} \tag{2.5}$$

If we consider the case of a VCSEL operating at λ=850 nm, L=1.2 μm and n=3.6 we obtain $\Delta\lambda_m$ = 84 nm which is of the same order of magnitude as the bandwidth of the optical gain spectrum. Therefore, the single longitudinal mode operation is favorable to VCSELs contrary to the edge emitting lasers. But it is important to notice that, depending on the lateral size of the VCSEL, several transverse modes can oscillate simultaneously.

Longitudinal modes imply light travelling on the same path but at different speeds, in other side, transversal modes got slightly different optical paths as depicted in Figure II-6. The output beam signal is given by 2 modes travelling in different directions. Each transverse mode

travelling a precise path can also creates different longitudinal modes. The lowest order transversal operation mode is the TEM00 corresponding to the beam intensity profile of a Gaussian function in the transverse direction of the propagation. This is the most desired mode since it propagates with the lowest beam divergence and so can be focused to a very small spot.

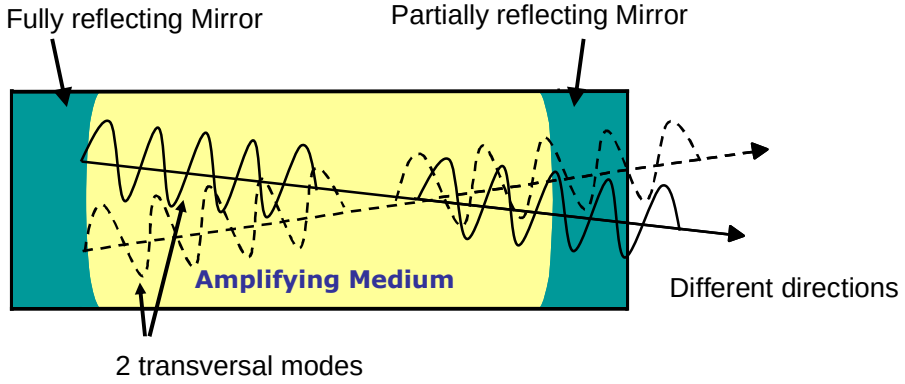

Figure II-6 – Illustration of two transversal modes propagating inside the cavity

The modes are bias dependent and the number of transversal modes can increase with higher bias current. The most typical second mode of VCSELs is the TEM11 mode which provides a doughnut-shaped beam which can be seen on the Figure II-6 where the angled mode is rotationally symmetric.

II.B.1.3 Radiation Efficiency

This section takes into account the conventional radiation efficiency figures of merit which are commonly found in the literature. The current injection efficiency (or internal quantum efficiency) indicate the fraction of injected electrons that is converted into photons through radiative recombination. Can be written as:

$$\eta_i\,[\%] = \frac{R_{rr}}{R_{tot}} = \frac{R_{rr}}{R_{rr} + R_{nr}} \tag{2.6}$$

where R_{rr} is the radiative recombination rate (related to the stimulated and spontaneous emission - $R_{stim} + R_{spon}$), R_{nr} is the non-radiative recombination rate and R_{tot} is the total recombination rate. Non-radiative recombinations reduce the internal efficiency by reducing the internal electron-holes pairs which emit light. The LEDs are lead by spontaneous emission where we can neglect R_{stim}. Since R_{spon} has the same magnitude as the R_{nr}, the η_i is approximately 50 %. In the case of lasers, as stimulated emission (R_{stim}) takes place, the internal efficiency goes up to 100 %.

The differential quantum efficiency is defined as the ratio of the increase in light intensity to the increase in injection current. It characterizes the percentage of generated coherent light that is available above threshold η_d. It is defined as the number of photons emitted outward per injected carrier. It is given as:

$$\eta_d\,[\%] = \eta_i \cdot \frac{Mirror\ Loss}{Total\ Loss} \tag{2.7}$$

Including the mirror losses, η_d can be written as:

$$\eta_d\left[\%\right]=\eta_i\cdot\frac{\log\left(1/R_t\cdot R_b\right)}{2\cdot L\cdot\alpha_{in}+\log\left(1/R_t\cdot R_b\right)} \tag{2.8}$$

A quantity of practical interest is the slope of the light-current (L–I) curve for $I > I_{th}$. It is known as the Slope Efficiency (S_{LD}), or responsivity, and is defined as the ratio of the increase in light intensity to the increase in injection current given by:

$$S_{LD}\left[W/A\right]=\frac{\partial P_{opt}}{\partial I_{LD}}=\frac{h\cdot\upsilon}{q}\cdot\eta_d \tag{2.9}$$

Above the threshold current I_{th}, the output power increases linearly with driving current I

$$P_{opt}\left[W\right]=\eta_d\cdot\frac{h\cdot\upsilon}{q}\cdot\left(I-I_{th}\right) \tag{2.10}$$

where $h\cdot\upsilon$, q are the photon energy and the electron charge, respectively. Figure II-7 shows an illustration of a typical L-I curve represented by the threshold current and by the slope efficiency. At low input current the spontaneous radiation occurs in the typical operation region of a LED. The stimulated emission dominates in the lasing region, giving a high and constant slope efficiency until the saturation region at high current injection, which is related to the thermal effects.

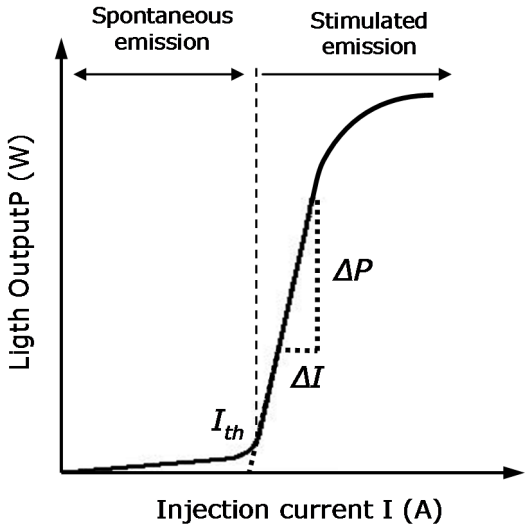

Figure II-7 – Typical laser L-I Curve

Another quantity of practical interest is the shape of the current-voltage (I–V) curve, expecting a current-voltage characteristic of the form, for an ideal device:

$$V\approx V_k+R_s\cdot I \tag{2.11}$$

where $R_s = dV/dI$ is the differential series resistance and V_k the Kink voltage which is related to the separation of quasi-Fermi energies that can be approximated by $V_k = h\cdot\upsilon/q$.

A typical laser radiation figure of merit is the wall-plug efficiency equally known as the power conversion efficiency. It is defined as the ratio of coherent light output power and electrical input power given by

$$\eta_c\left[\%\right]=\frac{P_{opt}}{I\cdot V}=\frac{P_{opt}}{I^2\cdot R_s+I\cdot V_k} \tag{2.12}$$

where V is the voltage and I the current applied across the laser diode. Substituting the Eq. (2.10) into Eq. (2.12) we get:

$$\eta_c[\%] = \eta_d \cdot \frac{h \cdot \upsilon}{q} \cdot \frac{I - I_{th}}{I^2 \cdot R_s + I \cdot V_k} \quad (2.13)$$

η_c increases with the decrease of the threshold current and a value higher than 50 % [43].

II.B.1.4 State-of-the-Art

Many industrial companies, universities and research laboratories have focused their activities in high speed VCSELs emitting at different wavelengths. Going from shorter wavelengths (850, 980, 1100 nm) to longer ones (1300 and 1550 nm) the technology complexity increases as well as the cost. Thereby, in the recent years, the shorter wavelength VCSELs become a center of a big interest. Thus we will focus our discussion on wavelengths of 850, 980 and 1100 nm with a special interest in 850 nm VCSEL.

The 850 nm VCSELs are the most interesting wavelength for LAN applications and will surely play an important role in the future optical communications. Different materials for active region can be used and have been reported, including GaAs [46] [49] [56]-[61] [67] [71] [78] [81]-[82], InGaAs [48], [50]-[51] [66]-[69], [87] and InGaAlAs [70]. New concepts in order to increase the VCSEL performance, like the modulation bandwidth, have been applied, including optical/electrical confinement techniques: oxide aperture [60] [61], proton implantation [50]] [59], Photonic Crystals (PhC) [53] [61] and a few years back double oxide aperture [66]-[69].

Bit rates up to 40 Gbit/s have been reached recently [66] [70] [75] using double oxide aperture, with an aperture diameter of 6-9 μm and using InGaAs QW (see Table II.4).

Table II.4 – State of the art for three wavelengths: 850, 980 and 1100 nm

λ(nm)	AUTHORS	FEATURES	ACHIEVEMENTS
850	P. Westbergh e al. 2010 [66] Chalmers University of Technology	strained InGaAs QW shallow etch (top DBR) double oxide aperture	I_{th}=400 μA for 7 μm device 23 GHz bandwidth 40 Gb/s operation @ 8 mA Pout=6.4 mW @ 10 mA
980	Y.-C Chang et al. 2007 [65] University of California	BCB InGaAs QW Deep oxidation layers Tapered oxide aperture Intracavity Bottom-emitting	Ith=144 μA for 3 μm device >20 GHz bandwidth 35 Gb/s operation @4.4 mA Pout=3.1 mW @ 7 mA
1100	T. Anan et al. 2007 [96] NEC Corporation, NR Laboratories	Polyimide InGaAs QW Ion implantation Buried tunnel junction Optimized active region	Ith<1 mA for 6 μm devices 24 GHz bandwidth 40 Gb/s operation @ 5 mA

In the case of 980 nm VCSELs active region materials can be GaAs [62], [92] or InGaAs [45] [47] [52] [54] [65] [73] [74] [86] [89]-[91]. Bit rates up to 35 Gbit/s have been achieved in

the last years [65] using tapered-deep-oxide aperture with an aperture diameter of 3 um and using InGaAs QW.

Lastly for 1100 nm VCSEL devices, the material used is InGaAs [55] [63] [72] [76] [96]. Bit rates up to 40 Gbit/s have been achieved [96] recently using tapered-deep-oxide aperture with an aperture diameter of 5 μm and InGaAs QW.

The Figure II-8 shows the slope efficiency evolution on the last years focusing on the short wavelength operation VCSELS, comparing the active material most used – GaAs and InGaAs. Over the years the slope efficiency increased approaching of 1 W/A for both materials.

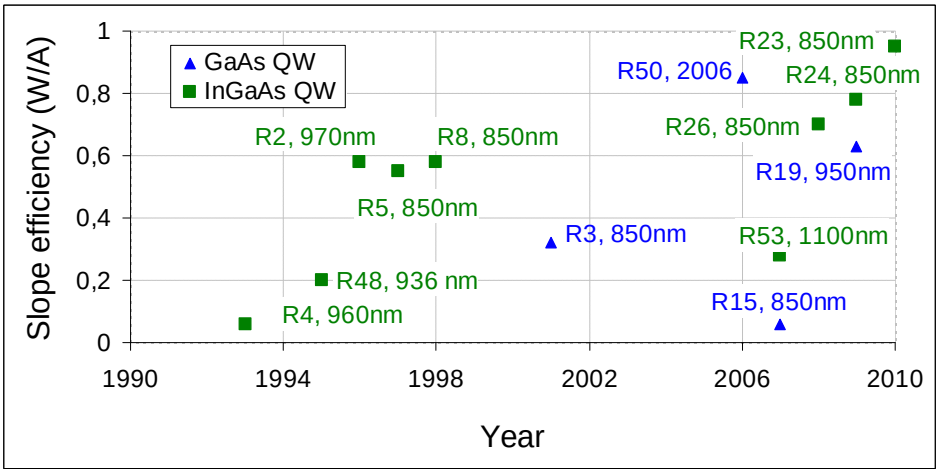

Figure II-8 – VCSEL slope efficiency as a function of the last years R2-[45], R3-[46], R4-[47], R5-[48], R8-[51], R15-[58], R19-[62], R23-[66], R24-[67], R26-[69], R48-[91], R50-[93], R53-[96]

We can see in Figure II-9 the threshold current evolution in the last years where it decreases quickly to values around 500 μA. It can be explained by the decrease on the size of the devices in order to reach high speed operation.

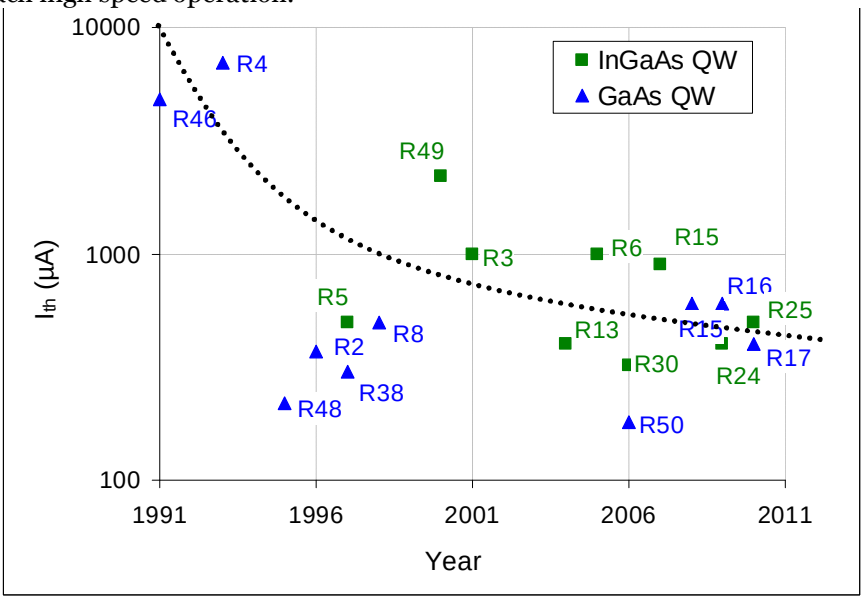

Figure II-9 – VCSEL threshold current as function of the last years focusing on the short wavelength range. R2-[45], R3-[46], R4-[47], R5-[48], R6-[49], R8-[51], R9-[52], R13-[56], R15-[58], R16-[59], R17-[60], R24-[67], R25-[68], R30-[73], R38-[81], R46-[89], R48-[91], R49-[92], R50[93]

We can see in Figure II-10 the efficiency evolution as a function of the device size.

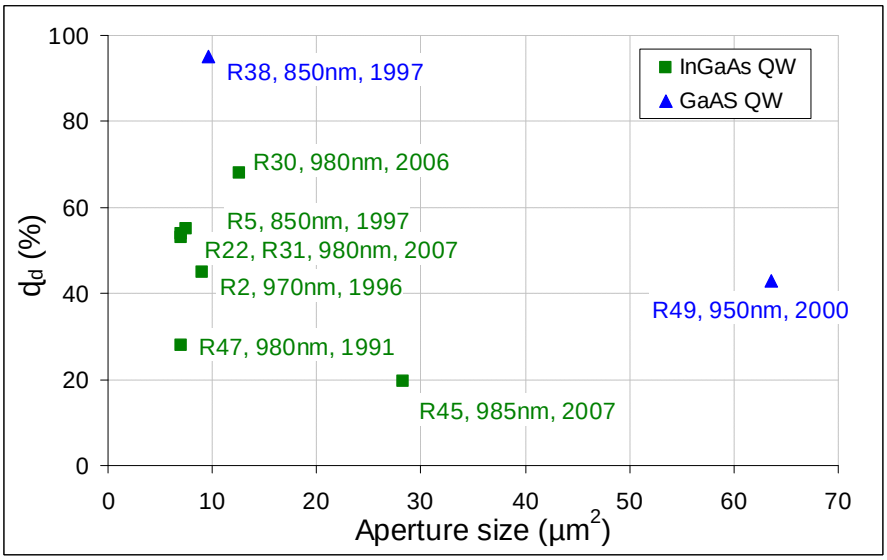

Figure II-10 – Differential quantum efficiency as a function of the aperture area size.R2-[45], R5-[48], R22-[65], R30-[73], R31-[74], R38-[81], R45-[88], R47-[90], R49-[92]

High differential efficiency can be achieved for small aperture sizes typically around 10 μm² which means aperture around 1.5 and 3 μm in terms of diameter. These results were expected according to Eq. (2.7), as small aperture diameter means small total internal losses, the total losses are lead by the mirror losses giving a high η_d. Single transverse mode operation requires oxide aperture smaller than 4 μm diameter [61] [81].

The cut-off frequency of the VCSEL response is shown in Figure II-11 as a function of date in years. The tendency is to use InGaAs-QW based VCSELs which provide faster devices up to 23 GHz (at 850 nm).

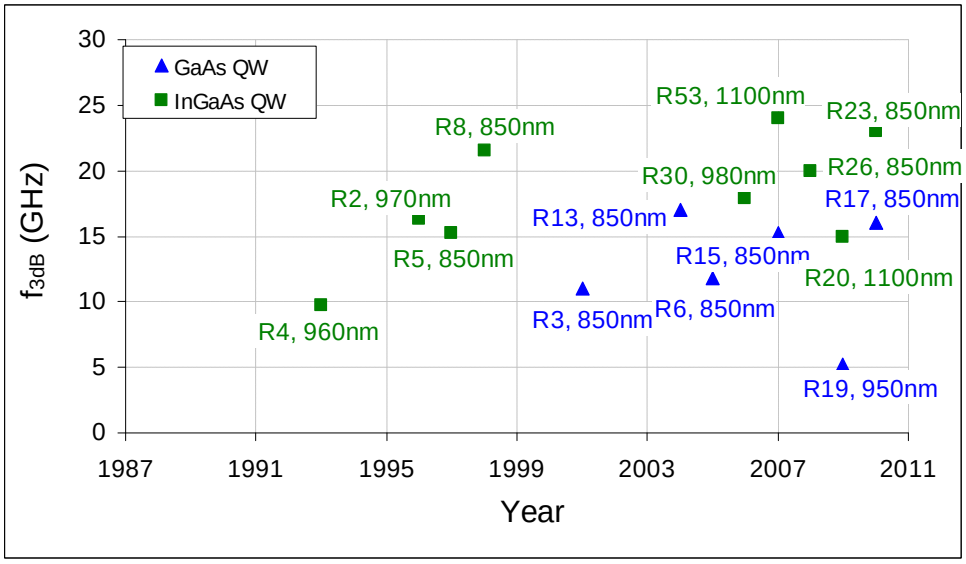

Figure II-11 – VCSELs cut-off Frequency as a function of the recent years within the short wavelength range focus. R2-[45], R3-[46], R4-[47], R5-[48], R6-[49], R8-[51], R13-[56], R15-[58], R17-[60], R19-[62], 20-[63], R23-[66], R26-[69], R30-[73], R53-[96]

As a synthesis, the recent main improvements in VCSEL technology are:

- The replacement of the GaAs QWs by the strained InGaAs QWs on the active material improving the device performances. It increases the differential gain, which

enhances the high-speed performances, and it also, suppresses the dislocation motion, improving the reliability.

- Current and optical confinement can vary applying different technology methods: oxide aperture, proton-implanted aperture, etched mesa, buried heterostructure and photonic crystals. The technology, which shows better results, is the oxide aperture with a double oxide layer approach. It decreases the parasitic capacitances allowing high modulation bandwidth reaching more than 20 GHz.
- It was found an evolution on the mirror (DBR) by the replacement of the conventional ternary compound AlGaAs/AlGaAs by the binary compound AlAs/AlGaAs. It introduces low thermal resistances and, therefore, reduces the self-heating effect.

More recently, 2013, a VCSEL operating at 56.1 and 57 Gbps was reported with a 24 GHz bandwidth at 850 nm with an aperture diameter of 7 and 8 µm, [97] and [98] respectively.

II.B.1.5 Speed Limitations

The purpose of this section is to present and explain in detail the different VCSEL speed limitations. The modulation bandwidth of the VCSEL is attributed to intrinsic and extrinsic components, as depicted in Figure II-12.

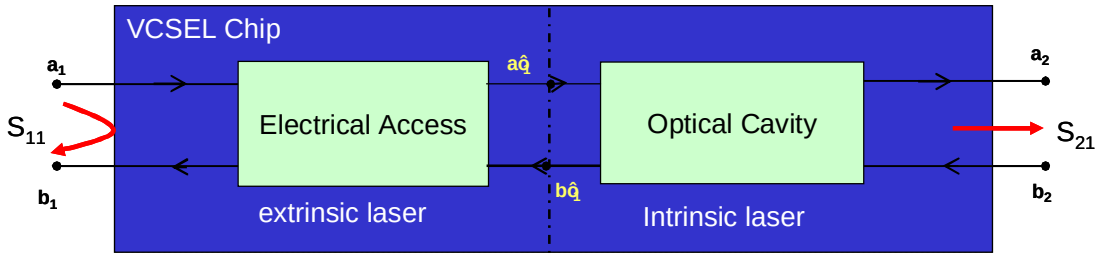

Figure II-12 – VCSEL functions of the device

The intrinsic laser is defined as the active region in the aperture area where carriers and photons interact to each other through absorption and emission phenomenons. The extrinsic laser (or parasitics) is defined between the intrinsic laser and driving circuit. We can split into the pad and chip parasitics at the metal contacts.

The overall modulation frequency response is typically given as a 3rd order system:

$$H(f) = \frac{1}{1 + j \cdot \frac{f}{f_P}} \cdot \frac{f_R^2}{f_R^2 - f^2 + j \cdot f \cdot \frac{\gamma}{2\pi}} \qquad (2.14)$$

where on the left side a low pass filter represents the electrical parasitics effect on the access lines (f_P is the parasitic cutoff frequency). On the right, a second order function models the optical behavior of the laser: f_R is the relaxation oscillation frequency and γ the damping factor.

Considering the intrinsic laser limitations, the modulation response can be approximated to a 2nd order system as:

$$H(f) = \frac{f_R^2}{f_R^2 - f^2 + j \cdot f \cdot \frac{\gamma}{2\pi}} \qquad (2.15)$$

From Eq. (2.14), the relaxation oscillation frequency is the natural oscillation frequency between carriers and photons in the laser cavity. It is given by [43]:

$$f_R\left[GHz\right]=\frac{1}{2\pi}\cdot\sqrt{\frac{\eta_i\cdot v_{gr}\cdot a}{q\cdot V_a}}\cdot\sqrt{I-I_{th}}\propto\sqrt{\frac{1}{V_a}}\,, \tag{2.16}$$

where v_{gr}, a, V_a are the group velocity, the differential gain and the active region volume, respectively. As shown in Eq. (2.16) it is important to get a higher differential gain and to reduce the volume of the active region in order to increase the relaxation resonance frequency. Since the relaxation oscillation frequency increases with bias current, a figure of merit to evaluate the efficiency of an intrinsic laser modulation is the D-factor that evaluates the slope between the relaxation oscillation frequency and the bias current:

$$D\left[GHz/\sqrt{mA}\right]=\frac{f_r}{\sqrt{\left(I-I_{th}\right)}} \tag{2.17}$$

Another important parameter which evaluate the device's overall high speed performance is the Modulation Current Efficiency Factor (MCEF):

$$MCEF\left[GHz/\sqrt{mA}\right]=\frac{f_{3dB}}{\sqrt{\left(I-I_{th}\right)}} \tag{2.18}$$

It is often given to specify the increase of the 3dB cutoff frequency (f_{3dB}) of the modulation transfer function. If the parasitics and damping are small enough f_{3dB} can be written as

$$f_{3dB,Thermal}\approx 1.55\cdot f_R \tag{2.19}$$

The damping factor increases proportionally to the square of f_R :

$$\gamma\propto N_p\propto f_R^2 \tag{2.20}$$

The proportionality between γ and f_R^2 is the K-factor, which determines the intrinsic maximum 3dB frequency (neglecting electrical parasitics)

$$f_{3dB,damping}\approx\sqrt{2}\cdot\frac{2\pi}{K} \tag{2.21}$$

The extrinsic laser parasitic (resistances and capacitors) limits the modulation bandwidth further because of the low pass RC-filter response made with the device intrinsic component

$$H\left(f\right)=\frac{1}{1+j\cdot\frac{f}{f_P}} \tag{2.22}$$

where f_P is the electric cut-off frequency. It has been proved that parasitics play a major role in modulation bandwidth limitations. That is why it is of great interest to develop an optoelectronic model in particular for the electrical access to optimize parasitics effect.

II.B.1.6 Selected VCSEL Technology

The VCSEL technology has been selected for this PhD, based on comparative measurements since it achieves high bandwidth, high power and linearity together with low Relative Intensity Noise (RIN). Philips Technologie GmbH U-L-M Photonics has been chosen (ULM VCSEL). Its platform is based on mesa etching and subsequently laterally oxidized current apertures.

General details about the ULM VCSEL technology are extracted from white papers [120]-[123] available in [119]:

- The epitaxial structure used for the fabrication consists of high contrast top- and bottom AlGaAs DBR, typically built of 32 and 24 layer pairs, respectively.
- Three GaAs QWs are embedded in $Al_{0.2}Ga_{0.8}As$ barriers.
- The mesas are formed by wet chemical or dry etching down to the current confinement layer.
- Polyimide passivation is used.
- Oxide confinement is realized to achieve a double oxide aperture.
- Applications targeted with a bandwidth in excess of 10 Gbps

The chip layout of the 250x350 µm² footprint design is shown in Figure II-13.

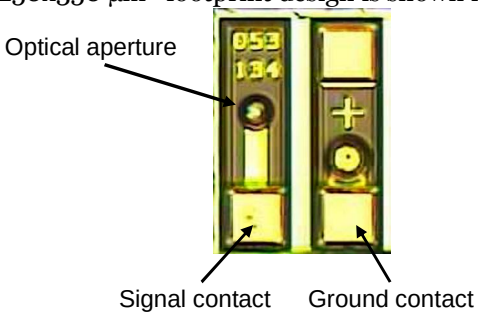

Figure II-13 – 10 Gbps VCSEL photography from Philips Technologie GmbH ULM Photonics: 8µm aperture diameter [119].

A technology evolution is explored in Chapter VI, based on GaAs active material with epitaxial optimization in the direction to reach 20 Gbps applications.

II.B.2. Heterojunction Bipolar Phototransistor

Phototransistors are of main interest as photo-detected current can be amplified in the same device. Phototransistor has typical base and collector layers larger than the conventional transistor to provide an extra access for the optical input. This transistor is then a 3-ports heterojunction bipolar phototransistor (HPT) with two electrical ports and one optical access. The HPT can use the 3 electrical terminals corresponding to a 3 terminal (3T) operation, or the base connection can be left as an open circuit corresponding to a 2 terminal (2T) operation. The general structure of an HPT is depicted in Figure II-14.

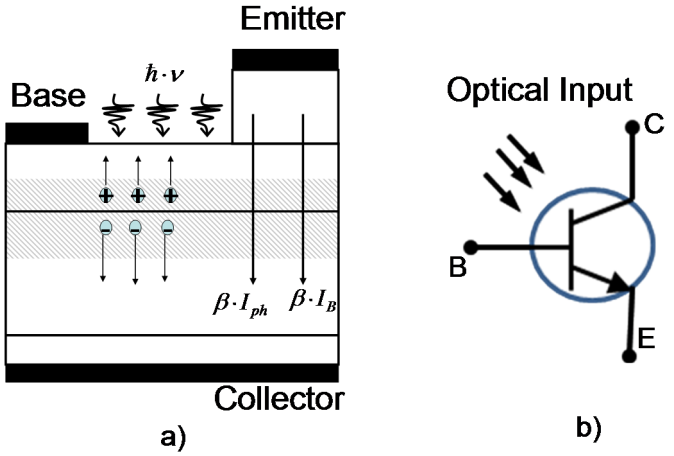

Figure II-14 - HPT: a) basic principle; b) schematic symbol [99].

HPTs are well known as high gain optoelectronic devices and as a low cost and compact photodetector. But they do not have a very high frequency response, because of the large capacitance associated with the base-collector junction. This junction is designed to be relatively large in order to pick up sufficient quantities of light. SiGe HPTs offer a solution to balance this effect by reducing the RC limitations through a highly doped base, thus enabling the potential of a direct integration of a high speed detector directly into a commercial Silicon IC technology.

II.B.2.1 State-of-the-Art of the SiGe HPTs

SiGe layers into photodetectors were first meant to detect light at 1300 nm and 1550 nm wavelength through the use of multi-quantum-wells (MQW) structures and super-lattices (SLS). However, this approach proved inefficient due to critical thickness limitations and low quantization effects into the MQW. Structures were essentially photodiodes, but also MQW phototransistors.

First SiGe HPTs were proposed, however on a different basis: to improve the speed of silicon detection at 850 nm using single SiGe layer into the base rather than SiGe MQW in the base-collector junction. The latter was indeed proved to slow down photodetection mechanism as holes and electrons had to flow up and down across quantum wells energy barriers. The first experimental appearances of SiGe HPT ocurred in 2003 [101] [102] and then in [99] with theoretical developments previously in [103] [99]. It is important to notice that the approach follows a convergence scheme between optics and electronics, providing photodetection into commercial available SiGe Heterojunction Bipolar Transistor (HBT) technology, named as a core technology to the phototransistors. Two other groups joined the move, with either AMS SiGe BiCMOS technology [99] or IBM SiGe BiCMOS technology [107].

A group in Austria [108] had in parallel a different approach while using SiGe layers of HBT to improve the detection of Silicon photodiode in the blue region to provide high speeds into blue-ray DVD. Equally, some combinations of different SiGe strain onto SiGe virtual substrate were studied in [109] and photodiode-phototransistor structures were proposed in [110]. A previous approach was to take benefit of the SiGe epitaxy to form a PiN integrated into a BiCMOS process, developing thereafter a trans-impedance amplifier (TIA) combined with SiGe/Si monolithically integrated photodiode [111].

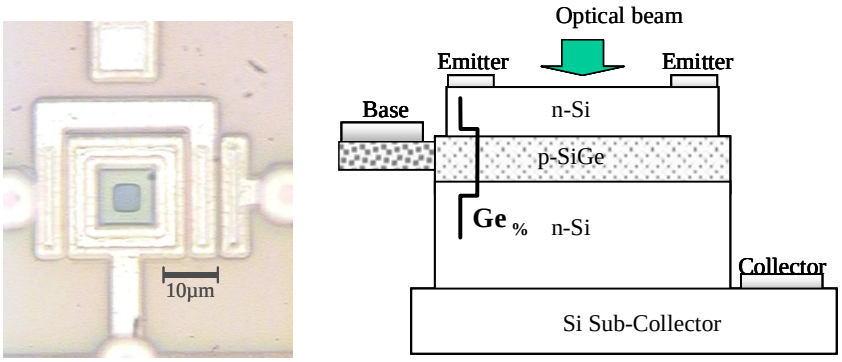

a) b)

Figure II-15 – SiGe HPT: a) Photograph of the top view with a 10x10 µm² optical window in the emitter; b) Sketch of the vertical stack.

ESYCOM experience on SiGe HPTs started in 1999 by Jean-Luc Polleux, [99] [103] [104]. First a SiGe HPT was developed into a commercial Bipolar SiGe process from Atmel GmbH [101], now named Telefunken GmbH, and the physical modeling was developed in [102]. Those HPTs were developed in the SiGe1RF generation of the Atmel GmbH SiGe technology. The HBT was made with an abrupt profile of Germanium into the base, as depicted in Figure II-15. This permits to have high Germanium content in the 20-25 % range. It was evaluated to be 23 % by means of physical simulations. Therefore, the optical absorption in the base is favored, and from an electrical point of view, the HBT can be fast even if large in size. This is useful in making phototransistors with large optical windows while being fast.

II.B.2.2 Development on SiGe HPT: approach and technology

Previous SiGe HPTs were developed into a SiGE1RF technology of Atmel GmbH. This technology was limited to 50 GHz f_T/f_{max}. It is important to move forward to integrate phototransistor into faster SiGe HBT technology.

The Telefunken technology evolution (SiGE2RF) exhibits f_T and f_{max} as high as 80 GHz. This makes this technology able to provide circuits working above 10GHz and potentially up to 60 GHz in some configurations [112]. The minimum critical dimension is controlled by the emitter width and is a value of 0.8 µm, spacer included. During the process, those spacers are removed and the final smallest emitter size is 0.5 µm.

As in SiGE1RF technology, the Germanium content is high and might be almost flat across the base. However, no information is given in detail, as this is key industrial information for the company.

In the frame of our relation with Telefunken, a Non-Disclosure Agreement (NDA) has been signed and no information about the detailed process cross-section can be given. It is however important to give the general scheme of the cross-section of the HBT which is given in Figure II-16:

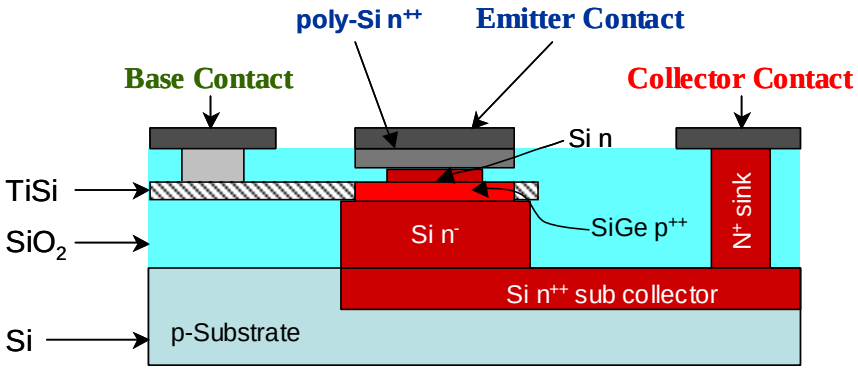

Figure II-16 – Schematic cross-section of SiGE2RF technology from Telefunken

SIGE2RF is a 0.8µm lithography double-poly heterojunction bipolar technology for wireless communication and fiber optics. The minimum emitter size is 0.8x1.4 µm² for vertical npn HBT transistors. This technology has two transistor types: one with a selectively implanted collector (SIC) and the other one without. The difference between them is the additional mask required by the SIC-transistor, influencing the high frequency performances and static characteristics. This option allows transition frequency (f_T) to reach the 80 GHz value. SIC transistor reaches up to 75-80 GHz, while non-SIC transistor reaches 50 GHz only.

The design of the phototransistors involves using the layers that are used to design a SiGe HBT as specified by the Telefunken SiGe2RF design kit. The main concern to fabricate a heterojunction bipolar phototransistor (HPT) was the optical injection and the optimization of the cut-off frequency. This work was recently continued in Marc ROSALES, PhD in ESYCOM laboratory. Four topology approaches were pursued as sketched in Figure II-17, but only one is presented here since it is the one chosen because of its opto-microwave performance.

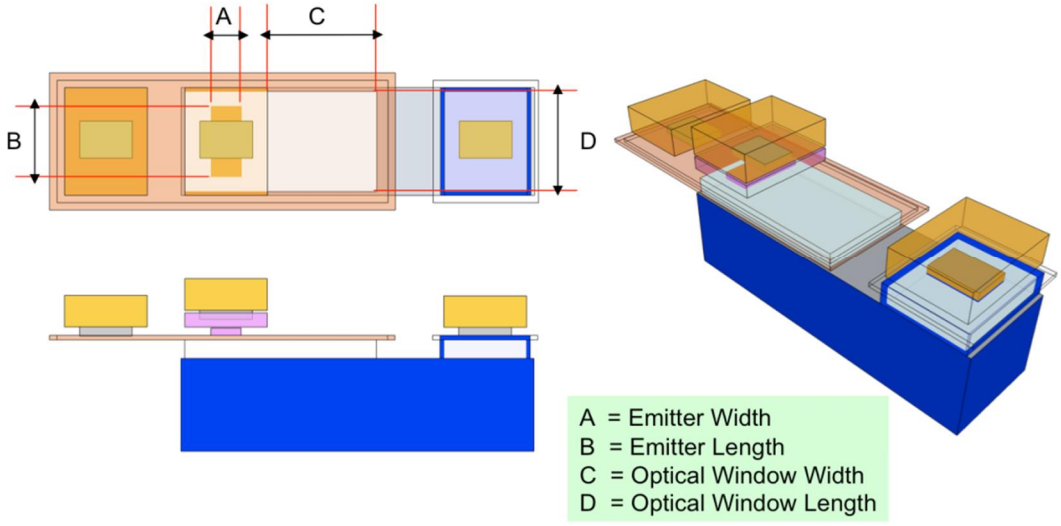

Figure II-17 – SiGe HPT's schematic cross-section of the "initial" run1

This topology is designed by extending the emitter and the emitter polysilicon over the optical window. This results in an increase of width of the inherent transistor.

Different technology options could be realized, but, again, for our study, we focus on a specific device which is with squared shape (SQ), with extended emitter, base, collector (xEBC) and with etched oxide (eO). The nomenclature used from now on is SQxEBC_eO HPT.

The work on phototransistor at the ESYCOM lab has been carried out by Marc Rosales and Julien Schiellein, both PhD students, focusing their work on HPT layout optimization

(respectively in SiGe and InGaAs/InP), optoelectronic integrated circuit integration development for RoF applications [1], [139] and phase noise signal regeneration, [115]-[116]. The SiGe development will continue on with Zerihun Tegegne, PhD student, going towards the millimeter-wave operation of the RoF data communications applications.

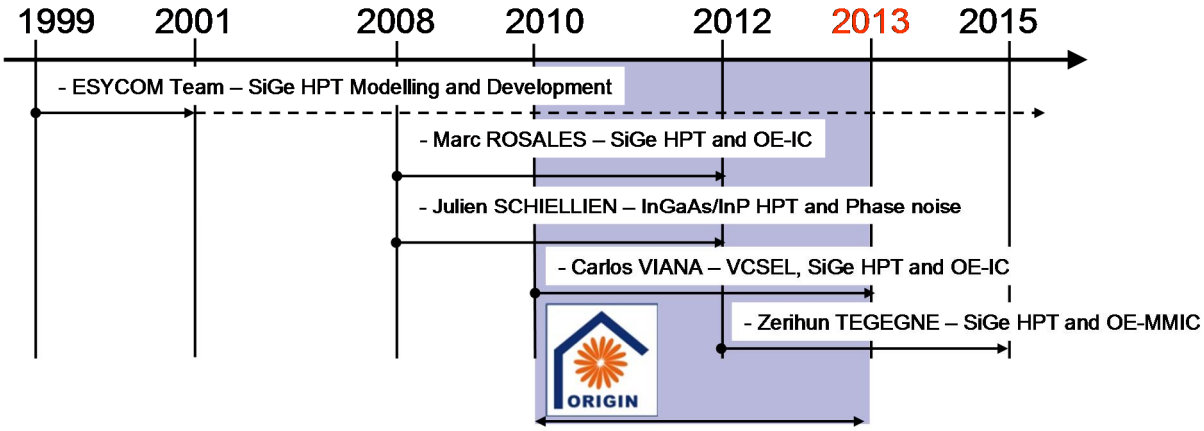

Figure II-18 - ESYCOM laboratory roadmap

In the case of this work, we are not concerned about SiGe HPT technology development, but on its performances which will be described in Chapter III. Together with its integration into the ORIGIN RoF system and its system performance evaluation for the first time in Chapter V.

II.C. The ORIGIN Project: the ultra high data rate Wireless Network in the Home

The ORIGIN (Optical Radio Infrastructure for Gigabit/s Indoor Network) project was a national project dedicated to increasing the data rate and the radio coverage inside the home using the combination of the 60 GHz wireless communication technology and RoF technology. The concept is shown in Figure II-19 which presents the future wireless communication network with different services and devices. A home network concept is created using optical fiber infrastructure to interconnect the different rooms of the house each other. Antennas collect the wireless signal and feed RoF transceivers to distribute the signal to each room simultaneously. At the other end of the fiber, another RoF transceiver (TRoF) converts the modulated optical signal and radiates it into the air.

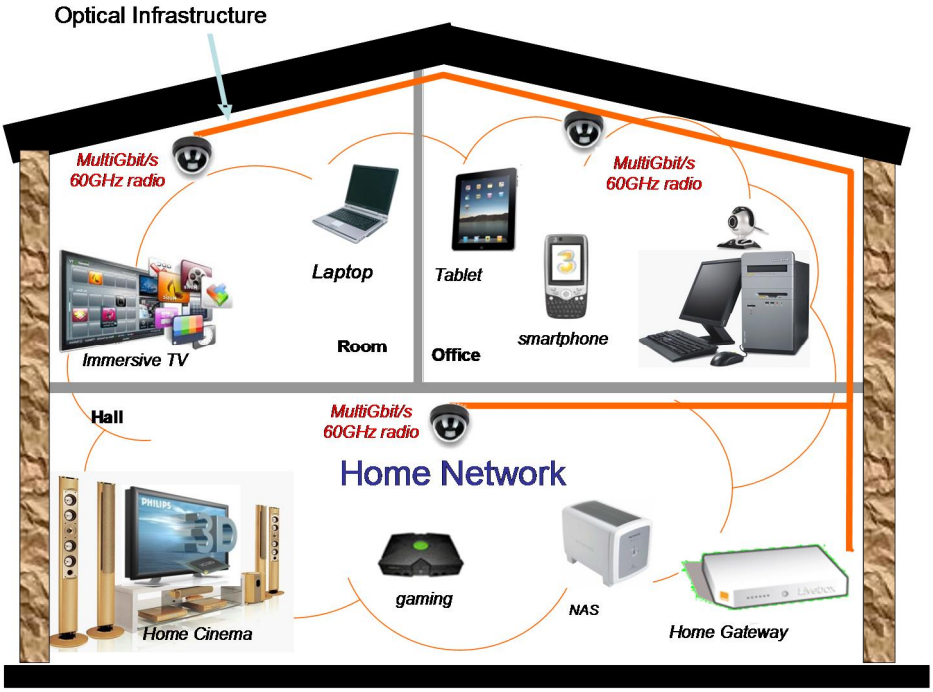

Figure II-19 - ORIGIN project concept illustration

On one hand, the 60 GHz band communication with high bandwidth availability allows us to reach multigigabit/s communication. On the other, the RoF technology permits to transpose the 60 GHz wireless signal to different rooms creating a domestic cloud concept, with some important characteristics:

- MultiGigabit/s communication system;
- Low-Cost;
- Low radiative electromagnetic technology;
- Flexible and transparent technology;
- New revolutionary services toward a domestic cloud;
- Domestic Cloud.

The ORIGIN project started in January 2010 for three years and a half and finished in July 2013. It was composed of different teams of industrial and academic partners, see Figure II-20.

Figure II-20 - ORIGIN Partners

The project is transverse and covers multidisciplinary fields such as:

- market and players analysis to identify services and applications of interest with the goal to create the system specifications;
- RoF transducer prototype design, characterization and assembling. The performances are measured and simulated in the course of this PhD within the whole system.
- A pre-industrial prototype demonstration platform is created and presented here.

In terms of organization it was based on the teamwork between the different partners who were divided into seven sub-projects (SP), as depicted in Figure II-21.

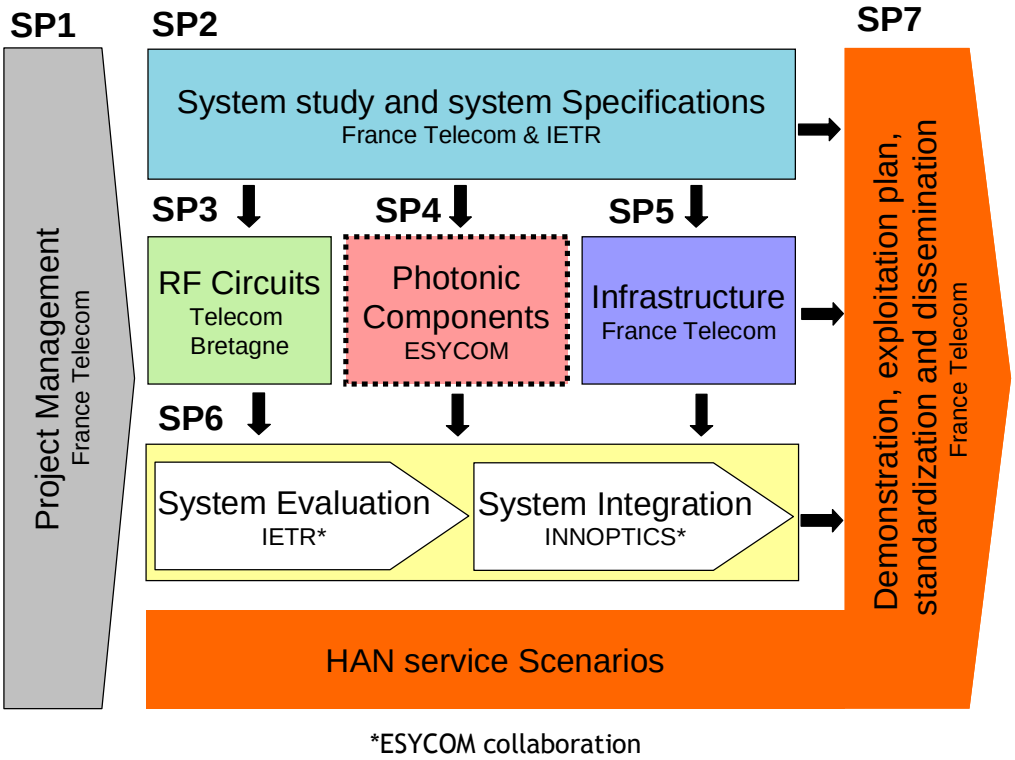

Figure II-21 – The ORIGIN structure and the Partners location of each sub-project

This PhD subject was proposed in the frame of the SP4 team, responsible for the development of optoelectronic and photonic circuits within the RoF infrastructure domain for 60 GHz wireless communications and SP6 team, responsible of TRoF integration and system evaluation. The project should lead to a final prototype as an eventual future commercial solution.

II.C.1. ORIGIN architecture

Two different architectures are considered: the Point-to-Point (P2P), for its simplicity, and the Multipoint-to-Multipoint (M2M) since the goal is to create HAN in order to cover the whole house. As we can see in Figure II-22, in the M2M concept each radio cell is connected to a TRoF in order to expand the coverage distance to the whole house.

The RoF Transducer nomenclature from now on is "TRoFG<.N>" where G corresponds to the TRoF generation ("1", "2" or "3") and the ".N" is the TRoF ID number (optional). For instance: TRoF2.3 is the TRoF of the second generation with ID number 3 (which can be seen as house room number 3).

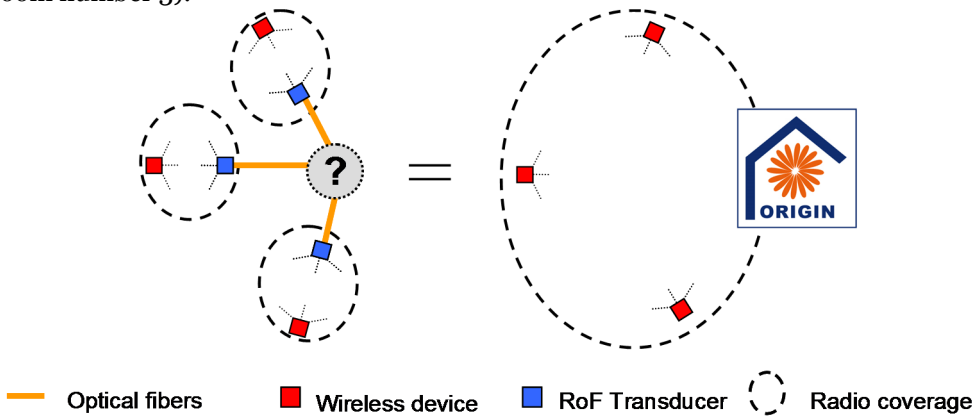

Figure II-22 - ORIGIN Home Area Network concept

Consequently, with optical fiber we connect together all rooms, no matter their position inside the building in order to create a single equivalent radio cell, as depicted on the right side of Figure II-22. Considering the center node two architectures appear: Optical Multipoint-to-Multipoint with Electrical multiplexing (MME) and Optical multiplexing (MMO). In ORIGIN project the RoF transducer is based on the IF-RoF concept, as shown in Figure II-23, where both 60 GHz and 5 GHz blocks are integrated. The 60 GHz block has both TX and RX modules in order to provide the duplex communication with downlink and uplink paths. The uplink path is realized by a low noise amplifier (LNA) as a first amplification stage, followed by a mixer for the down conversion. In the download link, an amplification stage with High Power Amplifier (HPA) is planned after the up conversion mixer. A filtering stage may be used to remove eventual spurious frequencies from the mixer nonlinear operation. The 60 GHz antennas were integrated on both mm-wave modules. The 60 GHz block was developed by Telecom Bretagne partner (it will be described in Chapter V, section V.B).

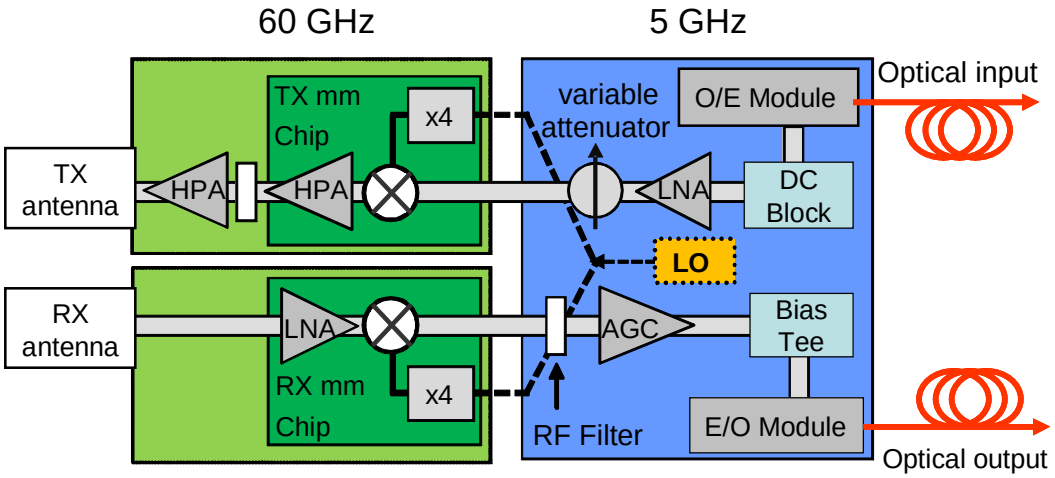

Figure II-23 – Block diagram of the RoF transducer based on IF-RoF concept

The 5 GHz IF block does the interface between the optical signal and the 60 GHz signal. The E/O conversion is made by a laser diode and the reverse (O/E conversion) by a photodetector. The electrical signal from optical-to-electrical conversion is amplified and a cascaded variable attenuator controls the power level injected into the mixer on the mm-wave board. In the uplink path, the signal coming from the down conversion stage is filtered and controlled by an Automatic Gain Control (AGC). The AGC is very important since the wireless device can operate at different distances from the RoF transducer.

The free space losses are given by the following equation:

$$Losses[dB] = 20 \cdot \log_{10}\left(\frac{4 \cdot \pi \cdot d_0 \cdot f_{RF}}{c}\right) \qquad (2.23)$$

where d_0 is the free space propagation distance, f_{RF} the operation RF frequency and c is the speed of light in a vacuum.

For the 60 GHz signals and distances between 30 cm (typical minimum distance) and 10 meters (typical maximum distance) the free-space losses varies from 57.5 dB to 88 dB. That corresponds to a high signal power dynamic range up to 31 dB. The AGC amplifier is, thus, essential to provide the optimized laser diode input power. This target corresponds to avoid the compression gain region for high received power (wireless device close to the RoF transducer) and the laser noise effects of low received power.

The Point-to-Point (P2P) architecture is the simplest and fundamental architecture where two radio cells are connected each other by the optical fiber. Figure II-24 represents the direct path of the P2P architecture known as optical tunnel providing a direct link between the radio emitter and receiver. This architecture is limited to the coverage of 2 rooms. It serves the project as a reference system. From the left to the right of Figure II-24 the wireless radio emitter emits the 60 GHz wireless signals through free space which is received by the TRoF antenna of the first room (TRoF3.1 e.g.). The signal is then amplified, filtered and down converted to an intermediate frequency before transmitting through the RoF block. RoF transducer provides the radio signals conversion to optical (E/O conversion – TRoF3.1), optical tunnel (optical fiber) and, again; conversion to electrical (TRoF3.2 - O/E conversion). The optical signal is recovered on the second room amplified and up-converted to 60 GHz where is transmitted by the antenna (TRoF3.2). The signal is finally propagated through the free space and recovered by the wireless radio receiver.

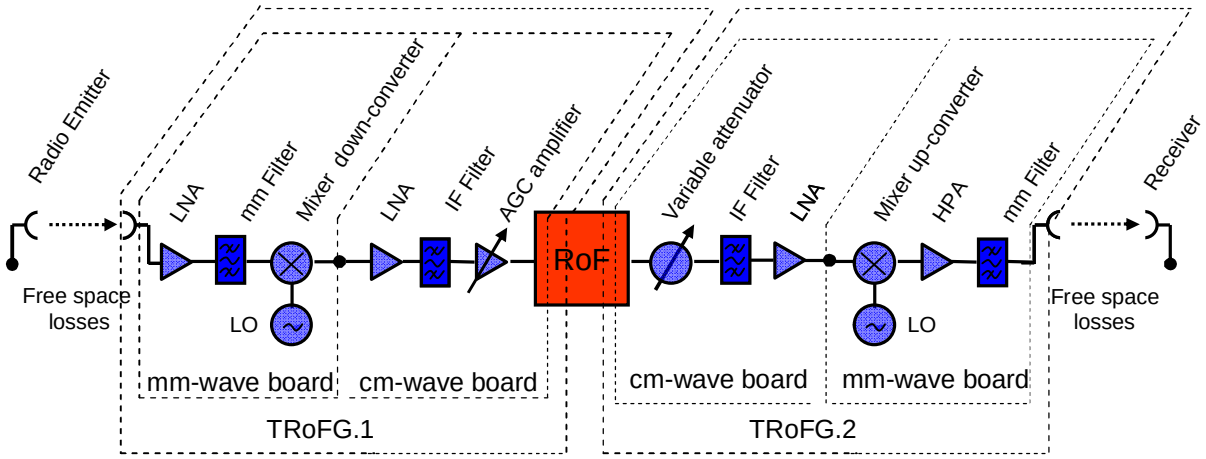

Figure II-24 - Point-to-point RoF architecture based on IF-RoF concept

In terms of RoF devices a compromise between cost, integration and performances had to be found where the RoF link was decided to be based on an IM-DD (Intensity Modulation-Direct Detection) architecture: On E/O module, direct intensity modulation using laser diode (LD); On the O/E modules, direct detection using two device options: a photodiode (PD) or a heterojunction bipolar phototransistor (HPT). A multimode fiber operating at 850 nm was chosen because of a simplified packaging and an easier alignment of end devices at a lower cost. On the other side transverse multimodes of the LD can degrade the SNR. The choice of the optoelectronic devices is directly related to Intermediate Frequency (IF) architecture approach in which allows relaxed performance and cost.

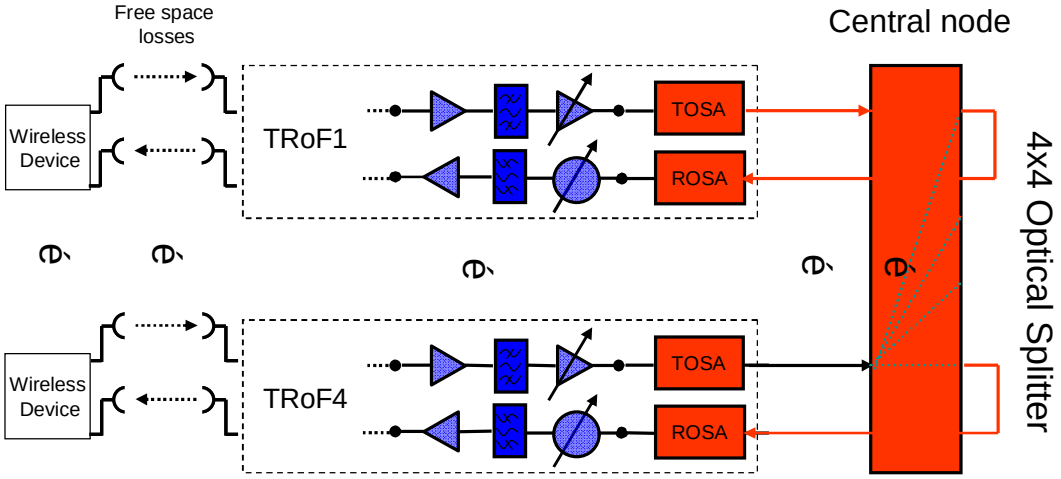

Figure II-25 - Optical Multipoint-to-Multipoint architecture with Optical multiplexing (MMO)

As depicted in Figure II-25 the MMO architecture is based on an NxN optical splitter (between the Transmitter Optical Sub-Assembly (TOSA) for the laser source and the Receiver Optical Sub-Assembly (ROSA) for the photodetector). The optical splitter is characterized by its optical losses and modal behavior which both can limit the number of communicating rooms. This directly influences the optoelectronic device choice in terms of performances and cost. Nevertheless, the optical nature of the central node provides low power consumption and full transparency to the protocols. Every E/O device of each remote antenna is connected to an input of the optical splitter and the O/E device to an output of the optical splitter. This means that the transmitted signal is divided between each optical output feeding every antenna.

A radio protocol is needed to manage the communication in order to avoid signal collision problems. The simplicity of the central node by using only a simple passive optical splitter providing transparency can have, however, some challenges: every TOSA emits an optical power, even with no data, which can saturate the ROSAs and add noise. The laser simultaneous operation will generate laser beating creating spurious on the output spectrum, which may deteriorate the SNR. An improvement on the radio protocol was proposed in [113]-[114] to avoid this effect which could be considered as collision avoidance.

In the MME architecture (Figure II-26) the central node is based on an NxN RF splitter. As we can see an extra optoelectronic stage conversion is needed for the RF splitter interface. However, in this architecture, there is no laser beating phenomenon.

However, the noise, the nonlinearities and the consumption are increased by the introduction of the extra optoelectronic devices. This architecture gives full transparency property to the system and do not require the radio protocol for collision avoidance as the laser beating problem is solved out. At the end the system can be more relaxed on the optoelectronic devices, but the complexity and the cost increase. A trade-off must be found between performance, complexity and cost.

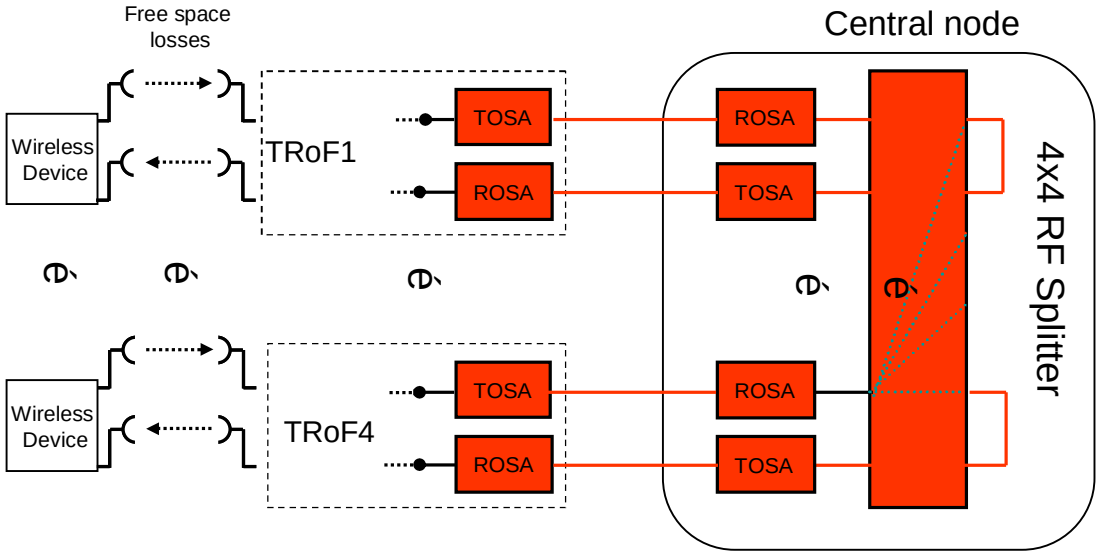

Figure II-26 - Optical Multipoint-to-Multipoint architecture with Electrical multiplexing (MME)

II.C.2. RoF transducers evolutions

The first generation of RoF transducer prototype (TRoF1) was based on commercial low cost devices in order to test the ORIGIN concept and to provide a reference for the next generations. It is composed of a Vertical Cavity Surface Emitting Laser (VCSEL) as a light source from Finisar Company packaged and integrated into a TOSA module. The Finisar TOSA module operates at 850 nm and is based on Gallium-Arsenide (GaAs) VCSEL. This is a multimode operation laser with low-cost applications target providing LC connector on the optical interface and SMA connector on the electrical interface. On the other side the O/E conversion is implemented by a ROSA module from the same company. The Finisar ROSA module is based on a GaAs PIN photodiode operating at 850 nm wavelength with an integrated Trans-

Impedance Amplifier (TIA). Both TOSA and ROSA modules were designed for 10 Gbit/s digital applications.

The second generation of RoF transducer prototype (TroF2) is proposed in this thesis to improve the system performances by changing the Finisar TOSA module. An ULM Photonics GaAs VCSEL is proposed to be the TOSA core using a home-made package in connection with INNOPTICS partner. The ULM Photonics VCSEL should improve the system performance in terms of frequency response (gain), noise and nonlinearities. On probe characterization is performed with the target of link system optimization and to provide information to create a model which enables the link system design and optimization. Electrical interface is developed for the TOSA module. An interconnection substrate is optimized and considered to interconnect the VCSEL. Preliminary optimizations are considered to prepare future matching networks that will feed TRoF3. The optical interface is created using a mechanical receptacle based on a ball lens optical coupling technique. Both electrical and optical interfaces are developed with INNOPTICS partner.

Last generation (TRoF3), but not least, aims to improve the system from the TRoF2 mainly on the photodetector side, replacing the Finisar ROSA module by a home-made SiGe ROSA module solution. The ROSA module is based on SiGe Heterojunction Bipolar Phototransistor (HPT) technology. The packaging and integration are based on the previous home-made TOSA. Improvements are employed to enable matching networks and multi-chip integration to optimize the complete SiGe based ROSA. Then the TRoF3 pretends to improve the system performances by the low cost solution offered by the SiGe photodetector technology.

II.D. Summary and Discussion

The evolution on the broadband wireless network towards the multiGbit/s data ranges is inevitable taking in consideration the increase of wireless devices and the required quality of service. The 60 GHz band, allowing four channels with 2 GHz bandwidth, is a potential solution with the recent Wi-Fi standardization (IEEE 802.11ad). To leverage the low distance range of the 60 GHz propagation, the RoF technology is a suitable solution. At the end the combination between 60 GHz wireless and RoF technology is essential to create a home network allowing multiGbit/s data rates. These two technologies define the ORIGIN project where a low cost RoF transducer (TRoF) is developed for this purpose. The choice of multimode 10 Gbps optoelectronic modules operating at 850 nm appears to be the most suitable solution for the low range operation at low cost. From the three most important data communication windows, 850 nm provides a less complex source and a more relaxed packaging of OE/EO devices taking into consideration alignment issues. VCSEL technology is a promising solution. When operating at a low wavelength range, cut-off frequency up to 23 GHz was found in the literature. On the photodetector side operating at the same wavelength the SiGe HPT technology is an interesting solution since it provides the perspective of very low cost and high integration capability by direct integration of the photodetector and integrated circuits together on Silicon.

The challenge for the RoF system to distribute the 60 GHz wireless signal into the home comes from the noise, bandwidth and linearity of the optoelectronic modules where the IF-RoF approach was chosen. Three RoF transducer generations are designed: the TRoF1 which is based on commercial TOSA and ROSA modules to be a reference for the next generations; the TRoF2 which intends to improve the TOSA module and the TRoF3 which intends to have an optimized system (cm and mm chain) and should enable the integration of a SiGe ROSA for the first time. The improvements are on the gain and nonlinearities of both TOSA and ROSA with low cost. Previous studies from ORIGIN partners in terms of multipoint to multipoint architectures reveals the MMO architecture to be simpler, but with difficulties due to multi laser operation: ROSA saturation and laser beating. The MME architecture, despite consuming more and needing extra optoelectronics modules, reveals subsequently to be the most suitable and keep fully independent from the protocol.

Chapter III - **E/O and O/E die characterizations**

This chapter investigates on the low cost EO/OE components for the ORIGIN project with the topic to look for advanced chip. It is vital to evaluate in depth their performances through original setups before to select them for a further integration. Noise and linearity are key points for the performances of the RoF system. This study is focused on two technologies of choice: the Philips ULM Photonics 850 nm 10 Gbps VCSEL technology, which was selected due to its high bandwidth, but also for its first experimental evaluation that reveals its high potential in terms of power and linearity; The SiGe HPT which is believed by our team to be a novel technology with the promise of a great integration capability on Silicon and interesting analog characteristics for RoF applications. The characterization at the die level is important as it will be used to feed the model with data and to prepare their integration in an optimized module before being integrated into the whole ORIGIN architecture. Results will also feed the state-of-the-art of those advanced 850 nm EO/OE devices in terms of noise and linearity performances within a 60 GHz RoF system. These dies are implemented in packaged modules in the next chapters, until their integration into the final system. On wafer optoelectronic device

characterization requires experimental bench setups specifically developed to extract accurate measurements which are presented here. The optoelectronic devices targets are the 850 nm GaAs VCSEL and the 850 nm SiGe HPT which in both cases are measured in an optical link configuration. Therefore, references O/E receiver and E/O emitter are required, respectively.

The first section presents the 850 nm GaAs VCSEL complete characterization which includes the experimental bench setups. The reference photodetector is the commercial New Focus Photodiode (NFPD) [117]. Measurements will cover the 4 main characteristics: static performances (LIV curve, Optical Spectrum), dynamic response (Small-Signal Response), noise behavior (Relative Intensity Noise) and nonlinearities (compression gain and intermodulation distortion). Finally, two more parameters are measured which are related with all the previous ones simultaneously: Spurious Free Dynamic Range (SFDR) and the system performance metrics with Error-Vector-Magnitude (EVM).

The final section intends to present the 850 nm SiGe HPT characterization comparing two size structures of a 10x10 μm^2 and 30x30 μm^2 optical windows. The main focus here is the opto-microwave frequency response.

III.A. 850 nm GaAs VCSEL characterization

The VCSEL technology under study was fabricated by Philips Technologie GmbH U-L-M Photonics as introduced in II.B.1.6, Chapter II.

The diagram of the main experimental bench setup used for all measurements on the optical source is given in Figure III-1. On-wafer measurements uses a 100 µm pitch GSG probe to bias the VCSEL. The RF modulated signal is applied through a bias tee. The laser output beam is coupled to a lens multimode fiber placed in a Lightwave probe. Its position is precisely fixed on the wafer with a nanopositioner. A Matlab program was developed to control the nanopositioner and optimize the coupling efficiency as a function of the illuminated spot window. This optical probe presents a defined angle around 6° between the fiber and the right angle of the wafer, in order to avoid parasitic optical cavities [124].

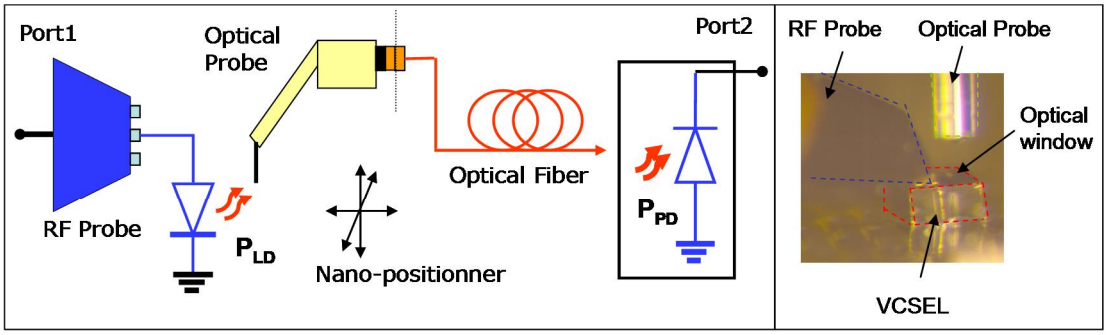

Figure III-1 – On wafer Measurement bench setup for the laser: a) schematic using an 850 nm GaAs based VCSEL and a reference photodiode – NFPD; b) photo of the RF and optical probing positioned on the VCSEL.

The fiber length between the optical probe and the detector is a few tens of centimeters using 2 connectors FC / PC and two connectors E2000 / APC (APC allows to reduce eventual lasing cavity). To detect the emitted light, a reference multimode photodiode was used with a

flat frequency response up to 25 GHz and responsivity of 0.222 A/W (New Focus PD 1434) [118].

The first subsection focuses on the static performances with typical LIV curve measurement and the optical spectrum behavior. From both measurements, we are able to extract certain parameters such as the radiation efficiency and the thermal behavior.

The second subsection introduces the dynamic response with small-signal characterization, providing the measured S-parameters. Since the New Focus photodiode has a flat response, the laser intrinsic parameters are extracted such as the relaxation resonance frequency, parasitic frequency and damping factor.

The third subsection exposes the noise experimental setup, including its calibration procedure, and presents the RIN extraction.

The fourth subsection intends to present the nonlinearities with the definition and measurement of the compression gain and the intermodulation distortions.

The final two subsections consider system global measurements in terms of gain, noise and distortion by the Spurious Free Dynamic Range (SFDR) and the system performance metrics Error-Vector-Magnitude (EVM).

III.A.1. Static Performances

The VCSEL characterization starts typically with the LIV curve providing its DC behavior. The operation biasing point is one of the most important parameter which will influence the laser characteristics and, therefore, the link system too. It will be optimized in terms of best performances regarding the frequency response, noise behavior and nonlinearities.

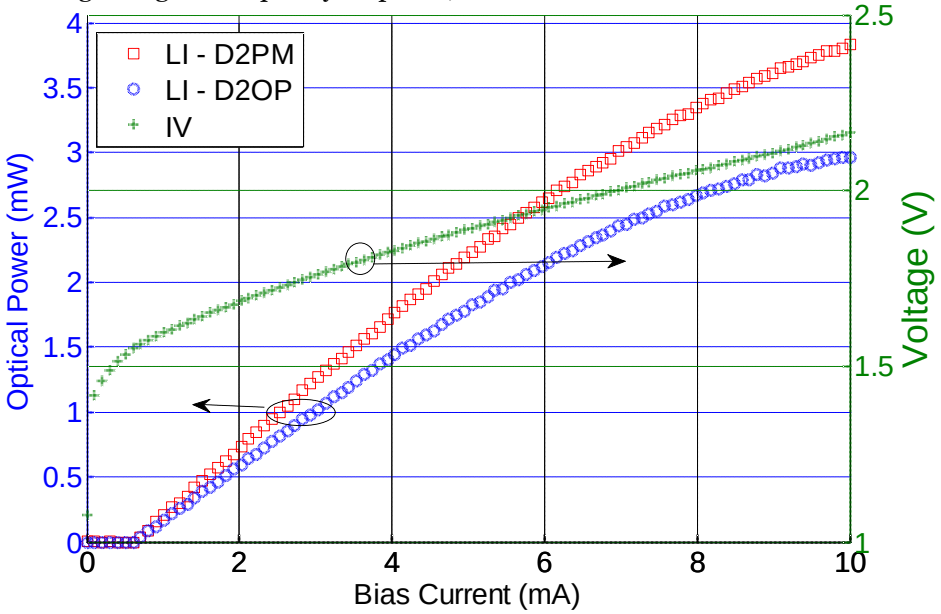

Figure III-2 – LIV Curve comparing: Directly Coupled to Power Meter (DC2PM) and Directly Coupled to Optical Probe (DC2OP)

Figure III-2 provides the LIV curve of the ULM die VCSEL measured on wafer. We can define 3 regions: first region which is until the threshold current is reached around 610 µA; second region which is the linear region where the stimulated emission dominates; and the third one which shows saturation and compression resulting, mainly, from the thermal effects. Two LI curves are presented corresponding to two test configurations, the DC2PM curve and

the DC2OP curve, as described hereafter: the VCSEL was biased with the RF probes using a Bias-Tee and the optical power was first measured directly by a power meter placed as close as possible to the die optical output (~ 1mm). As the sensor of the power meter has a large surface (few cm^2), and as the divergence of the VCSEL is usually less than 30°, it is expected that 100 % of the optical power is measured. This leads to the DC2PM curve (Directly Coupled to the Power Meter), shown by the squared symbol in Figure III-2; the circle symbols curve represents the LI curve of the VCSEL coupled directly to the optical fiber probe (DC2OP – Directly Coupled to Optical Probe). The difference between both curves is due to the limited coupling efficiency to the lensed fiber. The maximum optical power is 3.8 mW for the DC2PM configuration, which is supposed to be 100 % of the emitted power. It corresponds to 0.52 W/A in terms of slope efficiency. In the case of the DC2OP, the losses of misalignment and coupling efficiency reduce the maximum optical power to 3 mW and the slope efficiency to 0.42 W/A. We achieved 79 % of coupling efficiency with this optical probe. This optical probe was also analyzed in [124] when illuminating a photodetector. It is produced by Cascade. It is made up of a MM fiber with a Grin lens at the extremity to focus the beam from the fiber to a spot size of typically 30-50 µm at a distance of 50 µm from the fiber end. Indeed a 79 % coupling efficiency is high enough for further measurements. It could be improved further with control of the alignment angle. Its precise evaluation helps to calibrate the following measurements that will need the VCSEL to be measured through the pigtailed reference photodiode. However the next static measurements are measured by the DCPM method to guarantee the full 100 % coupling for greater simplicity.

From the IV curve, we can determine the differential series resistance associated to the VCSEL as depicted in Figure III-3 a). It is given by the derivate of the VI curve. Typically, this parameter should be as small as possible corresponding to a high output power and a high efficiency.

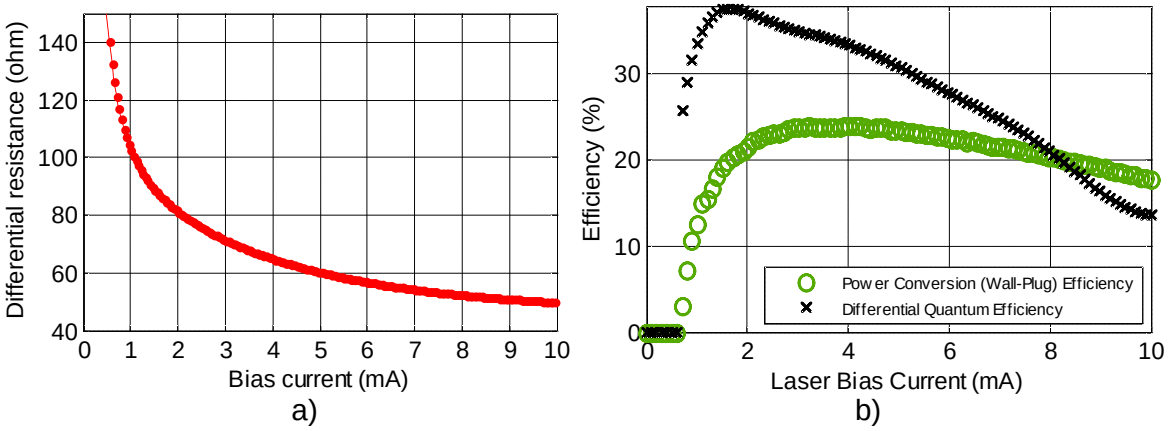

Figure III-3 – Static characteristics: a) Series resistance; b) Radiation efficiency – η_c and η_d (DC2PM)

Figure III-3 b) - depicts the radiation efficiency of the VCSEL extracted from the LIV curve. The cross symbol curve is the differential quantum efficiency reaching a maximum of 37 % just after the threshold current. In the case of the wall-plug efficiency (circular symbols curve) the maximum is 24 %.

The optical spectrum is then measured as a function of the bias current in Figure III-4. The operating wavelength is shown to be around 855 nm as expected for a GaAs based VCSEL with a typical transverse multimode behavior that impact the spectrum. A wavelength red-shifting could also be observed when the current increases.

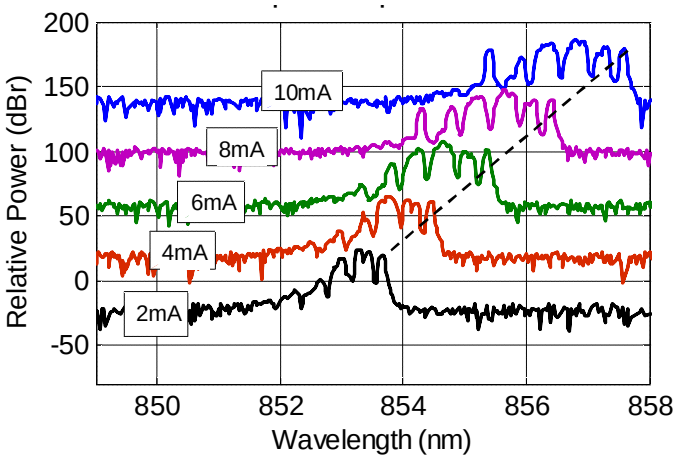

Figure III-4 – VCSEL Optical spectrum as a function of the wavelength for different bias currents (DC2OP) at 20°C room temperature

This is mainly due to the temperature increase since there is no dissipation structure on the die. From these results we can estimate the temperature increasing ratio induced by the drive current. The wavelength tuning over the bias current is found to be 0.5 nm/mA (considering the mode with higher wavelength). Since the emission wavelength shifts at a rate about 0.07 nm/°C on VCSELs with GaAs-based [125], we can estimate that the temperature rises about 71 °C from the room temperature (25 to 91°C) at the highest current bias with a rate of 7.1 °C/mA.

III.A.2. Dynamic Small-signal Response

We measured the small-signal modulation characteristics under a 40GHz-VNA (Vector Network Analyzer). A complete optical link system is measured where the gain (S21) response follows the influence of each optoelectronic device, including the eventual optical losses by the optical probe, optical fiber and misalignment. The input reflection coefficient (S11) corresponds to the laser diode reflection coefficient and the output reflection coefficient (S22), to the photodiode one. The photodetector response is crucial to characterize precisely the laser diodes. As a reference photodetector we use a New Focus multimode photodiode model 1414-50 with the specifications shown in Table III.1.

Table III.1 – Photodiode: NFPD 1414-50 Specifications [117]-[118]

	Units	1414-50
Wavelength	nm	800-1630
Bandwidth (3dB)	GHz	25
Conversion gain	V/W	11
Responsivity (@850 nm)	A/W	0.222
Detector Material		InGaAs
Output Impedance	Ω	50
NEP	pW / Hz	40
Saturation Power CW	mW	8
Optical Input		Multimode FC
Output Connector		K

The 1414-50 High Speed Photodetector shows a flat response in both amplitude and phase up to 25 GHz and is optimized for frequency-domain applications (Figure III-5). This information will simplify the laser frequency response extraction. The high-sensitivity Model 1414 near-IR photodetectors use 25 µm diameter back-illuminated InGaAs Schottky photodiodes with peak responsivity of 0.5 A/W at 1300 nm. The conversion voltage gain with a 50 Ω load is 11 V/W. It has an FC 50 µm multimode input. Multimode versions have an internal GRIN lens for focusing onto the photodetector.

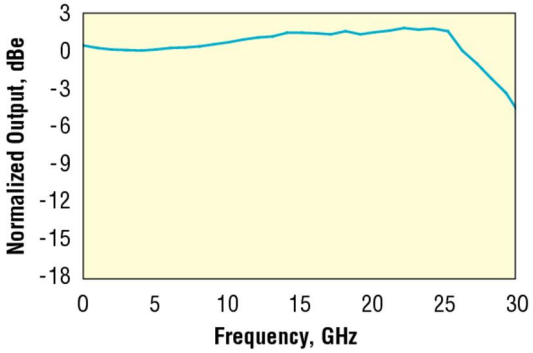

Figure III-5 – New Focus 1414-50 model specifications: Normalized frequency response up to 30 GHz [117]-[118]

The DC and RF calibration procedures were done previously to remove the cable, connectors and RF probes effects. Figure III-6 a) shows the link gain measurement as a function of the frequency for different bias currents, and Figure III-6 b) shows the input reflection coefficient of the VCSEL. The extraction of individual OM quantities of the VCSEL will be developed in Chapter III.

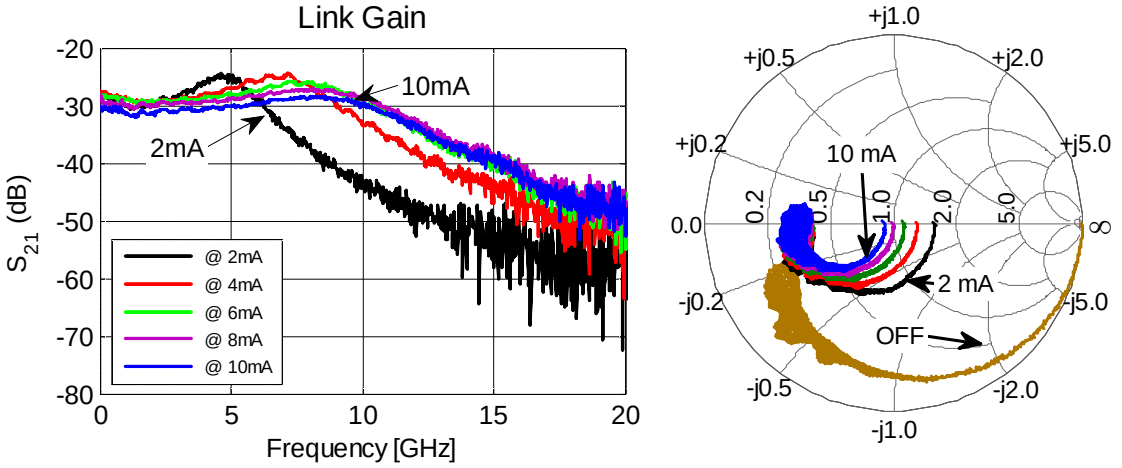

Figure III-6 – Small-signal characteristics of the 10 Gbps ULM VCSEL die with: a) S21 Link gain; b) VCSEL reflection coefficient (S11) at 2, 4, 6, 8 and 10 mA

As we increase the bias current the relaxation oscillation frequency moves towards high frequency and the damping factor decreases providing a smooth frequency response. The gain slightly decreases when the bias current increases. This can be explained by the shift of the operating point to a region where the slope efficiency is reduced. The gain variation goes from —28 dB to —31 dB with bias current from 2 mA to 10 mA.

The VCSEL reflection coefficient is provided in Figure III-6 b). We can see the typical capacitive behavior of a laser diode where the impedance moves toward the 50 Ohm impedance

as the bias increases. This means that the impedance matching is not crucial for high bias current and frequencies up to 15 GHz. Still, it might improve the gain and the noise behavior.

The Figure III-7 shows the normalized frequency response which allows the different dynamic parameter extraction, such as the 3dB cutoff frequency (f_{3dB}), relaxation oscillation frequency (f_R) and damping factor (δ). The cutoff frequency goes up to 12 GHz for 8 and 10 mA.

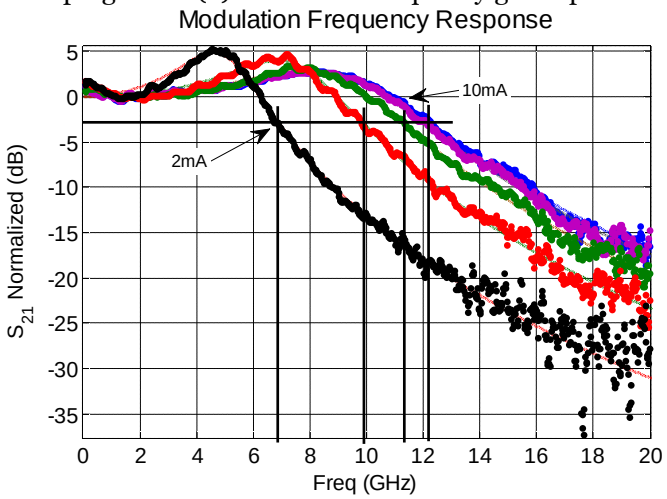

Figure III-7 – Extracted normalized link gain at 2, 4, 6, 8, 10 mA of the 10 Gbps ULM VCSEL.

A fit to the empirical Eq. (2.14) was done to allow the intrinsic and extrinsic limitation parameters extraction from the modulation frequency response (see Chapter II, section II.B.1.5). These parameters help us to identify the frequency limitation [125] [126]. They are summarized in Table III.2. The K factor is fitted to 0.27 ns corresponding to a large damping limited modulation bandwidth of 32.9 GHz induced by the small cavity dimensions. The D-factor (Eq. (2.17)) was extracted with a value of 3.966 GHz/√mA which is the rate at which the relaxation oscillation frequency increases with the current above the threshold (I_{th}). The D factor is proportional to the relaxation oscillation frequency and it should be increased to improve the high speed performance of the laser.

Table III.2 –Summary of the extracted dynamic parameters for the10 Gbps ULM VCSEL

K-factor (ns)	0.27
D-factor GHz/(mA)$^{1/2}$	3.97 @ I_{bias}<5mA
MCEF GHz/(mA)$^{1/2}$	5.995 @ I_{bias}<5mA
Fp (GHz)	10.9
$F_{3dB\_thermal}$ (GHz)	15.5
$F_{3dB\_damping}$ (GHz)	32.9
F_{3dB_max} (GHz)	12.31 @I_{bias}=10mA

The relaxation oscillation frequency is the natural oscillation frequency between the carriers and the photons in the laser cavity and can be seen as how fast an intrinsic laser can be modulated. The relaxation oscillation frequency is inversely proportional to the square root of the active volume (see Eq. (2.16)). Therefore, a decrease of the volume (size) of the VCSEL will increase the modulation bandwidth. The MCEF (Eq. (2.18)) which gives the evaluation of the device's overall high-speed performance is 5.995 GHz/√mA. In both results the deviation from the linearity at high currents is due to thermal effects.

We, therefore, conclude that the modulation bandwidth is limited primarily by extrinsic parasitics and then by thermal limitation. Reduction of the parasitic capacitances and resistances should increase the bandwidth. Heat dissipation should also improve the bandwidth performances. However, this device already exceeds the desired 10 GHz of bandwidth.

III.A.3. Noise Behavior

The optical power emitted from the laser diode exhibits intensity, phase and frequency fluctuations. The main noise source is the spontaneous emission resulting from the electron hole recombinations and from mode partition noises due to the multimode behavior of the cavity [127]-[132]. The photons generated by spontaneous emission are based on incoherent light, resulting on random phase and amplitude of the photons. Some of those photons will coincide with stimulated emission photons and then add small components on the phase and amplitude creating the fluctuations.

This subsection is organized in 4 parts:

The first part of the subsection presents the theoretical analysis and RIN definition.

The second part of the subsection introduces the experimental bench setup to perform RIN measurement. Here a measurement method is introduced and developed.

The next part of the subsection presents the calibration of the measuring system and the measurement limitations are described.

Last part of the subsection presents the RIN measurement results of the 10 Gbps GaAs VCSEL.

III.A.3.1 RIN definition

The noise behavior of the laser is characterized conventionally by the Relative Intensity Noise (RIN) which is the main quality indicator of laser devices in terms of intensity stability (noise). If we consider the fluctuations on the amplitude of the emitted optical power as written by:

$$P_{opt}(t) = \langle P_{opt} \rangle + \delta P_{opt}(t) \quad \text{Equation Section 3} \tag{3.1}$$

The RIN definition, assuming that is white noise (constant for all frequencies), can be quantified as

$$RIN\left[dB/Hz\right] = 10 \cdot \log\left(\frac{\left\langle \delta P_{opt}(t)^2 \right\rangle}{\bar{P}_{opt}^2 \cdot B_N}\right) \tag{3.2}$$

where $\delta P_{opt}(t)$ represents the optical intensity fluctuations (<> denotes the time average), $\bar{P}_{opt}$ is average of the optical power and B_N the noise bandwidth (detection system bandwidth over a 50 Ohm load). Therefore the RIN is the ratio of optical noise relative to the optical signal power. Indeed, it can be thought to a type of inverse carrier-to-noise measurement [133].Thus, the lowest RIN value corresponds to better laser noise performances.

Depending on photodetector system, the RIN is detectable if dominant over other noise sources such as shot noise of the photodiode and the thermal noise related to all the noise of the measuring system. Thus a definition of the RIN in electrical domain is suitable. Taking into

account that the RIN is not white noise and that the photodiode output electrical power is proportional to the square of the optical power ($R_L.I_{ph}^2 \propto P_{opt}^2$), RIN can be expressed as

$$RIN(f) = \frac{N_{LD}(f)}{\langle P_{elec,DC} \rangle \cdot B_N} \tag{3.3}$$

where $N_{LD}(f)$ is spectral noise power of the photocurrent related to the laser, $P_{elec,DC}$ is the average power of the photocurrent ($I_{ph,DC}^2$ multiplied by $R_L = 50\Omega$) and B_N is the noise bandwidth (normalization to 1 Hz).

III.A.3.2 Experimental setup

Since the output photocurrent from the detector is usually a weak signal, electrical microwave amplifiers (LNA) are usually placed after the detector. This amplification should be high enough to improve the sensitivity of the ESA. Therefore the RIN is measured using the bench setup presented in Figure III-8. The electrical spectrum analyzer (ESA) measures the sum of all noise contribution powers at the output of the link, such as

$$N_{total}(f)[W] = N_{LD}(f) + N_q + N_{th}(f) \tag{3.4}$$

where N_{LD} is the laser noise power contribution (related to the RIN), N_q the shot noise power from the photodetector and N_{th} the thermal noise power coming from all electronic devices used in the bench, including the ESA, the photodiode and the LNA (all contribution observed in the 50Ohm load impedance).

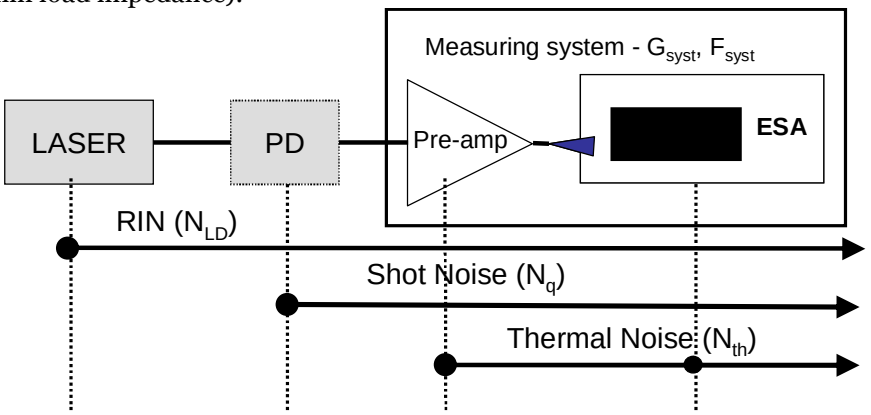

Figure III-8 – Noise bench setup and noise contribution of each device.

Our RIN measuring technique is known as the subtraction method. It considers all the noise sources independently, allowing the subtraction manipulation of the total noise given by Eq. (3.4). The contributions all noise (N_{total}) is measured with laser "on". The thermal noise is measured by the output noise when the laser is "off" where it includes the dark photocurrent of the detector and all the thermal noise sources of the electronics. The shot noise power spectral density (white noise) at the output of the photodiode is calculated from the measured photocurrent given by

$$N_q[W] = 2 \cdot q \cdot I_{ph} \cdot R_L \cdot B_N \tag{3.5}$$

where q is the elementary charge, $R_L = 50\Omega$ is the photodiode output load impedance and I_{ph} is the DC average photocurrent recovered by the bias monitor terminal on photodiode. The RIN

is finally obtained by subtracting the thermal noise power and the shot noise power from the total noise for each frequency.

All the electronics following the photodiode produces thermal noise observed in the load impedance over the effective noise bandwidth.

$$N_{th}[W] = F_{syst} \cdot k \cdot T \cdot B_N \tag{3.6}$$

where k is the Boltzmann constant, T is the absolute temperature in Kelvin and F_{syst} the noise factor of the measuring receiving electrical system, given as

$$F_{syst}[linear] = F_{LNA} + \frac{F_{ESA} - 1}{G_{LNA}} \tag{3.7}$$

where F_{LNA} is the LNA noise factor, F_{ESA} is the ESA noise factor and G_{LNA} is the LNA gain. The subtraction of those noise terms must me taken carefully to increase the measurement accuracy. It is important to know the frequency response for the total system before noise subtractions [133]. Some of the measuring system instruments do not have a flat response over the entire bandwidth which leads us to a calibration step (presented in III.A.3.4) crucial to compensate these results. The frequency response of the photodector, LNA and the ESA must be characterized and included into the RIN measurement results. Also, it is important to identify the limitations of the measurement bench setup (presented in III.A.3.3).

III.A.3.3 Measurement limitations

Figure III-9 sketches the different noise limitations as a function of the photocurrent. The thermal noise contributions with and without LNA are shown to illustrate its improvement on the system measurement sensitivity.

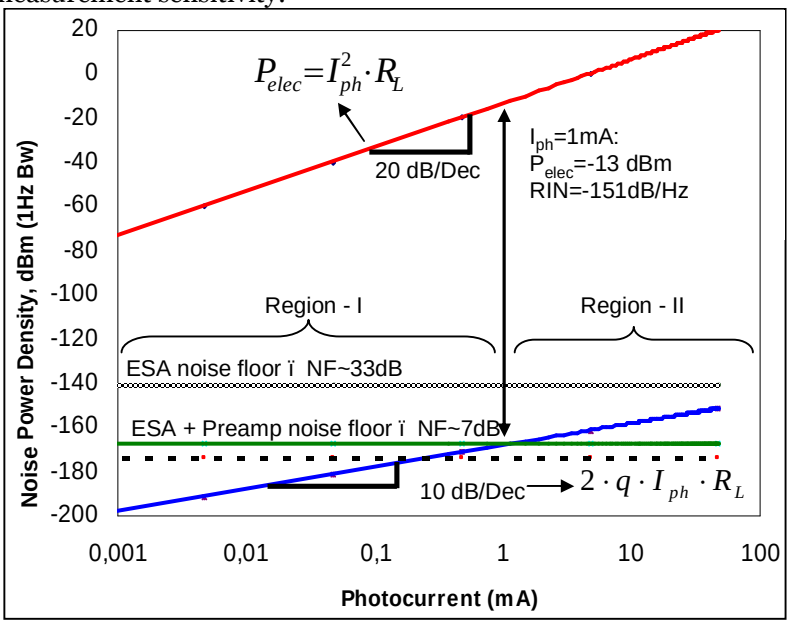

Figure III-9 – Noise measurement limits as a function of the receiver photocurrent

Unfortunately the spectrum analyzer measures all the noise contributions and therefore the measurement can be limited by the thermal noise floor or the shot noise expressed on the follow equation:

$$RIN(f) = \frac{N_{total}(f)}{I_{ph}^2 \cdot R_L} - \left(\frac{2 \cdot q}{I_{ph}} + \frac{k \cdot T \cdot F_{syst}(f)}{I_{ph}^2 \cdot R_L} \right) \quad (3.8)$$

At low photocurrent the bench is limited by the thermal noise and so the RIN value must be higher than the 3rd term of the Eq. (3.8) in order to be determined (region – I in Figure III-9). . When the incident optical power on the photodetector becomes large enough, the shot noise overcomes the thermal noise and becomes the RIN measurement with a slope of 10 dB per decade over the photocurrent (region – II in Figure III-9).

Our detection system is a thermally limited system since we do not use high optical power enough to produce high photocurrent. The shot noise limit (region - II) is not reached. Consequently the low RIN limit in our case is —168 dBm/Hz, theoretically, up to few mW of optical power.

III.A.3.4 Measurement calibration

Before starting the noise measurement, the bench setup (ESA plus pre-amplifier- system) must be characterized in terms of gain and noise figure – $G_{syst}(f)$ and $NF_{syst}(f)$. The Y factor method was performed to measure the noise figure using a noise source up to 18 GHz [134] [135]. Figure III-10 shows the ESA intrinsic noise figure measurement results compared with its specification up to 30 GHz. A noise figure higher than 35 dB was measured over the frequency range, clearly demonstrating the need of a pre-amplifier to improve its sensibility.

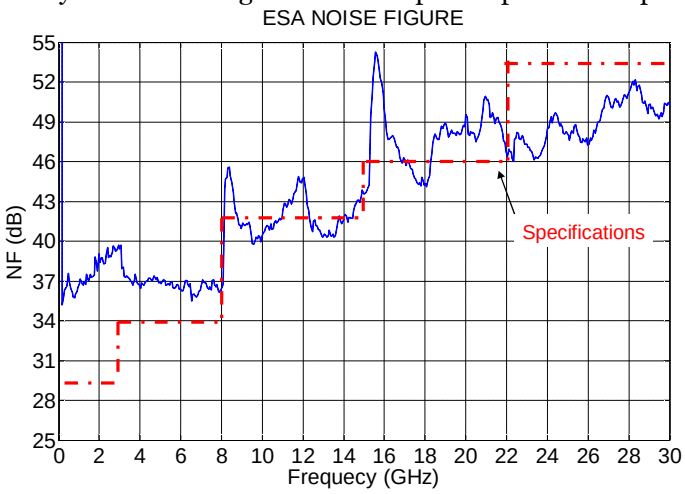

Figure III-10 – Electrical Spectrum Analyzer Noise figure: specifications and measured NF

The choice of the noise source and the pre-amplifier was made following the two guidelines [136]:

$$ENR_{dB} \geq NF_{dB}^{LNA} + 5dB \quad (3.9)$$

$$NF_{dB}^{LNA} + G_{dB}^{LNA} \geq NF_{dB}^{ESA} + 1 \quad (3.10)$$

The first guideline is given by Eq. (3.9) which shows the maximum noise figure measurable of a DUT when an ideal noise source with a given excess noise ratio (ENR) is used. As the available noise source has an ENR equal to 15 dB, we can measure devices presenting NFs lower than 10 dB. The second guideline is presented by the Eq. (3.10) and tells us the performances required from the pre-amplifier in terms of gain and noise figure compared to the ESA noise figure. If we consider the 46 dB ESA noise figure at 22 GHz given by the specifications (Figure

III-10), the pre-amplifier gain plus noise figure must be higher than 47 dB to get accurate measurement. The amplifier MITEQ Model JS41-00102000-27-10P was, thus, our choice as it has a gain of 44 dB and noise figure of 3 dB. It presents also a frequency bandwidth above 20 GHz [137].

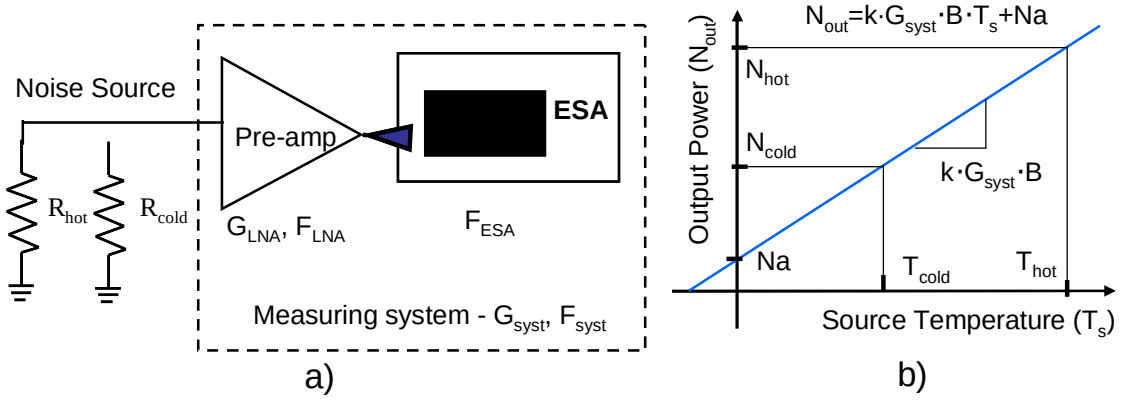

Figure III-11 – Y method: a) Noise measurement system; b) Noise Output power as a function of the source temperature

This choice fills up the requirements only until 18 GHz to keep, as according to Figure III-10, the noise figure lower than 46 dB (the ESA NF peak at 16 GHz will appear on our measurements as it results to a NF higher than 46 dB). This is also limited by the noise source which is valid up to 18 GHz.

Noise sources are commonly specified by their ENR which is expressed in dB. The relationship between noise temperature and ENR is shown in Eq. (3.11). The calibrated ENR values supplied by the noise source manufacturer are referenced to T_o=290 K

$$ENR[dB] = 10 \cdot \log_{10}\left(\frac{T_{hot} - T_{cold}}{T_0}\right) \tag{3.11}$$

The noise power is measured at the DUT output at 2 different temperatures: with room temperature noise source (noise source off) at the input (cold source); with a high temperature noise source (noise source biased with 28 V) at the input corresponding to the hot source – Figure III-11 a). We can determine the LNA gain, G_{LNA}, from the linear equation. The Y-intercept indicates the noise power Na added by the LNA. The slope of this line is proportional to the measurement bandwidth (in Hz), *B*, and to the Boltzmann's constant, *k* (1.38 x 10^{-23} Joules/HK).The Y factor can be found by taking the ratio of the measured (linear) noise power at the DUT output when the noise source is on and off.

$$Y = \frac{N_{hot}}{N_{cold}} \tag{3.12}$$

The Y factor can be used to calculate the noise temperature of the measuring system with the following equations [136]

$$Na = k \cdot G_{syst} \cdot B \cdot T_0 \cdot \left(\frac{ENR}{Y-1} - 1\right) \tag{3.13}$$

Then

$$F_{syst} = \frac{Na + k \cdot G_{syst} \cdot B \cdot T_0}{k \cdot G_{syst} \cdot B \cdot T_0} = \frac{ENR}{Y-1} \tag{3.14}$$

Considering the Friis equation of the two blocks

$$F_{syst} = F_{LNA} + \frac{F_{ESA} - 1}{G_{LNA}} \tag{3.15}$$

Since the LNA used has a high gain, the second term of the Eq. (3.15) is negligible, therefore the system noise factor is determine by the LNA. This is the reason to use a pre-amplifier on the noise measurement since it reduces the global measuring system noise factor. Figure III-12 shows the measured power spectral density for the measurement configuration without the pre-amp (LNA) and with it.

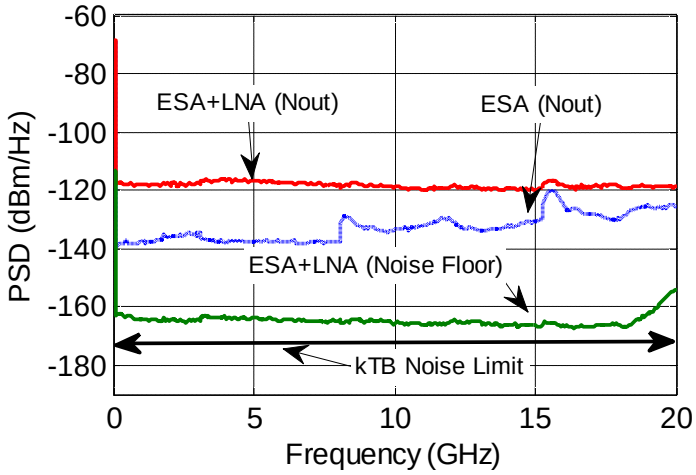

Figure III-12 – ESA Noise floor; ESA plus the pre-amplifier power density and Measurement Noise floor versus frequency

The output noise power density curve when the LNA is used has sufficient gain to remove the ESA frequency noise behavior except the peak at around 16 GHz. The measuring system sensibility was improved up to —167 dBm/Hz (ESA+LNA (noise floor)).

Figure III-13 a) shows the system noise figure, $NF_{syst}(f)$ and the uncertainty of that measurement. Noise figure lower than 3 dB and measurement uncertainty lower than 1 dB was measured up to 15 GHz. Several factors contribute to noise figure measurement uncertainty: the noise figure of the spectrum analyzer; uncertainty of the noise source ENR value and gain of the LNA have significant impact; impedance mismatches between noise source and LNA, between LNA and spectrum analyzer (during the calibration step).

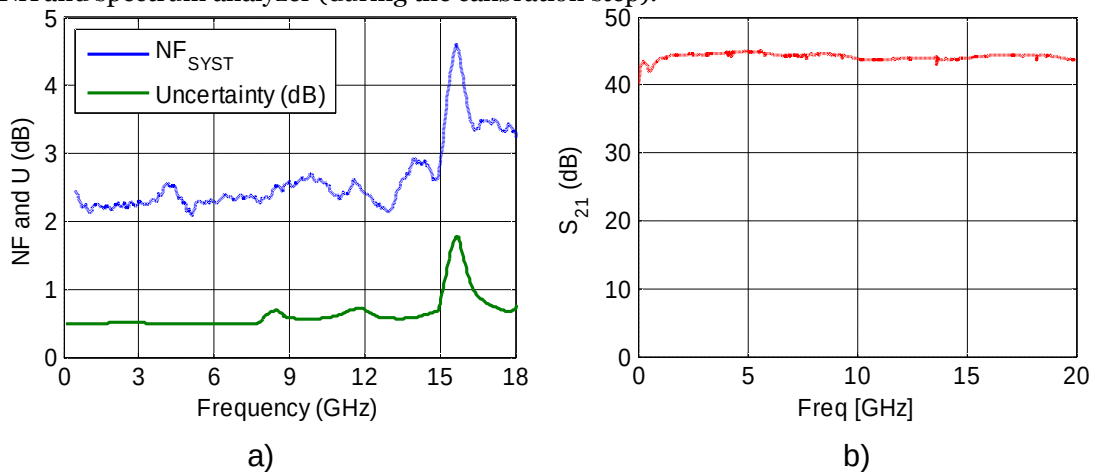

Figure III-13 – Measurement calibration: a) Noise figure of the system (NFsyst) and the uncertainties on the measurement; b) Pre-Amplifier Gain (Gsyst).

III.A.3.5 RIN measurement

The Figure III-13 b) provides the pre-amplifier gain and frequency response until 20 GHz where we can see the gain is constant around 44 dB. Since the ESA gain is considered as 0 dB the $G_{syst}(f)$ is given by the pre-amplifier gain response.

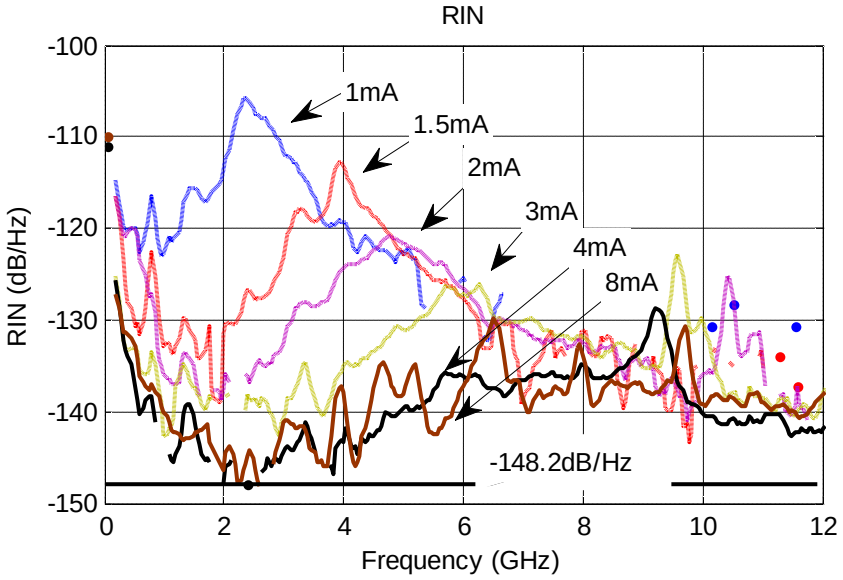

Figure III-14 – Relative Intensity Noise of ULM Die VCSEL using the NFPD

Finally the RIN measured on the ULM die VCSEL is presented in Figure III-14 for different bias conditions (1, 1.5, 2, 3, 4 and 8 mA). At low bias current curves we see clearly the relaxation oscillation frequency peak moving toward high frequencies. For these bias current values close to the threshold current the spontaneous emission is the main source of noise and is relatively high. As we can see the measurement bench is limited for some RF frequencies by the thermal noise, so certain curves are not completed mainly at low input bias currents (measured shot noise is —148.2 dB/Hz @ 8 mA). These results are very promising since the RIN is lower than —140 dB/Hz for the typical operating bias current higher than 4 mA. Indeed, at 8mA the RIN is lower than —140 dB/Hz in a range of frequencies between 1 and 6 GHz (despite few oscillations probably caused by multimode operation).

III.A.4. Dynamic Large-Signal Response: P1dB and IP3

Nonlinear devices exhibit complex behavior when input power is high. This subsection presents the dynamic large signal response figures of merit: compression gain point at 1dB (P1dB) and the third order intercept point (IP3). The definition is illustrated in Figure III-15:
P1dB - defines the output level at which the device gain is 1 dB less than the small signal gain, or is compressed by 1 dB. The device gain is given by the ratio between the output and input signals. The gain is constant at small signal, but increasing the input power, the gain is reduce.
IP3 - is determined by the third-order intermodulation products generated by a nonlinear device. Two tones, closely spaced in frequency, are fed into its input. It is given by the point where the extrapolated third order intermodulation distortion level (IMD3) is equal to the signal fundamental level (IMD1) (Figure III-15). The extrapolation is made from the region where the third order intermodulation follows the third order law (3:1 slope) and in the linear region (1:1 slope). This distortion product is usually so close (2f2-f1 and 2f1-f2) to the carrier

that it is almost impossible to filter out in a communication system and this can cause interference. The IP3 is commonly defined as a figure of merit that characterizes the device's tolerance to several signals that are present simultaneously outside the desired pass band and it is closely related to the 1 dB compression point.

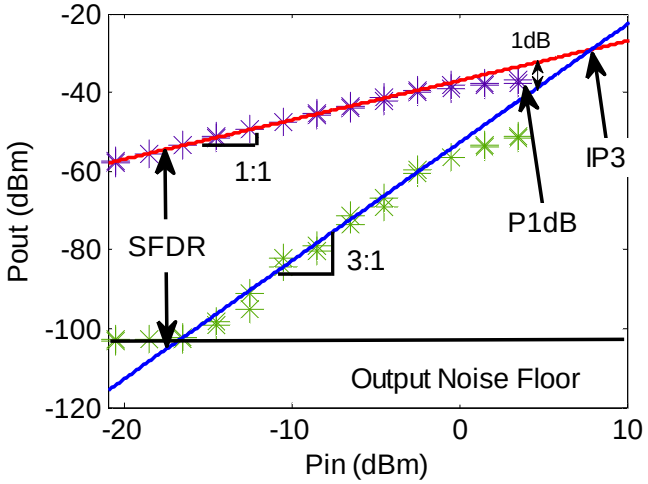

Figure III-15 – Plot of the output power versus the input power of a nonlinear system: P1dB, IP3 and SFDR definition (BW=1kHz)

The bench setup to measure both P1dB and IP3 is presented in Figure III-16. On the case of the P1dB, the measurement is based on the standard one tone power sweep at the device input using an RF generator (1-10 GHz). For the IP3, is based on two-tone intermodulation distortion measurement. Two fundamental tones, spaced by Δf=1 MHz, are injected directly on the laser creating IMD3 at the output. In both cases, the output signal is recovered by the electrical spectrum analyzer which was controlled by a Matlab procedure. The sweep in terms of laser biasing, optical losses and frequency are targets on our study using Matlab with a GPIB connection to control the different equipments.

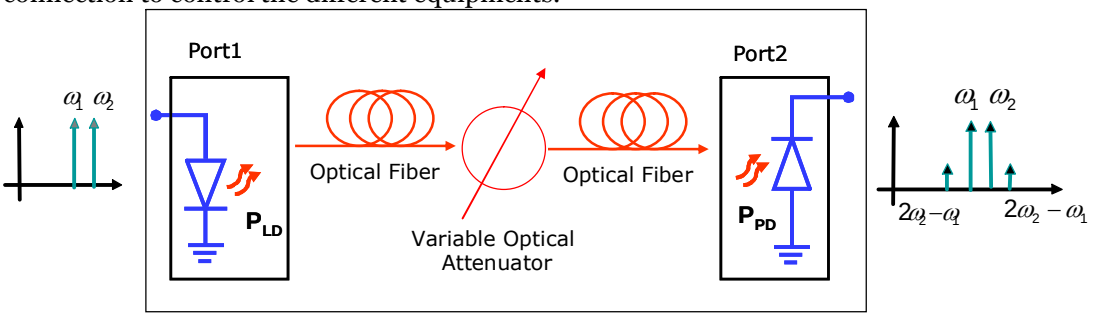

Figure III-16 – P1dB/IP3 Bench setup.

On both measurements the final measurement is dependent on both E/O and O/E devices and here the use of an optical attenuator is crucial to separate the nonlinearity behavior of the emitter from the receiver. Figure III-17 shows the typical behavior of the link nonlinearities as a function of the optical losses. The evolution of the input P1dB (and the IIP3) as the optical losses increases provides the information of which device is dictating the nonlinearities. If the input P1dB (same behavior for IIP3) increases with the increase of the optical losses, we are in the photodiode nonlinearity region. On the other hand, if not increases with the increase of the optical losses, we are in the laser nonlinearity region.

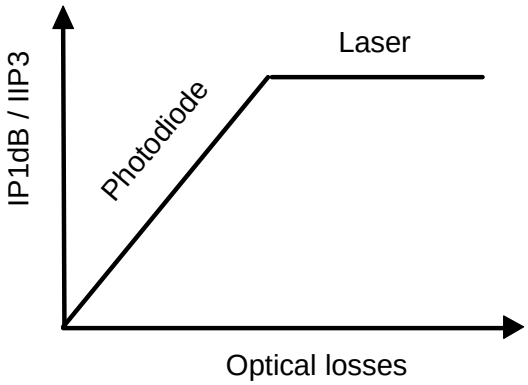

Figure III-17 - IIP3 and IP1dB of the link system in function of the optical losses.

The measurements on the input P1dB were then performed as a function of the frequency (up to 10 GHz) and of the supplied bias current, see Figure III-18 a). The input P1dB goes up to 9 dBm for a 10 mA bias current at 4 GHz. As we increase the bias current the optical power increases and the VCSEL can handle more power. It is interesting to observe that the compression point follows the shape of the VCSEL small-signal response in terms of frequency and thus confirming the VCSEL is indeed the limiting device in our VCSEL-reference photodiode link. The input IP3 measure is presented in Figure III-18 b) using 1 MHz in frequency difference between the tones. The same shape as the compression gain is observed. The measurements are limited to 6 GHz due to the characteristics of our generators. We achieved an input IP3 up to 15 dBm for 10 mA bias current and at 4 GHz.

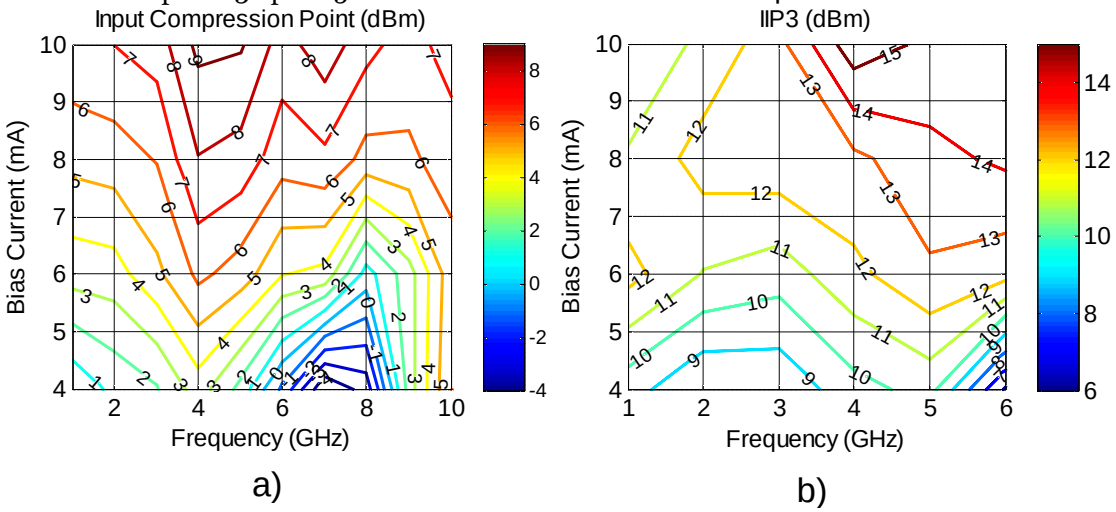

Figure III-18 – Die Nonlinearities of the link between the die VCSEL and the NFPD: a) 1dB Input compression gain; b) Input IP3

As we increase the bias current the IP1dB and IIP3 performance are even better until it reaches the saturation region of the LI curve. An important design guideline conclusion is also that we should avoid the relaxation oscillation frequency at low bias current as it results in strong nonlinearities.

Optical losses were thus added between the laser and the photodiode. The results are shown in Figure III-19. This figure shows that the input P1dB and the input IP3 are constant as we increase the optical losses, for bias current of 8 mA and center frequency of 3 GHz. This demonstrates that clearly the nonlinearity is due to the laser and not by the photodiode.

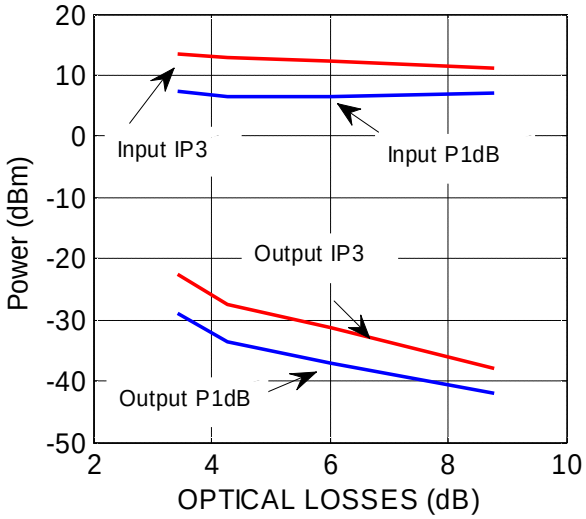

Figure III-19 – Die Nonlinearities of the link between the die VCSEL and the NFPD as a function of the optical losses at 8 mA and 3 GHz.

As the ORIGIN project intermediate frequency is 5 GHz with approximately 2 GHz bandwidth (4-6 GHz), laser biasing lower than 4 mA should be avoided to get rid of the influence of the nonlinearities and of the relaxation oscillation frequency as well. This proves the importance to design an optical link system below the laser diode relaxation oscillation frequency to avoid strong distortion.

III.A.5. Spurious Free Dynamic Range - SFDR

Spurious Free Dynamic Range (SFDR) is typically used for system characterization relating simultaneously the noise and intermodulation distortion limitations. It is determined by the output power range defined between output powers at fundamental and at the third order intermodulation distortion (IMD3) input power point that produces an IMD3 equal to the noise as defined in [138]. This definition is illustrated in Figure III-15, and leads to the following equation:

$$SFDR\left[dB\cdot Hz^{2/3}\right]=\frac{2}{3}\left[OIP3-N_{NOISE}^{OUT}\right] \tag{3.16}$$

where $OIP3$ is the link output 3rd order intercept point and N_{NOISE}^{OUT} is the output spectral noise density in 1Hz, defined as

$$N_{NOISE}^{OUT}=kT+NF+G \tag{3.17}$$

where k, T, NF and G are the Boltzmann constant, operational temperature, link noise figure and link gain, respectively. This definition provides an SFDR for the optical link as a whole. The next chapter will introduce a novel definition to isolate the SFDR contributions of the individual EO/OE devices. However, as this measurement is carried out using a highly linear reference photodiode in a dominant RIN link, the SFDR link is supposed to give a good indication of the VCSEL dynamic range.

The SFDR measurement results are shown in Figure III-20 as a function of the frequency (up to 6 GHz) and of the laser bias current. The SFDR is higher than 91 dB.Hz$^{2/3}$ and goes up to 98.8 dB.Hz$^{2/3}$ at 10 mA around 4 GHz. The SFDR is mainly limited by the laser noise (RIN) and nonlinearities (IP3). This figure also shows that the best operating frequency is between 3-5 GHz with biasing currents between 7-10 mA in order to benefit from the larger dynamic.

Increasing the relaxation frequency could enlarge this frequency band, thus some work on reducing parasitics and improving the thermal dissipation should be pursued. Reducing the optical coupling losses would also be beneficial in order to increase further the overall SFDR.

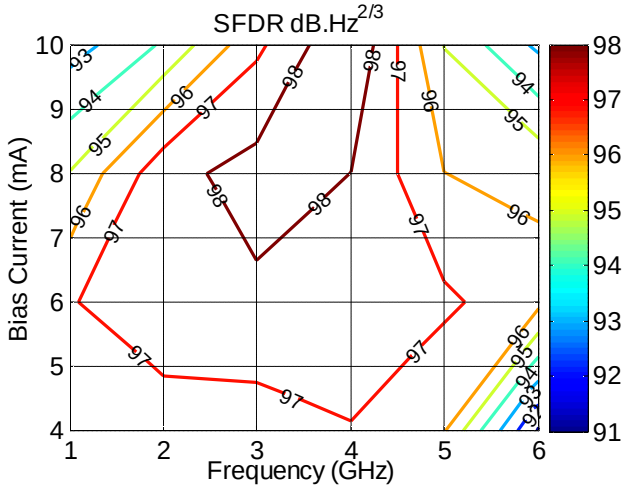

Figure III-20 – Die Nonlinearities of the link between the die VCSEL and the NFPD: SFDR

III.A.6. Error Vector Magnitude - EVM

One important figure of merit which characterizes the performances of a data transmission system is the Error vector Magnitude (EVM). EVM measurement defines the transmission of digital modulated signals such as Phased-shift Keying (PSK) or Quadrature Amplitude Modulation (QAM). Basically EVM compares the constellation between the received symbols and the ideal transmitted ones, depending upon the modulation scheme, as sketched in Figure III-21.

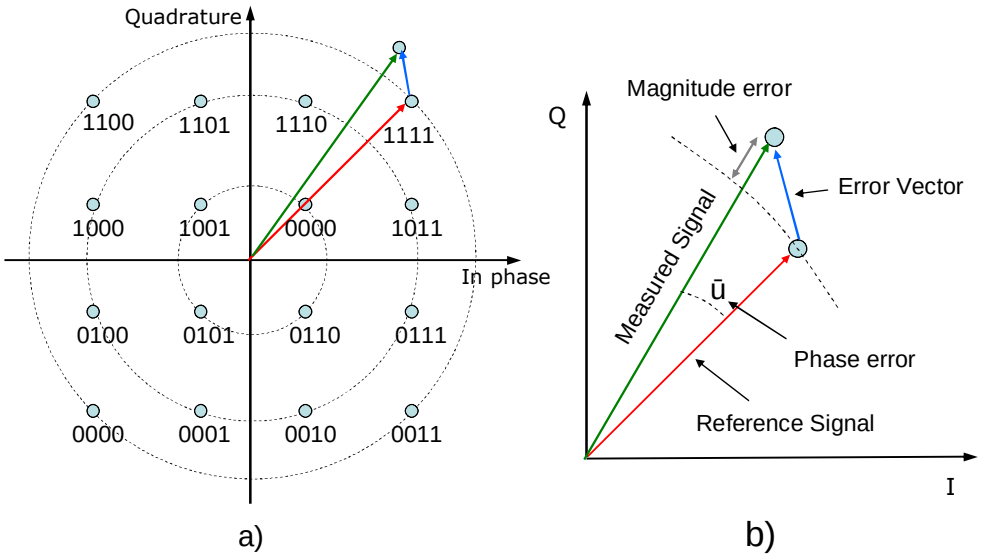

Figure III-21 – EVM definition: a) 16-QAM constellation; b) EVM representation

Mathematically EVM is the ratio of the error vector power to the reference vector power:

$$EVM\left[linear\right] = \sqrt{\frac{P_{error\_vector}}{P_{reference}}} \qquad (3.18)$$

The EVM measurement bench setup was performed using an Arbitrary Waveform Generator (AWG) with 12 bits resolution, 12 GSa/s sample rate and an analog bandwidth of 5 GHz (Agilent M8190A). An IF-OFDM signal is generated with QPSK modulation subcarriers working at 3.08 Gbit/s according to the IEEE 802.15.3c standard, HSI mode (see Table II.2, Chapter II). In terms of frequency response the AWG is limited up to 5 GHz analogue frequency by the datasheet specifications. Since we are using a signal with a bandwidth of 1.815 GHz we are limited to approximately 4 GHz in terms of the IF center frequency band. If we want to generate an IF-OFDM signal with a centered frequency up to 4 GHz we can use directly the AWG. But if we want to generate a signal centered at 5 GHz (main interest of our system) we need to generate an In-phase (I) and a Quadrature (Q) baseband signals with the AWG and then to transpose it externally, as depicted in Figure III-22. The I and Q signals are transposed to the IF by mixing them with an RF oscillator divided into two paths with a quadrature phase shift (90°). The signal is then combined to create the desired IF-OFDM signal which can be written as

$$s(t) = I \times \cos(2\pi \cdot f_0 \cdot t) + Q \times \sin(2\pi \cdot f_0 \cdot t) \tag{3.19}$$

where f_0 is the IF (5 GHz). The received signal is then analyzed with an oscilloscope.

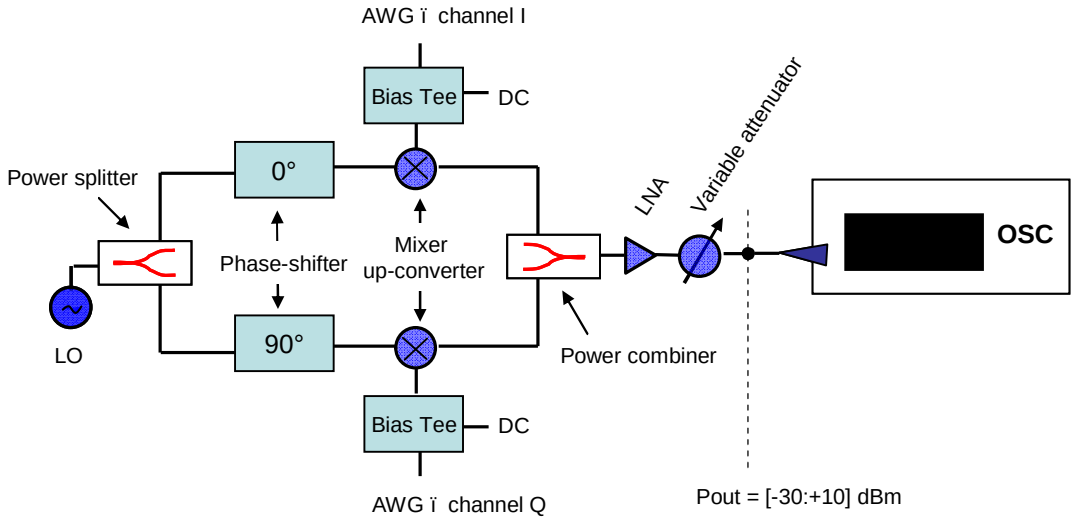

Figure III-22 – EVM bench setup using external frequency transposition: IF-OFDM signal with a QPSK modulation scheme

The signal is presented in Figure III-23 a) in time domain for QPSK modulation and Zero Pad Suffix (ZPS) as inter-symbol spacing. The ZPS consists in placing zeros between adjacent symbols with the goal to provide guard times and synchronization. The dynamic at the output is given by a 40 dB power range controlled by a wideband LNA and an RF variable attenuator. Powers from −30 dBm up to +10 dBm can be achieved. The output signal was captured using a Digital Storage Oscilloscope (DSO), with 13 GHz bandwidth and 40 GSa/s speed (Agilent DSO81004B). The EVM is then calculated with Matlab. An extra amplification after the device under test may be used to improve the oscilloscope sensitivity.

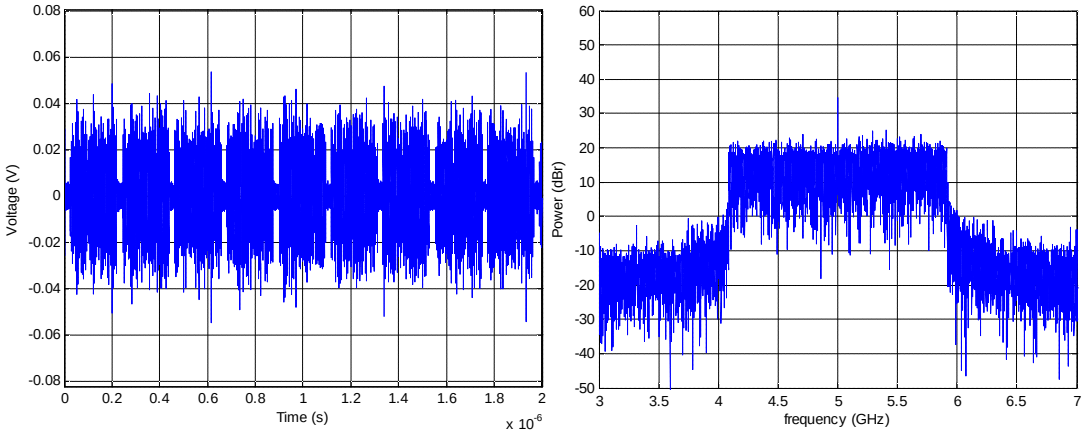

Figure III-23 – Generated IF-OFDM signal in time and frequency domains measured with the Agilent DSO81004B oscilloscope

The 5 GHz local oscillator level (Figure III-23 b)) is controlled and adjusted by adding a DC component to the baseband signals using a bias tee as depicted in Figure III-22. Inthis way, we avoid the possible saturation of the device under test. However the LO level has to remain above the others subcarriers to be detected and demodulated properly.

The nonlinearities are typically quantified by the IP3 and P1dB on analog characterization. In digital characterization, the nonlinearities are given by the Average Power (P_{avg}) and the Peak to Average Power Ratio (PAPR) both given by

$$P_{avg}\left[dBm\right] = 10 \cdot \log\left(\frac{mean\left(voltage^2\right)}{Z_{in}}\right) \tag{3.20}$$

$$PAPR\left[dB\right] = 10 \cdot \log\left(\frac{power_{peak}}{power_{RMS}}\right) = 10 \cdot \log\left(\frac{\max\left(\left|voltage\right|^2\right)}{mean\left(voltage^2\right)}\right) \tag{3.21}$$

where Z_{in} is the input impedance and voltage is the voltage signal as captured by the oscilloscope.

In practice the EVM measurement compares the constellation of the received symbol with nearest ideal symbol and not the originally sent. The EVM equation is, then, given by

$$EVM\left[linear\right] = \frac{1}{N_p}\left(\sum_{i=1}^{N_p}\sqrt{\frac{1}{P_{avg}\cdot N_s \cdot N_{dsc}}\sum_{j=1}^{N_s}\left(\sum_{k=1}^{N_{dsc}}\left(\left(I_{ijk}-I_{ijk}^*\right)^2+\left(Q_{ijk}-Q_{ijk}^*\right)^2\right)\right)}\right) \tag{3.22}$$

where:

N_p is the number of captured frames;

N_s is the number of symbols per frame;

N_{dsc} is the number of data subcarriers per OFDM symbol;

P_{avg} is the average power of the constellation;

I_{ijk},Q_{ijk} is the complex coordinates of the nearest constellation point for the j^{th} measured symbol in the k^{th} subcarrier of the i^{th} frame;

I^*_{ijk}, Q^*_{ijk} is the complex coordinates of the j^{th} measured symbol in the k^{th} subcarrier of the i^{th} frame.

Since the OFDM symbols generated on this bench are based on a pseudo random sequence without a frame structure, Eq. (3.22) is reduced to the root term. Figure III-24 a) shows the constellation results after demodulation and b) the measured EVM for the Back-to-Back configuration, the input power varying from —50 dBm to 10 dBm. We can see that the EVM is stable at 9 % for a [-30 dBm to 10 dBm] power dynamic range. If the input power gets lower than —30 dBm, we reach the sensitivity of the oscilloscope (1 mV/division) and EVM increases because of the receiver noise.

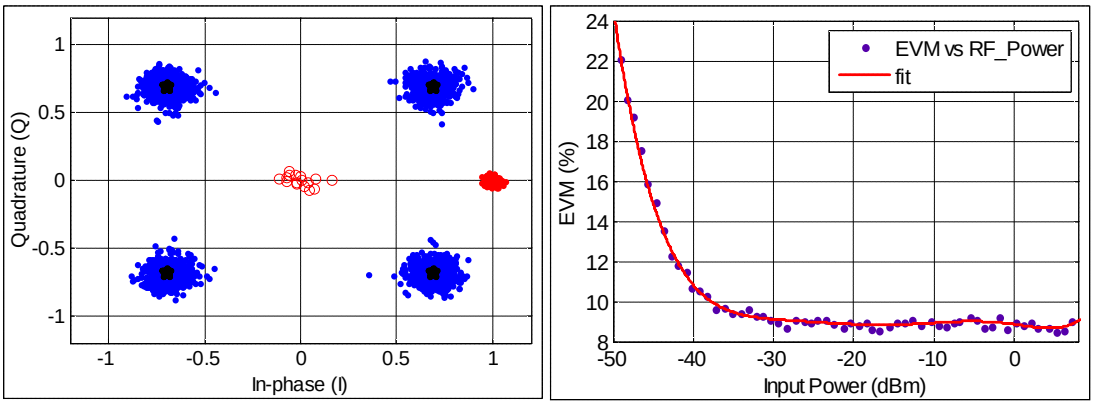

Figure III-24 – Back-to-back configuration for IF=5 GHz: a) constellation diagram of the QPSK modulation signal; b) EVM as a function of the input power

Now if we use 3 GHz as centered frequency without external transposition we got the results presented in Figure III-25. As expected the EVM is reduced to 6 % since we remove all the transposition system which add extra noises and distortion to the measurement. With these results we are ready to make accurate measurements for different centered frequencies with or without external transposition.

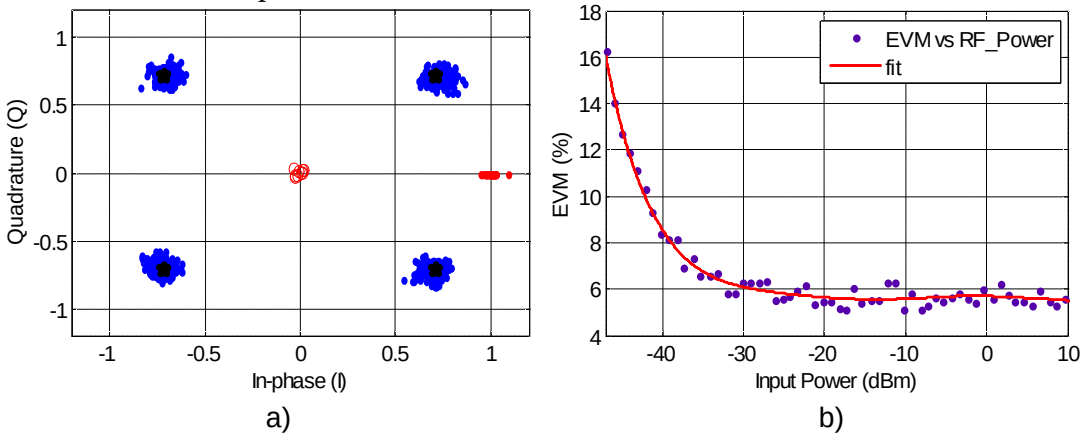

Figure III-25 – Back-to-back configuration for IF=3 GHz: a) constellation diagram of the QPSK modulation signal; b) EVM as a function of the input power

The EVM measurement as a function of the input RF power is presented in Figure III-26 for different laser bias conditions (a) and different optical losses (b). These measurements were performed at a center frequency of 3 GHz.

The typical EVM curve shape can be explained by the relationship between the EVM and SNR [172], [151]

$$EVM\left[linear\right]=\frac{1}{\sqrt{SNR\left[linear\right]}} \tag{3.23}$$

At low input power the SNR ratio is limited by the noise and at high input power is signal distortion instead.

At 2 mA, we are very close to the threshold current getting a high RIN and compressing at low input power and then a high EVM value concludes that this bias current should be avoided, as expected.

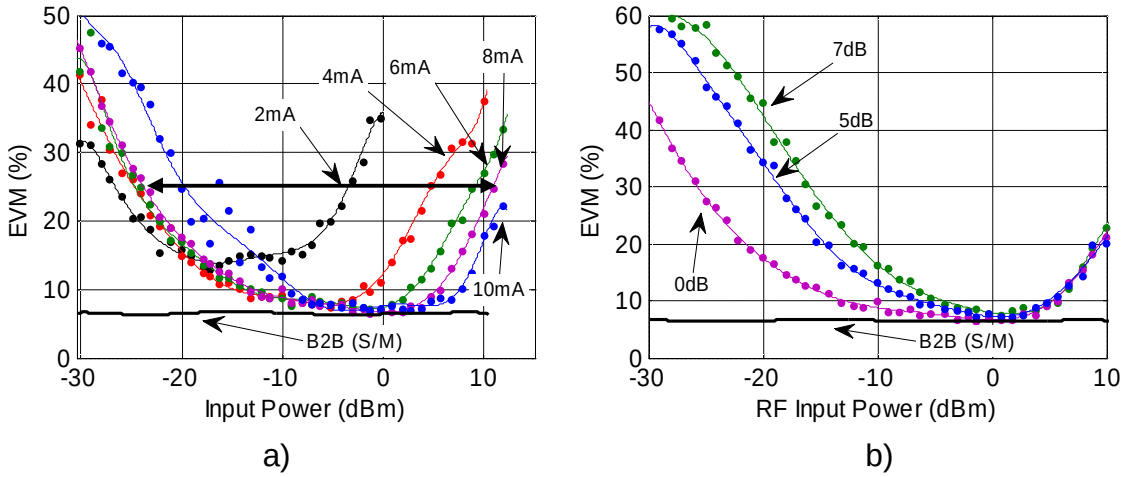

Figure III-26 – EVM of the link between the die VCSEL and the NFPD as a function of the input RF power: a) sweeping the laser bias current; b) sweeping the optical losses (at 8 mA)

From 4 to 10 mA, at low input power the EVM increases with the bias. That can be explained by the increase of the optical emitted power getting noise and saturation effects on the photodiode. For higher input RF powers the EVM decreases with the laser bias increase as we improve the linearity of the laser. We get better results for high bias current since the laser IP1dB is higher (Figure III-18). The laser bias current operation point reveals to be, as expected, a very important parameter to be optimized: 8 mA is considered the best choice on the 10 Gbps systems. This can be explained by the position on the LI curve: not close to the threshold current which could mean high RIN and lower compression point; not close to the saturation region which could reduce the optical microwave gain and add more nonlinearities.

At 8mA we find approximately a 35 dB dynamic range with an EVM degradation lower than 20 %, which can be interesting on the wireless technology system coupled to a RoF infrastructure. Indeed, the wireless device can be positioned at different distances from the fixed antenna, requiring a high power dynamic range (ex: 20 dB from 1 to 10 meters).

Figure III-26 b) shows the EVM as a function of the input RF power for different optical losses with a fixed 8 mA biasing laser current. At low input power the EVM increases because of the thermal noise added by the photodiode and the amplifier placed on the receiver. The dynamic range is reduced since the noise contribution increases and the nonlinearity keep the same. Optical losses pretend to reduce the photodiode input power to avoid saturation effects which is not applicable in this case since the NFPD is very linear. Indeed, the EVM has the same behavior at high input RF power whatever the optical losses are. This is the limit set by the VCSEL it self.

III.A.7. Mapping: Scanning Near Field Optical Microscopy

An extra measure was performed to map the VCSEL surface with the help of the optical probe (DC2OP) controlled by a nanopositioner providing the scan on the x- and y-positions. The emitted optical power was measured with a power meter as a function of the position (x and y) using a 8 mA laser biasing current, as depicted in Figure III-27. Indeed, not only along the spatial x and y position, but also for three heights from the VCSEL position: ΔZ=0, ΔZ=50 µm and ΔZ=100 µm. The first measurement performed with a height of ΔZ=0 above the surface, corresponds to the maximum of coupling efficiency from the lensed fiber to the VCSEL. This distance is typically in the range of 50 µm from the VCSEL surface according to its datasheet and a direct visual inspection through a 45° mirror. Although, the power is lower than the one measured on the LIV curve shown before in a similar DC2OP setup. A maximum of 2.31 mW instead of 3 mW (Figure III-2) is measured here. Indeed, the coupling efficiency is 61 % in this case. This can be explained by a different alignment (gel-pak probing) or temperature condition.

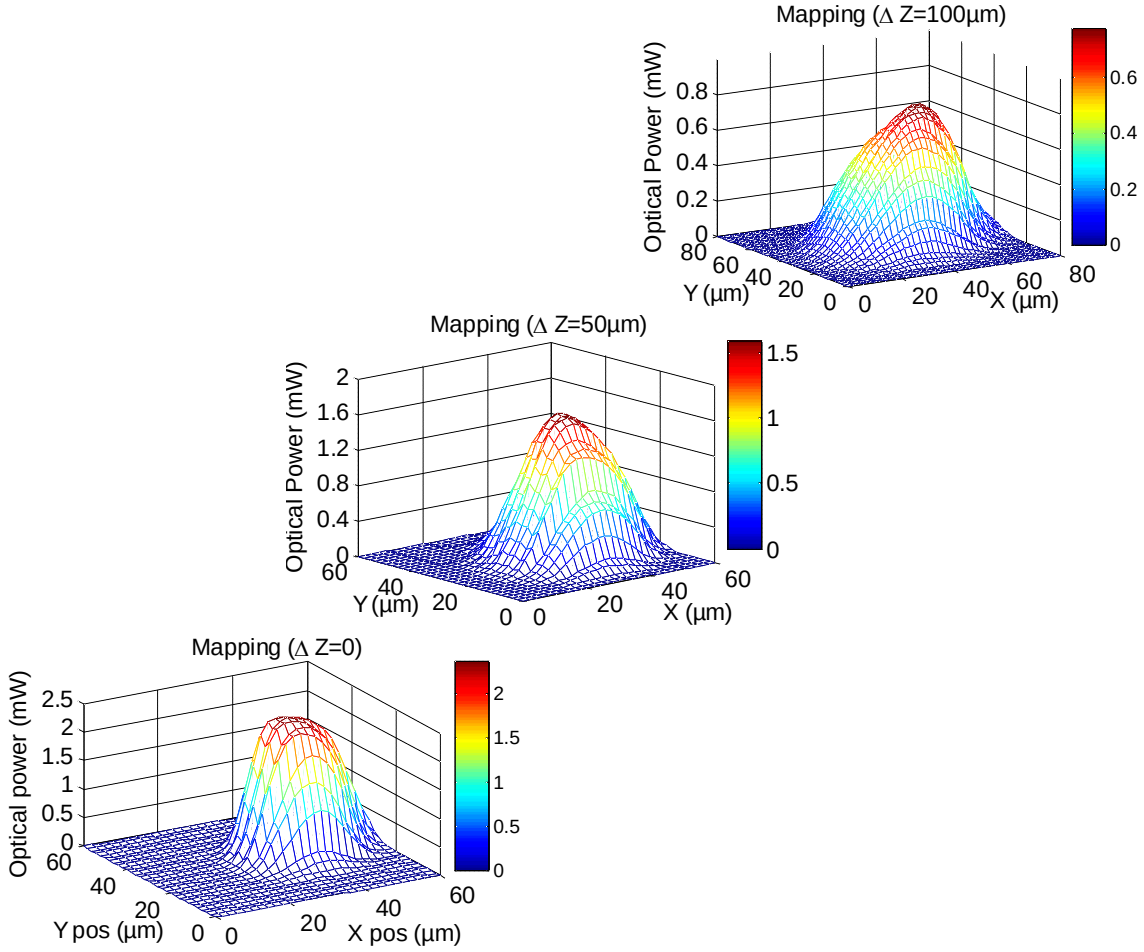

Figure III-27 – VCSEL mapping along the spatial x, y position for different position in terms of Z (transversal to the VCSEL optical power emitted plane) 8 mA

Same measurements have been performed at a ΔZ=50 and ΔZ=100 µm in order to verify the beam shape evolution and extract the beam divergence (target for future work). The laser mapping is important for the waveguide simulation and laser beam modeling, which will be needed in Chapter VI.

III.A.8. Synthesis

A complete link characterization was performed using 10 Gbps ULM GaAs VCSEL Die and a reference commercial photodetector, summarized in Table III.3. The coupling efficiency using an optical probe on the top of the VCSEL was estimated to be 79 % which depends strongly on the alignment condition. The VCSEL shows an interesting slope efficiency up to 0.52 W/A, considering 100 % coupling efficiency (DC2PM). Thermal effects were found to be important at high injection bias currents resulting in optical power saturation and, therefore, lower slope efficiency. In terms of frequency response characterization, the link results have shown link gain around —30 dB with a 3dB cut-off frequency up to 12.3 GHz. Comparing to the state-of-the-art on 850 nm GaAs-based VCSELs we found the modulation bandwidth maximum around 17 GHz in [56] [67] but with a constant control temperature chuck (20-25°C). Indeed, in [67] the temperature is compared between 25 and 85°C where the cut-off frequency is reduces from 16.5 GHz to 13.4 GHz.

Table III.3 –Summary of the extracted parameters for the10 Gbps ULM GaAs VCSEL

Measurement	Parameter	Units	Value	Condition
DC	p_{max}	mW	3.8	I_{bias}=10 mA
	I_{th}	µA	610	-
	S_{LD}	W/A	0.52	Maximum value
	η_d	%	37	
	η_c	%	24	
	λ vs. bias	nm/mA	0.5	From the spectrum shifting
	T vs. bias	°C/mA	7.1	
RF	Link gain	dB	-31	I_{bias}=10 mA, 79% coupling efficiency and R_{PD}=0.222 A/W
	f_{3dB}	GHz	12.31	
	MCEF	GHz/(mA)$^{1/2}$	5.995	
NOISE	RIN	dB/Hz	<-140	I_{bias}>I_{th}*6.5 and freq [1-5 GHz]
Nonlinearity	IP1dB	dBm	up to 9	I_{bias}=10mA and 4 GHz
	IIP3	dBm	up to 15	I_{bias}=10mA and 4 GHz
System	SFDR	dB.Hz$^{2/3}$	up to 98.8	I_{bias}=10mA and 4 GHz
	EVM dynamic	dB	35	I_{bias}=8 mA with 20 % degradation from the B2B

Two important parameters that could be optimized to increase the link performances are the coupling efficiency (79 % measured) and the thermal dissipation. Nonlinear characterization setup was developed based on a highly linear reference photodiode from New Focus, thus enabling the extraction of the VCSEL nonlinearities within the VCSEL-reference photodiode link. The SFDR shows good results (up to 98.8 dB.Hz$^{2/3}$) for a bias current higher than 6 mA and a frequency between 3GHz and 4GHz. The compression gain agrees with these results since the input compression point is up to of 9 dBm at 4 GHz. The last system measurement based on the EVM as a function of the bias current helps to estimate the optimum laser bias current to be 8mA, providing 35 dB power dynamic range with an EVM degradation of 20 %.

III.B. 850 nm SiGe HPT on wafer characterization

This section concentrates on the 850 nm SiGe HPT characterization. A ULM TOSA module which integrates an 8 µm aperture diameter 850 nm GaAs VCSEL presented in the previous section was used as the reference laser for the HPT characterization. We will cover the static performances in terms of Ic-Vce curves and Gummel plots in order to compare both 10x10 µm² and 30x30 µm² structures. RF and finally opto-microwave characterization are done in order to select the best device that is to be packaged and used in the final system.

Figure III-28 represents the on-wafer characterization setup used for the photodetectors (PDs and HPTs). RF probes are placed on the base and collector accesses of the HPT to bias the transistor and collect the output signal. The base is 50 Ohm loaded and the collector is connected to port 2 of the VNA. Port1 is connected to the reference directly modulated by the VNA RF signal. Its emitted light is injected through the fiber into the optical probe that illuminates the optical window of the HPT. The optical coupling between the optical probe and the HPT was analyzed in depth in [124]. It is the same with the one of the VCSEL bench setups from the previous section. The coupling was optimized controlling the illuminated spot as a function of the measured photocurrent.

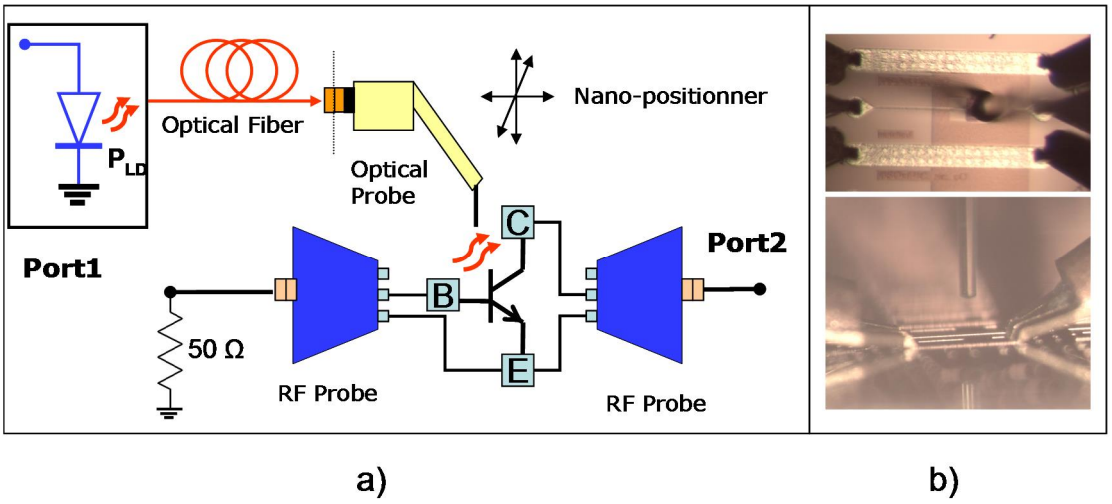

Figure III-28 – On wafer Measurement bench setup: a) Bench schematic for a 10x10 µm² size HPT and a reference 850 nm TOSA; b) Photo of the RF and optical probing placed on the HPT.

The SiGe HPT is based on the SiGE2RF technology from Telefunken GmbH, and was presented in Chapter II, section II.B.2.2.

III.B.1. Static Performances in dark conditions

Static electrical measurements were performed using a semiconductor analyzer B1500 from Agilent feeding voltage and current bias to the phototransistors through bias tees included into the VNA. Therefore, the same measurement bench is used for both static and dynamic measurements.

Phototransistors are here analyzed as electrical devices under dark conditions. They are biased in a common emitter configuration. Both static collector current curves versus Vce and Gummel plots are extracted.

Responses depend deeply on the surface size of the phototransistor. We therefore focus on the 10x10 µm² and 30x30 µm² squared window sizes. Initial measurements have shown that those HPT exhibited the highest opto-microwave link gain [139]. Figure III-29 shows the static response curves of the HPT (Ic-Vce) with 10x10 µm² on a) and 30x30 µm² on b). The measurements were made by sweeping the collector – emitter voltage Vce from 0 to 3 volts at different base currents Ib from 10 nA to 101 µA.

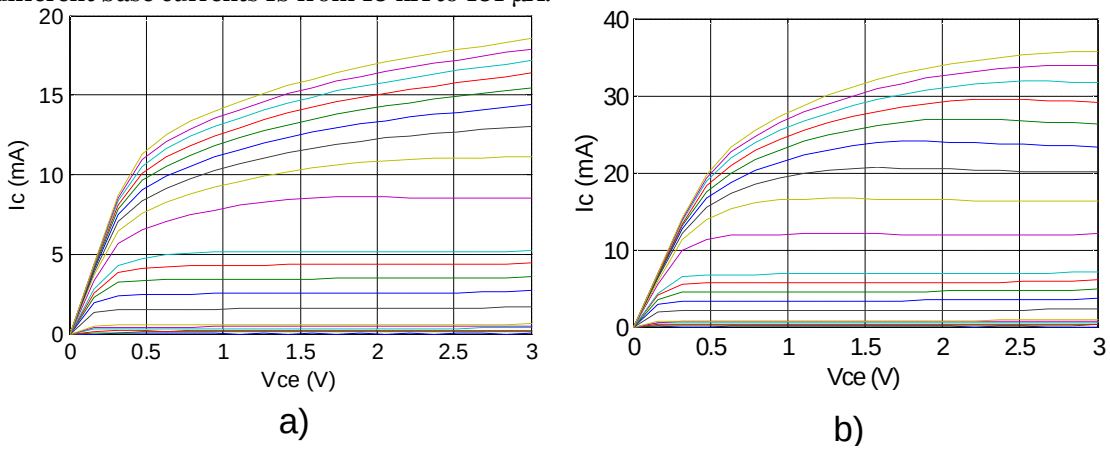

Figure III-29 – Ic versus Vce curve for the HPT with Squared shape, extended emitter, base, collector and with etch oxide (SQxEBC_eO): a) 10x10 µm2; b) 30x30 µm2. Both with Ib sweeping from 10 nA to 101 µA

The plot shows that the HPT structure has a turn "on" voltage V_{on} of 0 V. This is a common characteristic of SiGe HBTs. The static characteristic curves also show the quasi saturation region, wherein the measured collector current has a smooth transition between the saturation region and the active region (10x10 µm² devices present higher collector resistance). This is due to the increase of collector resistance at high currents and low voltages. The breakdown voltage effect starts above 3.5 V according to [139].

The Gummel Plot of the shows the collector current Ic and the base current Ib versus the base emitter voltage on a semi-logarithmic scale, with Vbc kept constant (typically 0 V). This reflects the quality of the emitter base junction at a constant Vbc. Some parameters can be extracted from the Gummel plot, such as the ideality factors, series resistances and leakage currents. Figure III-30 shows the Gummel plot of the HPT at Vbc=0 V. The Vbe/Vce values are swept from 0 V to 1.1 V. Ic can reach up to 20 mA and more.

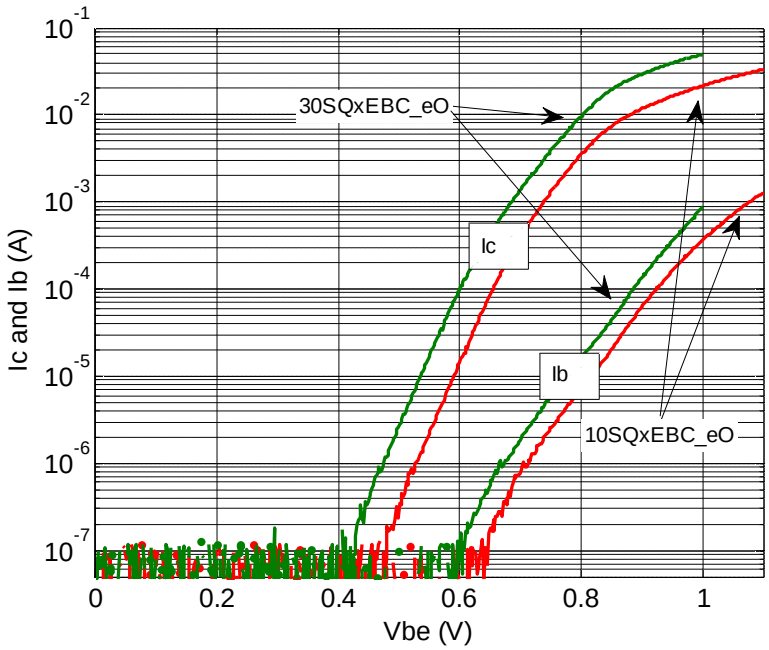

Figure III-30 – Gummel Plot at Vbc=0 comparing both 10 µm and 30 µm devices size (dark conditions).

Figure III-31 shows the extracted Beta plotted as a function of - Beta is defined to be Ic/Ib. The figure shows that the maximum Beta is around 500 for a 10 µm squared device and 700 for a 30 µm one.

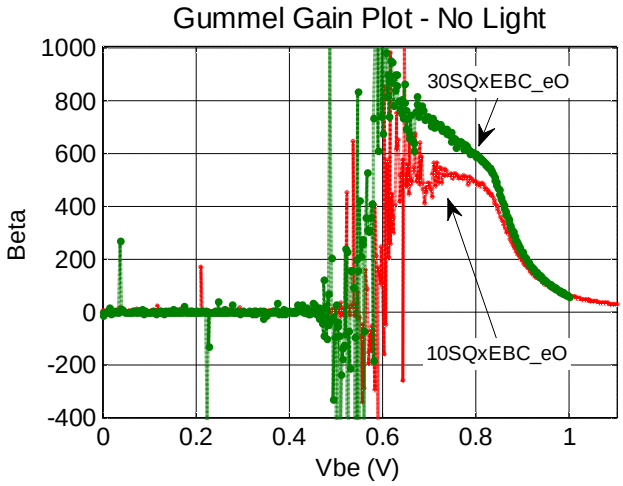

Figure III-31 – Gummel plot for the HPT: a) 10x10 µm² ; b) 30x30 µm²

III.B.2. RF response

Considering first the RF response the modulated port 1 of the VNA is connected to the HPT base and the port 2 to the collector. Figure III-32 shows the transistor electrical gain (E/E S21) for both sizes. The 10x10 µm² HPT has, as expected, a lower gain (up to 19 dB) and a faster electrical RF frequency response (electrical 3dB cut-off frequency up to 1.62 GHz). The 30x30 µm² HPT has a higher gain (up to 26 dB) and lower cutoff frequency (up to 400 MHz)

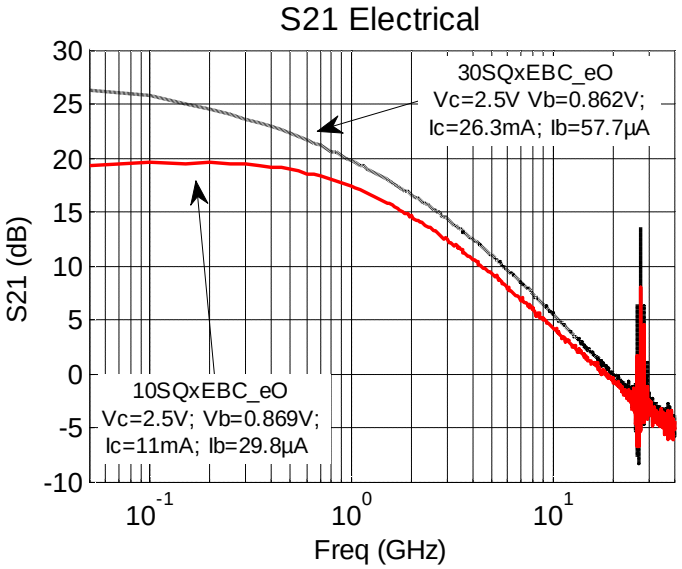

Figure III-32 – E/E S21 of both device 10 µm and 30 µm SiGe HPT

The reflection coefficients (Input-base and Output-collector) in Smith diagram representation is shown in Figure III-33 (frequency up to 10 GHz), showing a better matching to 50 Ohm at high frequency.

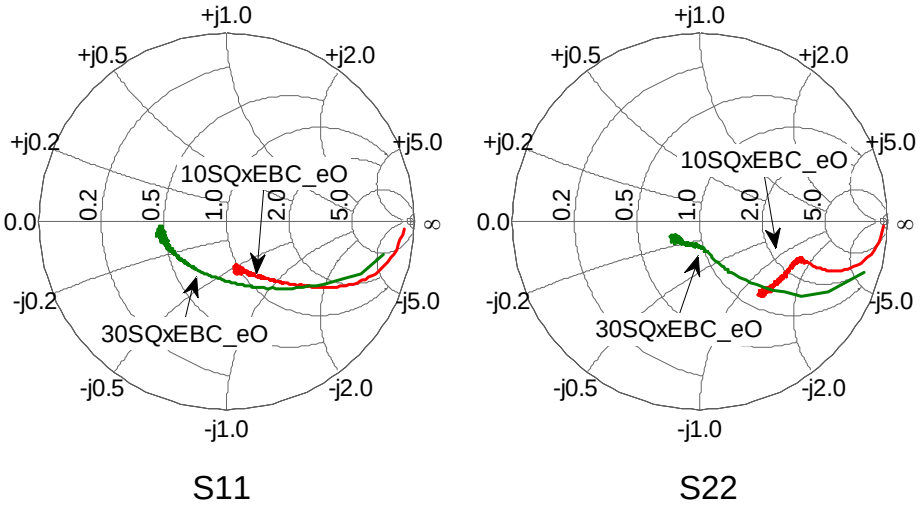

Figure III-33 – E/E Reflection Coefficients: S11 and S22

III.B.3. Opto-RF response

The Opto-microwave link response measurements (O/E S21) were made using a set of dies designed with the base terminal to be loaded to 50 Ohms through an integrated bias-T as depicted in Figure III-34. The fabrication revealed to be defective, making impossible actually to bias the base. We finally measure a 2T-HPT (two-terminal-HPT) configuration.

Due to constraints in the ROSA integration, only this die could be assembled. We thus still work with it and analyze it carefully hereafter.

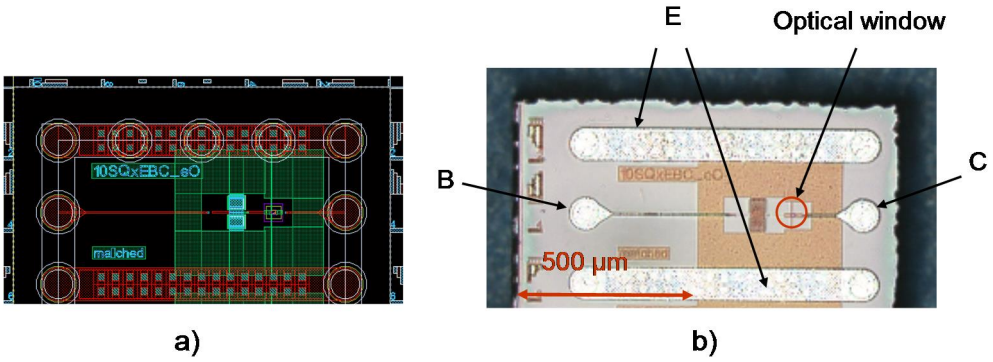

Figure III-34 – 10SQxEBC_EO HPT: a) Layout; b) Photo with an integrated 50 Ω and bias-tee on the base.

The reference light source is the 8 µm aperture size ULM VCSEL integrated into a TOSA module. Its electrical and optical interconnection development is presented in Chapter V, section V.A.2.1, as its performance results. Comparison between both 10 µm and 30 µm HPT devices and the NFPD are presented in Figure III-35. An optical attenuator with 0 dB (~2 dB IL) was used between the TOSA module and the different 3 detectors. The 2T-HPT is biased at the Vce=2.5 V. At low frequency the 30x30 µm² HPT has higher gain since it has more electrical gain and a higher optical window providing less optical losses (higher coupling efficiency). The 10x10 µm² HPT has lower gain (and more optical losses) but it presents a faster response. The O/E gain of the smallest structure is 7 dB higher in the operating frequency at 5 GHz than the 30x30 µm² HPT. A higher opto-microwave gain at the system operation frequency was our main criteria to select this HPT structure used in the SiGe ROSA module. The reference curve in the figure was the NFPD (RPD = 0.222 A/W) measure using an optical attenuator at 0 dB (IL=2 dB) and lighted by the ULM TOSA module. The 2T-HPT responsivity is estimated to be 2.38 A/W (DC) for the 30x30 µm² structure and 1.45 A/W (DC) on the 10x10 µm² size structure. It includes the coupling losses from the lensed optical fiber (~70%). The 10x10 µm² 2T-HPT provides higher responsivity (opto-microwave gain) even up to 2 GHz.

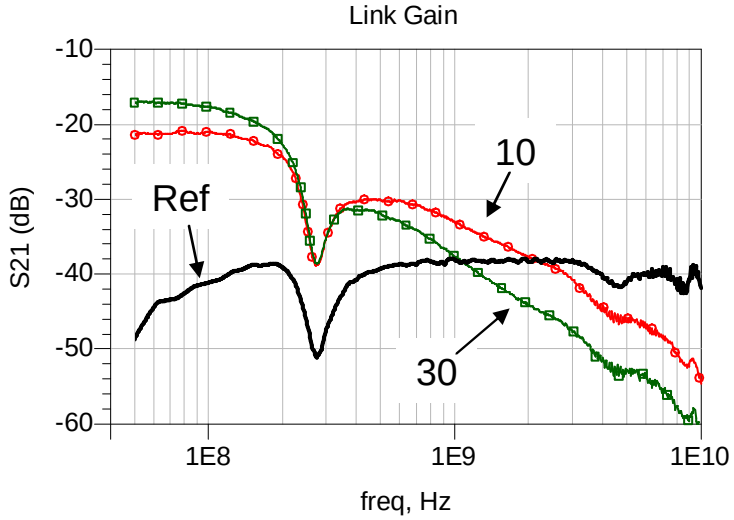

Figure III-35 – Opto-microwave link gain (O/E S21) measurements comparing the reference (using the NFPD and optical attenuator) with 10x10 µm² and the 30x30 µm² 2T-HPT under Vce=2.5 V

The final choice was put in the 10SQxEBC_eO HPT configuration. It shows, indeed, a better gain (responsivity) at 5 GHz (0.034 A/W) even through its optical coupling efficiency to the

fiber is lower. A similar coupling efficiency is also expected from its packaging into the ROSA module, which will be developed in Chapter V.

III.B.4. Synthesis

The static and RF performances of the SiGe HPT were measured comparing both 10 µm and 30 µm squared structures. As expected the smaller structure is faster, but the larger one has a higher E/E gain. A 2T-HPT configuration was then analyzed. The O/E response showed that the 30x30 µm² SiGe HPT has a low 3dB cutoff frequency (<400MHz) but with higher opto-microwave gain which is related to the detector window size. On the other hand the 10x10 µm² shows a faster response with a higher 3dB cut-off frequency (1.62 GHz) but with a lower gain related to the small optical window. However, the OM gain at 5 GHz (ORIGIN intermediate frequency operation) becomes 7 dB higher in the case of the 10x10 µm² 2T-HPT compared to the 30x30 µm² as a result of a greater cut-off frequency x responsivity product. This makes the 10x10 µm² 2T-HPT to be selected for a further packaging and integration into a ROSA module, despite some optical coupling losses which would need further improvements. The electrical gain of this device is about 500. Its electrical transition frequency is about 35 GHz as measured in [139]. An integrated bias-tee and 50 Ohm base load were included with the device. However, due to some defaults in the layout, the base was kept on. The device behavior, however, appears performing sufficiently well at this stage.

III.C. Summary and discussion

This chapter presented the characterization of optoelectronic devices at the die level that will feed the packaged module development for the next chapters.

The first section has shown the complete characterization of a RoF link composed by the 8 µm aperture diameter GaAs VCSEL and the reference New Focus photodiode. Two important parameters that strongly influence the link performances are the coupling efficiency (79 % measured) and the thermal dissipation. The SFDR have shown a good results up to 99 dB.Hz$^{2/3}$ with best biasing of 8 mA with frequency around 4 GHz. Complementary we measured a 35 dB power dynamic range with an EVM degradation of 20 % compared to the B2B.

Two different size structures of 2T-HPTs were chosen to be candidates for the packaging and integration into a ROSA module in the ORIGIN system – squared 10 and 30 µm. Both were characterized using a reference laser source. A trade-off has been taken in terms of speed and coupling efficiency. The choice was made based on the link gain at 5 GHz where the 10 µm squared 2T-HPT reveals to be 7 dB better than the 30 µm squared one despite lower responsivity and coupling efficiency. It exhibits a DC responsivity of 1.45 A/W and 0.034 A/W at 5 GHz, including the coupling losses from the lensed optical fiber (~70%).

This chapter was also especially useful to develop all those noise and nonlinear characterization bench setups that will subsequently allow modeling, design and characterizations in the further chapters.

Chapter IV - **Radio-over-Fiber link design**

In Chapter III, we showed that the individual device performance (laser or the photodiode) can be occulted on the system link measurements. The extraction of each individual block will help to study the link system performance and to identify the critical characteristics of each device. This chapter intends to overcome this problematic by the definition and simulation of novel opto-microwave figures of merit covering the three main analog characteristics: frequency response, noise and nonlinearity behaviors.

The first section proposes a definition of the opto-microwave figures of merit which allows the individual optoelectronic devices representation as an equivalent electrical two-port network. Opto-microwave gain and noise figures of merit are reminded, while novel opto-microwave nonlinear characteristics are given.

The second section presents flexible opto-microwave behavioral models for each RoF block: laser diode, optical fiber and photodetector. The models are implemented in a microwave RF electrical simulator such as Agilent Advanced Design Software (ADS).

The final section intends to extract the individual performances from the link measurements using the defined opto-microwave figures of merit implemented on the behavioral models. The performance comparison between different RoF system configurations is presented. The figures of merits simulated on ADS helped to solve out the opto-microwave figures for each individual block. The simulator is especially useful for the extraction of individual EVM characteristics which would be more difficult with a pure analytic approach.

IV.A. Opto-Microwave Figures of Merit definition

This section proposes the definition of the opto-microwave figures of merit. This topic has been target of interest over the years, usually limited to the gain and noise definitions. Definitions for analogue optical links have been presented mainly by C.H. Cox and E.I. Ackerman. [152]-[160] and followed by other authors such as Haus [161], Baney [162], Tucker [163] and Frigyes [164]. The ESYCOM photonic-microwave team, presented as well a definition of what we call quantum efficiency based definition of gain and noise figure as described in [165], [141]. We here develop, however, a responsivity based definitions that are expected to best fit to the experimental nature of the opto-microwave signals. This approach was initiated in [99]-[102], [140] and more recently in [115], [2], [3].

IV.A.1. Equivalent Opto-Microwave Power - P_{OM}

The first consideration to take into account is the nature of the modulated optical signal which is composed of static and dynamic components. The RF signal (signal information) is transferred onto the envelope of the optical signal and it is the core of our definition.

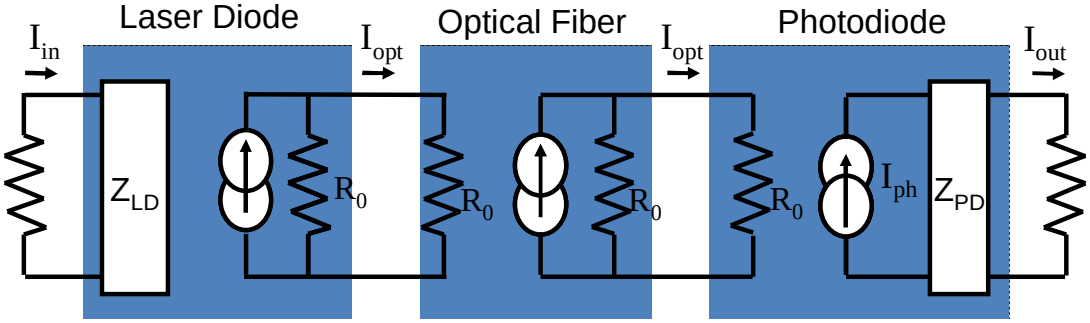

Figure IV-1 – RoF link OM equivalent model with indicudual two-port network devices: laser diode, optical fiber and photodiode

In fact, we apply the microwave approach to the propagation of the envelope modulation signal where we define an equivalent optical current (I_{opt}) as proportional to the optical power:

$$I_{opt} = \alpha_C \cdot P_{opt} = 1 \, {}^{A}\!/_{W} \cdot P_{opt} \quad \text{Equation Section 4} \tag{4.1}$$

where α_C is the conversion coefficient of the optical power to electrical current (α_C is considered equal to 1 A/W). Basically the optical power is represented by an electrical current ('optical') given by the photocurrent measured from a reference ideal photodetector with responsivity of 1 A/W (unity).

The equivalent opto-microwave power is essential to the definition of all following opto-microwave figures of merit. This quantity defines an equivalence to the optical power as an electrical power generated by a virtual probe, which is a theoretical photodetector loaded to 50 Ohms and having a responsivity of 1 A/W (unity). This equivalence has the advantage to allow the individual optoelectronic devices representation as an equivalent electrical two-port network, easily usable in RF simulator such as Agilent ADS, but also on which all microwave notions and concept can be transferred to. It is also easily related to the experimental conditions through a simple normalization procedure.

Figure IV-1 shows the equivalent model for all the modules of a typical optical link: laser diode, optical fiber and photodiode. Each block is defined as a two-port network block cascaded to others with no reflections and feedback on the propagated RoF signal.

$$P_{OM} = \frac{1}{2} R_0 I_{opt}^2 = \frac{1}{2} R_0 \left(\frac{I_{ph} \cdot \alpha_c}{R_{pd,ref}} \right)^2 = P_{out,pd} \cdot \left(\frac{\alpha_c}{R_{pd,ref}} \right)^2 \tag{4.2}$$

The measurement of the optical signal at any point of the link, such as the output of the laser, with the virtual probe, i.e. the 1 A/W reference photodiode, allows us to get the equivalent opto-microwave power defined in the Eq. (4.2).

IV.A.2. Opto-Microwave Gain - G_{OM}

The opto-microwave gain, starting by the photodiode, is defined as the ratio between the output electrical power and the equivalent input opto-microwave (Eq.(4.2)) power.

$$G_{PD}^{OM} = \frac{\frac{1}{2} \cdot R_0 \cdot I_{out}^2}{\frac{1}{2} \cdot R_0 \cdot I_{opt}^2} = \left(\frac{I_{out}}{\alpha_c \cdot P_{opt}} \right)^2 = \left| S_{21}^{OM} \right|^2 = \left(\frac{R_{PD}}{1 \, A/W} \right)^2 = R_{PD}^2 \tag{4.3}$$

where R_{PD} is the photodiode responsivity. A particular interesting case is a configuration where the photodiode is followed by a Trans-impedance Amplifier (TIA) as used in the 1st and 2nd TRoF module generations. In this case the opto-microwave gain is given by:

$$G_{PD+TIA}^{OM} = \frac{\frac{1}{2} \cdot \left(\frac{I_{out} \cdot Z_T}{R_0} \right)^2}{\frac{1}{2} \cdot R_0 \cdot I_{opt}^2} = \left(\frac{Z_T}{R_0} \right)^2 \cdot \left(\frac{I_{out}}{\alpha_c \cdot P_{opt}} \right)^2 = \left| S_{21}^{OM} \right|^2 = \left(\frac{Z_T}{R_0} \right)^2 \cdot (R_{PD})^2 \tag{4.4}$$

where Z_T is the typical trans-impedance gain (V/A).

Doing the same equivalence into the laser, we get

$$G_{LD}^{OM} = \left| S_{21}^{OM} \right|^2 = \left(\frac{S_{LD}}{1 \, A/W} \right)^2 = S_{LD}^2 \tag{4.5}$$

where S_{LD} is the Laser Diode Slope Efficiency.

For an optical fiber, we consider A_{FB} as the related optical losses with the attenuation on the RoF signal included (due to modal or monochromatic dispersion [140]). Then the final opto-microwave gain for the link, assuming of a photodiode without TIA integration, is given by:

$$G_{LINK}^{OM} = \left(S_{LD} \cdot A_{FB} \cdot R_{PD} \right)^2 \tag{4.6}$$

where the laser and the photodiode are considered perfectly matched to 50 Ohm.

If we consider a more general case where there is a mismatch on the both devices, the opto-microwave S-parameters could be involved as defined in [99] [140]. The opto-microwave gain for the complete optical link then becomes:

$$G_{LINK}^{OM} = \frac{1-\Gamma_S^2}{\left(1-\Gamma_S \cdot S_{11}\right)^2} \cdot \left|S_{21}^{OM}\right|_{LD}^2 \cdot \left|S_{21}^{OM}\right|_{FB}^2 \cdot \left|S_{21}^{OM}\right|_{PD}^2 \cdot \frac{1-\Gamma_L^2}{\left(1-\Gamma_L \cdot S_{22}\right)^2} \tag{4.7}$$

where Γ_S and Γ_L are the source and load reflection coefficients, respectively on the laser and photoreceiver output.

IV.A.2.1 Literature comparison

Figure IV-2 compares the different gain definitions of optical links from the literature:
Cox et al. definition [152] is based on the proportionality of the emitted optical power by the laser to the squared root of the RF input power and considers the RF output power given by the detected photocurrent being proportional to the square of the optical power. Those proportionalities are related to each individual device efficiency. Therefore the gain is defined as small signal efficiency;
Ackerman proposed a new definition [158] given by an “effective” gain with the goal to define the noise figure of a cascade optical link. Therefore, he proposed to remove the square-law nature of the modulation and detection processes;
In our case [2], [3] we propose a gain between homogeneous quantities and maintain the fact that the optical beam behaves as a current. Through a proper definition of the equivalent opto-microwave power, and further definition of the noise figure, we also achieve the noise figure composition target by Ackerman.

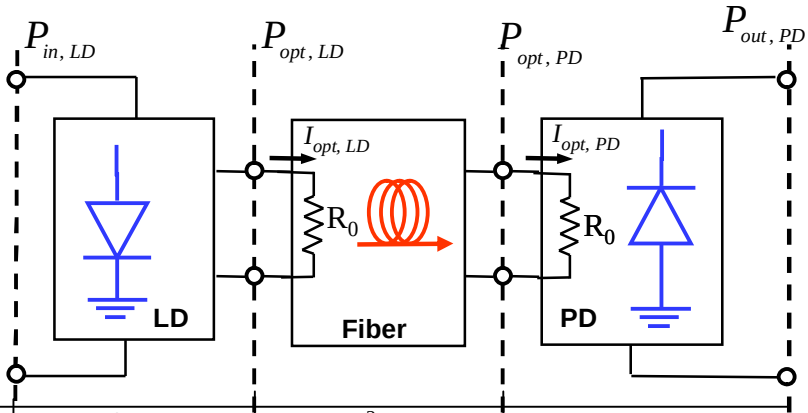

Cox et al.	$\frac{P_{opt,\,LD}^2}{P_{in,\,LD}}$	$\frac{P_{opt,\,PD}^2}{P_{opt,\,LD}^2}$	$\frac{P_{out,\,PD}}{P_{opt,\,PD}^2}$
Ackerman	$\frac{P_{opt,\,LD}}{P_{in,\,LD}}$	$\frac{P_{opt,\,PD}}{P_{opt,\,LD}}$	$\frac{P_{out,\,PD}}{P_{opt,\,PD}}$
This work	$\frac{1/2 \cdot R_0 \cdot I_{opt,\,LD}^2}{P_{in,\,LD}}$	$\frac{1/2 \cdot R_0 \cdot I_{opt,\,PD}^2}{1/2 \cdot R_0 \cdot I_{opt,\,LD}^2}$	$\frac{P_{out,\,PD}}{1/2 \cdot R_0 \cdot I_{opt,\,PD}^2}$

Figure IV-2 – Individual gain definition from literature compared to our definition: Cox - individual small-signal efficiencies; Ackerman - effective gain.

IV.A.3. Opto-Microwave Noise Figure - NF_{OM}

The noise definition of individual devices leads to identification of each device corresponding noise source.

The laser and photodiode noise factor can be determined by typical Signal-to-Noise (SNR) power ratio between the OM input and the OM output, given by:

$$F_{LD,\,PD}^{OM} = \left. \frac{SNR_{in}^{OM}}{SNR_{out}^{OM}} \right|_{T_o} \tag{4.8}$$

Our definition imposes to consider the noise at each optical side, to be the noise density of the equivalent opto-microwave power. It also imposes to consider the input noise reference signal as the thermal noise power density at a room temperature of 290 K. Thus the Opto-Microwave Noise Factor can be given by:

$$F_{LD,\,PD}^{OM} = 1 + \frac{N_{LD,\,PD}^{OM}}{G_{LD,\,PD}^{OM} \cdot k \cdot T} \tag{4.9}$$

Where $N_{LD,\,PD}^{OM}$ corresponds to the opto-microwave noise spectral power density added by the laser or the photodiode. Since the laser noise source is related to the RIN, we can define a noise spectral power density added by the laser as:

$$N_{LD}^{OM} = \left\langle i_{opt} \right\rangle^2 \cdot R_L = \left\langle \alpha_c \cdot P_{opt} \right\rangle^2 \cdot R_L = \left(1A/W \cdot P_{opt,DC} \right)^2 \cdot RIN \cdot R_L \tag{4.10}$$

Therefore, we define the laser opto-microwave noise factor, by

$$F_{LD}^{OM} = 1 + \frac{(1A/W \cdot P_{opt,DC})^2 \cdot RIN \cdot R_L}{G_{LD}^{OM} \cdot k \cdot T} \tag{4.11}$$

Concerning the photodiode, two noise sources are identified, first the shot noise produced by the quantum nature of the photons received by the detector second the thermal noise. The shot noise is directly proportional to the incident optical power, conventionally defined by Eq. (3.5) in Chapter III, section III.A.3. The second noise source is the thermal noise which it is not dependent on the optical power and which is constant with frequency, reason why it can be subtracted easily to the total noise. The thermal noise on the photodiode is typically quantified with the Noise Equivalent Power (NEP) which is the optical input power needed to produce an additional output power identical to that noise. It is given by:

$$NEP[W] = \frac{1}{R_{PD}} \sqrt{B_N \cdot \frac{N_{th\_PD}}{R_L}} \tag{4.12}$$

where N_{th_PD} is the photodiode thermal noise. At the end, taking into account both noise sources, the photodiode opto-microwave noise factor is given by:

$$F_{PD}^{OM} = 1 + \frac{2 \cdot q \cdot I_{ph} \cdot R_L + \left(NEP * R_{PD}\right)^2 \cdot R_L}{G_{PD}^{OM} \cdot k \cdot T} \tag{4.13}$$

If we consider the particular case of the photodiode followed by a TIA, the opto-microwave noise factor is then given as:

$$F_{PD+TIA}^{OM} = 1 + \frac{2 \cdot q \cdot I_{ph} \cdot R_L \cdot G_{TIA} + \frac{1}{2} \cdot \frac{\left(V_{out\_noise}\right)^2}{R_L}}{G_{PD}^{OM} \cdot k \cdot T} \tag{4.14}$$

Where G_{TIA} is the TIA gain, V_{out_noise} is the TIA output noise voltage. Replacing the transimpedance amplifier gain and the output voltage noise we get

$$F_{PD+TIA}^{OM} = 1 + \frac{2 \cdot q \cdot I_{ph} \cdot R_L \cdot \left(\frac{Z_T}{R_L}\right)^2 + \frac{\left(I_{eq} \cdot Z_T\right)^2}{2 \cdot R_L}}{G_{PD}^{OM} \cdot k \cdot T} \tag{4.15}$$

Where the I_{eq} is the noise current equivalent at the input of the TIA.

Finally, as each part of the opto-microwave link considers the same input reference noise, i.e. the thermal noise power density $k \cdot T$, the Friis equation is now applicable to compute the complete link opto-microwave noise factor:

$$F_{LINK}^{OM} = F_{LD}^{OM} + \frac{(F_{FB}^{OM} - 1)}{G_{LD}^{OM}} + \frac{(F_{PD}^{OM} - 1)}{G_{FB}^{OM} \cdot G_{LD}^{OM}} \tag{4.16}$$

In our definition we consider the optical fiber as a noiseless element ($F_{FB}^{OM} = 1$) but it still has an important contribution to the final noise factor with the gain (A_{FB}) as expressed by the Friis formula. Replacing equations (4.11) and (4.13) in (4.16), we get:

$$F_{LINK}^{OM} = 1 + \frac{\left(1A/W \cdot P_{opt,DC}\right)^2 \cdot RIN \cdot R_0}{S_{LD}^2 \cdot k \cdot T} + \frac{2 \cdot q \cdot I_{ph} \cdot R_0 + \left(NEP * R_{PD}\right)^2 \cdot R_0}{S_{LD}^2 \cdot A_{FB}^2 \cdot R_{PD}^2 \cdot k \cdot T} \quad (4.17)$$

IV.A.3.1 Literature comparison

Our definition differs from other authors cited previously where they define all the noise contributions, including the laser, at the output of the photodiode. That means they will not use the optical power (P_{opt}) but the photocurrent measured at the photodiode output which depends on the responsivity.

Ackerman [158] provided a definition which is based on the Friis relationship as well. The main difference with our model is that he considers the noise figure of the optical fiber as $NF_{FB}^{OM} = 1/G_{FB}^{OM}$.

In the case of Cox et al. [152] definition do not take into account the electrical thermal noise at the photodetector end and is not compatible with Friss.

Haus [161] has proposed a revised definition for the noise figure of an optical amplifier based of the optical signal-to-noise power ratios as given by optical field power spectra at the input and output of the optical amplifier instead of the detected electrical signal to noise power. He also explicitly uses the thermal noise power as the input reference which makes it consistent with standard electrical noise figure definition.

Baney [162] and Tucker [163] focused their work on the noise figure of the optical amplifiers. Their noise figure formulation is based on a general description of the SNR degradation of intensity modulated signals:

$$NF = 10 \cdot \log_{10}\left(\frac{SNR_{in,ref}}{SNR_{out}}\right) \quad (4.18)$$

Where the SNR_{in} is measured without the optical amplifier and is a fixed reference. And SNR_{out} gives the degradation when the optical amplifier is inserted in the measurement. An important characteristic is that they considered the input noise reference signal to be a shot-noise limited input reference instead of the typical definition used in electrical circuits where the input reference signal is based on thermal noise. Indeed, the optical amplifiers are low noise components and using thermal noise at the input could mask the noise produced by the amplifier. They provide two methods of optical noise figure measurement: using optical spectrum analyzer or using electrical spectrum analyzer. They recall also that the noise factor contributed by the passive element (i.e. optical fiber) is zero $NF_{FB}^{OM} = 0$.

A summary of the main differences between the different approaches is presented in Table IV.1. Our approach is characterized by: It is applicable to each individual parts of the link; it considers thermal input reference; it is compatible with Friis formula; the passive optical elements are noiseless.

Table IV.1 – Noise figure definitions founded in literature

	Ref.	Configuration	Input reference	Friis	NF_{FB}	Features
Cox et al.	[152]	link	thermal noise	no	-	opto-microwave link
Ackerman	[158]	individual	thermal noise	yes	$1/G_{FB}$	opto-microwave link
Tucker et al.	[162]	individual	shot-noise-limited	yes	0	optical amplifier
Haus	[161]	-	thermal noise	yes	-	optical amplifier
Frigyes et al.	[164]	link	thermal noise	-	0	opto-microwave link
Our work	[2] [3]	individual	thermal noise	yes	0	opto-microwave link

IV.A.4. Opto-Microwave Nonlinearities

We proposed to develop in this section the opto-microwave figures of merit that describe the nonlinearities of each device: we thus simply extend the gain compression at 1 dB (P1dB) and the 3rd order intercept point (IP3) into the opto-microwave domain. Both pure microwave definitions were presented in Chapter III, subsection III.A.4. The related opto-microwave definition ($P1dB_{OM}$, $IP3_{OM}$ and $SFDR_{OM}$) are presented in Figure IV-3.

They are based on the representation of signal levels in the opto-microwave equivalent powers, both on the input and output of each device.

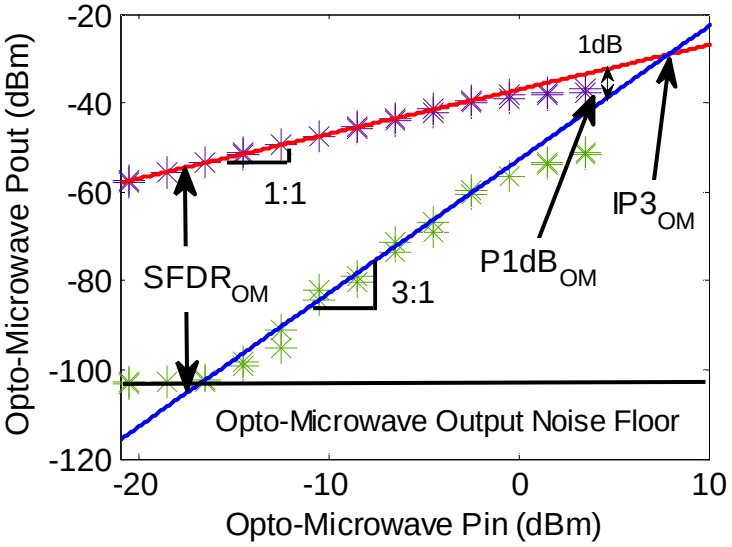

Figure IV-3 – Plot of the Opto-Microwave output power versus the Opto-Microwave input power of a nonlinear system: $P1dB_{OM}$, $IP3_{OM}$ and $SFDR_{OM}$ definition

Those definitions are detailed further in the following subsections.

IV.A.4.1 Opto-Microwave Gain Compression Point – $P1dB_{OM}$

The Opto-Microwave Gain Compression Point is defined by the opto-microwave output level at which the device gain is 1 dB less than the small signal opto-microwave gain, or is compressed by 1 dB (Figure IV-3). We are interested to analyze the link compression gain

expression as a function of the different individual devices using a typical cascade microwave link definition. The input 1dB compression point of the link gain can be expressed as a function of the laser, optical losses and photodiode gain and considering individual opto-microwave compression points $\left(IP1dB_{LD}, IP1dB_{PD}^{OM}\right)$ according to the microwave composition law given by [166]

$$IP1dB_{dBm}^{LINK} = IP1dB_{LD} - 10\cdot\log\left[1+\frac{G_{LD}^{OM}\cdot G_{FB}^{OM}\cdot IP1dB_{LD}}{IP1dB_{PD}^{OM}}\right] \tag{4.19}$$

With $G_{FB}^{OM} = A_{FB}^2$.

Conventionally two cases can be considered:

1 $$IP1dB_{PD}^{OM} >> G_{LD}^{OM}\cdot G_{FB}^{OM}\cdot IP1dB_{LD} \tag{4.20}$$

2 $$IP1dB_{PD}^{OM} << G_{LD}^{OM}\cdot G_{FB}^{OM}\cdot IP1dB_{LD} \tag{4.21}$$

Case 1 corresponds to the link input compression point dictated by the laser:

$$\Rightarrow IP1dB_{dBm}^{LINK} \approx IP1dB_{LD} \tag{4.22}$$

and case 2 corresponds to the link input compression point dictated by the photodiode:

$$\Rightarrow IP1dB_{dBm}^{LINK} \approx \frac{IP1dB_{PD}^{OM}}{G_{LD}^{OM}\cdot G_{FB}^{OM}} \tag{4.23}$$

Eq. (4.19) then helps to retrieve the typical behavior of the compression of the complete optical link as a function of the optical attenuation. This behavior is sketched in Figure IV-4. On the left, for low input losses (G_{FB}^{OM}), the linearity increases showing that we are on the photodiode nonlinearity limitation region. For high input loss the linearity does not change, we are on the laser nonlinearity region.

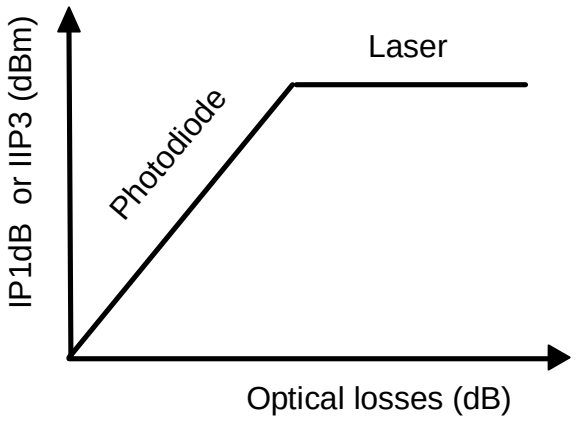

Figure IV-4 - IIP3 and IP1dB of the link system as a function of the optical losses.

Now the same consideration can be done in terms of the link compression point at the output. The composition law is now given by:

$$OP1dB_{dBm}^{LINK} = OP1dB_{PD} - 10\cdot\log\left[1+\frac{1}{G_{FB}^{OM}\cdot G_{PD}^{OM}}\cdot\frac{OP1dB_{PD}}{OP1dB_{LD}^{OM}}\right] \tag{4.24}$$

If we consider the case (1), it comes out that:

$$OP1dB_{PD} >> G_{FB}^{OM}\cdot G_{PD}^{OM}\cdot OP1dB_{LD}^{OM} \tag{4.25}$$

Then, this means that the system OP1dB is limited by the laser.

$$\Rightarrow OP1dB_{dBm}^{LINK} \approx G_{FB}^{OM}\cdot G_{PD}^{OM}\cdot OP1dB_{LD}^{OM} \tag{4.26}$$

Now if considering the situation of the case (2)

$$OP1dB_{PD} << G_{FB}^{OM} \cdot G_{PD}^{OM} \cdot OP1dB_{LD}^{OM} \tag{4.27}$$

Then, this means that the OP1dB from the photodiode limits the system.

$$\Rightarrow OP1dB_{dBm}^{LINK} \approx OP1dB_{PD} \tag{4.28}$$

By changing the optical losses (G_{FB}^{OM}) between the laser and the photodiode we can verify the influence of each device on the gain compression.

From this new $IP1dB^{OM}$ and $OP1dB^{OM}$ definitions, it is then possible to better characterize the laser and photodiode devices. Indeed, the $OP1dB^{OM}$ of the laser is useful to include the value of the laser slope efficiency. Indeed having a large $IP1dB$ and a small slope efficiency may not be worth, while giving the value of the $OP1dB^{OM}$ gives a clear answer.

IV.A.4.2 Opto-Microwave 3rd Order Intercept Point – IP3OM

Opto-microwave 3rd order intercept point is given by the point where the extrapolated opto-microwave third order intermodulation distortion level ($IMD3_{OM}$) is equal to the opto-microwave signal fundamental level ($IMD1_{OM}$) (Figure IV-3). Microwave composition laws [166] can easily be transferred to the new $IP3_{OM}$ definition. The input 3rd order intercept point (IIP3) in dBm for an optical system is thus given by:

$$IIP3_{dBm}^{LINK} = IIP3_{LD} - 10 \cdot \log\left[1 + \frac{G_{FB}^{OM} \cdot G_{LD}^{OM} \cdot IIP3_{LD}}{IIP3_{PD}^{OM}}\right] \tag{4.29}$$

If we consider the two extreme situations:

1 $$IIP3_{PD}^{OM} >> G_{FB}^{OM} \cdot G_{LD}^{OM} \cdot IIP3_{LD} \ \ then \ \ IIP3_{dBm}^{LINK} \approx IIP3_{LD} \tag{4.30}$$

2 $$IIP3_{PD}^{OM} << G_{FB}^{OM} \cdot G_{LD}^{OM} \cdot IIP3_{LD} \ \ then \ \ IIP3_{dBm}^{LINK} \approx \frac{IIP3_{PD}^{OM}}{G_{FB}^{OM} \cdot G_{LD}^{OM}} \tag{4.31}$$

From these equations and taking into account $OIP3 = IIP3 + Gain$, we can express the OIP3 by:

$$OIP3_{dBm}^{LINK} = OIP3_{PD} - 10 \cdot \log\left[1 + \frac{1}{G_{FB}^{OM} \cdot G_{PD}^{OM}} \cdot \frac{OIP3_{PD}}{OIP3_{LD}^{OM}}\right] \tag{4.32}$$

We can also consider the 2 cases: when OIP3 is limited by the laser

$$OIP3_{PD} >> G_{FB}^{OM} \cdot G_{PD}^{OM} \cdot OIP3_{LD}^{OM} \ \ then \ \ OIP3_{dBm}^{LINK} \approx G_{FB}^{OM} \cdot G_{PD}^{OM} \cdot OIP3_{LD}^{OM} \tag{4.33}$$

or by the photodiode

$$OIP3_{PD} << G_{FB}^{OM} \cdot G_{PD}^{OM} \cdot OIP3_{LD}^{OM} \ \ then \ \ OIP3_{dBm}^{LINK} \approx OIP3_{PD} \tag{4.34}$$

Same considerations can me made using nonlinearity evolution presented in Figure IV-4 in terms of the IIP3.

IV.A.5. Opto-Microwave Spurious Free Dynamic Range – SFDROM

The SFDR is typically used for system characterization relating the noise, the frequency response and the intermodulation distortions. The Opto-microwave SFDR proposed is defined as the opto-microwave output power range defined between opto-microwave output powers at the fundamental and at the third order intermodulation distortion ($IMD3_{OM}$) when input power produces an $IMD3_{OM}$ equal to the opto-microwave noise (Figure IV-3):

$$SFDR_{LD,PD}^{OM}\left[dB\cdot Hz^{2/3}\right]=\frac{2}{3}\left[OIP3_{LD,PD}^{OM}-N_{NOISE}^{OUT}\right] \quad (4.35)$$

where $OIP3_{OM}$ is the Opto-microwave output 3rd order intercept point and N_{NOISE}^{OUT} is the opto-microwave output spectral noise density in 1Hz, defined as:

$$N_{NOISE}^{OUT}=k\cdot T+NF_{LD,PD}^{OM}+G_{LD,PD}^{OM} \quad (4.36)$$

where k, T, NF_{OM} and G_{OM} is the Boltzmann constant, operational temperature, opto-microwave noise figure and opto-microwave gain, respectively.

IV.A.6. Opto-Microwave Error-Vector-Magnitude – EVM_{OM}

EVM_{OM} compares the constellation between the received complex equivalent OM symbols and the ideal transmitted ones, depending upon the modulation scheme, as sketched in Figure IV-5 (applicable also the photodiode side). Mathematically EVM_{OM} is the ratio of the OM error vector power to the reference vector power:

$$EVM_{OM}\left[linear\right]=\sqrt{\frac{P_{error\ vector}^{OM}}{P_{reference}}} \quad (4.37)$$

Finally we can also define an individual Opto-Microwave SNR which can be directly related to the Opto-Microwave EVM by:

$$EVM_{LD,PD}^{OM}\left[linear\right]=\frac{1}{\sqrt{SNR_{LD,PD}^{OM}\left[linear\right]}} \quad (4.38)$$

It is important to take into account that the input SNR of each optoelectronic device considers the reference noise to be the thermal noise at a room temperature of 290 K.

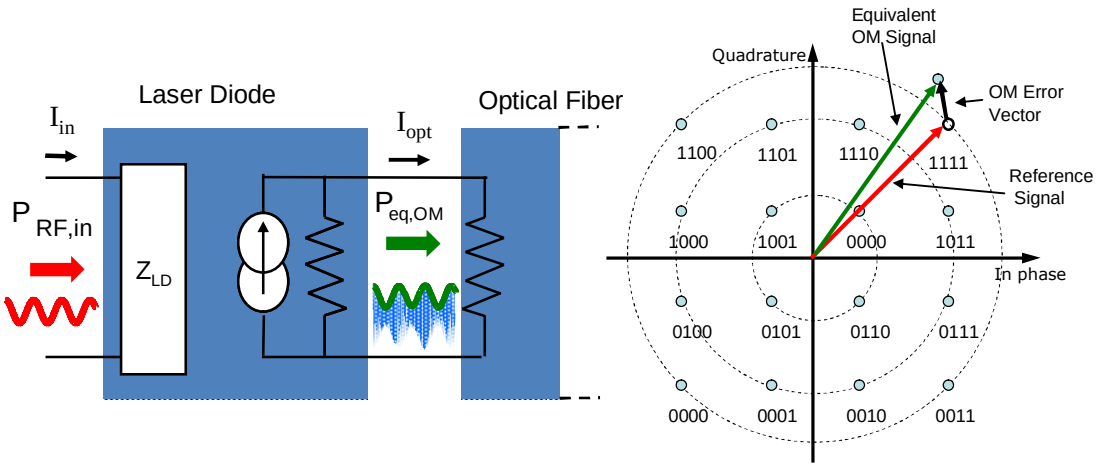

Figure IV-5 – Definition of Opto-Microwave EVM: a) Laser OM model representation; b) 16-QAM OM constellation

IV.A.7. Synthesis

The definition of the opto-microwave figures of merit was presented and compared to other authors. It covered the frequency response by defining an OM gain, the noise behavior by the OM NF and the nonlinearities by both OM P1dB and OM IP3. The definition is based on

conventional microwave formulation which was complemented by an equivalent OM power approach. This is to say the extension of microwave tools in the opto-microwave domain. Two more OM figures of merit (OM SFDR and OM EVM) are used for the system performance characterization where each component is individually evaluated in the opto-microwave domain.

IV.B. Opto-Microwave Behavioral Model

This section we propose an optical microwave behavioral model based on symbolically defined device (SDD) developed by Agilent ADS. The concept is to use a black box in which mathematical equations can be implemented to specify the relationships between input and output currents and voltages as we can see in Figure IV-9. The use of SDD has a particular interest to simulate large and small signal behaviors of a nonlinear device. It enables a simple, fast way to develop and modify complex models and simulation results can be compared to measured data. A SDD with n ports is described by n equations between the n port currents and the n port voltages specified in time domain. The time derivative and integration are also available. In the example of Figure IV-6, we use an explicit representation: currents at the ports 1 and 2 are specified as a function of the port voltages. In this example, the current at port 1 is calculated by dividing the voltage at port 1 by 50 Ohm.

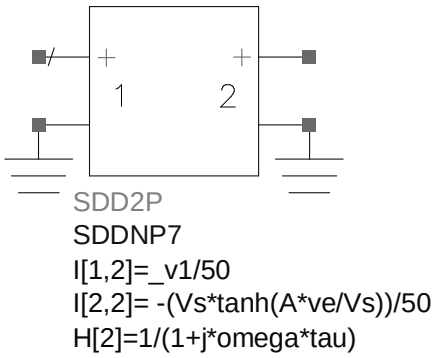

Figure IV-6 – Symbolically Defined device (SDD) example: model of an amplifier.

The current at port 2 is the same, but a nonlinear behavior is defined using a tangent hyperbolic function. The weighting (H [2]) function is a simple low pass filter of 1st order.

We decided to implement one SDD for each component of the RoF system (see Figure IV-7): Laser, photodiode and optical fiber. Our main focus is on the Laser (LD) and the photodiode (PD) models defined by the user input variables (measured in Chapter III) that contribute to the opto-microwave figures of merit. The optical fiber model is characterized only by optical losses (misalignment and connectors).

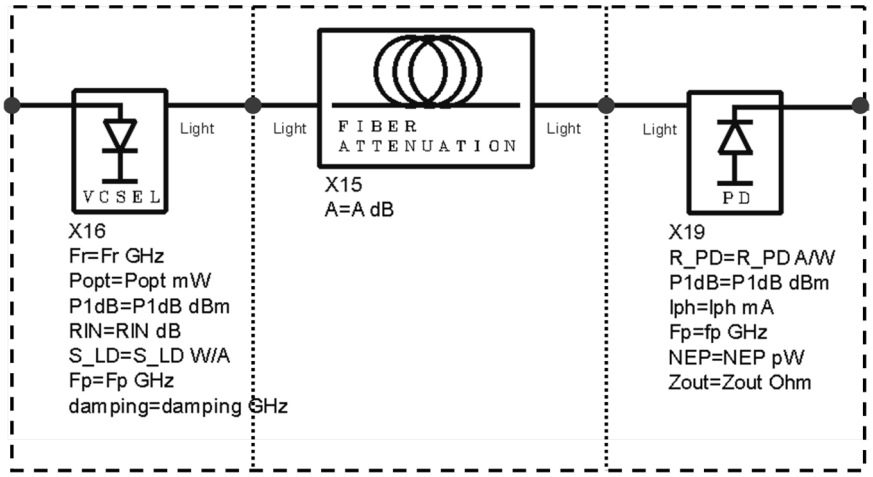

Figure IV-7 - RoF Behavior models developed in Agilent ADS.

Figure IV-7 shows the behavioral model of the link system with 3 main blocks: Laser on the left; optical attenuation on the center and the photodiode on the right. This link model

simulates the link between an ULM VCSEL die connected to the NFPD photodiode. All the measurements done previously, feeds the model with the different parameters as shown in the figure. The optical fiber model helps to fit the model to the measurements by providing the optical losses from the fiber and from eventual misalignments not necessarily well-known in advance. The model focused on one bias operation current of 8mA, which the most interesting bias point for the final system (see Chapter III).

Optoelectronic devices modeling for Radio-Over-Fiber link system simulation is very important to help us to predict their behavior and to optimize the system performances. The figures of merit were introduced in Chapter III (link characterization) and developed in section IV.A by the opto-microwave definition. The Figure IV-8 illustrates our modeling approach by defining an individual behavioral model to each block in order to understand the global performances given by the link measurements.

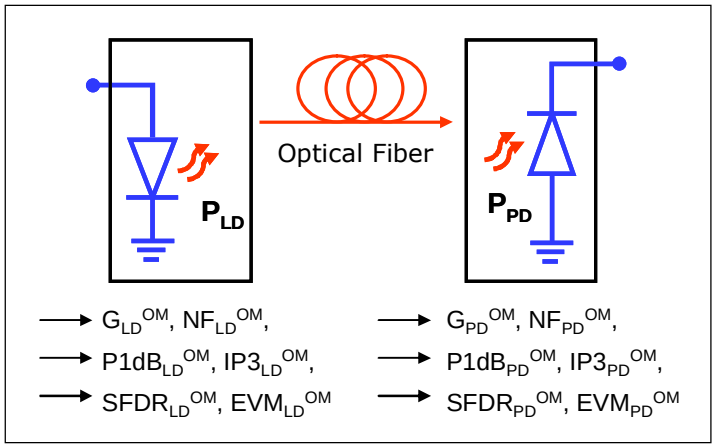

Figure IV-8 – RoF block model with corresponding Opto-microwave Figures of merit.

Modeling nonlinear systems is a topic of high interest during the last years, mainly on the RF power amplifiers. System modeling in general can include equivalent circuit modeling or behavioral modeling. A good knowledge of the circuit and component levels is required for equivalent circuit modeling. On the other hand, behavioral modeling does not require details at the component level. Basically the system behavior is implemented using a mathematical equation that linked the input to the output signals. Non-linear behavioral system models can be separated into three types: memory-less, quasi memory-less and models with memory [142]. Memory-less models consider only AM/AM conversions and a constant phase. In the case of the quasi memory-less models, the amplitude (AM/AM) and the phase (AM/PM) distortions are taken into account. Memory effects imply that the system output signal depends not only on the current input signal, but also on the precedent past signal. The main source of memory phenomenon is thermal effects and can be observed by the asymmetries in lower and upper sidebands and bandwidth dependent variations in the magnitude of IMD products. The Non-linear Memory-less and Quasi-Memory-less Models used are typically: Rapp Model [143], Saleh model [144], Ghorbani model [145], Hyperbolic Tangent Model [142] (the last will target on this work for its simplicity). In the case of non-linear Models with Memory, the most widely used are: Volterra Series [149]-[151], Wiener Model [149], Hammerstein Model [146], parallel Hammerstein Model [147] and Memory Polynomial Model [148] .

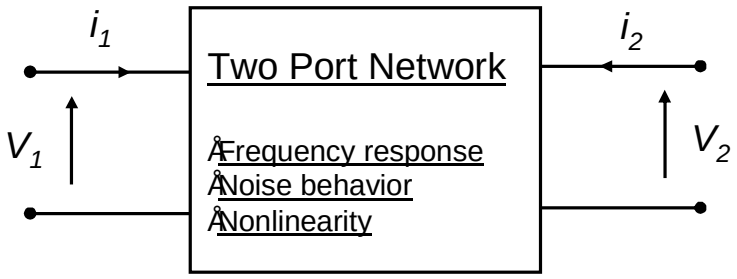

Figure IV-9 – Two-Ports Network model representation: SDD

IV.B.1. Laser diode behavioral model

The laser model is represented in Figure IV-10. The output opto-microwave current is

$$\frac{I_{opt}}{\alpha_C} = P_{opt} = I_{in} \cdot S_{LD} \tag{4.39}$$

It also introduces the unidirectional path of the optoelectronic devices where the current source is given by $2 \cdot I_{opt}$ and a 50 Ohm load which produces a perfect match without optical reflections.

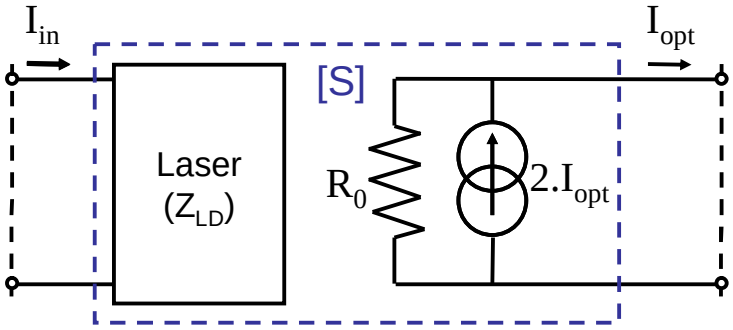

Figure IV-10 – Laser equivalent two-port network with optical output access

The large signal behavior was implemented into the model by introducing the tangent hyperbolic [142] function on the I_{opt} definition as

$$I_{opt} = I_S \cdot \tanh\left(\frac{G \cdot I_{in}}{I_S}\right), \tag{4.40}$$

where G is the gain in the linear region (Eq. (4.5)), I_{in} the input current and I_S the limit value of the output signal which provides the saturation effect. The last parameter on the opto-microwave gain is the frequency response of all devices. The laser frequency response $H(f)$ is commonly represented by Eq. (2.14) given in Chapter II, section II.B.1.5.

The noise sources of the laser were identified in the section IV.A.3 and are implemented into the laser model through noise voltage sources given in $\mu V/\sqrt{Hz}$. The laser noise figure implementation requires 3 parameters founded in Eq. (4.11) presented in section IV.A.3: the optical power, the RIN value and the slope efficiency (in Figure IV-7). The RIN quantity was implemented using the conventional frequency response given by [131]

$$RIN(f) = A \cdot \frac{4\pi^2 \cdot f^2 + B}{16\pi^4 \left(f_R^2 - f^2 \right)^2 + 4\pi^2 \cdot \gamma^2 \cdot f^2} \tag{4.41}$$

where A and B are device-dependent constants. The laser noise behavior was implemented on the laser model by the typical RIN parameter including its frequency response.

IV.B.2. Photodiode behavioral model

The photodiode model is represented in Figure IV-11. The output photocurrent of the photodetector is

$$I_{out} = I_{ph} = R_{PD} \cdot P_{opt} = \frac{R_{PD} \cdot I_{opt}}{\alpha_C} \tag{4.42}$$

The optical access input is given by the 50 Ohm (R_0) resistance which introduces the notion of the equivalent opto-microwave power $\left(P_{OM}\right)$. It, also, introduces the unidirectional path with a perfect match without optical reflections. The OM gain given by Eq. (4.3) is implemented using the hyperbolic tangent given by the Eq. (4.40) as the nonlinearities. The photodiode frequency response, typically flat up to the cut-off frequency, was implemented with a 1st order low pass filter with 25 GHz cutoff frequency.

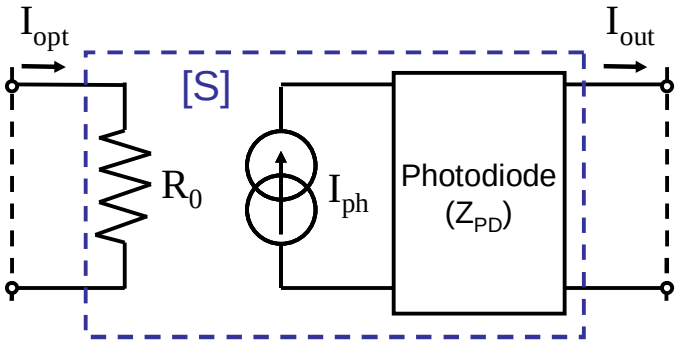

Figure IV-11 – Photodiode equivalent two-port network with optical input access

An important parameter to take into consideration is the photodiode output impedance where it can include a 50 Ohm resistive matching (New Focus PD) which will reduce the OM gain by 6dB since the output current is divided by two when the PD is loaded to 50 Ohm.

The noise on the photodiode model was implemented by the given photocurrent which gives the shot noise plus the NEP parameter responsible for the thermal noise (all this variables are founded Eq. (4.13)). A noise voltage source was used for this purpose as well.

IV.B.3. Opto-microwave gain simulation

The simulation of this subsection considers the optical link presented on the Chapter III and composed of the 8 μm aperture diameter ULM VCSEL and the New Focus reference photodiode. The calculated link gain based on the Eq. (4.6) (section IV.A.2) was fitted using measurement values for the slope efficiency (SLD=0.31 W/A) and the responsivity (RPD=0.222 A/W) and the fiber coupling efficiency implemented by the parameter 'A' (see Figure IV-7). The coupling losses reveal to be 0.55 dB which corresponds to 88 % coupling from the initial total power (DC2PM).

$$G_{LINK}^{OM}\left[dB\right]=10\cdot\log_{10}\left(0.31\cdot 0.88\cdot {}^{0.222}\!/_{2}\right)^{2}=-30.4\ dB \qquad (4.43)$$

The responsivity divided by two is explained by the output 50 Ohm resistive matching providing a division of the output current on the presence of a typical measurement equipment (R_L=50 Ohm). The alignment on this measurement was better than the measurement on the LI curve (79 %) since we got better coupling efficiency.

Figure IV-12 shows the simulation of the different blocks of the system and the measured link gain. The photodiode frequency response, typically flat up to the cut-off frequency, was implemented with a 1st order low pass filter with 25 GHz cutoff frequency. The laser frequency response, given by the intrinsic parameters (f_R, f_P and γ founded in Figure IV-7), was extracted from the link gain measurement, considering the low-pass filter of the photodiode. The laser reflection coefficients were considered too by including the real measured laser S11 on the model. The photodiode output was considered perfectly matched since it is a commercial device with 50 Ohm output resistive impedance matching.

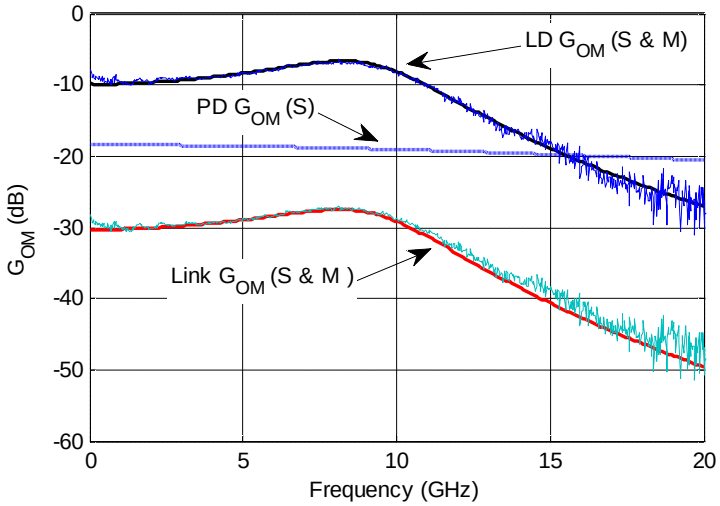

Figure IV-12 – Opto-microwave Gain extraction from measurement: ULM VCSEL biased at 8 mA followed by the New Focus Photodiode (Considering 88 % coupling efficiency of the lensed optical probe)

The OM gain definition was presented and simulated successfully including the frequency response of each device. Link OM gain extraction revealed, as expected from the DC responsivities, a higher laser OM gain of around —10 dB compared to approximately —18 dB of the photodiode OM gain including the —6 dB losses due to the two parallel resistances (see Table IV.2).

IV.B.4. Opto-microwave noise figure simulation

Both modules contributions are presented in Figure IV-13 compared to the measurement. The LD noise figure measurement is computed by the RIN measurement with laser bias current at 8 mA given in Figure III-14, Chapter III. As expected, we can see that the main noise source is coming from the laser related to the RIN. We can observe a good agreement between the simulation and the measurement, except at low and high frequencies.

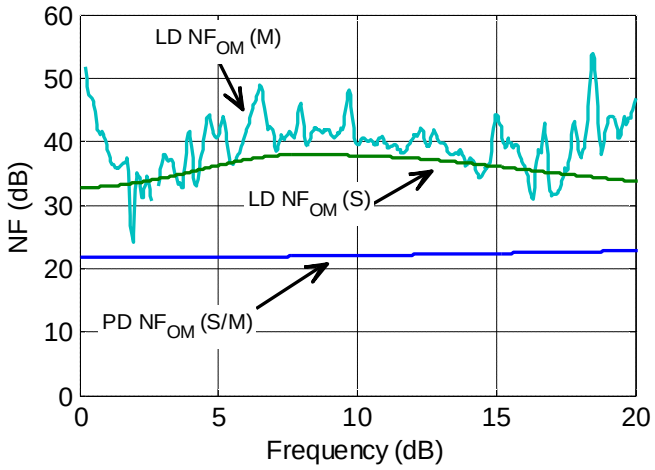

Figure IV-13 – Opto-microwave NF extraction: ULM VCSEL biased at 8 mA followed by New Focus Photodiode (considering 88 % coupling efficiency of the lensed optical probe)

At high frequency (higher than 18 GHz) the measurement setup is not valid according to the calibration analysis done previously, see section III.A.3. At low frequency the difference comes from the RIN frequency response, Eq. (4.41), which does not take into account the low frequency noise behavior. This could also come from other low frequency noise sources from the test bench, which are not modeled.

The final laser OM NF is around 35dB ± 5dB. Even if the laser noise is dominant we can see also that the noise contribution of the New Focus PD (OM NF of around 22 dB), will be of importance for high optical transmission losses or long distance (link) if optical losses are larger than 20 dB.

IV.B.5. Opto-microwave nonlinearities simulation

Because of the simplicity of the hyperbolic tangent, the parameters P1dB or IP3 are easily implemented. The disadvantage is that the sharpness of the transition between the linear region and the saturation one is fixed by the gain value. Basically, this means that the difference between the IP3 and P1dB power points is theoretically around 10 dB. The value obtained on simulations will be higher than 20 dB. This limitation is shown in Figure IV-14 (left) where the compression point was implemented to fit the measurement, but the sharpness is much smoother on the model simulation.

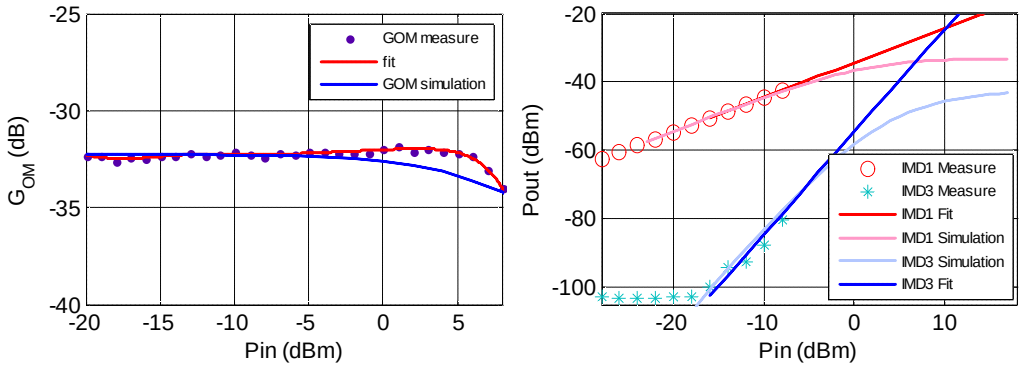

Figure IV-14 – Model nonlinearity behavior: compression gain (left) and IP3 (right) characteristics at 5 GHz and 8mA of laser bias current (considering 70 % coupling efficiency of the lensed optical probe).

The OM nonlinearities were implemented in the model using the nonlinear behavior of the hyperbolic tangent function. We got a good agreement with the measurement despite a saturation sharpness smoother than the real measurement.

IV.B.6. Opto-microwave Spurious Free Dynamic Range simulation

We have now the SFDR defined at each optoelectronic device, allowing the simulation and comparison between each block. The nonlinearities were added in the model with the P1dB/IP3 parameters. The $SFDR_{OM}$ of each block was extracted as depicted in Figure IV-15. As expected the laser is the limiting device. We observe an $SFDR_{OM}$ for the NF photodiode of 117.5 dB.Hz$^{2/3}$ which is much above the value of the VCSEL value (~100 dB.Hz$^{2/3}$) at 5 GHz. The NF photodiode is thus proved to be very linear, only the VCSEL would limit the nonlinearity of the system as expected from Chapter III.

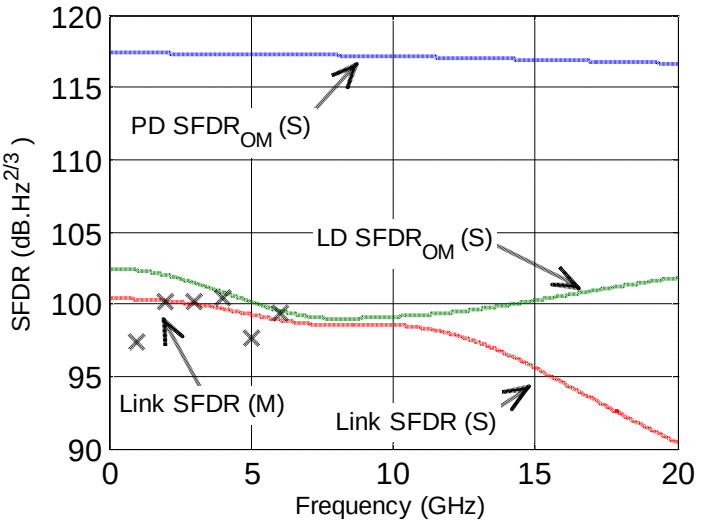

Figure IV-15 – Opto-microwave SFDR extraction (considering 88 % coupling efficiency of the lensed optical probe)

The link SFDR is simulated with a reasonably good agreement with the measurements. It is important to remark the divergence at low frequency because of the noise frequency response implemented into the model does not take into account the low frequency behavior, as depicted in Figure IV-13. The individual simulation results show as expected, that the laser is the main limitation device.

IV.B.7. Opto-microwave Error-Vector-Magnitude simulation

In terms of EVM a co-simulation was used using Matlab and ADS (Figure IV-16): Matlab generates the signal to be injected at the input of the DUT behavioral model of ADS software; we import the voltage data in function of the time from Matlab and injecting to a voltage source to be used as an input in the behavioral model in ADS; at the end we recover the model output signal and go back to Matlab to do the demodulation and compute the EVM.

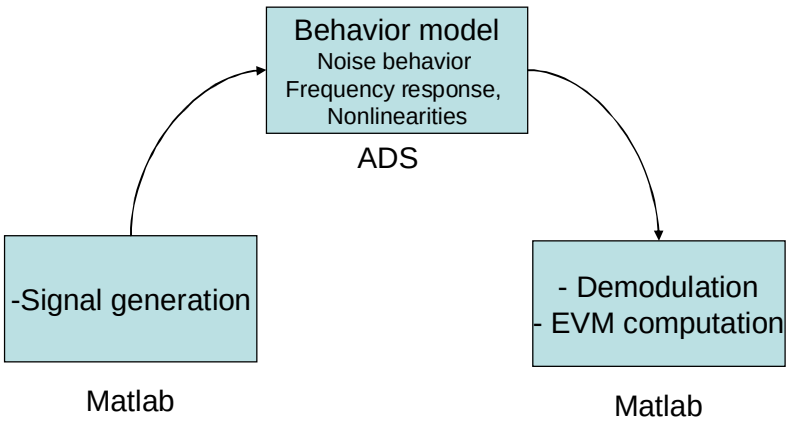

Figure IV-16 – EVM co simulation procedure using Matlab and ADS

The EVM simulation as a function of the input RF power compared with the measurement is presented in Figure IV-17. In Figure a) the measurement was fitted by tuning the RIN parameter at the low input RF signal where the EVM curve is dictated by the noise behavior. The RIN was tuned from -130 dB/Hz down to -160 dB/Hz with a step of 5 dB getting the optimum value of -147.5 dB/Hz where we get the best agreement with the measurement in terms of EVM. This value fits with the RIN curve measured at 8 mA given in Figure III-14. As we can see the RIN is dominant down to -155 dB/Hz where the influence of the PD becomes relevant. Complementary in Figure b) we fix the laser parameters, including the RIN (-147.5 dB/Hz at 3 GHz), and tune the optical losses having a good agreement with measurement. The optical losses matched with the photocurrent monitored at the time of the EVM measurement. The optical losses extracted here include all the losses from the total output laser optical power to the input photodiode optical window. We fit the EVM curve with 1.26 dB optical losses which represent 75 % coupling efficiency from the total emitted power of the laser. This is consistent with the typical coupling losses from the die to the optical probe. EVM_{OM} measurement then proves a very precise tool to investigate the performances of each parts.

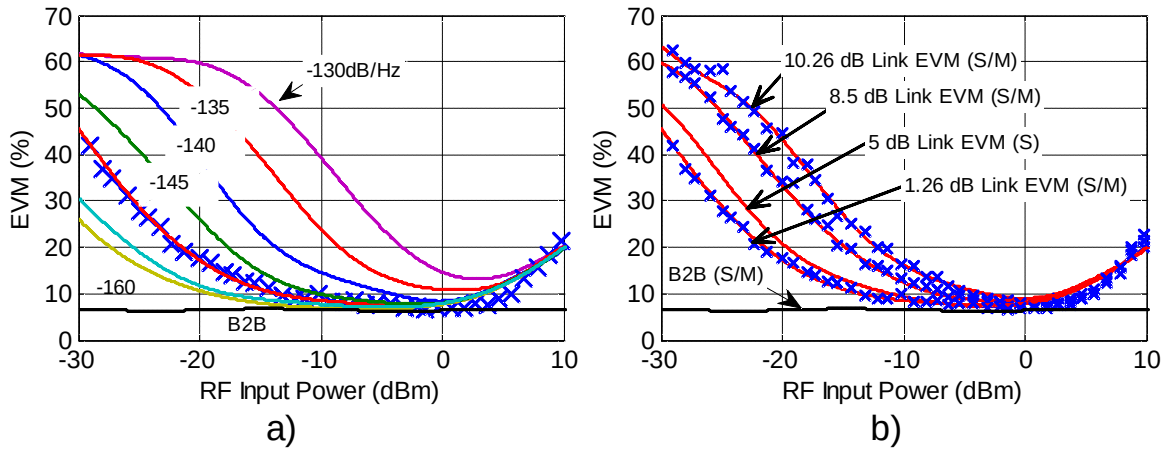

Figure IV-17 – EVM model simulation as a function of the input RF power of the link system using the laser diode and the NFPD at 8 mA and 3 GHz: a) Model fitted with tuning the RIN parameter; b) Measurement fitting with different optical losses

As we fit the link measurement, the individual Opto-microwave EVM was extracted for each device. The simulations are presented in Figure IV-18 for one bias (8 mA) and one center frequency (3 GHz). Here we see, as expected, the laser opto-microwave EVM is very close to

the link EVM with the only difference at low input power as the optical losses contribute as well to the link noise figure.

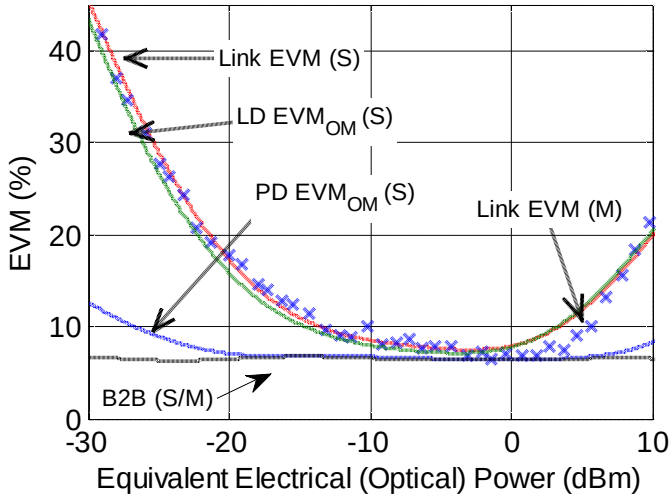

Figure IV-18 – Opto-microwave EVM extraction for 8mA at 3 GHz and 1.26 dB optical losses

The photodiode is very linear and low noise, but still, we can see the noise effect at low input power. From the EVM measurement, we can extract the different individual figures of merit by fitting the simulation. At high RF power, the LD nonlinearities effect appears clearly on the EVM. The simulation of the hyperbolic tangent can also be seen.

IV.B.8. Synthesis

The defined opto-microwave figures of merit were implemented into behavioral models. It covered the frequency response by defining an OM gain, the noise behavior by the OM NF and the nonlinearities by both OM P1dB and OM IP3. The behavioral model was fitted to the measurements done previously. The simulation results got a good agreement with link measurement and the individual performance simulations were successfully extracted and validated. The large-signal behavior limitations from the hyperbolic tangent function were identified, with however a 1st order approximation in sufficient agreement with the measurements. Two more OM figures of merit (OM SFDR and OM EVM) which typically are used for link system characterization were simulated individually with good agreement with measurements, validating once again our model definition. The final model simulation for the OM EVM parameter allowed us to adjust the model identifying eventual variable optimization such as the RIN and optical losses. Therefore, even with only the system EVM measurement, we are able to extract precisely the figures of merit such as OM NF, OM P1dB, OM IP3, OM Gain and OM SFDR.

IV.C. Performance of different RoF devices extracted from link measurements

This section uses the previous results on the opto-microwave figures of merit and behavioral models in order to simulate the different RoF system generations, extracting the individual performance of each device and identifying the eventual critical points.

The first subsection considers the reference RoF link using the 8 μm aperture diameter ULM VCSEL and the New Focus Photodiode which corresponds to the characterization done in the previous chapter and to the OM figures of merit simulation from the previous section IV.B. The main critical device is the VCSEL since the New Focus PD is very linear. It then allows the extraction of all the performances of the laser. Therefore the laser becomes the reference for the next RoF system characterizations and parameter extraction.

The second subsection intends to extract the individual performance of the RoF devices from the second TRoF module generation which is composed by the 8 μm aperture diameter ULM VCSEL (performances extracted in previous section) integrated into a TOSA module and the Finisar ROSA module. Since the laser was the reference, we can now extract the Finisar ROSA module performance and, this time, make it as the reference for the next RoF system configuration and its related device parameter extractions.

The last subsection, then takes into account the RoF system of the first generation composed of the Finisar TOSA module and the reference Finisar ROSA module whose characteristics were extracted before.

IV.C.1. RoF link reference: ULM VCSEL plus New Focus Photodiode

Table IV.2 presents the complete individual parameter extraction, covering all the figures of merit defined previously with the standard ULM VCSEL die and the reference NF photodiode. All those parameters were used in our model. Most of them were measured and some were fitted for an 8 mA bias current at a 3 GHz operating frequency. The simulation results in Figure IV-18 correspond to the parameters given in Table IV.2. The optical microwave gain on each device was extracted, including the coupling efficiency. From the previous conclusion, we know that the link performance in terms of linearity are dictated by the laser. Therefore the PD linearity value was fixed at IP1dBOM=15 dBm corresponding to the worst case.

Table IV.2 – Opto-microwave parameters extraction from 10 Gbps ULM Photonics VCSEL die and reference photodiode (NFPD). Values for 8 mA and frequency of 3 GHz

	Laser	Optical Losses	Photodiode	Link
S_{LD} ,R_{PD}	0.31 (W/A)	75 %	0.222 (A/W)	-
P_{opt} (mW)	3.40	3	-	-
RIN (dB/Hz)	-147.5	-	-	-
I_{ph} (mA)	-	-	0.565	-
G_{OM} (dB)	-10.17	-2.5	-19.1*	-31.8
$IP1dB_{OM}$ (dBm)	6	-	15**	$6(IP1dB_{LD})$
$OP1dB_{OM}$ (dBm)	-4.17	-	-4.09**	$-25.8(IP1dB_{LD}+G_{OM,LINK})$
$IIP3_{OM}$ (dBm)	12.6	-	23**	$12.6\ (IIP3_{LD})$
$OIP3_{OM}$ (dBm)	2.43	-	3.91**	$-19.2\ (IIP3_{LD}+G_{OM,LINK})$
NF_{OM} (dB)	34.3	0	21.03**	36.9
$SFDR_{OM}$ (dB.$Hz^{2/3}$)	101.5		117.3**	99.9

*including 50Ohm resistance matching

**worst case scenario

The noise behavior, mainly influenced by the RIN, was fitted by the EVM measurement as we can see in Figure IV-17. The computation on the SFDR was done showing 101.5 dB.$Hz^{2/3}$ on the laser, much lower than the photodiode taking into account the linearity and the low noise of the PD. This extraction allows us to calibrate our laser model which now can be used on different photodetectors.

IV.C.2. RoF2: ULM TOSA plus Finisar ROSA

The Figure IV-19 shows the simulation and the measurement comparison of the link EVM composed of the ULM VCSEL TOSA and the ROSA Finisar. The simulation shows a good fit with the measurement taking into account a quite small deviation only caused by the limit of the hyperbolic tangent nonlinear model function. Clearly the power dynamic range is strongly reduced by the nonlinearities of the photodetector which includes an integrated TIA.

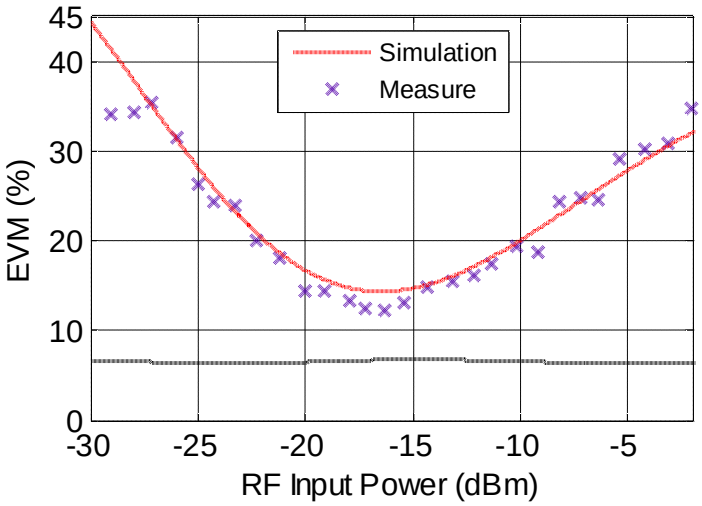

Figure IV-19 – EVM measured and simulated results for RoF2 configuration (ULM TOSA followed by the Finisar ROSA) including 9.1 dB optical losses

The Table IV.3 presents the complete individual parameter extraction, covering all the figures of merit that best fit the measurement. In terms of the laser performances we used the extracted VCSEL performances given in Table IV.2 because the ULM TOSA performances are similar to the ULM VCSEL die. The main difference is the OM gain, which is adjusted by the optical losses value. The measured link performances were fitted tuning the optical losses to achieve the correspondent photocurrent and the transimpedance gain to match the total gain. Comparing the photodetector Finisar to the reference NFPD we remark the high opto-microwave gain (~ 45 dB difference) and the low opto-microwave compression point of — 41.2 dBm. The high gain results in a very low opto-microwave noise figure, but the low $IP1dB_{OM}$ and $IIP3_{OM}$ imply a low link SFDR of 88 $dB.Hz^{2/3}$. It also requires the insertion of high optical losses to avoid the saturation and push the photodetector nonlinearities toward higher values.

Table IV.3 – Opto-microwave parameters extraction from 10 Gbps ULM Photonics VCSEL TOSA and Finisar ROSA. Values for 8 mA and frequency of 3 GHz

	Laser	Optical Losses	Finisar ROSA	Link
S_{LD} ,R_{PD}	0.31 (W/A)	12.3 %	0.5 (A/W)	-
P_{opt} (mW)	3.4		-	-
ZT (V/A)			2000	
RIN (dB/Hz)	-147.5	-	-	-
Ieq (pA)			10	
I_{ph} (mA)	-	-	0.21	-
G_{OM} (dB)	-10.17	-18.2	25.6	-2.2
IP1dB (dBm)	6	-	-41.2	-14.3($IP1dB_{PD}$+$G_{OM,FB+LD}$)
OP1dB (dBm)	-4.17	-	-15.6	-17.3
$IIP3_{OM}$ (dBm)	12.6	-	-32	-3.96 ($IIP3_{PD}$+$G_{OM,FB+LD}$)
$OIP3_{OM}$ (dBm)	2.43	-	-6.4	-6.16
NF_{OM} (dB)	34.3	0	8.5	37.9
$SFDR_{OM}$ (dB.$Hz^{2/3}$)	101.5		89	88.1

IV.C.3. RoF1: Finisar TOSA plus Finisar ROSA

From the previous results we have now a calibrated Finisar ROSA model that can be implemented in the simulator to different laser sources. Therefore, we integrate the model for the Finisar TOSA with the goal to simulate the first RoF generation. The TOSA model is based on the ULM VCSEL model where we introduce the different parameters from Table IV.2 and Table IV.3. The link measured EVM compared to the simulation is presented in Figure IV-20 and the parameter extraction in Table IV.4.

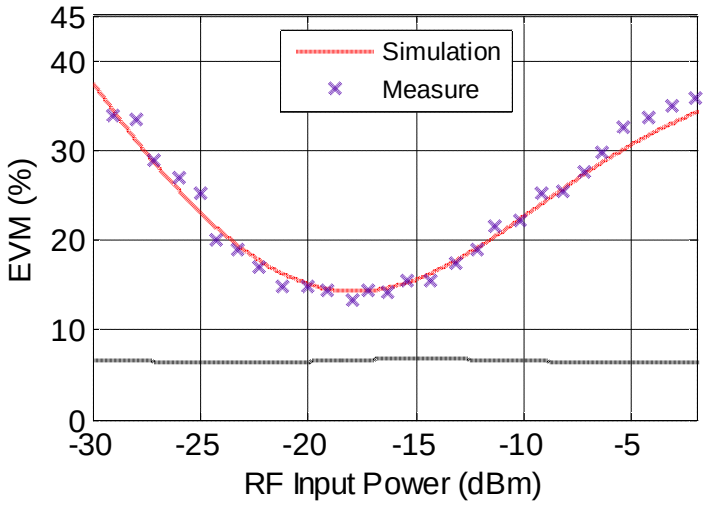

Figure IV-20 – EVM measured and simulated results for RoF1 configuration (Finisar TOSA followed by the Finisar ROSA) including 0.4 dB optical losses

As we are using the Finisar ROSA module, the strong nonlinearities given by the photodetector degrade the link. As we can see in Figure IV-19 and Figure IV-20, similar EVM curves are obtained for an RF power higher than -15 dBm for both RoF2 and RoF1. In the Finisar TOSA followed by the Finisar ROSA (RoF1) there are no optical losses inserted since the Finisar TOSA module has a very low slope efficiency and optical power emission.

These extracted results show that the TOSA Finisar has a very low opto-microwave gain corresponding to the low slope efficiency, but 4 dB better NF_{OM} from the lower RIN than the ULM VCSEL TOSA, with NF_{OM} of 30.7 dB and RIN of -153 dB/Hz. The Finisar ROSA presents some slight variations as compared to Table IV.3. This may attributed to the measurement conditions and because the Finisar ROSA modules were different between the two measurements. However the values are very close together.

Table IV.4 – Opto-microwave parameters extraction from Finisar TOSA and Finisar ROSA modules. Values for 8 mA and frequency of 3 GHz

	Laser	Optical Losses	Finisar ROSA	Link
S_{LD} ,R_{PD}	0.05 (W/A)	91.2 %	0.5 (A/W)	-
P_{opt} (mW)	0.68		-	-
ZT (V/A)			2000	
RIN (dB/Hz)	-153.7	-	-	-
Ieq (pA)			10	
I_{ph} (mA)	-	-	0.31	-
G_{OM} (dB)	-26.1	-0.8	25.6	-0.9
IP1dB	4	-	-42.2	-15.2($IP1dB_{PD}$+$G_{OM,FB+LD}$)
OP1dB	-23	-	-16.6	-17.54
$IIP3_{OM}$ (dBm)	10	-	-33.4	-6.1 ($IIP3_{PD}$+$G_{OM,FB+LD}$)
$OIP3_{OM}$ (dBm)	2.43	-	-7.4	-2.7
NF_{OM} (dB)	30.7	0	8.5	36.9
$SFDR_{OM}$ (dB.$Hz^{2/3}$)	102.6		88.4	87.3

IV.C.4. Synthesis

The RoF of first (RoF1) and second (RoF2) generations were modeled and simulated with the corresponding individual performances extraction. The main critical parameters were identified in all RoF system configurations.

The link reference using the NFPD (very linear) allowed us to identify the ULM VCSEL performance and to extract the corresponding individual parameters such as the G_{OM} of — 10.17 dB, $OP1dB_{OM}$ of —4.17 dBm, $OIP3_{OM}$ of 2.43 dBm, NF_{OM} of 34.3 dB and finally an SFDR of 101.5 dB.$Hz^{2/3}$. Although, the NFPD is a very linear device we were able to evaluate that its IP1dBOM is 15 dBm (OP1dB is -4.09 dB).

Finisar ROSA characteristics were then extracted from the same approach using RoF2 configuration. We adjust the transimpedance to fit the link measurement corresponding to a

G_{OM} of +25.6 dB. NF_{OM} was found to be equal to 8.5 dB and $IP1dB_{OM}$ to −41 dBm which is the most critical point of this device. The strong nonlinearities behavior of the Finisar ROSA limits its SFDR to 89 dB.Hz$^{2/3}$. If we compare the reference link with RoF2 link:
Finisar ROSA provides a high OM Gain mainly attributed to the integrated TIA. Nevertheless, it needs extra optical losses to compensate for its strong nonlinearities which still limit its OM SFDR of 12 dB compared to the ULM VCSEL.
The noise figure is similar for the 2 links, mainly due to the laser OM NF.

The first generation RoF configuration was then simulated successfully from the Finisar ROSA calibrated model. The Finisar TOSA shows a G_{OM} gain decrease on one hand and a NF_{OM} improvement on the other. It presents an OM SFDR similar to the ULM VCSEL one (slightly better) of 1 dB.

Finally, we conclude that the photodetector (Finisar ROSA) limits the RoF1 and RoF2 by its strong nonlinearities. That is why RoF3 will be designed using ULM VCSEL and an HPT photoreceiver in order to improve the system performance as an SFDR increase 88 dB.Hz$^{2/3}$ up to 100 dB.Hz$^{2/3}$.

Table IV.5 presents an evaluation of all RoF configurations in terms of gain, noise figure, nonlinearities and SFDR linking together the three previous characteristics. RoF3 performance are estimated from the SiGe HPT on-wafer measurements given in Chapter III, section III.B. The SiGe HPT performances extraction and modeling could be the target for future work.

Table IV.5 – Summary on the all RoF configurations

	RoF reference	RoF1	RoF2	RoF3*
Gain	-31.8	-0.9	-2.2	-45
Optical losses	0	0	-18.2	0
NF	36.9	36.9	37.9	-46
Nonlinearities	6		-14.3	6
SFDR	99.9	87.3	88.1	89.3

*estimated values

In terms of gain, the TIA from the Finisar ROSA module gives advantage on the RoF1 and RoF2 compared to the reference RoF (using the NFPD) and to the RoF3. As the ULM laser has a higher OM gain compared to the Finisar TOSA, RoF2 is better in gain than RoF1. This gain advantage is wasted in the noise figure because of the necessary high optical losses needed to improve the nonlinearities and avoid the DC optical saturation of the Finisar ROSA revealing a low SFDR. The reference RoF, using the NFPD, has the best SFDR because of the good linearity of the photodiode which implies no need to add optical losses. At the end RoF1 and RoF3 have similar SFDR despite a lower gain on RoF3 thanks to a better linearity. However, the RoF3 is a potential solution for the ORIGIN project since it can integrate an amplifier to improve the gain and NF and therefore the SFDR. Improvements should clearly be put on the gain of the SiGe HPT (see Chapter VI)

IV.D. Summary and Discussion

A new approach to the definition of the Opto-microwave figures of merit for each individual optoelectronic device was proposed. The goal was to understand the global performances in terms of the influence of each block. Optical Microwave Gain (G_{OM}), Optical Microwave Noise Figure (NF_{OM}), Optical Microwave compression Point ($P1dB_{OM}$), Optical Microwave Third-Order Intercept Point ($IIP3_{OM}$), Optical Microwave Spurious-free dynamic range ($SFDR_{OM}$) and finally Opto-microwave Error Vector Magnitude (EVM_{OM}) definition was proposed and evaluated for each individual device.

The optical microwave definition allowed the representation of each device as an equivalent electrical two-port network, where an RF simulator as Agilent ADS could be used. Therefore a behavioral model was proposed and implemented using a SDD based model where the opto-microwave figures of merit could be simulated and compared with the measurements. The model presents good results. Its main limitation is the nonlinear behavior, that was modeled using a hyperbolic tangent and has to be further optimized. Even so, the model provides a good fit with EVM measurements where the RIN and the optical losses were tuned and fitted accurately. Therefore, the developed model not only gives the possibility to include the different measured figures of merit, but it also can extract the different individual device parameters from the link measurements. The simulation of the ULM VCSEL die was then fitted with the link measurements using the reference NFPD (RoF reference). G_{OM} of 10.17 dB, $OP1dB_{OM}$ of -4.17 dBm and $OIP3_{OM}$ of 2.43 dBm were extracted. The NF_{OM} was measured to be 34.3 dB imposing an SFDR of 101.5 $dB.Hz^{2/3}$. Using this calibrated model, we were able to extract the TOSA and Finisar ROSA devices and therefore to understand their influence on the system operation. The Finisar ROSA (RoF1 and RoF2) limits the link system performances by its strong nonlinearities but has high gain. On RoF3, the link SFDR is forecasted to be increased by a value of 12 dB.

Chapter V - **Final Demonstrator**

The ORIGIN project tackles to assemble a full demonstrator with 4 rooms connected. The demonstrator uses 60 GHz modules developed by Telecom Bretagne, centimetric boards fabricated by IETR Nantes, and novel TOSA and ROSA modules that will be developed on the basis of ULM VCSELs and SiGe HPT. Our contribution, which is the topic of this chapter, is the

assembling and test of these TOSA ROSA modules, and the design of the system power budget to precise the chain for the centimetric boards.

The first section provides the development of home-made Optical Sub-Assembly modules for the 8µm aperture diameter 10 Gbps ULM GaAs VCSEL and the 10x10 µm² window SiGe HPT integrated with LNA post-amplification stages: both electronic interconnection and optical packaging are developed. The implementation of the optical interconnection is based on a ball lens technique supported by a mechanical receptacle. The electrical interface is developed through the design of transmission lines, the implementation of electrical matching network and active IC integration, using interconnection glass substrates. The performances of the dies and the TOSA/ROSA modules are compared in order to evaluate the performances evolution in terms of thermal dissipation, coupling efficiency and frequency behavior.

The second section provides a study on the power link budget to design the complete system. The Point-to-Point architecture and the Multipoint-to-Multipoint architectures (electrical and optical) are considered. Each block is considered in terms of gain and noise, identifying eventual critical points on the comparison for both RoF transducers generations (second and third ones).

The last section implements the final demonstrator using a communication between 2 rooms based on optical Multipoint-to-Multipoint architecture with electrical multiplexing (MME) using a 4x4 central node and the signal controlling box. The RoF transducer generations are compared until the final demonstrator, using a real HD video transmission through two 60 GHz wireless commercial modules with data rate of 3 Gbps.

V.A. Optical Sub-Assembly Modules

The implementation of the Optical Sub-Assembly (OSA) is very important, since it provides a support for the optoelectronic die in terms of thermal dissipation, electrical interfaces and optical coupling. All these characteristics will strongly influence the module performances and, therefore, the final system results. This section presents the development of the two following optoelectronic devices: a Transmitter OSA module based on the 8 µm aperture diameter 10 Gbps ULM GaAs VCSEL; a Receiver OSA module based on the 10x10 µm² window SiGe HPT.

The ORIGIN solution for the interconnection of the optoelectronic devices is represented in Figure V-1. This solution provides a packaging and integration solution for light source devices, to form the Transmitter Optical Sub-Assembly (TOSA), and for photodetectors, to form the Receiver Optical Sub-Assembly (ROSA). It is developed by INNOPTICS. We contributed in the design of electrical interconnections and the characteristics.

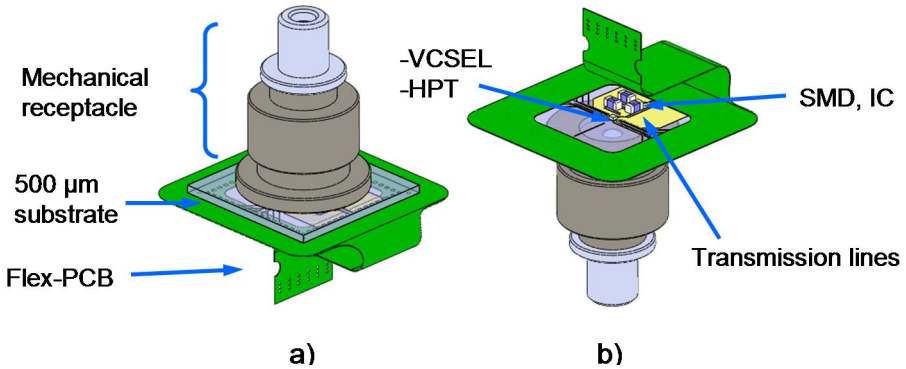

Figure V-1 – 3D illustration of the electrical and optical interconnections in TOSA and ROSA modules: a) top view; b) bottom view

A mechanical receptacle provides the optical coupling between the optical fiber (MMF) and the optoelectronic device. The fiber-receptacle interface is a standard LC/PC connector, providing the passive alignment. The receptacle is glued on a transparent substrate made from either Glass or Sapphire with a thickness of 500 μm. The substrate provides, on its up side, the support for the mechanical receptacle and, on its back side, the RF transmission lines connecting electrically the active device or any other subsystem (matching network, Integrated Circuit (IC), etc.) to the flex PCB output connectors. The interconnection substrate needs to be transparent at the optical wavelength to provide low optical losses. It also needs to have good electrical properties and good thermal dissipating characteristics. The thermal dissipation is important mainly for the laser device to which a variation of temperature changes its properties drastically. The RF lines will provide the connection of the optoelectronic die (VCSEL or HPT) with any other electrical related ICs. Theirs RF characteristic impedance must be matched to the die input impedance in order to minimize reflection losses. The use of a passive matching network is thus prepared. Integrated circuits and optoelectronic dies are mounted on the substrate through a thermo-compression technique. Finally the substrate is mounted on a flexible printed circuit board (flex-PCB) to provide the external electrical connections (e.g.: SMA connector). The flex PCB is a well known solution, largely used for optoelectronic packaging modules.

The first subsection presents the optical interconnection technique implemented equally on TOSA and ROSA modules.

The second subsection presents the electrical interconnections developed for the transmitter and the receiver optoelectronic devices. Transmission lines are optimized through electromagnetic simulations and fit to experimental results. A passive reactive matching network is considered in the RF transmission line design to improve the reflection losses.

V.A.1. Optical Interconnections

The optical coupling elaborated by INNOPTICS, subcontractor in ORIGIN project, is based on the mechanical receptacle, depicted in Figure V-2. This technique is compatible with both, the source (VCSEL) and the photodetector (HPT). The optical coupling is operated by a Sapphire ball lens placed inside the receptacle to focus the beam emitted from the fiber or the VCSEL, to the detector or the fiber, respectively. The selected ball lens diameter is 1000 μm. The VCSEL aperture is 8 μm in diameter. The HPT optical window is 10 μm large.

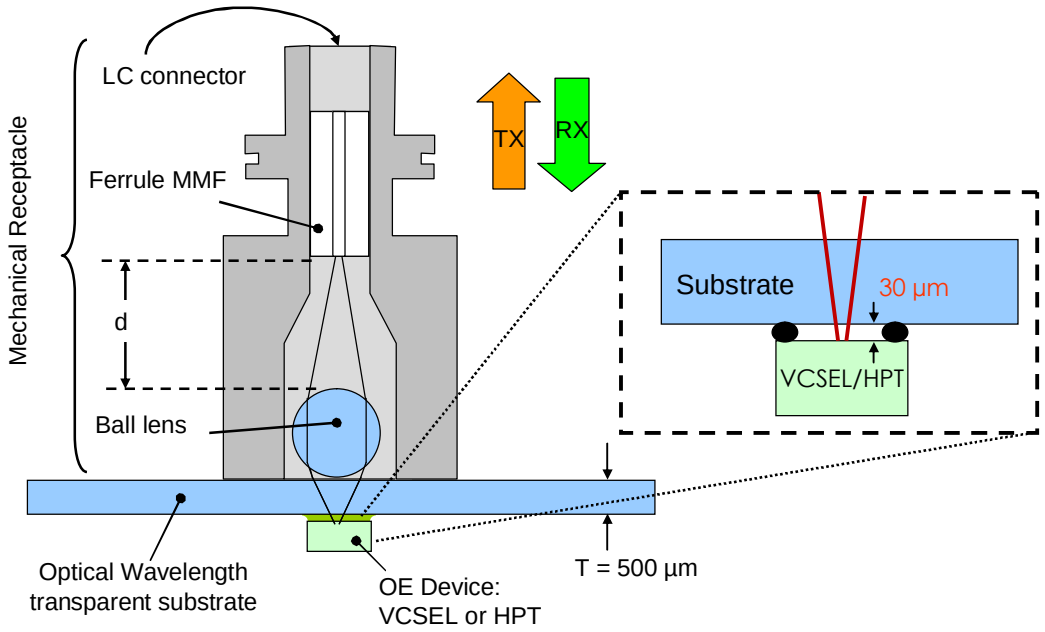

Figure V-2 – Mechanical receptacle structure for the TOSA and ROSA modules.

The distance (d) between the ferrule and the ball lens varies dynamically in order to optimize the coupling efficiency for different optoelectronic device beam profiles. It was fixed to 1160 µm for both TOSA and ROSA modules, maximizing the optical coupling efficiency. The light emitted by the VCSEL (or received by the HPT) travels through a small air gap, due to the bump making the electrical contact connection. These connections are made through thermo-compression. A gap of 30 µm is estimated, as depicted in Figure V-2 (zoom section). The distance between the ball lens and the optoelectronic chip is imposed by the thickness of the interconnection substrate (500 µm) and the thickness of the bump interconnection. The mechanical receptacle is glued onto the optical transparent substrate and is centered on the OE/EO module using an active alignment that measures either the optical power from the TOSA or the photocurrent detected by the ROSA. The UV curing polymerization process is the final step to provide a solid and durable module.

V.A.2. Electrical Interconnections

In this subsection both E/O emitter and O/E receiver are considered with specific developments for each one because of the different intrinsic characteristics of the VCSEL and the HPT. The RF transmission lines are designed and simulated taking into account the die integration, the impedance matching (using SMT elements) and the IC integration.

The first part develops the electrical interconnection on the optoelectronic transmitter device using the 8 µm aperture diameter 10 Gbps ULM GaAs VCSEL. We design an interconnection substrate with access lines and passive matching circuits including SMT devices. The material of the substrate is either glass or sapphire. Two RF designs with two matching network approaches are explored and simulated using an electromagnetic simulator (ADS Momentum). This simulation calculates precisely the impedance loaded in the VCSEL input, and can determine the specific matching network. Finally, the TOSA performances are compared with previous results of the die characterization. Comparisons between simulations

and measurement results are performed using the two approaches on the impedance matching design.

The second part presents the electrical interconnection of the 10x10 μm² window SiGe HPT receiver to realize the Receiver Optical Sub-Assembly module (ROSA). The same principle for the interconnection substrate is used here for the integration of two RF amplifiers together with the HPT (3 dies mounted on the substrate).

V.A.2.1 Transmitter modules

The RF transmission line design is important to integrate the VCSEL with the appropriate impedance matching. This interconnection substrate and the metal from its transmission lines are also very important on the thermal dissipation.

We designed, simulated, implemented and measured two structures to provide the electrical interconnection of the VCSEL. The first structure has a simple RF transmission line (Figure V-3) with a 50 Ω characteristic impedance connected to the VCSEL input. Figure V-3 a) shows the structure that was designed to be compatible with an array of 5 connected VCSELs, where only the half way RF line is used for one VCSEL.

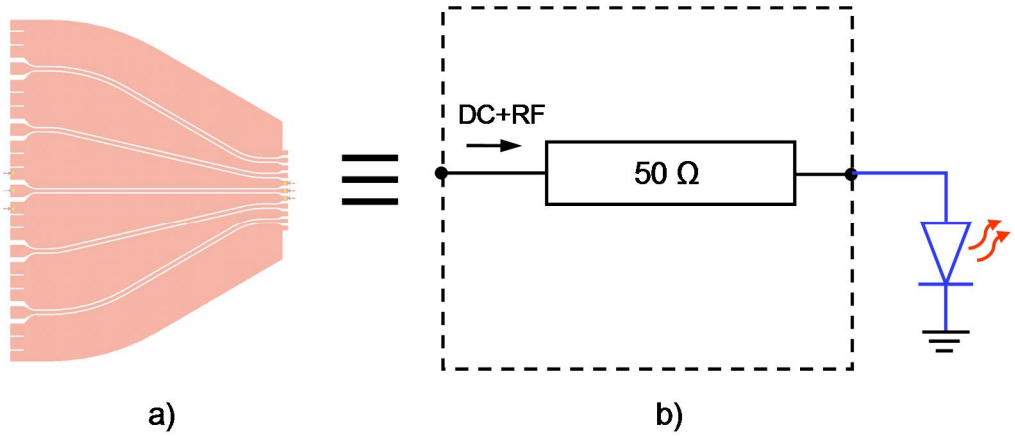

Figure V-3 – RF transmission line simple design structures for the VCSEL electrical connections in the form of a simple 50 Ω line: a) transmission line design; b) equivalent schematic design

The VCSEL was flip-chipped and mounted on the top of the substrate using a bump thermal compression process. The emitted light from the VCSEL goes through the transparent substrate and is coupled to the optical fiber through the optical receptacle described previously.

The second structure is presented in Figure V-4 in which the VCSEL performance is improved by adding a reactive impedance matching network as a π-network.

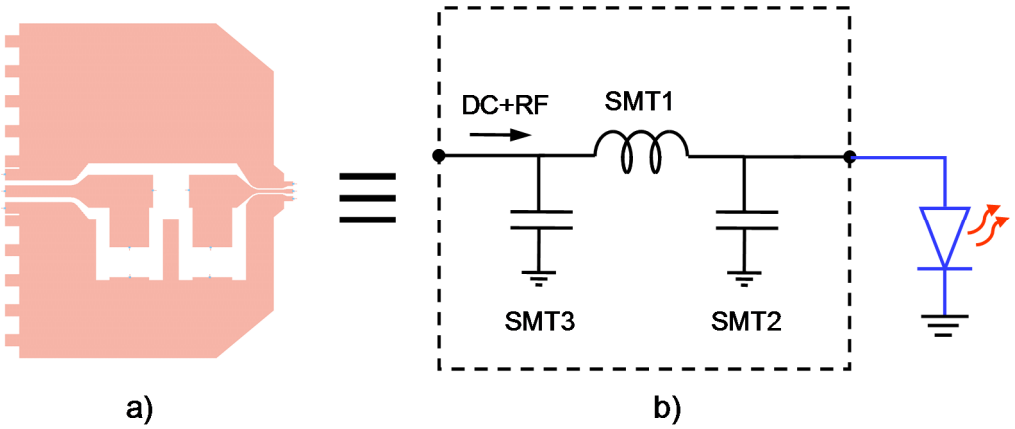

Figure V-4 – RF transmission line design structure of the VCSEL electrical connections in the form of a π-network: a) transmission line design; b) equivalent schematic design.

The SMT1 device (Surface Mounted Technology) used in this network must be an inductive element to allow the VCSEL DC biasing. The SMT numbers 2 and 3 must be capacitive elements for the same reasons. These two RF transmission designs were fabricated on two different optical transparent substrates with a 500 µm-thickness: Glass and Sapphire. The TOSA based on these two RF transmission line structures had the label 'TOSA XXn': the first 'X' letter goes for the substrate used; the second one for the RF line design; last one for the device number. Therefore, two options could be chosen for the substrate: letter 'S' for Sapphire substrate; letter 'G' for Glass substrate. Two options could be chosen for the RF lines: letter 'S' for Simple design with a 50 Ohm transmission line; letter 'P' for the matching π-network. So we could have the following combinations: TOSA SSn; TOSA GSn; TOSA SPn; TOSA GPn.

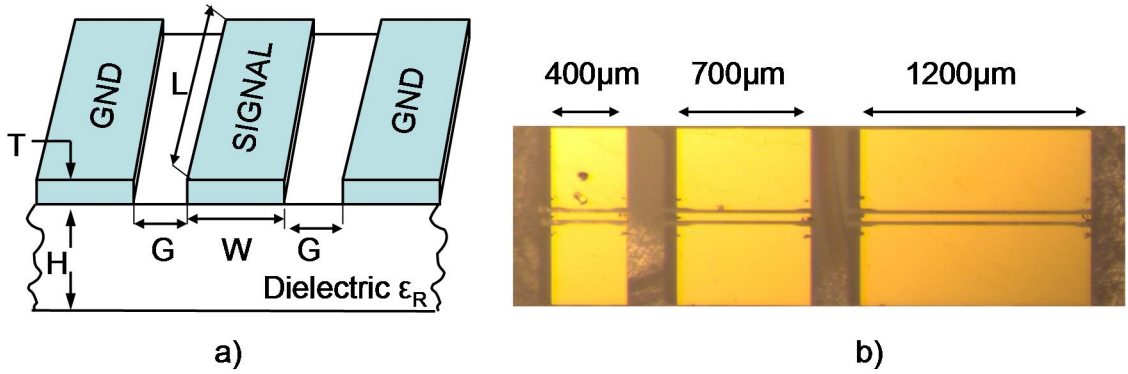

Figure V-5 – CPW line structure: a) technology; b) photo of 3 transmission lines on wafer

Both interconnection structures are based on coplanar waveguide technology (CPW line) as depicted in Figure V-5. The first guess of the characteristic impedance was simulated by using the *lineCal* tool which can be found in the Agilent ADS software. The parameters used on the simulator can be found in Table V.1 for both materials, Glass and Sapphire. The conductor metallization used is gold (Au) with thickness around 1.5 µm. The main differences between both substrates are a dielectric constant higher for the Sapphire material and a loss tangent higher for the Glass substrate. The RF operating frequency is 5.18 GHz, corresponding to the intermediate frequency value used in the ORIGIN architecture. The simple 50 Ω transmission lines were designed with three different lengths, as depicted in Figure V-5 b). Those transmission lines were designed, implemented and measured in order to adjust experimentally the simulation parameters, using momentum simulator, to fit the measurements.

Table V.1 – Glass and Sapphire substrate electrical parameters: (ADS-I) theoretical from [167], (ADS-II) modified to fit the experimental results

	Glass (SiO_2)		Sapphire (Al_2O_3)	
	ADS-I	ADS-II	ADS-I	ADS-II
Substrate thickness H (µm)	500		500	
RF Lines Material	Au		Au	
Metal thickness (µm)	1		1	0.5
Dielectric constant	3.8	3.5	9.3	9
Loss tangent	15e-4		1e-4	
Refractive index (~850 nm)	1.54		1.76	

Momentum simulator provided by the Agilent ADS software was used to determine precisely the transmission line response. The 1200µm-length transmission line measurement is presented in Figure V-6 for both substrates: glass and sapphire. The line dimensions are 50 µm in width with a 22 µm gap for both substrates.

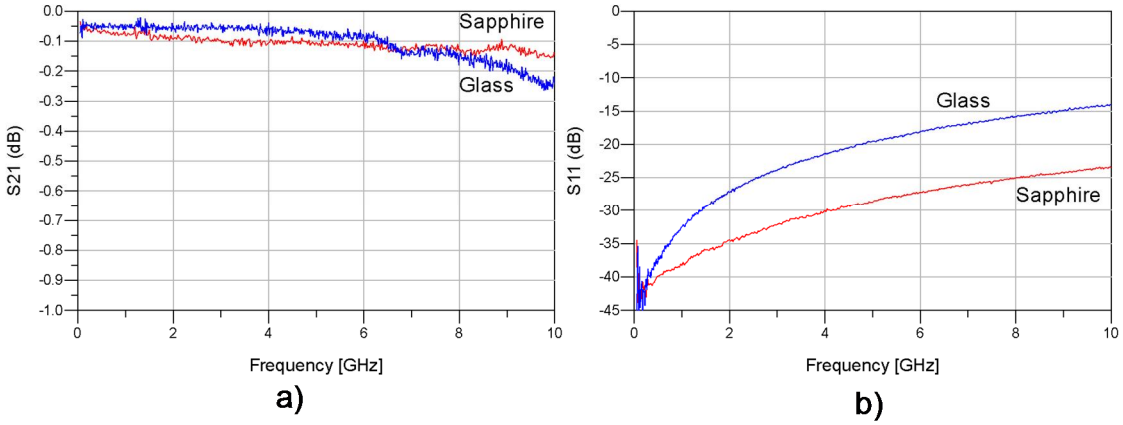

Figure V-6 – 50Ω RF transmission lines measured s-parameters (W=50 µm and G=22 µm)

The transmission lines present low insertion losses until 10 GHz, with losses below 0.3 dB (thus 0.25 dB/mm). The sapphire substrate exhibits, however an improvement with losses 0.125 dB/mm at 10 GHz. At 5 GHz the transmission losses are around 0.1dB for both substrates, the reflection coefficient is 8 dB higher for glass substrate because of its permittivity value and the consequently characteristic impedance value. The sapphire substrate is the best choice for transmission lines operating at high frequency. Nevertheless, as the system operating frequency is 5 GHz, the glass substrate is an acceptable solution at lower cost and easier manufacturability.

From these measurements, the characteristic impedance of those lines was extracted, following the conventional symmetrical two-port network approach [1][168] [169] using the S-parameters measurements. The RF lines were measured and fitted with ADS momentum simulator changing the substrate parameters set from ADS-I to ADS-II (Table V.1). These modifications on the simulation substrate parameters are: the dielectric constant was reduced to 9 and the metal thickness (T) to 0.5 µm on the Sapphire substrate; the dielectric constant was reduced to 3.5 and the metal thickness (T) was unchanged and kept to 1 µm for the glass substrate (Table V.1). The characteristic impedance (Zc) measured and simulated are shown in Figure V-7 for both a) Sapphire substrate and b) Glass substrate. Finally, simulation of the Sapphire substrate best fits with measurements than Glass substrate does. However, a good accuracy is found in both cases with a difference below 5%.

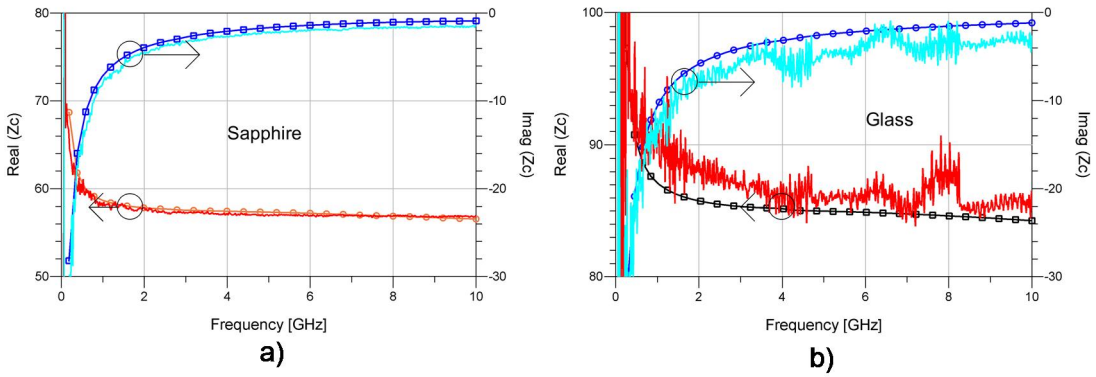

Figure V-7 – Characteristic impedance (real and imaginary) simulation and measurement as a function of the frequency: a) Sapphire substrate (Zc~58 Ω); b) Glass substrate (Zc~85 Ω)

This model calibration of our substrate and transmission lines allows to simulate the complete structure of an interconnecting substrate. Figure V-8 c) shows the complete TOSA module. Figure V-8 a) presents the zoom on the electrical contact between the VCSEL and the RF transmission lines (visible thanks to the optical transparent substrate). The SMT components mounted on the transmission lines, and the VCSEL die, are shown in Figure V-8 b).

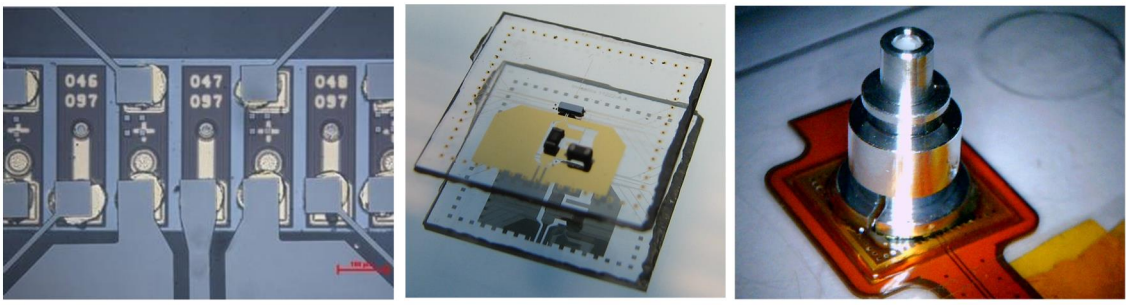

Figure V-8 – TOSA integration and packaging developments: a) ULM 10 Gbps VCSEL contact into the RF transmission lines using thermal compression process; b) final electrical interconnection development using the pi design structure; c) top view with optical mechanical receptacle mounted on the flex.

The TOSA module integrates both optical and electrical interconnections. A model integrating the electrical interconnections was done in order to simulate and optimize the SMT elements on the matching network.

V.A.2.1.1 TOSA Performance

We present, in this section, the comparison between the die and the home-made TOSA module characteristics. The comparison focuses on the static behavior (LI curve and optical spectrum), dynamic response small-signal and finally system performance metrics (EVM).

a) Static behavior

Figure V-9 provides the LI curves comparison between the 10 Gbps VCSEL die studied in Chapter III and the complete TOSA module as presented previously. The die is represented by the same two curves as given in Figure III-2: the total emitted power (DC2PM) and the power measured through the optical probe (DC2OP). The TOSA module is implemented with a Sapphire substrate and with a simple RF line design (SS3). Comparing the total emitted power from the die and from the module, we can extract the optical losses and deduce the coupling efficiency, which is then 67 % at 8mA. TOSA made from a glass substrate (GSn) is not shown here as its static performances revealed similar as the one on Sapphire. Compared to the optical coupling for a lensed fiber (DC2PM coupling efficiency of 79 %), the INNOPTICS optical coupling technique detailed previously, thus reveals to be a good coupling technology taking into account the light path and the different interfaces from the laser to the fiber (see Figure V-2). The threshold current increases from 610 µA for the die to 730 µA for the TOSA module. This 20 % variation can be explained by the variations from die to die, as it was not the same die in the module as in the on-probe measurements.

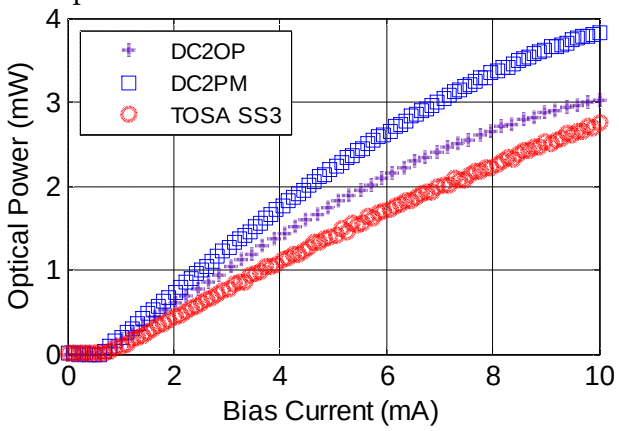

Figure V-9 – LI curves comparison between the die and the TOSA SS3 module

From the LI curve, we observe, as expected, that the thermal dissipation is better for the TOSA module: an increase of the bias current implies a linear LI curve up to 10 mA which means a constant slope efficiency, even for high injection current. The TOSA SS3 optical spectrum is shown in Figure V-10 with a central wavelength emission at around 853 nm. It shows a spectrum which is again typical from a longitudinal multimode VCSEL. The red shift in wavelength as we increase the bias current is lower than the one measured on the die because of the better thermal dissipation improvement. Indeed, the wavelength tuning over the bias current is equal to 0.237 nm/mA compared to 0.5 nm/mA for the die (Figure III-4). Considering again the GaAs-based VCSELs temperature increasing ratio, we can estimate that the temperature rises about 27.1 °C, from the room temperature, at the highest bias of 10 mA, with a rate of 2.71 °C/mA. This value is twice smaller as compared to the isolated die (5.9 °C/mA).

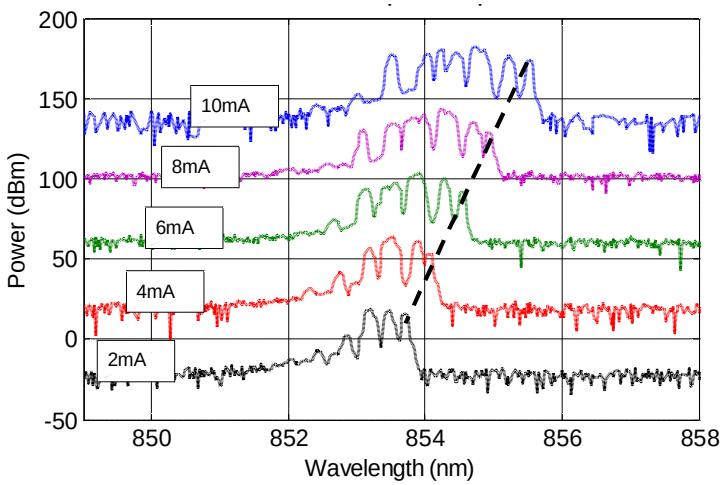

Figure V-10 – Optical Spectrum of the TOSA SS3 module as a function of the wavelength for different bias currents

b) Dynamic response

Figure V-11 a) shows the dynamic small-signal response of the TOSA module: measured (M) and simulated (S) results, compared to the die measurement (full line). The TOSA characterization was performed using a test board that includes biasing circuit fabricated on a PCB. The same New Focus photodetector was used as a reference in each case. Two main differences are then observed in the measurements: a) the gain amplitude is reduced with the TOSA module because of the coupling efficiency reduction and due to the increase in input reflection coefficient at higher frequencies; b) the frequency response of the TOSA module is affected by the RF response of the test board where SMT components and RF lines increase the RF losses.

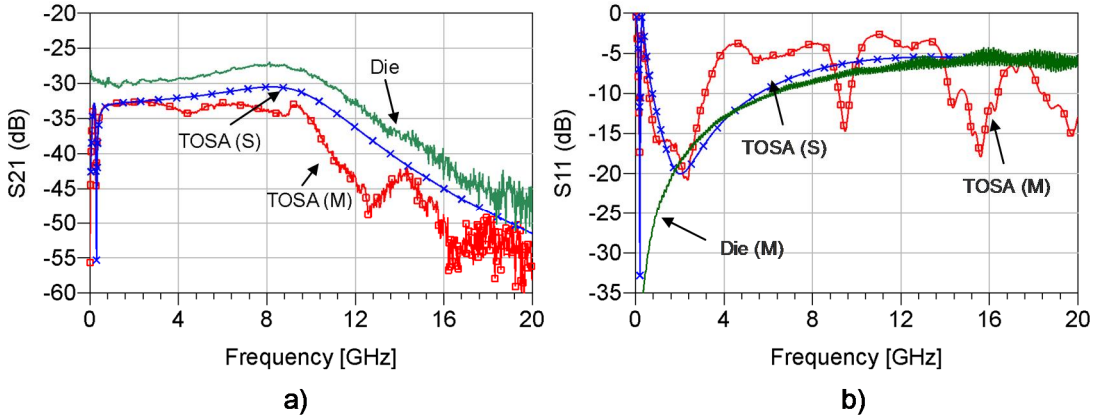

Figure V-11 – Dynamic small-signal response of the VCSEL die and of the TOSA SS3 module for 8 mA bias current using the NFPD as a reference photodetector: a) Gain; b) Input reflection coefficient

The TOSA module was simulated with ADS and momentum (behavioral model in Chapter IV). A fine tuning of the optical coupling ratio injected into the simulation brings to a new value of 60 % of coupling efficiency, compared to the 67 % value extracted from the LI curve. This can be explained by the extra losses due to test board. At high frequency the simulation does not fit entirely in the measurement.

c) Input compression gain point

Figure V-12 shows the opto-microwave input gain compression point at 1 dB of the TOSA SS3 module as a function of the frequency and of the bias current. The same behavior is found here as compared to the die measurements (Figure III-18): As we increase the bias current the optical power increases and the VCSEL can handle more power. The compression point in terms of frequency shows the same behavior as frequency response shape which means, and confirms, that we are in the presence of the laser $IP1dB_{OM}$ and not of the detector one. The opto-microwave input compression point goes up to 12 dBm for a 10 mA bias current for frequency between 4 and 8 GHz

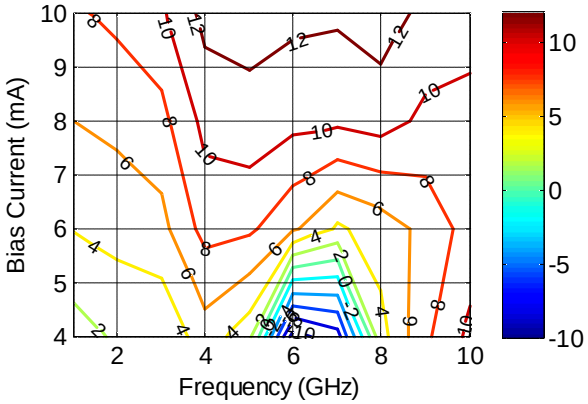

Figure V-12 – TOSA SS3 module opto-microwave (OM) input compression gain

Compared to the die results, we find an improvement not only on the value (3 dB better) but also on the frequency range (flatness for bias current higher than 8 mA in the frequency range 4 to 8 GHz). This improvement in linearity is supposed to be mainly due to a more linear LI curve as resulting from a better thermal dissipation.

c) System performance metrics

We consider here the performance of the link between the TOSA and the New Focus reference photodetector to transmit one channel of the IEEE 802.15.3c standard, in HSI mode at 3.08 Gbps and QPSK modulation. The resulting EVM measurements are shown in Figure V-13 where the TOSA module EVM degradation is compared to the Back-to-Back (B2B) performance of the bench for two center frequencies (3 and 5 GHz). The die performances at 3 GHz are also shown.

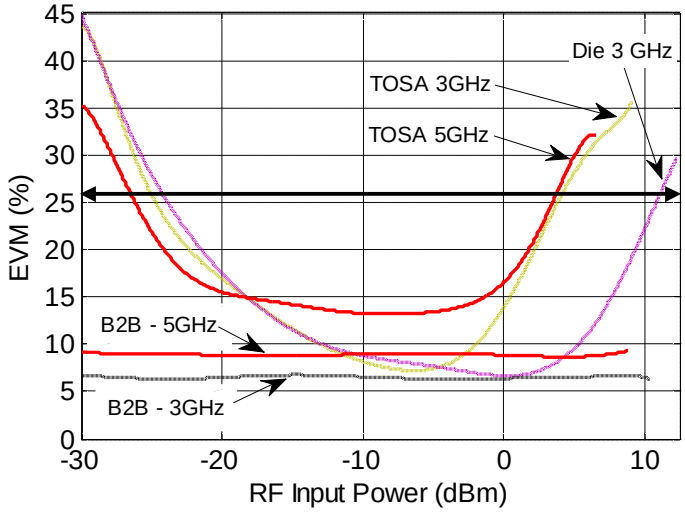

Figure V-13 – EVM measurement of the link between the TOSA SS3 module and the NFPD as a function of the input RF power compared with the DIE at 8mA

The power dynamic range of the TOSA with a maximum of 20 % EVM degradation for the QPSK modulation scheme (from the B2B) is 29.3 dB at 3 GHz as compared to a value of 35 dB for the die performances at the same frequency. At low input power, the EVM is identical because of the same noise sources, but at high input power, the TOSA modules present higher nonlinearities, contrary of what was expected from the LI curve and from the measured input compression point. The measurement differences might be explained from the degradation of the bandwidth of the system and from phase distortion, due to electrical interconnection and test board mainly. Also for so large bandwidth (3 Gbps) the dynamic responses are quite different for die and TOSA.

The dynamic range at 5 GHz is 3 dB better than at 3 GHz. This is consistent with a reduction of the IP3 at higher frequency.

V.A.2.1.2 A Step toward making a TOSA with a matching network

The approach of this section was to proceed with a first guess design of a matching network, prior to the knowledge of the interconnection electrical characteristics and thus prior to the RF model fit to the experimental data. The target was thus mainly to get some data to feed further the simulations and to check the validity of our model on the influence of the impedance on the VCSEL. These results will be used further in Chapter VI, with a real matching circuit. The TOSA SP4 module based on the π network structure and using Sapphire substrate (SP), see Figure V-4, was used with SMT elements that are respectively equal to: SMT1 - 3.4 nH; SMT2 – open circuit; SMT3 – 3.7 pF. The inductor SMT manufacture is [170] and the capacitor is [171] (the design kits imported into the ADS simulator are available on the respective websites). That was our first guess to match the laser input impedance without having yet an accurate model, and using directly the measured die impedance without taking into account the impact of the interconnection substrate. The simulation condition was those described for the die simulation as taken from Chapter IV, see Figure IV-12. The final measurements of the SP4 module are then shown in Figure V-14. They are then compared to a retro simulation of the system with the new model developed in section V.A.2, then now taken into account all the interconnections and access influences. The difference is the gain magnitude with optical losses that were tuned to fit the measurement (2.5 dB) which means a coupling efficiency of 56 %. As we can see the matching network does not work at 5 GHz and therefore the SMT values were absolutely not the right guess. Indeed the transmission line platform has an important impact on the impedance presented to the laser input as was expected. Even so, it gives the possibility to calibrate our model in order to fit to the measurement. The test card behavior was neglected in the simulations. This can explain the variation in high frequency. The SMT elements model can give certain uncertainties, especially, at high frequency above their resonant frequency.

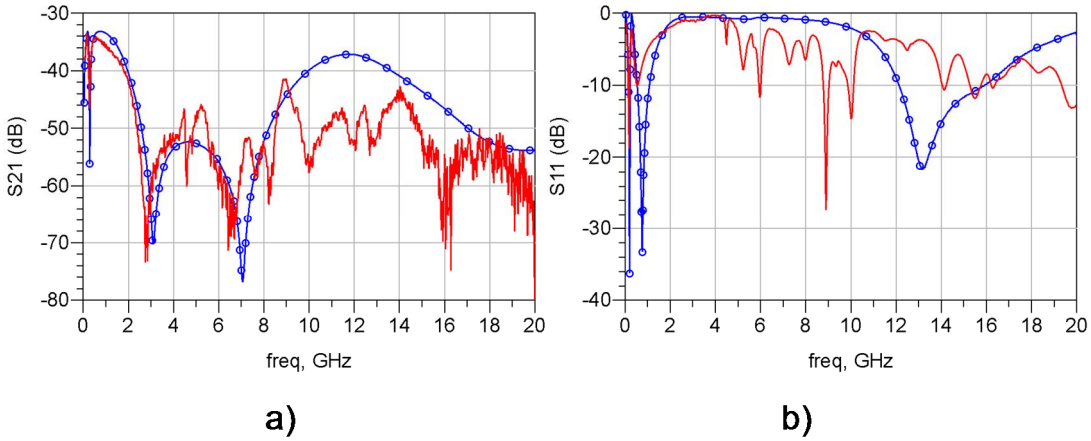

Figure V-14 – Frequency responses using TOSA SP4 and the reference NFPD: a) S21 measure (full line) and simulation (◦); b) S11 measurements (full line) and simulation (◦) (2.5 dB optical losses – 56 % CE)

The conclusion of these results is that at the end a good fit that validates again our model even for the π matching interconnection substrate with the introduction of SMT elements up to 5 GHz. With this proven accuracy of the model, we can now re-simulate and re-optimize the SMT component values to provide the best performances at 5 GHz.

V.A.2.1.3 TOSAs link performances using a Finisar ROSA photodetector

Measurement using the Finisar ROSA was performed and allowed the validation of the developed model. As the input saturation optical power of the Finisar ROSA is 1 mW and the ULM TOSA module output optical power can reach up to 3 mW, we used an extra 5 dB optical attenuator to avoid its saturation. Figure V-15 shows the comparison between the measurement and simulation of the sapphire TOSA (SS) module followed by a Finisar ROSA. The fit between simulations and measurements needs to consider a 7.2 dB optical loss, achieving a 60 % coupling efficiency of the TOSA module. The high link gain (+5 dB) is related to the high opto-microwave gain of the Finisar ROSA where an integrated TIA (Z_T=2000 Ω) is used (see Table IV.3).

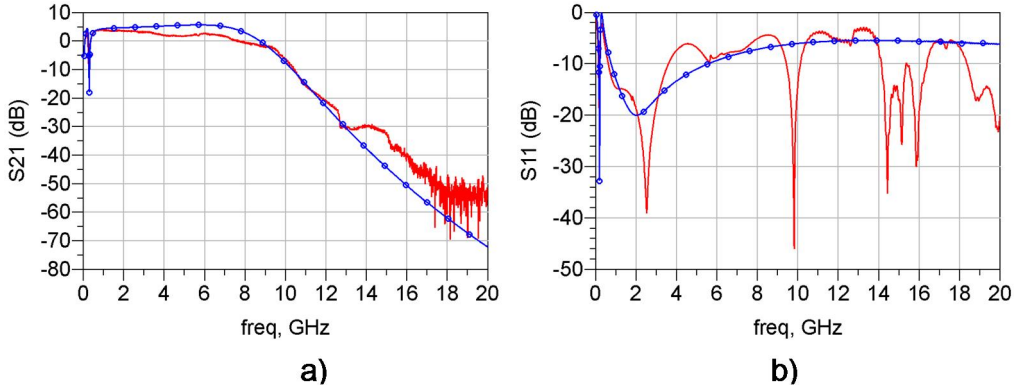

Figure V-15 – TOSA SS3 module S-parameters using the ROSA Finisar: a) S21 measure and simulation; b) S11 measure and simulation (5+2.2 dB optical losses – 60 % CE)

The gain fits properly as shown in Figure V-15 and is similar to the previous TOSA+NFPD link. The reflection does not fit so well, however, as the test board was not included in our simulation.

The analysis was also performed with the TOSA module including a matching network. This is shown in Figure V-16. A good fit of the model is also reported. The test board still plays a role which is not taken into account in our model.

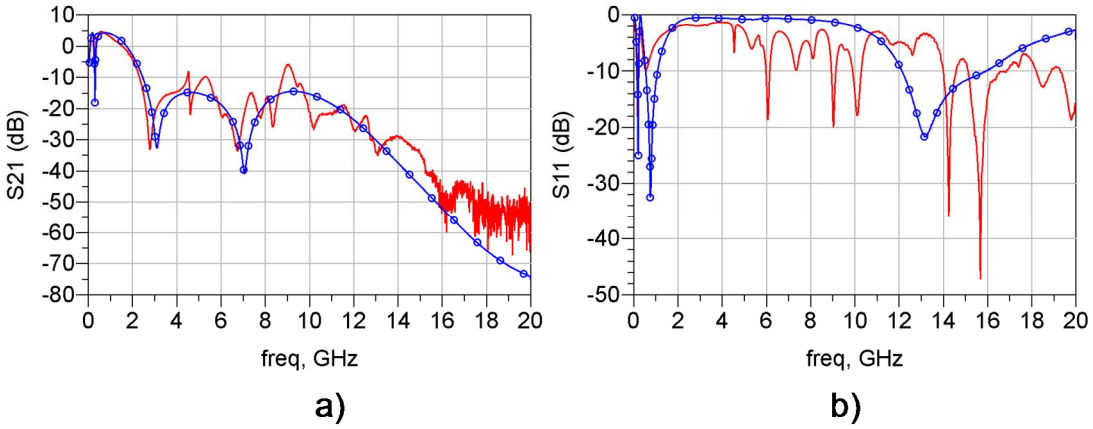

Figure V-16 – TOSA SP4 module S-parameters using the ROSA Finisar: a) S21 measure and simulation; b) S11 measure and simulation (5+2.3 dB optical losses – 60 % CE)

The high link gain has the same explanation as before, since we are using the Finisar ROSA with an integrated TIA.

V.A.2.1.4 Synthesis

The TOSA module was fully developed, from its electrical interconnections to its coupling and packaging. The ball lens coupling technique was implemented and integrated on a mechanical receptacle. The optical coupling efficiency of the TOSA module was measured up to 67 %. The electrical interfaces were developed with the aim of die and impedance matching integration on a transparent substrate through thermo-compression technique. The final result shows a good thermal dissipation, providing a linear optical power even at high current biasing. The RF transmission lines were tested and simulated. Test structures enable to build an efficient model. It will serve in next chapter to improve those electrical interconnections designs. Especially to reconsider the potential of a matching network. The power dynamic range of the TOSA module with 20 % EVM degradation (in relation to the B2B) is 29.3 dB at 5 GHz compared to a value of 35 dB from the die EVM. The simulations are in good agreement with measurements for two different photodetectors, validating our model approach.

V.A.2.2 Receiver module

We desire to integrate in this section a SiGe HPT followed by LNA into a ROSA module, to realize a complete and efficient photoreceiver module in the ORIGIN final demonstrator. The electrical connections of the receiver are based on the same electrical interconnection substrate approach than in the TOSA module case. We decide to implement the lines on Glass substrate, instead of Sapphire, because it was not found relevant differences in terms of frequency response. Moreover, Glass substrate has lower cost and easier implementation.

The first part of this section is devoted to the design and implementation of the ROSA circuits, with two LNA stages included to increase the module opto-microwave gain and to fit with the 2 GHz bandwidth requirement at the center frequency of 5 GHz. Specific LNA IC is designed and fabricated using a SiGe Technology from Telefunken. This IC is characterized and then associated with a SiGe HPT through hybrid integration.

The second part presents the integration of those chips, their assembling in a ROSA module and its final characteristics. Evaluated performances are the static characteristic, the dynamic response (small-signal) and the system performance metrics (EVM)

V.A.2.2.1 Hybrid OE-IC design

The low gain of the link using the SiGe HPT requires the need of adding a Low Noise Amplification stage. For the LNA design, SIGE2RF process of Telefunken Semiconductor Technology was used. More information about this technology can be found in Chapter II, section II.B.2.2.

For the LNA topology, a cascode structure is used in order to enlarge the bandwidth (Figure V-17): an input common emitter transistor drives an output common base transistor. It eliminates the Miller effect and thus contributes to a much higher bandwidth, as the Miller effect increases the base to collector capacitance leading to a limitation of the bandwidth. The cascode structure also improves input-output isolation since there is no direct coupling from the output to the input. The complete electrical schematic is presented in Figure V-17: T1 and T2 transistors are size optimized to give the best performances in terms of noise and gain at the operating frequencies. The choice was a SIC transistor technology (details in Chapter II, section II.B.2.2) with an emitter width of 0.5 µm and an emitter length of 30 µm.

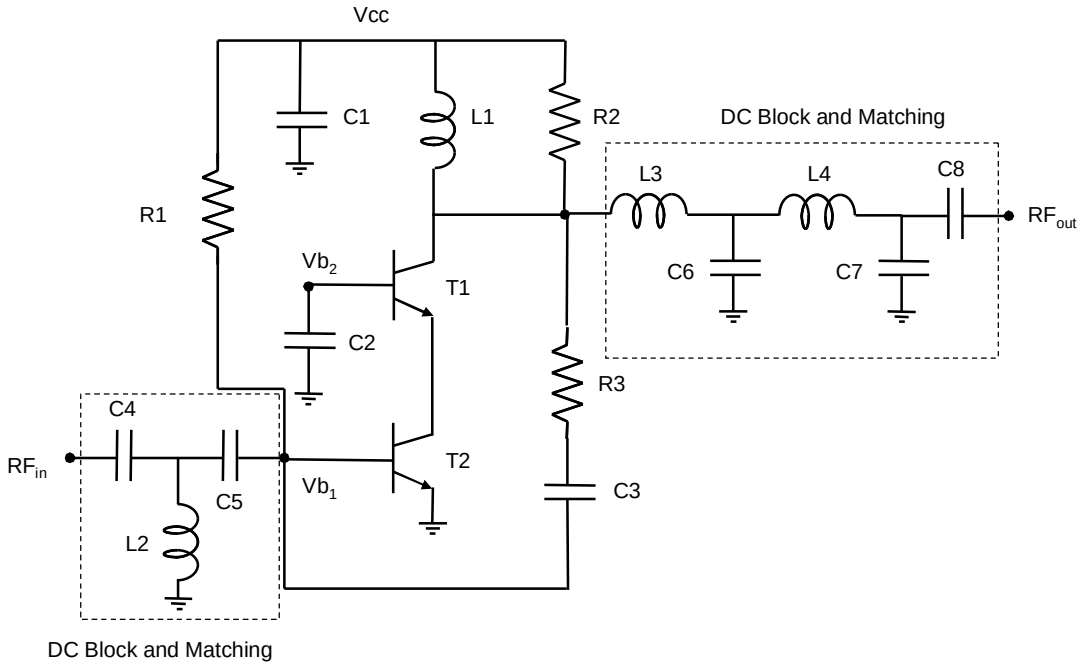

Figure V-17 – Schematic of the LNA proposed to be integrated on the ROSA SiGe

The resistive shunt feedback technique was applied to provide the circuit stability with R3. This resistor helps to stabilize the transistor, but also affects the other performances: High values of R3 increase the gain at high frequencies (extending the bandwidth) and decrease the

noise figure. But those high values increase the S22 parameter leading to some difficulties for matching over the bandwidth. The grounded capacitor C2 mainly affects the gain bandwidth and improves its flatness. The parallel resistor R2 decreases the output reflection. The resistor R1 fixes the bias current of T2 base and provides RF choke. The capacitors C1 and C3 work as bypass and DC block, respectively. The series inductor L1 works as RF choke and interferes on the output reflections. Finally the input and output matching networks match the circuit on a 2 GHz bandwidth at 5 GHz.

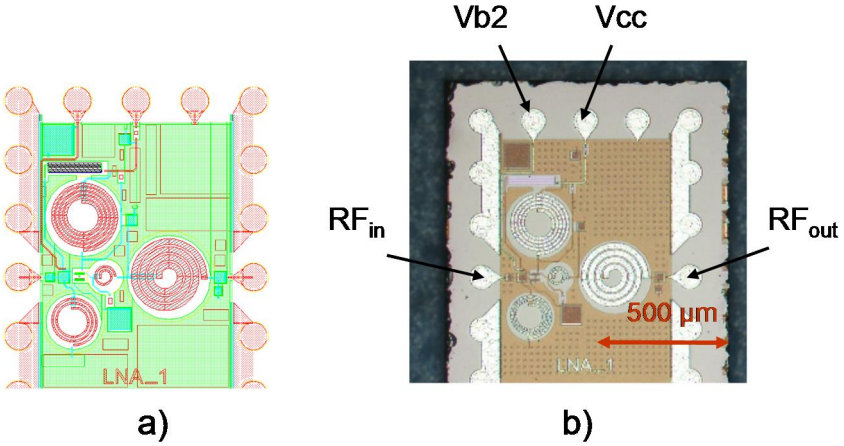

Figure V-18 – LNA circuit: a) Layout; b) Photo

Figure V-18 shows the LNA layout on Cadence software and its die photo. The characterization was made with RF (GSG) and DC probes with 200 µm pitch. The simulated and measured static performances are presented in Table V.2. The measured currents are slightly lower compared to simulation (Icc of 7.9 mA instead of 10.3 mA). This difference can be explained by the thermal effects and the parasitic resistances on the layout lines which were not taken into account.

Table V.2 – LNA simulated and measured static parameters

	Simulation	Measure
Vb2 (V)	2.5	2.5
Ib2 (µA)	22	19
Vcc (V)	4	4
Icc (mA)	10.3	7.9
Consumption(mW)	41.3	31.6

The RF characterization results (full line) compared to simulation ones (◦) is provided in Figure V-19 (VNA power equal to -30 dBm to avoid gain compression). The maximum measured gain is equal to 10.3 dB, which is 5 dB lower than in simulation. It could be attributed to higher losses in the technology, not so well taken into account in the simulation or the difference in technology process. The center frequency shift of the gain response is relatively small (500 MHz) and could be attributed to a mismatched input or output which is maximum at a frequency higher than 5 GHz.

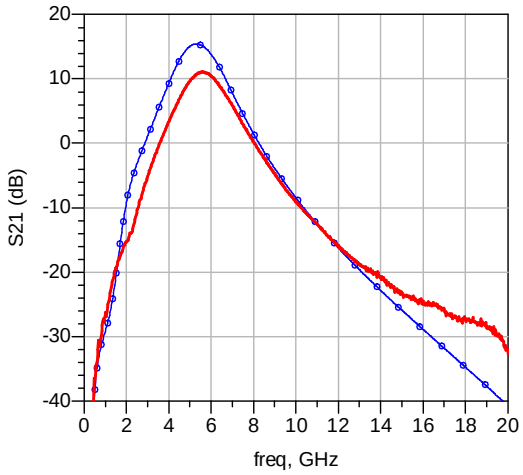

Figure V-19 – LNA frequency response characterization (full line) and simulation (◦)

In Figure V-20, the simulated input reflection coefficient (S11) is found to match perfectly the measurements (◦) where the best value is obtained at a frequency of 5.5 GHz, corresponding to a shift of 500 MHz from the center frequency. Optimization of the matching input could decrease this shift. Differences between the simulation and the measurement mainly appear on the output reflection coefficient (S22) that is still, however, below -5 dB in the bandwidth of interest (4-6 GHz) as -10 dB is the goal to be reached for reflection coefficient.

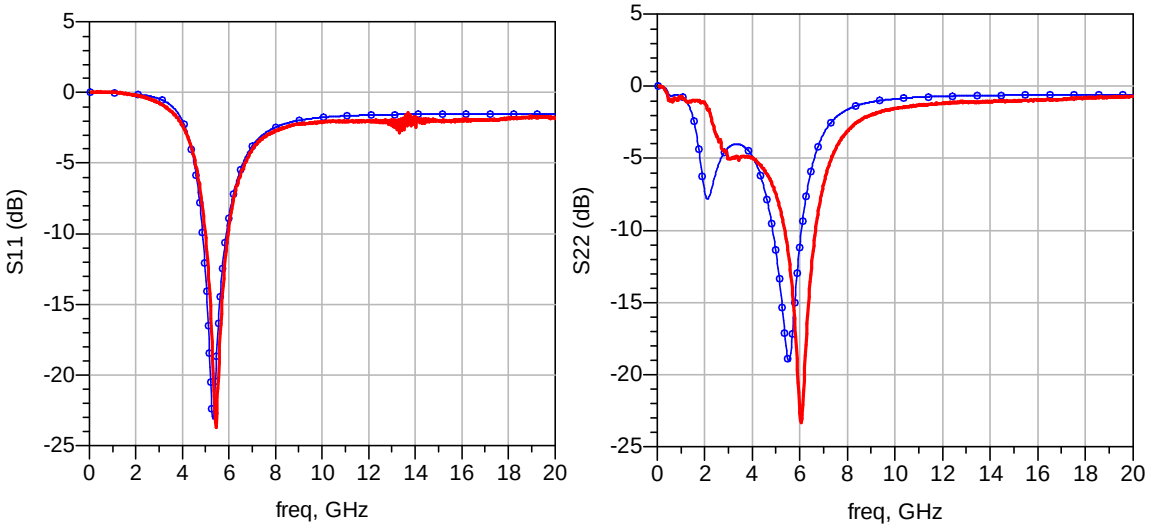

Figure V-20 –LNA frequency reflection coefficient characterization (full line) and simulation (◦)

A summary of the LNA characteristics is presented in Table V.3 comparing simulation and measurement results. RF and distortion performances (gain, P1dB and IP3) are affected by the same effects of the parasitics and thermal issues that reduced the gain. Even if improved performances could be achieved with a more complex matching network and with more precise simulations that would include the layout parasitics, the LNA is proved operational.

Table V.3 – LNA simulation and measurements of RF characteristics at 5.18 GHz

	Simulation	Measurements
S21 (dB)	15.3	10.3
IP1dB (dBm)	-15	-12
IIP3 (dBm)	-4.5	NA
NF (dB)	4	NA

The hybrid ROSA module was designed to integrate 2 cascaded LNAs to provide a 20 dB gain after the SiGe HPT, as depicted in Figure V-21 a). Thus, the module is expected to provide a -25 dB opto-microwave gain. A parallel inductor is placed between the two LNA to improve their matching. Figure V-21 b) shows two curves: the simulation using real measurements (S2P files, extracted from the VNA, imported into the ADS simulator) of the 2 LNA cascaded-stages; and the second one is the same simulation but it includes an inductor[1] (◦) between the 2 LNAs data measurements. The goal of the inductor is to match both LNAs shifting center frequency to 5 GHz required for the system operation on the ORIGIN project. Taken into account the compression gain on the cascaded-stages, the input compression point of the first stage is -22 dBm. Considering ULM TOSA input compression point of +10 dBm and link gain lower than -40 dB over the band of interest, the integrated ICs saturation is avoided.

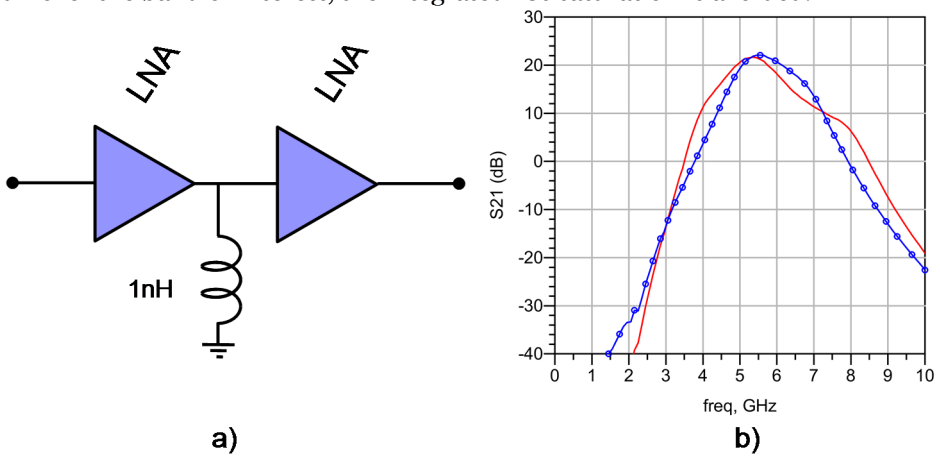

Figure V-21 – 2 cascades LNA are used on the ROSA SiGe: a) electrical schematic; b) comparison between simulation of the data measurements with (full line) and without (◦) the inductor.

To complete the ROSA integration, two more SMT components were added to provide the bias on the HPT collector and the matching network between the HPT output and the amplification input (Figure V-22).

[1] The inductor and capacitor SMT manufactures are [170] and [171], respectively (the design kits imported into the ADS simulator are available on the respective websites)

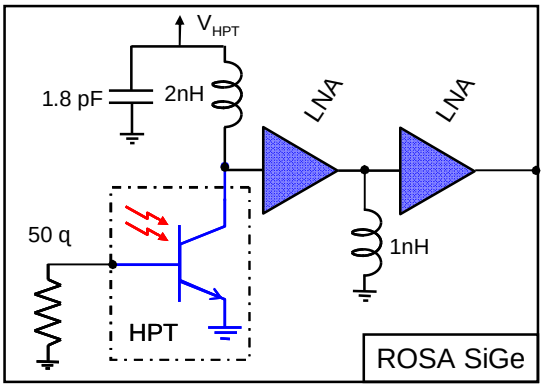

Figure V-22 – Complete electrical interconnection in the ROSA module

Figure V-23 shows a view of the interconnection substrate layout, viewed through the glass material, with the SiGe HPT die on the left side and the two LNA dies on the right side. Bias interconnections and matching SMT components are included.

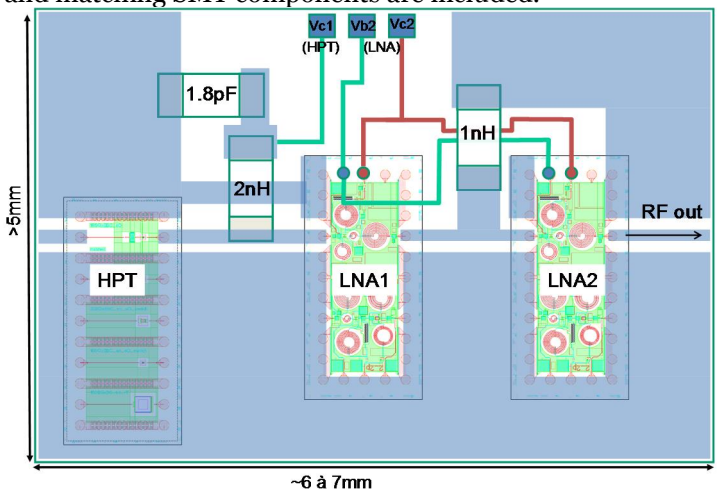

Figure V-23 – Electrical interconnection of the SiGe ROSA view from the top of the module (through the glass substrate)

Finally, the glass interconnection substrate is mounted on the flex PCB and an optical package with its mechanical receptacle is assembled as in the case of the TOSA module. Figure V-24 shows the photo a) from the bottom view and b) from the top view. The dies are mounted through thermo-compression while SMT devices were fixed using conductive glue.

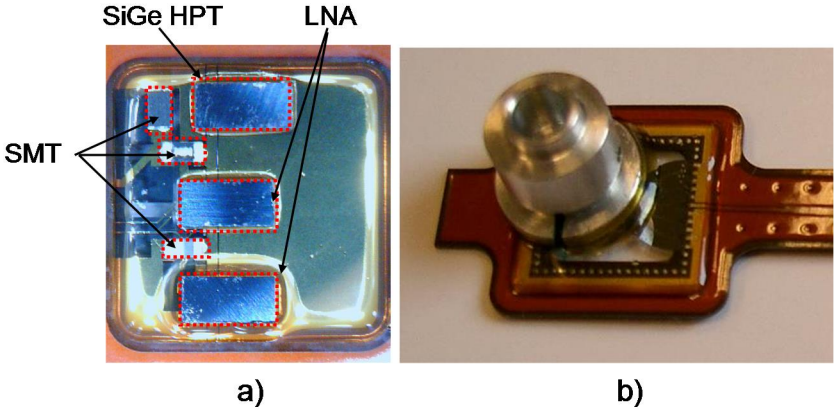

Figure V-24 – SiGe ROSA final integration and packaging: a) bottom view with electrical interconnections; b) Top view with optical mechanical receptacle mounted on the flex PCB

The optical mechanical receptacle is shifted to the border of the glass substrate as showing in Figure V-24 b) as the SiGe HPT is not centered on the interconnection substrate in order to keep its size compatible to other TOSA interconnection substrate sizes.

V.A.2.2.2 SiGe ROSA Performances

a) Static and dynamic characteristics

The DC photocurrent of the SiGe ROSA is measured at the output of the SiGe HPT. It is presented in Figure V-25 as a function of the TOSA SS1 module (the reference on the SiGe ROSA characterization) output. Although, is important to take into account that the IL curve presented considers the SiGe ROSA module and not the SiGe die i.e. it includes the optical coupling efficiency due to the INNOPTICS optical packaging.

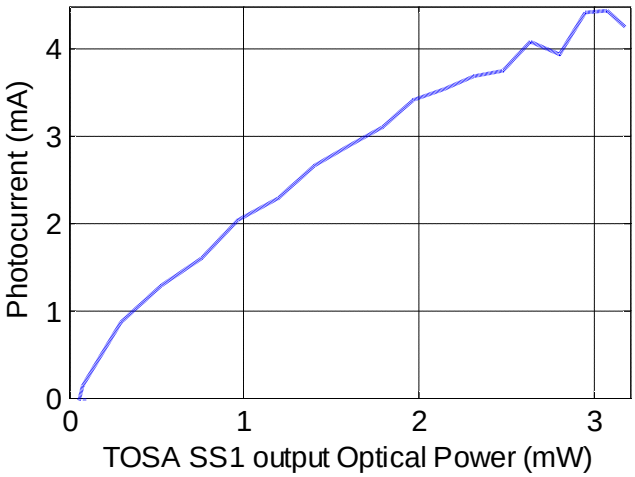

Figure V-25 – IL curve of the SiGe ROSA module.

The SiGe ROSA module responsivity is measured to be up to 5.6 A/W at low input optical power and reduces down to 0.8 A/W at 2.7 mW (8 mA TOSA SS1 biasing). This large reduction on the responsivity can be explained by lower coupling efficiency of the ball lens coupling technique for high laser bias current injection and consequently higher light divergence. Figure V-26 shows the frequency response of the SiGe ROSA photodetector compared with the NFPD reference photodetector when the reference TOSA SS1 is used. We can notice the amplification stage influence at 5 GHz, providing a final link gain of -30 dB, which is 5 dB higher than the NFPD link gain. Considering this difference and knowing the opto-microwave gain of the NFPD (-19.1 dB extracted in Chapter IV), the OM gain of the SiGe ROSA module is -14.1 dB.

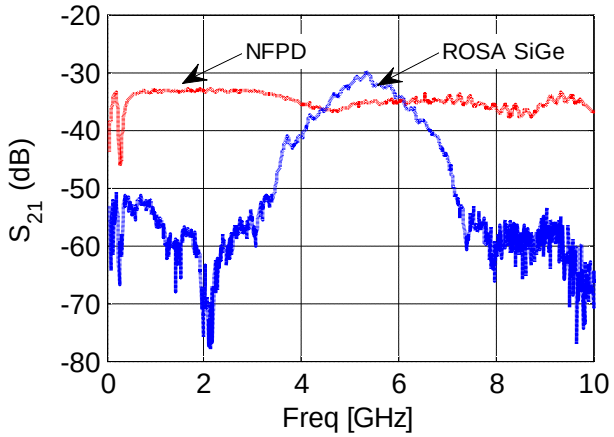

Figure V-26 – Measurement of the frequency response using TOSA SS1 as a reference laser: photodetector NFPD ref; ROSA SiGe

Figure V-27 presents the comparison between measurements and simulations of various parts of the module. The simulations presented are actually dataset measurements (S2P file of the measured link TOSA SS1 module followed by the SiGe HPT die (full line); S2P file of measured LNA) imported into the ADS software and simulated in different configurations: link TOSA SS1 – SiGe HPT followed 2 LNA (including the inductor between them – see Figure V-21) with (□) and without (◦) matching network (consisting of 2 SMT elements presented in Figure V-22). Comparing these two last curves we see the improvement on the flatness over the 2 GHz bandwidth of interest by the inclusion of the matching network. Comparing link of the TOSA SS1 module followed by the SiGe ROSA module in terms of measurement (x) and simulation (□), it appears that the matching networks with 2 GHz bandwidth centered at 5 GHz is not efficient. Indeed, we have around 10 dB ripple on the desired frequency bandwidth which can be a problem for the system operation. The reasons are probably the parasitic effects and the behavior of the SMT elements. The SiGe ROSA module measurement gain is 5 dB lower at its maximum compared to simulated one (it includes the measurement dataset file of TOSA module followed by an optical attenuator (IL=2 dB) and the HPT die given in Chapter III, section III.B and Figure III-35). By adding the optical losses to the 5 dB measure difference we got an opto-microwave reduction of 9 dB, which can be explained by the SiGe ROSA optical packaging. Therefore, we can estimate the coupling efficiency of the SiGe ROSA module to be 35.4 %. This result shows that the ball lens optical coupling technique is less efficient on the downlink light path where the light is coupled from the MMF into the 10x10 μm^2 detectors. Indeed, in terms of uplink light path between the 8 µm aperture diameter VCSEL and the MMF fiber within the ULM TOSA module we measured 60 % coupling efficiency.

We have measured an OM gain of -14.1 dB and now we know that from this value, 9 dB is from the optical coupling. Therefore the actual OM gain of the SiGe ROSA without the optical losses is -5.1 dB. Take into account the 20 dB measured gain added by the LNAs we extract the OM gain of the SiGe HPT to be -25 dB. Finally, it gives a SiGe HPT responsivity of 0.056 A/W around 5 GHz.

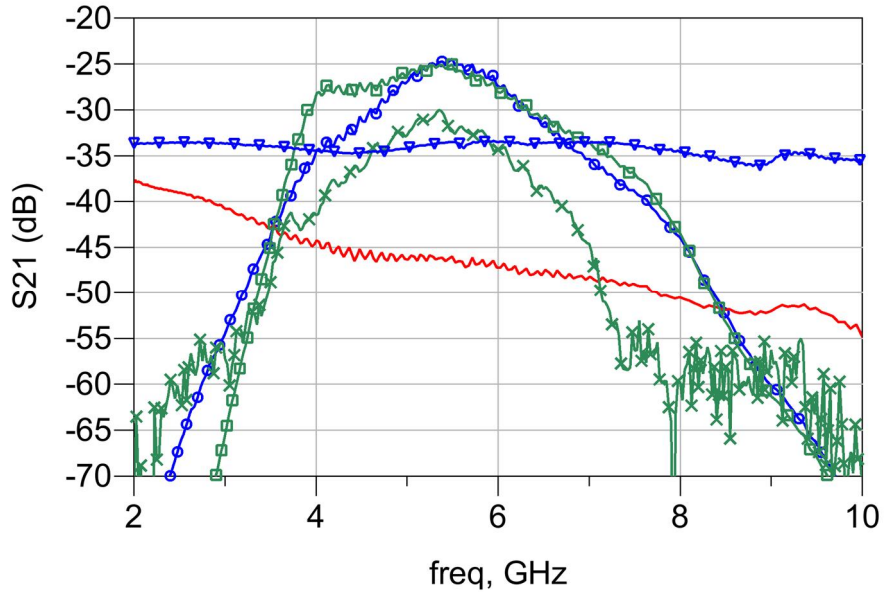

Figure V-27 – SiGe ROSA comparisons between simulation and measurements: x – Measurement of a TOSA SS1 followed by the SiGe ROSA; Δ – Measurement of a TOSA SS1 followed by the NFPD; full line – Measurement of a TOSA SS1 followed by the 10SQxEBC_eO SiGe HPT; ◦ -Simulation of a TOSA SS1 followed by the SiGe ROSA link without matching network; □ – Simulation of a TOSA SS1 followed by the SiGe ROSA with matching network

b) System performance

The EVM measurement was performed at 5 GHz and the results are presented in Figure V-28. The minimum EVM is increased drastically compared to the NFPD link (13 to 25 %). One of the causes is the HPT added noise (shot noise related to I_{ph} and thermal noise) which is much higher than in the NFPD case. Another reason is the unflatness frequency response of the SiGe ROSA, for which the gain changes from -40 dB to -30 dB in the channel band. The linearity limit proves to be the TOSA contribution only. However, a 25 % EVM is demonstrated at 0 dBm input power which is an error free transmission after Cyclic Redundancy Check (CRC) compensation. This is a first promising result that could be improved by further optimizations, both on the HPT and LNA stage design.

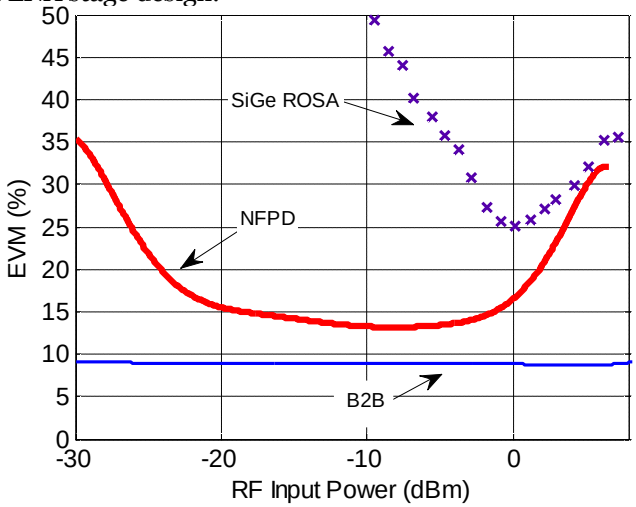

Figure V-28 – EVM curve of the TOSA plus SiGe ROSA comparing with the NFPD at an IF of 5 GHz

In terms of the nonlinearities, the SiGe ROSA reveals to be very linear. We can see this at high input power where the EVM has the same shape as the ULM TOSA using the NFPD which means that the nonlinearities are fixed by the ULM TOSA module. Four directions should be taken into account to improve the overall HPT ROSA performance:

- Gain and flatness improvement: IC with a 30 dB-gain and matching network on a 2 GHz-bandwidth around 5 GHz would be desired for the detector;
- Coupling efficiency improvement: Vertical Optical Waveguides (introduced in Chapter VI) technique could be an interesting method of packaging to improve the 35.4 % coupling efficiency achieved with the ball lens technique;
- Connecting the base of the HPT, to move from a 2T-HPT to a 3T-HPT;
- Noise study and improvement: here the size and shape of the HPT is important. As well the HPT base load connection was not properly considered and should be optimized in terms of gain and noise. A model of the HPT which includes the noise is an important direction take for further improvement. Indeed, the SiGe ROSA EVM curve presented in Figure V-28 could be a basis for parameters extraction by using the method presented in Chapter IV as we did for the Finisar ROSA.

V.A.3. Synthesis

The section V.A intended to develop the optoelectronic modules to be integrated into the RoF transducer, starting from the single chip (VCSEL and HPT) to the packaged modules. The evolution was done successfully on the optical and electrical side. The optical interconnections were implemented using a ball lens coupling technique integrated into a mechanical receptacle. The electrical interconnections included an impedance matching optimization taking into account the HPT-LNA interface and LNA-LNA interface.

The ULM TOSA module development included two versions in terms of impedance matching presented to the VCSEL input. In all cases the coupling efficiency was found to be 60 % compared to the VCSEL die. The home-made TOSA module represents a good EVM result, which allows the E/O device to be integrated on the RoF transducer (minimum 3 % EVM degradation from the B2B).

A SiGe ROSA module based on the 10 µm squared SiGe HPT was realized. An interconnection substrate was designed and fabricated to include a SiGe HPT and two LNAs, together with a passive matching network.

LNAs were fabricated in the SIGE2RF process of Telefunken Semiconductor. Its opto-microwave gain was extracted to be equal to -5.1 dB at the 5 GHz operating frequency without considering the optical coupling losses.

However, the gain over the 2 GHz bandwidth exhibits a strong ripple of 10 dB, revealing the need to improve the matching network. The coupling efficiency was measured to be 35.4 %, which represents a point to be improved, too.

Although the need for improvements on the IC, matching network and optical coupling, we measured a minimum EVM of 25 %, which represents a degradation of 16 % compared to Back-to-Back measurement from the test bench. This degradation could be mainly attributed to the photoreceiver that must be improved by optimizing its design. Also, a complete study on the HPT noise must be achieved, but this was not the purpose of this work. Although, for a first prototype, this result can be seen as very promising as it shows an error free transmission of a 3.08 Gbps IEEE 802.15.3c HSI signal at 5 GHz, after CRC correction.

V.B. System Power Budget Design

Home-made TOSA and ROSA can be integrated into the transducers and used on the system demonstrator. The purpose of this section is to build up the system architecture and to define its link budget. The study will focus on the gain, the noise and the nonlinearities of each block of the system considering three architectures: Point-to-Point (P2P optical tunnel); Optical Multipoint-to-Multipoint architecture with Electrical multiplexing (MME) and Optical Multipoint-to-Multipoint architecture with Optical multiplexing (MMO). We focus this section on the final demonstrator which will integrate the TRoF3. However, it is important to compare the RoF2[2] and the RoF3[3] links, so it has to be compatible with either the Finisar ROSA or the SiGe ROSA developed in the previous section.

Table V.4 shows the summary of the intended architecture configuration in terms of: architecture study, wireless-hop distance scenario; RoF configurations.

Table V.4 – Summary of the architecture study configurations

Architecture		Hop Scenario	TOSA	ROSA
P2P		1m 5m 10m	ULM	Finisar
				SiGe
M2M	Electrical	1m 5m 10m	ULM	Finisar
				SiGe
	Optical	1m 5m 10m	ULM	Finisar
				SiGe

The first subsection will present the P2P architecture and considers the three distances of the air hop: 1, 5 and 10 meters. All the electronics are designed around the RoF element which provides the power range limitation. The system budget considers the gain, its compression and noise in order to optimize the link and find eventual critical points. The results found in this subsection are important and are considered as a reference for the next architectures.

The second section considers the MME architecture of the TRoF3 considering both RoF2 and RoF3 cases. It includes the definition of the central node for the electrical multiplexing of the 4 rooms.

The last subsection presents the MMO architecture budget design of the TRoF3 considering both RoF2 and RoF3 cases.

V.B.1. Point-to-Point architecture (Optical Tunneling): P2P

The point-to-point architecture, presented in Chapter II represents the simplest ORIGIN approach (Figure V-29). Here we considered two wireless-hops between the radio emitter and the radio receiver (both distances equal to d). To determine the system power budget, the

2 RoF2 – ULM VCSEL home-made TOSA followed by Finisar ROSA (PiN plus TIA)

3 RoF3 – ULM VCSEL home-made TOSA followed by SiGe HPT home-made ROSA (HPT plus 2 LNA)

maximum EIRP is defined to be 27 dBm on the radio emitter (see subsection II.A.2 in Table II.3). Although, to keep margin and to fit with 60 GHz commercial chips, available, we put the limit to a maximum EIRP of 20 dBm.

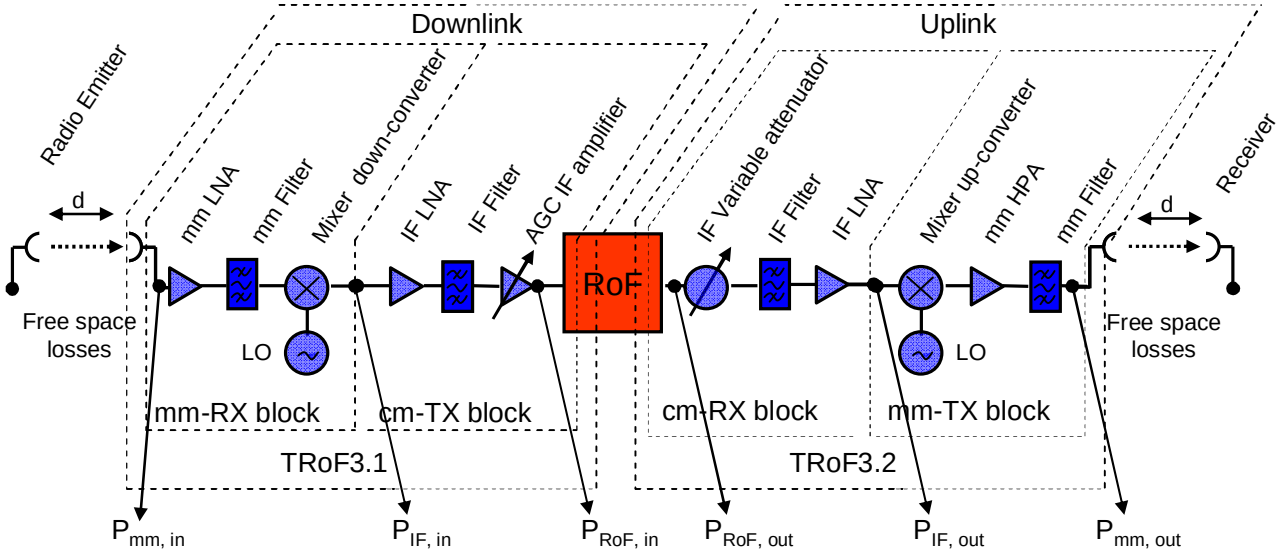

Figure V-29 – The point-to-point RoF architecture illustration based on the IF-RoF concept

Three important characteristics must be considered for each system module (mm, cm and RoF parts): frequency response, noise behavior and nonlinearities. The system is divided according to the two data flows: downlink between the radio emitter and the RoF part and the uplink between the RoF and the Radio receiver. In the downlink, the mm-signal signal is amplified, filtered and down converted to the intermediate frequency through the mm-RX block. Then (cm-TX block) this IF signal is amplified, filtered and powered controlled by an AGC to provide the optimum power at the input of the RoF link (cm-mm block).The Uplink starts with the cm-RX which recovers the signal from the RoF photoreceiver and provides the signal to the mm-TX block input after filtering and power regulation by an IF variable attenuator and LNA. Finally the mm-TX block up-converts the signal to the mm frequency, filters and amplifies it. The final ORIGIN prototype was proposed to use 12 dBi horn antennas at 60 GHz developed by Telecom Bretagne.

The first step is to compute the power delivered from the antenna which feeds the mm LNA ($P_{mm,in}$). The three scenarios were considered in terms of distance *d* between the radio emitter and the TRoF antenna: 1, 5 and 10 meters. The results are presented in Table V.5, where the free space losses are calculated using Eq. (2.23) presented previously.

Table V.5 – Downlink Power budget

EIRP	Distance *(d)*	Free space losses	Power from the antenna $P_{mm,in}$	TRoF RF Gain (G_{mm}xG_{cm})	$P_{RoF,in}$*
27 dBm	1m	68 dB	-29 dBm	+9 dB +27 dB +31 dB	-20 dBm (min) -2 dBm (opt) +2 dBm (max)
	5m	82 dB	-43 dBm	+23 dB +41 dB +45 dB	-20 dBm (min) -2 dBm (opt) +2 dBm (max)
	10m	88 dB	-49 dBm	+29 dB +47 dB +51 dB	-20 dBm (min) -2 dBm (opt) +2 dBm (max)

*Extracted from Figure V-30

The RoF input power ($P_{RoF,in}$) is determined to optimize the EVM performances of the RoF link (Chapter IV; section IV.C.2; Figure IV-19). Figure V-30 presents the EVM curves as a function of the input RF power ($P_{RoF,in}$) for different optical losses. With an optical attenuation increase, the non-linearity of the photodetector is rejected toward higher values of input power. From this curve, it can be inferred that a maximum input RF power of 2 dBm should be injected into the laser in order to keep EVM below 25% (when optical losses are equal to 15 dB). With the maximum input RF power of 2 dBm and 22 dB dynamic range measured, in order to keep below 25%, the optimum $P_{RoF,in}$ range is then determined to be from -20 dBm to +2 dBm.

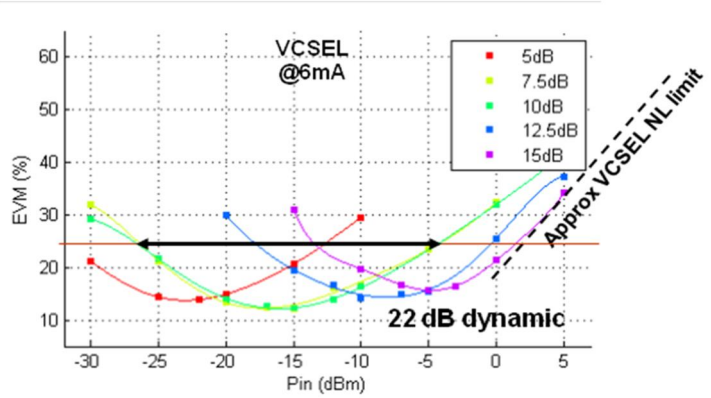

Figure V-30 – EVM curves versus input RF power within an optical link realized with RoF2: an ULM TOSA, an optical attenuator and a Finisar ROSA. The TOSA is biased at 6 mA. The optical attenuator varies from 5 to 15 dB. The VCSEL non-linearity limit to the EVM curve is inferred and sketched with a dashed bold line.

The input compression point of the ULM TOSA was measured to be +10 dBm at 5 GHz with an 8 mA biasing, according to Figure V-12. The input power backoff is, therefore, 8 dB if we consider the maximum input power on the system of +2 dBm.

We find three important parameters which will influence all the components of the system: the 20 dB dynamic power range on the mm-RX power ($P_{mm,in}$ from -29 to -49 dBm) imposed by the 1-10 m range and the 20 dBm EIRP; the RoF input dynamic power range which is fixed by the optoelectronic components behavior; the fixed desired RoF output power which needs to be controlled in order to provide the desired EIRP on the second room of the uplink ($P_{mm,out}$ + 12 dB=+20 dBm).

The following subsections intend to separate the behavior of the downlink and uplink paths from the system link:
Downlink path: the mm-RX block plus the cm-TX block from the receiving 60 GHz antenna until the input of the RoF block. It includes the antenna and the TOSA module, the last one is identical for both RoF2 and RoF3: home-made ULM TOSA.
Uplink path: the cm-RX block plus the mm-TX block from the output RoF block until the transmitting 60 GHz antenna. It includes the antenna and ROSA module. In this case, two configurations are taken into account depending upon the RoF generation: RoF2 is the Finisar ROSA and the in RoF3 the SiGe ROSA. Eventual optical losses can be considered.

V.B.1.1 Downlink path study

The cm-TX block is compatible with both RoF generations and is presented in Figure V-31. Two switches allow us to turn on and off (25 dB isolation) the IF transmission by controlling the input RF power and the DC bias of the TOSA module. An LNA and an HPA amplify the signal and feed it into the ULM TOSA module. The AGC has a 30 dB dynamic range which helps to fix the input power of the VCSEL whatever the free space communication distances (1 to 10 meters). AN RF bandpass filter isolates the signal in the desired bandwidth (centered at 5 GHz with 2 GHz bandwidth). The overall cm-TX block dynamic gain ranges from 8.7 dB to 38.7 dB, due to the dynamic of the AGC (30 dB).

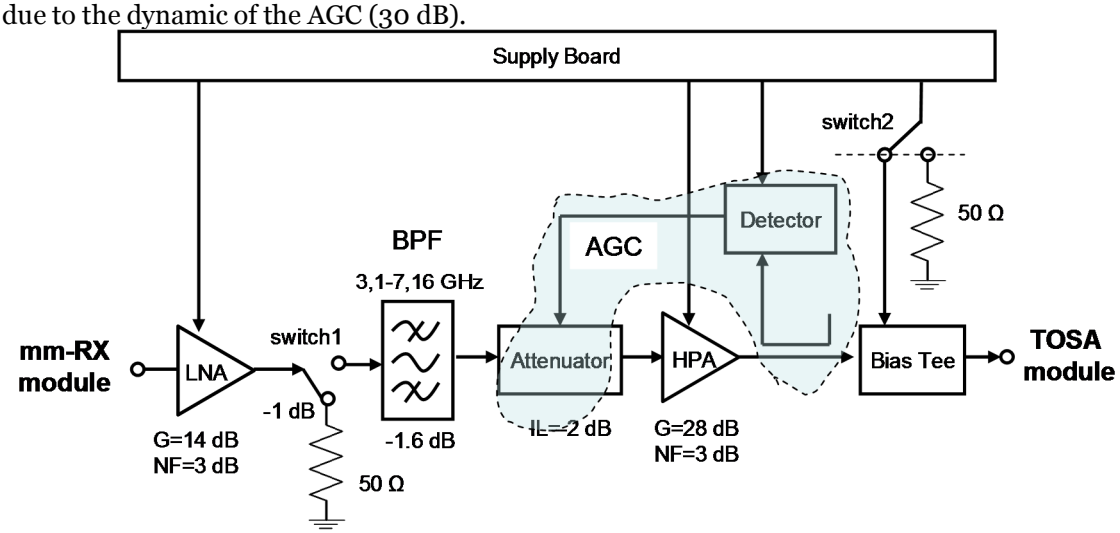

Figure V-31 – Block diagram representing the cm-TX on the downlink path designed by IETR partner.

The mm-RX block schematic is detailed in Figure V-32. It is basically a MMIC down-converter from Gotmic[4] made up of a multiplier, a mixer and a LNA. The conversion gain of the mm-RX block is 10 dB and its noise figure is around 8 dB.

[4] RXQ060A01 available in www.gotmic.se

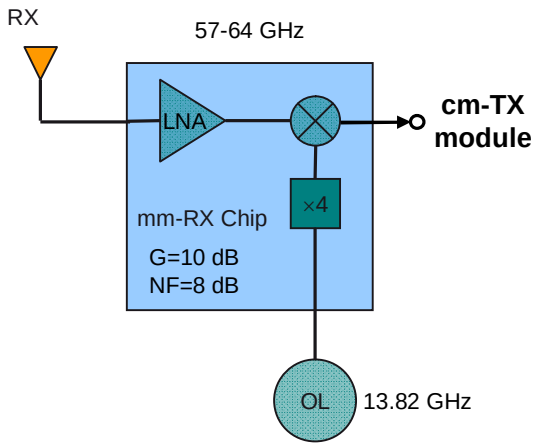

Figure V-32 – The mm-RX block diagram designed by Telecom Bretagne partner.

The 60 GHz part is fixed and defined by what was possible to assemble from ICs available from the market. They were assembled by Telecom Bretagne partner.

Table V.6 shows electrical specifications of the downlink blocks. They are presented in Figure V-29 from the radio emitter to the RoF module. They include the mm-wave antenna, mm-RX block, cm-TX block and the TOSA module, representing the first half part of the P2P link system. This table template gives the bases of the following architecture link budget study.

The first row shows the different cascaded device elements which correspond to the signal path from the 60 GHz antenna to the ULM TOSA module. The first column presents the key parameters of each device: input power (Pin), gain (Gain), output power (Pout), Input compression point (P1dB,in) and finally noise figure (NF). The minimum and maximum values of the power correspond to the 2 extreme scenarios presented in Table V.5 (1 and 10 meters of the wireless-hop). Consequently, gain value could be minimum, nominal and maximum, corresponding to the Automatic Gain Control device (AGC) with a gain range of 30 dB, plus 2 dB of Insertion Loss (IL). The noise figure is deduced from the Friis equation, which allows the influence evaluation of each block onto the system. The ULM TOSA module OM figures of merit are extracted from Table IV.2, Chapter IV, where the OM gain includes the 60 % coupling efficiency. We assume that the TOSA behavior at 3 GHz is equal to the one at 5 GHz. Table V.6 indicates that to achieve the power constraint previously described in V.B.1 introduction, the cm-part need to be composed of two LNA of 14 dB and an HPA of 28 dB (2x14 dB) as is available off-the-shelf. This component was designed and assembled by IETR Nantes within the project, according to the budget evaluation that we performed.

We identify two critical points (yellow highlighted values in Table V.6): the signal compression point of the down-converter when we consider the worst case for the free space distance *d* of 1 meter (the input power on the mm down-converter (-32 dBm) is close to its input gain compression point (-30 dBm)); the AGC input power which is -10.6 dBm when its input gain compression point is -4 dBm.

Table V.6 – P2P on TRoF3: downlink path (mm-RX, cm-TX blocks and TOSA)

	mm-RX block			cm-TX block				TOSA
	Antenna in	Transitions	Down-converter	LNA	Switch + filter	AGC	HPA	ULM
Pin,max (dBm)	-	-29,0	-32,0	-22,0	-8,0	-10,6	-32,6	-4,6
Pin,min (dBm)		-49,0	-52,0	-42,0	-28,0	-30,6	-32,6	-4,6
Gain, min (dB)	**12,0**	**-3,0**	**10,0**	**14,0**	**-2,6**	-32,0	**28,0**	**-14,6**
Gain, nominal (dB)						**-22,0**		
Gain,max (dB)						**-2,0**		
Pout,max (dBm)	-29,0	-32,0	-22,0	-8,0	-10,6	-32,6	-4,6	-19,2
Pout,min (dBm)	-49,0	-52,0	-42,0	-28,0	-30,6	-32,6	-4,6	-19,2
P1dB,in (dBm)	-	-	-30,0	0,0	-	-4,0	0,0	10,0
NF (dB)	-	3,0	8,0	3,0	2,6	22,0	3,0	34,3
NF per section (dB)		11,0		3,1		32,4		34,3
		11,0		21,1				
		15,8						

Therefore, the desired back-off of 8 dB on the gain compression is not achieved on these two devices where the mm down converter reveals to be the most critical module at this distance scenario (1m). Another point to take into account is the input power on the ULM TOSA (-4.6 dBm), blue highlighted in Table V.6, regulated and fixed by the AGC. Its gain value is then changed to -2 dB for a distance of 1 m. Therefore, the input power range of the ULM TOSA module can vary from —14.6 dBm (if the AGC gain is regulated to [-32;-12] dB) to -4.6 dBm (if AGC gain regulated to [-22;-2] dB as shown in Table V.6, green highlighted). In order to achieve the maximum acceptable input power on the ULM TOSA is +2 dBm, the High Power Amplifier gain of 28 dB should be increased by 5.4 dB. However, only 14 dB stages were available.

Since we consider the noise contribution per section we can see that the final link noise of 15.8 dB of the downlink path is influenced mainly by the mm-RX block, with a NF of 11 dB.

V.B.1.2 Uplink path study

The cm-RX block must be compatible with both the expected 2 RoF generations (either Finisar or SiGe ROSA). Its design is presented in Figure V-33. Two switches control the RF and the DC feeds on the ROSA. The ROSA module output signal is amplified by two 14 dB LNAs. The power delivered into the TX-mm module is then controlled by a variable attenuator (30 dB dynamic range) to avoid an eventual saturation. AN RF bandpass filter is implemented to isolate the signal in the desired bandwidth (centered at 5 GHz with 2 GHz bandwidth). The global dynamic gain range of the cm-RX module varies from -6.2 dB to 23.8 dB.

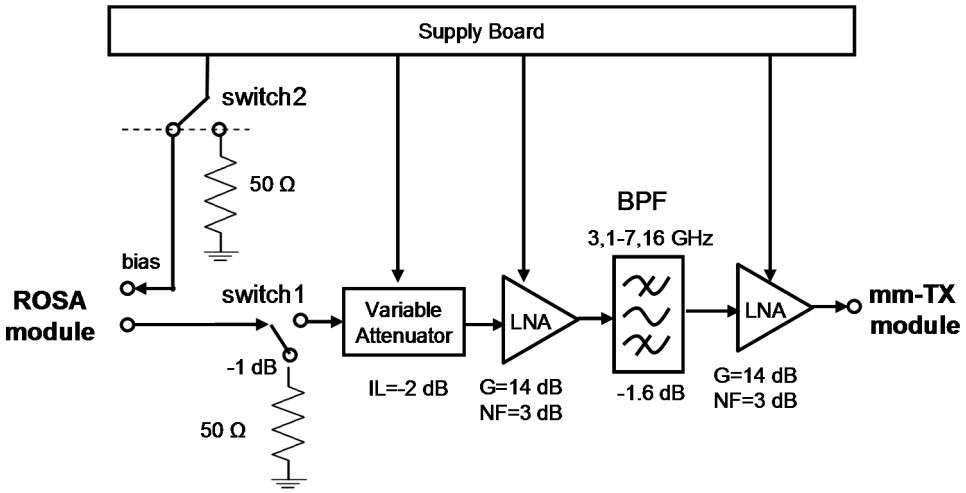

Figure V-33 – Block diagram representing the cm-wave board on the uplink path (compatible with both Finisar and SiGe ROSAs).

The mm-TX block schematic is detailed in Figure V-34. It is designed with a MMIC up-converter[5] followed by a band pass filter and a High Power Amplifier[6] (HPA). The up-converter transposes the IF input signal to 60 GHz using a 4x multiplier, mixer and amplifier. A Band pass filter is used for LO signal suppression on the final RF output and the signal is then amplified to achieve the EIRP targeted. This was designed and assembled by Telecom Bretagne.

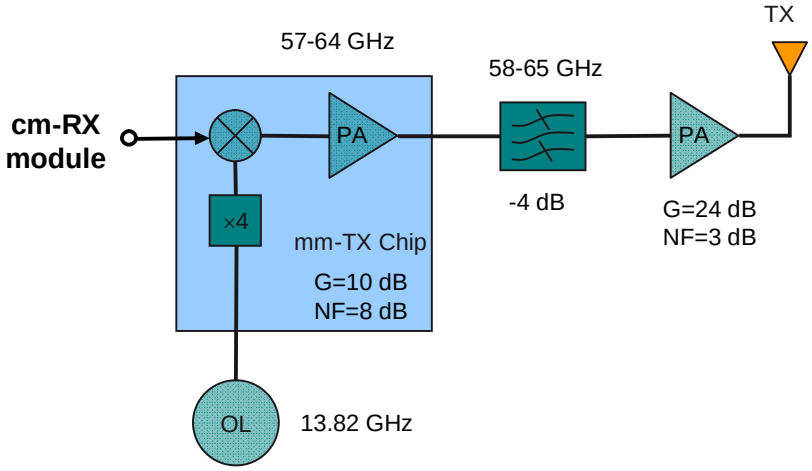

Figure V-34 – The mm-TX block diagram.

The mm-TX block is fixed without any modifications possible in contrary to the cm board that can be optimized according to our RoF budgeting. As expected, the 2 generations of RoFs (2 and 3), lead to different results because of the difference of the ROSA module. The following parts of the subsection present the uplink path for each RoF configuration distinctively.

a) TRoF3: integrating the RoF2

As in Table V.6, Table V.7 shows electrical specifications of every block presented in Figure V-29 from the RoF part to the radio emitter. This uplink includes the Finisar ROSA module, cm-RX block, mm-TX block and mm antenna. The OM figures of merit of the Finisar ROSA were extracted in Chapter IV (Table IV.3) and we assume equal values at 3 and 5 GHz. The most

[5] TXQ060A01 available in www.gotmic.se

[6] HMC-ABH241 available in www.hittite.com

critical parameter is the Finisar ROSA OM input compression point of -41 dBm (yellow highlighted). Clearly, considering the ULM TOSA input power and its corresponding OM gain, high optical losses are required (higher than 11 dB) to prevent the ROSA nonlinearities. Indeed, 15 dB of optical losses would have been better by the given margin. Nevertheless, if 15 dB optical losses are added to avoid saturation of the ROSA module, its gain (32 dB) is then 'wasted' by these optical losses corresponding to +30 dB equivalent electrical losses. To use lower optical losses (a minimum of 5 dB is required to avoid optical saturation) we have to reduce the ULM TOSA input power. As the minimum is -14.6 dBm (AGC limitation), 10 dB optical losses are necessary. Therefore the optical losses, which optimize the OM input power on the Finisar TOSA, vary from 10 to 15 dB. The Variable Attenuator (Vatt - green highlighted) plays an important role to be adjusted as a function of the ULM TOSA input signal and the optical losses to maintain an EIRP of 20 dBm.

Table V.7 – P2P with TRoF3: uplink path (RoF2, cm-RX block, mm-TX block and mm antenna) budget

	Opt. L.	ROSA		cm-RX block					mm-TX block				
	15 dB	Finisar		RF Switch	Vatt	LNA1	Filter	LNA2	Up-Convert.	HPA	Filter+ Transit.	Antenna Out	EIRP
		PD	TIA										
$P_{in,max}$	-19,2	-49,2	-55,2	-23,2	-24,1	-52,4	-38,4	-40,0	-26,0	-16,0	12,0	8,0	
$P_{in,min}$	-19,2	-49,2	-55,2	-23,2	-24,1	-52,4	-38,4	-40,0	-26,0	-16,0	12,0	8,0	
G_{nom}	-30,0	-6,0	32,0	-0,9	-28,3	14,0	-1,6	14,0	10,0	28,0	-4,0	12,0	
$P_{out,max}$	-49,2	-55,2	-23,2	-24,1	-52,4	-38,4	-40,0	-26,0	-16,0	12,0	8,0		
$P_{out,min}$	-49,2	-55,2	-23,2	-24,1	-52,4	-38,4	-40,0	-26,0	-16,0	12,0	8,0		20,0
IP_{1dB}		-41,0		-	-4,0	0,0	-	0,0	-10,0	-7,0	-		
NF		8,5		0,9	28,3	3,0	1,6	3,0	8,0	3,0	4,0		
NF per section	-	8,5		29,2		3,2			8,1				
		33,1				3,2							
		36,3											

The noise figure of the uplink (36.3 dB) is mainly due to the attenuator level which is placed at the 1st stage (NF of 29.2 dB). To reduce the noise contribution we must reduce the attenuation value from the Vatt. However, this reduction will require (in order to maintain the EIRP): either to decrease the AGC gain, reducing the ULM TOSA input power further or/and to increase optical losses. However, the improvement expected from the Vatt attenuation reduction. The removal of one LNA would have been useful to save up to 14 dB on the NF.

The final global system (considering both downlink and uplink paths) gain and noise is 37 dB and 26.9 dB, respectively, without considering the antennas gain. The mm-RX block still contribute by 11 dB to this global NF, the cm+TOSA by 4.8 dB and the ROSA+cm part by almost 10 dB.

The main critical points of the P2P architecture based on this RoF2 generation are:
The mm down-converter linearity and its compression for short distance of free space communication (1m).
The ULM TOSA module input power range of 10 dB from a maximum power of -4.6 dBm (AGC of -2 to -22 dB) to a minimum -14.6 dBm (AGC from -12 to -32 dB).

The Finisar ROSA module with its OM compression input point of -41 dBm requiring optical losses from 10 to 15 dB.

b) TRoF3: integrating the RoF3

The TRoF3 uplink path budget where the photoreceiver is now the home-made SiGe ROSA module is presented in Table V.8. The OM gain of the SiGe ROSA (-14.1 dB) was extracted in section V.A.2.2. The SiGe HPT gain includes the -9 dB opto-microwave gain related to the optical coupling efficiency. In this configuration we can see that there is no inclusion of an optical attenuator as opposed to the RoF2 case since the SiGe ROSA is very linear. From Table V.8, it appears that the same architecture as before fits to the power and gain requirements. The EIRP is assured by the -18.2 dB (green highlighted) attenuation from the Vatt. Once again, the second LNA appears to be in excess. Thus it could have been removed and the Vatt attenuation reduced. The noise contribution from the SiGe ROSA is given by an approximation considering the sum of the noise of the electrical transistor, known from its modeled NF through the Telefunken design kit, and of the shot noise induced by the measured DC photocurrent (around 4 mA from Figure V-25).

It is clear that the noise contribution here is the weakness of SiGe ROSA module (yellow highlighted) compared to the Finisar ROSA module. We found the NF of the uplink path 15 dB higher compared to the RoF2 (36.3 dB).

The global system gain (considering both downlink and uplink paths) and noise figure are, respectively, 37 dB and 37.1 dB, respectively, without considering the antennas gain.

Table V.8 – P2P with TRoF3: uplink path (RoF3, cm-RX block, mm-TX block and mm antenna)

	ROSA			cm-RX block					mm-TX block				
	SiGe			RF	Vatt	LNA1	Filter	LNA2	Up-	HPA	Filter +	Antenna	EIRP
	HPT	LNA_{IC}	LNA_{IC}	Switch					converter		Transit.	Out	
$P_{in,max}$	-19,2	-59,2	-49,2	-39,2	-40,1	-52,4	-38,4	-40,0	-26,0	-16,0	12,0	8,0	
$P_{in,min}$	-19,2	-59,2	-49,2	-39,2	-40,1	-52,4	-38,4	-40,0	-26,0	-16,0	12,0	8,0	
G_{min} / G_{nom} / G_{max}	**-34,1**	**10,0**	**10,0**	**-0,9**	**-18,2**	**14,0**	**-1,6**	**14,0**	**10,0**	**28,0**	**-4,0**	**12,0**	
$P_{out,max}$	-53,3	-43,3	-33,3	-34,2	-52,4	-38,4	-40,0	-26,0	-16,0	12,0	8,0		20,0
$P_{out,min}$	-53,3	-43,3	-33,3	-34,2	-52,4	-38,4	-40,0	-26,0	-16,0	12,0	8,0		
IP_{1dB}	-*	-12,0	-12,0	-	-4,0	0,0	-	0,0	-10,0	-7,0	-		
NF	46,1	3,0	3,0	0,9	18,2	3,0	1,6	3,0	8,0	3,0	4,0	-	
NF per section	46,4			19,1		3,2			8,1				
	46,6					3,2							
	46,8												

*higher than $IP1dB_{LD}xG_{LD}$

The main critical points on the P2P architecture based on the third generation are:

No optical losses needed, but the SiGe ROSA OM gain is too low and this impact on the link noise figure.

The Vatt adjusted to -18.2 dB, which, as previously, suggest that we can remove one of the cm LNA (14 dB gain) and re-adjust it to -4.2dB (-18 dB+14 dB). Although, this will not have a large impact on the overall noise since the uplink noise figure is dictated by the SiGe HPT (37.1 to 36.7).
The mm down-converter linearity is a limiting factor for short distances in the air gap with a 2 dB backoff.

V.B.1.3 Synthesis

This subsection presented the power link design of the P2P architecture, considering the third generation RoF transducers (TRoF3) compatible with both RoF2 and RoF3 links. Simplex communication architecture was considered by the downlink and uplink paths.

The downlink path was identical for both RoF2 and RoF3 based on the home-made ULM TOSA module. The two extreme scenarios for the free space communication (1 and 10 meters) were explored. It revealed two points needing a special attention: the gain compression of the down-converter at 1 meter and short distances; the choice is the optimum power at the input of the ULM VCSEL which can be chosen from -14.6 dBm to 4.6 dBm and maintained fixed by the AGC.

The uplink path presents differences depending upon the chosen ROSA module in the two RoF link cases: RoF2, based on the Finisar ROSA module, requires high additional optical losses to avoid the ROSA nonlinearities. The, TIA gain is 'wasted' by the optical loss. The RoF3 based on the SiGe ROSA module does not need additional optical losses, but is characterized by a lower OM gain, which, at the end, corresponds to the same overall link gain. It is also responsible of a high noise figure revealing a link noise figure increase of 10.2 dB compared to the RoF2 case. Although, one of the two cm LNAs should be removed to improve noise performances of both RoF2 and RoF3. Indeed, that will make the global system noise figure of 17.7 dB and 36.7 dB for the RoF2 and RoF3, respectively, which will correspond to a 19 dB improvement on the RoF2.

Based on this results and illustrations, the following subsections will focus on the link budget of the optical multipoint-to-multipoint architecture. We consider both electrical and optical multiplexing (MME and MMO) for the TRoF3 (compatible with RoF2 and RoF3 as previously).

V.B.2. Optical Multipoint-to-Multipoint architecture with Electrical multiplexing

The MME architecture presented in Chapter II is shown as a block diagram in Figure V-35. We consider a simplex communication link. The first part is a TRoF3.1 block (mm-RX, cm-TX and TOSA modules – presented in Table V.6) placed after a wireless hop. The TRoF3.1 block is followed by a central node which implements the electrical multiplexing from 1 room to the 4 rooms, through a 4x4 RF splitter. The signal from the fiber is detected, splitted and then reemitted. The central node is then made up of a cm-RX, a 4x4 RF splitter, a cm-TX and a TOSA. Then the central node is followed by TRoF3.2 (ROSA, cm-RX and the mm-TX modules– presented in Table V.7) before a second wireless hop. In this subsection we will focus, precisely, on the central node design for the TRoF3, considering again the compatibility for both RoF2 and RoF3. In both cases the starting points of this study are, as in the P2P architecture: -4.6 dBm optimum input power on the ULM TOSA for both RoF2 and RoF3; 15 dB optical losses when the Finisar ROSA is used; no additional optical losses when SiGe ROSA is used. The cm-RX block for TRoF3 modules and for the central node must be the same, so as to minimize the number of different boards to be fabricated by IETR Nantes. However, the impact of the choice to use 2 LNAs rather than 1 only, as suggested previously, will be analyzed as well.

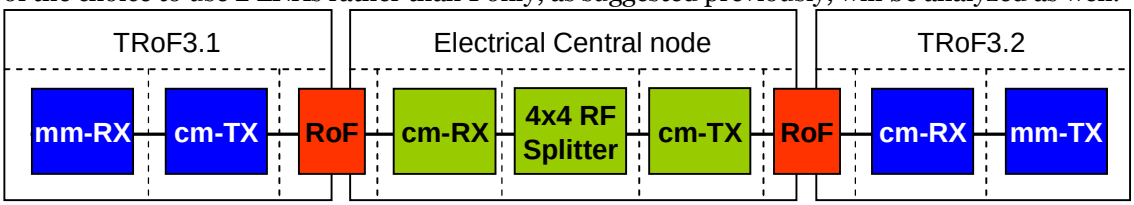

Figure V-35 - Optical Multipoint-to-Multipoint architecture with Electrical multiplexing (MME)

The first part of the subsection presents the central node based on the RoF2 link.

The next part of the subsection considers the central node based on the RoF3.

V.B.2.1 Central node based on RoF2

The link budget of the central node based on RoF2 is presented in Table V.9. The input power on the ULM TOSA is fixed to -4.6 dBm (blue highlighted). The variable attenuator Vatt should be low in order to reduce the noise contribution (green highlighted), nevertheless, it s attenuation has to be increased in order to avoid the saturation of the AGC component (yellow highlighted). To achieve -4.6 dBm at the input of the TOSA, the AGC and the variable attenuator are then set to be fixed with a gain of -22 dB and -17.3 dB, respectively.

These conditions give a global noise figure of 27.3 dB and an overall gain of 37 dB, considering both downlink (Table V.6) and uplink paths (Table V.7). Once again, the removal of one LNA rather than two would have been usefull in order to regulate again the Vatt to -3.3 dB (-17.3 dB + 14 dB) and obtain an overall noise of 19.2 dB (improvement of 8.1 dB).

Table V.9 – Electrical Central Node budget for the MME with Finisar ROSA solution (RoF2)

	Opt. L	ROSA		cm-RX block					Coupler	cm-TX block				TOSA
	15 dB	Finisar		RF Switch	Vatt	LNA	Filter	LNA	4x4	LNA	RF Switch	AGC (IL_2dB)	HPA	ULM
		PD	TIA											
$P_{in,max}$	-19,2	-49,2	-55,2	-23,2	-24,1	-41,4	-27,4	-29,0	-15,0	-22,0	-8,0	-10,6	-32,6	-4,6
$P_{in,min}$	-19,2	-49,2	-55,2	-23,2	-24,1	-41,4	-27,4	-29,0	-15,0	-22,0	-8,0	-10,6	-32,6	-4,6
$G_{ain,\ min}$ / G_{nom} / G_{max}	**-30,0**	**-6,0**	**32,0**	**-0,9**	**-17,3**	**14,0**	**-1,6**	**14,0**	**-7,0**	**14,0**	**-2,6**	**-22,0**	**28,0**	**-14,6**
$P_{out,max}$	-49,2	-55,2	-23,2	-24,1	-41,4	-27,4	-29,0	-15,0	-22,0	-8,0	-10,6	-32,6	-4,6	-19,2
$P_{out,min}$	-49,2	-55,2	-23,2	-24,1	-41,4	-27,4	-29,0	-15,0	-22,0	-8,0	-10,6	-32,6	-4,6	-19,2
IP1dB		-41,0		-	-4,0	0,0	-	0,0	-	0,0	-	-4,0	0,0	10,0
NF		8,5		0,9	17,3	3,0	1,6	3,0	7,0	3,0	2,6	22,0	3,0	34,3
NF per section	-	8,5		18,2		3,2			7,0	3,1		25,0		34,3
		22,3				3,2			10,1			29,9		
		25,4							25,7					
		26,9												

V.B.2.2 Central node based on RoF3

Comparing with RoF2, the Vatt is now reduced to its minimum attenuation to fit with the lower OM gain of the ROSA. Vatt (green highlighted) equaled to -8.6 dB respects the AGC backoff of 8 dB. The global system gain, considering both downlink (Table V.6) and uplink paths (Table V.8), is the same 37 dB and the noise figure is 45.3 dB, 18 dB higher than for RoF2. If one 14 dB LNA only is considered, the Vatt can be re-adjust to its minimum of -2 dB. However the overall noise improvement is negligible since the main contribution comes from the SiGe HPT.

Table V.10 – Electrical Central Node budget for the MME with SiGe ROSA solution (RoF3)

	ROSA			cm-RX lock					Coupler	cm-TX block				TOSA
	SiGe			RF										
	HPT	LNA_{IC}	LNA_{IC}	Switch	Vatt	LNA	Filter	LNA	4x4	LNA	Switch	AGC	HPA	ULM
$P_{in,max}$	-19,2	-53,3	-43,3	-33,3	-34,2	-42,8	-28,8	-30,4	-16,4	-23,4	-9,4	-12,0	-32,6	-4,6
$P_{in,min}$	-19,2	-53,3	-43,3	-33,3	-34,2	-42,8	-28,8	-30,4	-16,4	-23,4	-9,4	-12,0	-32,6	-4,6
$G_{ain,\ min}$ / G_{nom} / G_{max}	**-34,1**	**10,0**	**10,0**	**-0,9**	**-8,6**	**14,0**	**-1,6**	**14,0**	**-7,0**	**14,0**	**-2,6**	**-20,6**	**28,0**	**-14,6**
$P_{out,max}$	-53,3	-43,3	-33,3	-34,2	-42,8	-28,8	-30,4	-16,4	-23,4	-9,4	-12,0	-32,6	-4,6	-19,2
$P_{out,min}$	-53,3	-43,3	-33,3	-34,2	-42,8	-28,8	-30,4	-16,4	-23,4	-9,4	-12,0	-32,6	-4,6	-19,2
IP1dB	-	-12,0	-12,0	-	-4,0	0,0	-	0,0	-	0,0	-	-4,0	0,0	10,0
NF	46,1	3,0	3,0	0,9	8,6	3,0	1,6	3,0	7,0	3,0	2,6	20,6	3,0	34,3
NF per section	46,4			9,5		3,2			7,0	3,1		23,6		34,3
	46,4					3,2			10,1			28,5		
	46,5								24,3					
	46,5													

V.B.3. Optical Multipoint-to-Multipoint architecture with Optical multiplexing

The MMO architecture presented in Chapter II is shown as a block diagram in Figure V-36. It is simpler than the MME architecture because the central node is reduced to a simple 4x4 optical splitter.

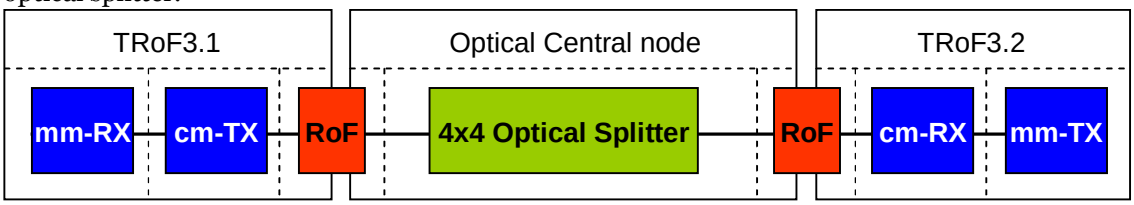

Figure V-36 - Optical Multipoint-to-Multipoint architecture with Optical multiplexing (MMO)

Table V.11 shows the characteristics of the central node (optical splitter) for both RoF link cases (RoF2 and RoF3) considering the same downlink path as given in Table V.6.

Table V.11 – Central Node of the MMO architecture for both RoF2 and RoF3

	Coupler 4x4
Pin,max (dBm)	-19,2
Pin,min (dBm)	-19,2
Gain, min (dB)	
Gain, nom (dB)	-12,0
Gain,max (dB)	
Pout,max (dBm)	-31,2
Pout,min (dBm)	-31,2

Because of the 6 dB intrinsic losses of the optical splitter, the optical losses of the uplink in RoF2 are reduced to 10 dB (Table V.12). The EIRP is guaranteed by regulating the Vatt to -26.3 dB (green highlighted). The overall system gain (considering both downlink (Table V.6) and uplink paths (Table V.12)) is 37 dB and the noise figure is 27 dB. If we remove one LNA of 14 dB we can reduce the overall noise down to 18.3 dB.

Table V.12 – Uplink path budget of the MMO architecture using the RoF2

	10 dB ATT.	Finisar ROSA		RF Switch	Vatt (IL_2dB)	LNA1	Filter	LNA2	Up-converter	HPA	Filter + transitions	Antenna Out	EIRP
		PD	TIA										
$P_{in,max}$	-31,2	-51,2	-57,2	-25,2	-26,1	-52,4	-38,4	-40,0	-26,0	-16,0	12,0	8,0	
$P_{in,min}$	-31,2	-51,2	-57,2	-25,2	-26,1	-52,4	-38,4	-40,0	-26,0	-16,0	12,0	8,0	
G_{min}													
G_{nom}	-20,0	-6,0	32,0	-0,9	-26,3	14,0	-1,6	14,0	10,0	28,0	-4,0	12,0	
G_{max}													
$P_{out,max}$	-51,2	-57,2	-25,2	-26,1	-52,4	-38,4	-40,0	-26,0	-16,0	12,0	8,0		20,0
$P_{out,min}$	-51,2	-57,2	-25,2	-26,1	-52,4	-38,4	-40,0	-26,0	-16,0	12,0	8,0		
IP1dB		-41,0			-4,0	0,0		0,0	-10,0	-7,0			
NF		8,5		0,9	26,3	3,0	1,6	3,0	8,0	3,0	4,0		
NF per section		8,5		27,2		3,2			8,1				
		21,4				3,2							
		24,5											

In the case of the RoF3 (Table V.13), the Vatt is regulated to -6.2 dB (green highlighted). The overall system gain, considering both downlink (Table V.6) and uplink paths (Table V.13), is 37 dB and the noise figure is 48.6 dB. In this configuration removing a LNA would reduce the EIRP down to 10 dBm.

Table V.13 – Uplink path budget on the MMO architecture using the RoF3

	SiGe ROSA			RF	Vatt	LNA	Filter	LNA	Up-	HPA	Filter +	Antenna	EIRP
	SiGe HPT	LNA_{IC}	LNA_{IC}	Switch	(IL_2dB)				converter		transitions	Out	
$P_{in,max}$	-31,2	-65,3	-55,3	-45,3	-46,2	-52,4	-38,4	-40,0	-26,0	-16,0	12,0	8,0	
$P_{in,min}$	-31,2	-65,3	-55,3	-45,3	-46,2	-52,4	-38,4	-40,0	-26,0	-16,0	12,0	8,0	
G_{min} / G_{nom} / G_{max}	**-34,1**	**10,0**	**10,0**	**-0,9**	**-6,2**	**14,0**	**-1,6**	**14,0**	**10,0**	**28,0**	**-4,0**	**12,0**	
$P_{out,max}$	-65,3	-55,3	-45,3	-46,2	-52,4	-38,4	-40,0	-26,0	-16,0	12,0	8,0		20,0
$P_{out,min}$	-65,3	-55,3	-45,3	-46,2	-52,4	-38,4	-40,0	-26,0	-16,0	12,0	8,0		
IP1dB	-	-12,0	-12,0	-	-4,0	0,0	-	0,0	-10,0	-7,0	-		
NF	46,1	3,0	3,0	0,9	6,2	3,0	1,6	3,0	8,0	3,0	4,0	-	
NF per section	46,4			7,1		3,2			8,1				
	46,4					3,2							
	46,4												

When the RoF2 is compared with RoF3 on MMO architecture configuration we remark that we have the same overall system gain but the overall noise figure has a difference of 21.6 dB manly coming from the SiGe ROSA module.

V.B.4. Synthesis

The architecture link system was designed and optimized taken into account the power transmitted by each block considering the gain, nonlinearities and Noise Figure. We were able to use successfully the OM figures of merit extracted in Chapter IV for the TOSA/ROSA modules. The summary of the obtained results for the 3 architectures (P2P, MME and MMO) are presented in Table V.14. The last generation of TRoF modules for the ORIGIN project (TRoF3) compatible with the ULM TOSA+ Finisar ROSA RoF link (RoF2) and the ULM TOSA + SiGe ROSA RoF link (RoF3) were then defined.

Table V.14 – Architecture link budget summary with the overall gain and noise figure (considering both downlink and uplink paths)

TRoF3	P2P		MME		MMO	
	RoF2	RoF3	RoF2	RoF3	RoF2	RoF3
Gain (dB)	37					
NF (dB) (*)	26.9 (17.7)	37.1 (36.7)	27.3 (19.2)	45.3 (45.2)	27 (18.3)	48.6 (48.6**)

*Configuration with only one LNA instead of two inside the cm-RX block with constant 20 dBm EIRP
**Configuration with only one LNA instead of two inside the cm-RX block with EIRP of 10 dBm

The cm-wave and mm-wave modules are compatible with both RoF generations. The reemitted EIRP was regulated to 20 dBm for both architectures. The removal of one LNA in the cm-RX block has a big impact when the RoF2 module is used with an improvement of around 10 dB in the noise figure. Although when the RoF3 module is used, the improvement is

negligible because of the low gain of the SiGe HPT, which mainly impacts the noise. The MMO architecture using the RoF3 and only one LNA would impose a reduction of the EIRP down to 10 dBm. We can estimate an important improvement by developing further the optical coupling of the SiGe HPT which was considered -9 dB in our computations. Its noise must be developed further too, especially using a 3T-HPT rather than 2R-HPT as was the case here.

The MMO architecture reveals to be a good option with RoF2 given system performance equivalent to the MME ones. Indeed, we achieve the best performances in term of noise figure down to 18.3 dB in the configuration of only one LNA in the cm-RX block. Although, during the ORIGIN project the MMO architecture revealed few disadvantages: multiple lasers working simultaneously create optical heterodyning interferences i.e. optical beating between the different laser optical wavelengths; furthermore as all lasers are simultaneously on, they might increase their RIN impact on the system and the shot noise induced by the sum of all DC optical powers on the photodetectors; Last, since we are using lasers with multimode operation, the optical splitter must be well balanced. To overcome those problems the lasers operation could be controlled by the medium access protocol.

V.C. The Final Demonstrator Performances

This section focuses on the integration of the TRoF modules (TRoF3) into the final demonstrator. The integration is made step by step, analyzing performance to understand the influence of each part of the system: the RoF transducer (optoelectronic devices, cm-wave circuit board, mm-wave circuit board, power supply circuit board, LO circuit board) and the architecture (signal controlling).

The first subsection intends to present the comparison of the optical link performance metrics (EVM) using the 3 RoF generations. The study takes into account the TOSA bias condition and the optical losses in order to optimize the performances on both E/O and O/E devices.

The second subsection shows the integration of the different circuit boards within the TRoF transducer. Each board is presented with its performances in order to evaluate the system performance degradation.

The final subsection presents the final demonstrator with corresponding performance characterization.

V.C.1. RoF Systems Comparison: The optical link

The performances of the 3 RoF generations are presented. Comparison based on the EVM measurement allows us to optimize different intrinsic and extrinsic parameters such as the laser bias condition, input RF power and optical losses.

Before analyzing the results, some principles need to be considered such as the relationship between the EVM and SNR given by Eq. (3.23) in Chapter IV. This equation explains the typical shape of the EVM curve as a function of the input RF power that can be related directly to the SNR evolution. For the SNR analysis, we need to take into account the 3 main noise components see Eq. (4.17), and their evolution with optical losses:

When the RIN is the dominant noise: for a fixed input RF power the EVM keeps constant with an increase of the optical losses, indeed for 1 dB optical loss, both the RIN and the signal OM power decrease by 2 dB keeping the same SNR (one dB optical losses means 2 dB electrical losses)

When the shot noise is dominant: for a fixed input RF power the EVM increases as we increase the optical losses since. In each 1 dB of optical losses added, the signal OM power decrease by 2 dB and the shot noise power reduces 1 dB. Therefore, the SNR reduces 1 dB.

When the thermal noise is dominant on the link: for the same input RF power the EVM increases as we increase the optical losses since it only affects the signal power while the noise level is constant.

V.C.1.1 Finisar TOSA and Finisar ROSA – TRoF1

The Opto-microwave link between the Finisar TOSA and Finisar ROSA is considered here. It defines the so called RoF1 link, which feeds the TRoF1 architecture.

Figure V-37 presents the EVM measurement results using RoF1 modules. In Figure V-37 a) the EVM is shown as a function of the input RF power for different TOSA bias currents (2:2:10 mA). It includes the initial calibration with Back-to-Back (B2B) measurement (~6 %).

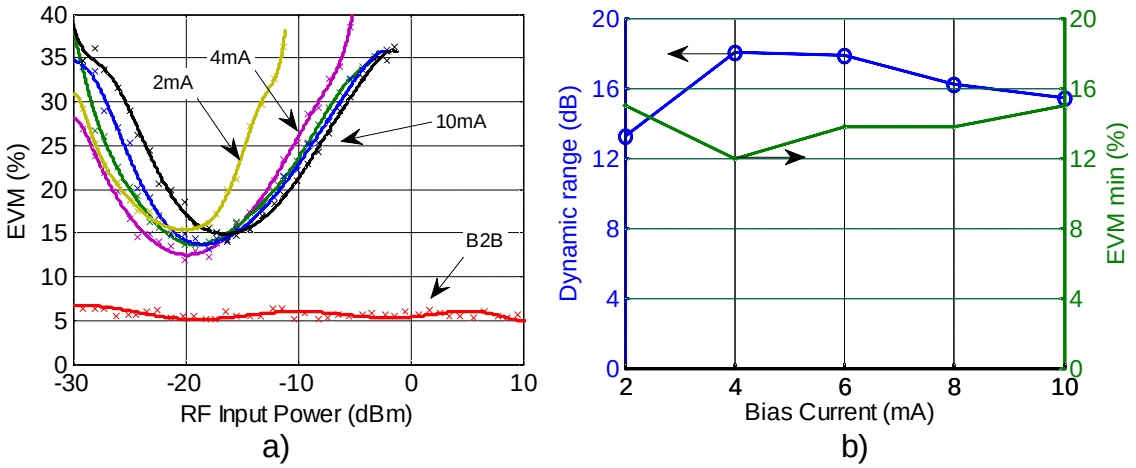

Figure V-37 – Finisar TOSA plus Finisar ROSA (RoF1) EVM measurement at IF of 3 GHz: a) EVM curve as a function of the input RF power for different bias currents; b) Dynamic range, at 25 % of EVM and minimum EVM evolution, as a function of the bias condition.

The analysis of those results can be separated into 2 regions: low input power and high input power.

Low Input Power Region: Noise influence

From 2 mA to 4 mA the EVM decreases, which can be explained by the TOSA RIN, which decreases with an increase in bias current (Figure III-14).

From 4 mA to 10 mA the EVM increases since the optical power emitted from the TOSA increases, adding additional noise from the photodiode (shot noise).

High Input Power Region: Nonlinearities influence

We notice the decrease of the EVM as we increase the bias current. It is expected from the increase of the TOSA linearity.

An important parameter to be extracted is the power dynamic range, see Figure V-37 b), dictated by the noise and nonlinearities of the link system. At low bias current we are limited by the TOSA performances, noise and nonlinearities, which give a low power dynamic range. As the bias current increases, the dynamic range increase up to 18 dB by the reduction on the RIN and the linearity improvement of the VCSEL, getting a minimum EVM of 12 % at 4 mA. After 6 mA the dynamic range reduces since the noise and nonlinearities of the ROSA increases. With these results we decide to use 6 mA to bias the TOSA.

As the bias current is optimized, the next step is the introduction of optical losses to improve the ROSA performances by regulating its input power (nonlinearities pushed toward higher values of input power). Figure V-38 shows the results of the EVM curve for different ROSA optical input powers. The TOSA bias current is fixed at 6 mA. If we consider a low input RF power fixing a 20 % of EVM for instance, we remark that the input RF power needs to be increased by approximately twice the added optical losses to get the same EVM. It suggests that the thermal noise is dominant (from the TIA). In the case of the high input RF power injection: as we increase the optical losses the EVM decreases since the ROSA nonlinearity is rejected toward higher values until the TOSA saturates with its nonlinearities.

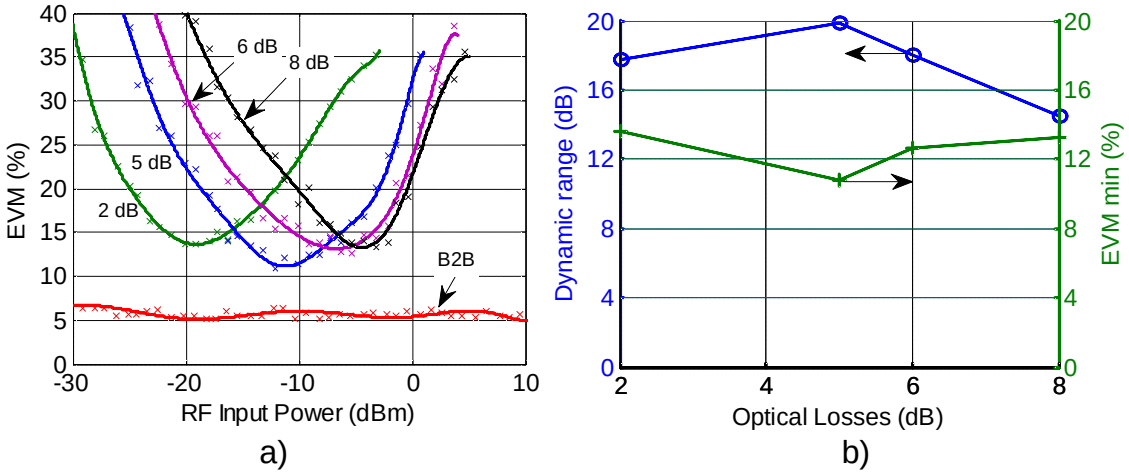

Figure V-38 – Finisar TOSA plus Finisar ROSA (RoF1) EVM measurement at IF of 3 GHz (6 mA): a) EVM curve as a function of the input RF power for different Optical losses; b) Dynamic range, at 25 % of EVM and minimum EVM evolution, as a function of the optical losses.

Figure V-38 b) shows the power dynamic range evolution with the increase of the optical losses. At low optical losses we are limited by the thermal noise and nonlinearities of the ROSA. The increase of the optical losses increases the dynamic range up to 19.8 dB by improving the linearity on the ROSA. Although, for high optical losses (>5 dB) the noise level decreases the dynamic range.

V.C.1.2 ULM TOSA plus Finisar ROSA – TRoF2/3

The Opto-microwave link between the ULM TOSA and Finisar ROSA is considered here. It defines the so called RoF2 link, which feeds the TRoF2 and eventually final TRoF3 architectures.

The same measurements were done with RoF2 where the TOSA Finisar was replaced by the home-made ULM TOSA module. Figure V-39 presents the results on EVM measurement. In Figure V-39 a), the EVM is shown as a function of input RF power for different TOSA bias currents (2:2:10 mA).

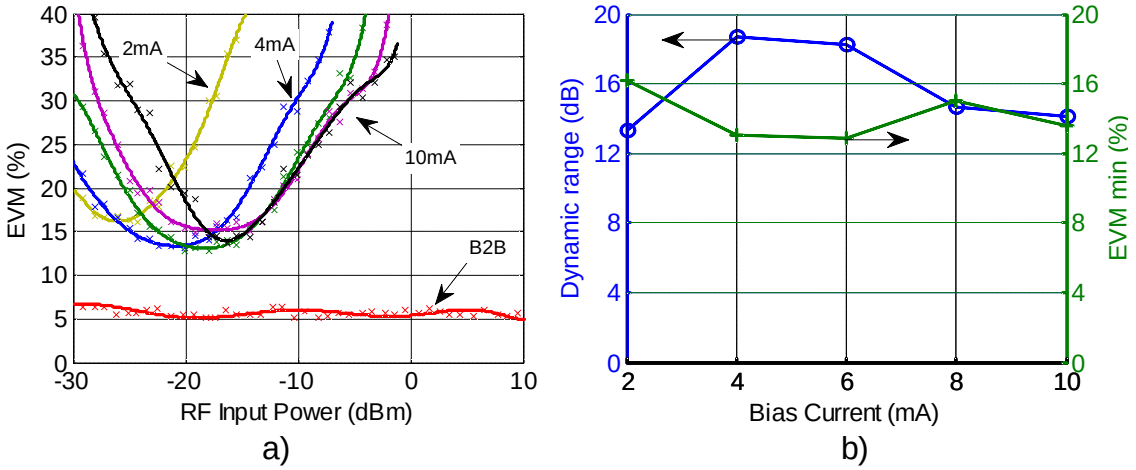

Figure V-39 – ULM TOSA plus Finisar ROSA (RoF2) EVM measurement at IF of 3 GHz: a) EVM curve as a function of the input RF power for different bias current; b) Dynamic range, at 25 % of EVM and minimum EVM evolution, as a function of the bias condition.

The same analysis made previously for TRoF1 applies here. The shot noise is dominant at low input RF power where the EVM increases as the photodiode input increases with the TOSA bias current. At high input RF power, the EVM decreases as the TOSA linearity improves until the ROSA saturation is limiting for bias current higher than 6 mA. Figure V-39 b) shows the increase of the power dynamic range up to 18.7 dB and then saturation limit of the ROSA (>6 mA). As previously, the minimum EVM is achieved simultaneously to the maximization of the power dynamic range, down to 12.8 % with bias current between 4 and 6 mA.

The EVM is also evaluated as a function of the optical losses, as shown in Figure V-40. For comparison purposes between RoF1 and RoF2 the bias current was fixed to 6 mA.

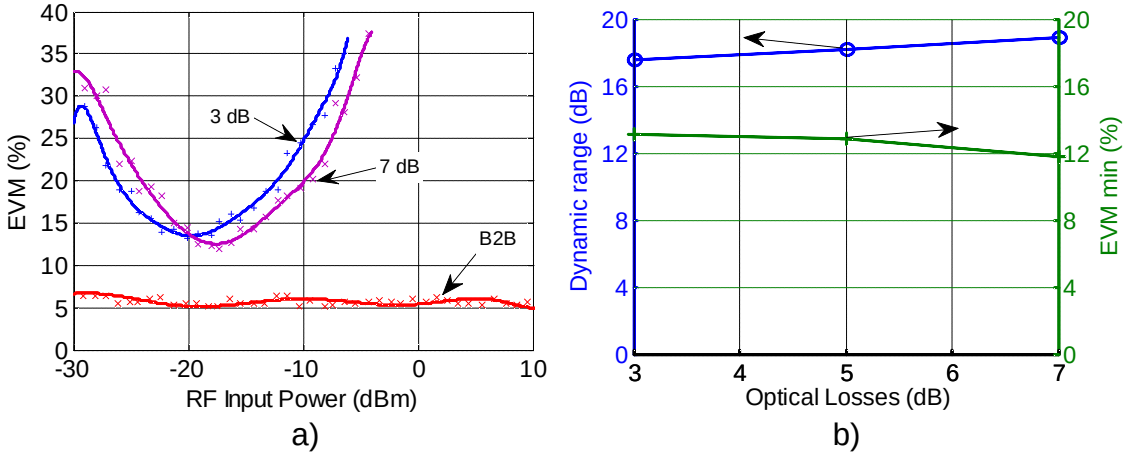

Figure V-40 – ULM TOSA plus Finisar ROSA (RoF2) EVM measurement at IF of 3 GHz (6 mA): a) EVM curve as a function of the input RF power for different Optical losses; b) Dynamic range, at 25 % of EVM and minimum EVM evolution, as a function of the optical losses.

Optical losses increase provides shift of the EVM curves towards higher RF input power. This proves that the ULM TOSA is more linear than the Finisar TOSA, thus increasing the dynamic range with the optical losses, as depicted in Figure V-40 b). We express some imprecision on the optical losses values in this specific Figure V-40 case (due to uncalibrated measured that was solved later on).

More measurements were done at an IF of 5 GHz in order to be in the context of the ORIGIN project. The ULM TOSA was biased at 8 mA because of its better linearity performance (see Chapter III). Figure V-41 shows similar results illustrating better proportionality between the optical losses and the EVM curve shifting. As the bias current is 8 mA, the optical losses used are higher.

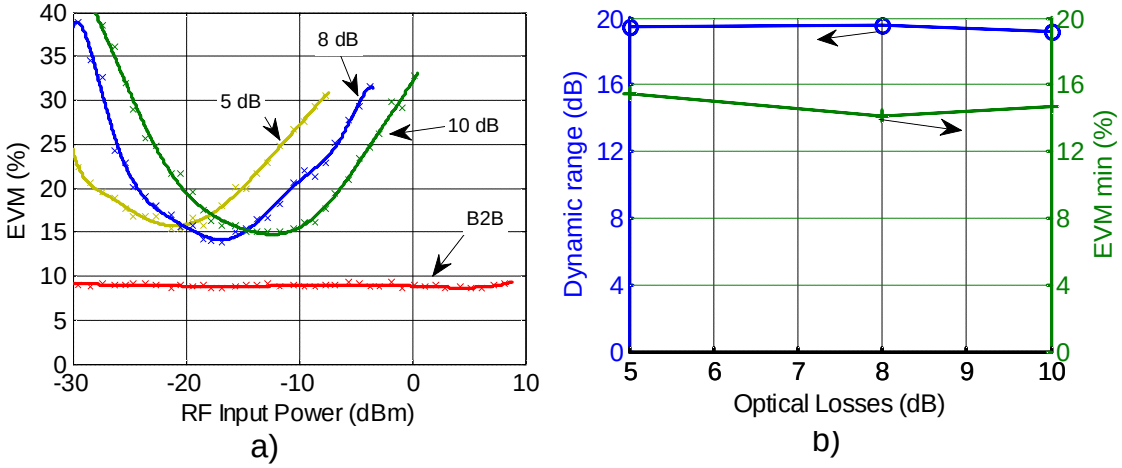

Figure V-41 – ULM TOSA plus Finisar ROSA (RoF2) EVM measurement at IF of 5 GHz (8 mA): a) EVM curve as a function of the input RF power for different Optical losses; b) Dynamic range, at 25 % of EVM and minimum EVM evolution, as a function of the optical losses.

Since we are doing an external converter to generate the 5 GHz signal the back-to-back EVM was slightly deteriorated to around 9 %, instead of 6 %. This explains as well the increase of the minimum EVM for each curve.

V.C.1.3 ULM TOSA plus SiGe ROSA – TRoF3

The Opto-microwave link between the ULM TOSA and SiGe ROSA is considered here. It defines the so called RoF3 link, which feeds the TRoF3 architecture.

The third RoF configuration, considers an ULM TOSA and a SiGe 2T-HPT based ROSA, which was in section V.A. The EVM curve was presented in Figure V-28. The results have shown a minimum EVM of 16 % degradation when compared to the B2B measurement. These results give us a good indication for a future development and study, but it will not be integrated in the system transducer as a mechanical failure happened.

V.C.1.4 Synthesis

The three RoF configuration system performances were presented and compared as a function of the input RF power, bias condition and optical losses. Indeed, those three parameters were optimized. The main drawback of the first generation (RoF1) was the nonlinearities on both TOSA and Finisar ROSA modules. The nonlinearities of the TOSA were improved by replacing the Finisar TOSA by the home-made ULM TOSA module (RoF2). The drawback of this generation (RoF2) is its higher optical output power and responsivity compared to the Finisar TOSA, which excites the nonlinearities of the Finisar ROSA, reducing the SNR. Consequently, high optical losses are required. The third (RoF3) generation tried to

override this situation but also to propose an higher integration by replacing the Finisar ROSA module by a much linear SiGe ROSA module. The first results of the SiGe ROSA show that it is a promising candidate, but 3 main improvement goals must be considered: moving toward a 3T-HPT solution, IC optimization design, better electrical matching network and finally a better optical coupling efficiency. The final RoF Transducer (TRoF3) will integrate the ULM TOSA and Finisar ROSA modules (RoF2) only due to mechanical failure.

V.C.2. Integration of the RoF Transducer module: P2P communication

This subsection presents the four electrical circuit boards integrated in the RoF transducer: the centimeter-wave circuit board; the LO circuit board; the power supply circuit board and the millimeter-wave circuit board. The system evaluation will be done in terms of EVM. The last part presents the integration of the four circuit boards into the final RoF transducer. It will be used in the final demonstrator where a Point-to-Point communication will be demonstrated.

V.C.2.1 The centimeter-wave circuit boards

The centimeter wave board was design previously through the link budget study. It was fabricated by IETR Nantes partner. Figure V-42 shows a picture of the final cm circuit PCB board.

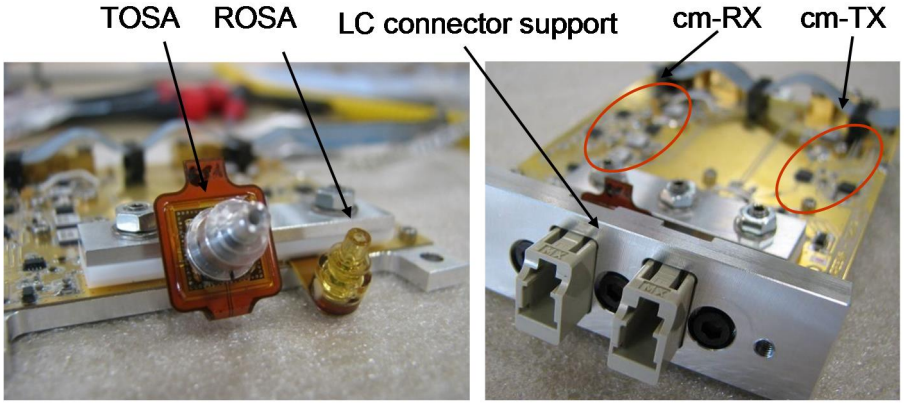

Figure V-42 – The centimeter-wave circuit board picture, from IETR ORIGIN partner: a) TOSA and ROSA integration into the cm circuit board; b) cm circuit PCB board

Figure V-43 shows the experimental setup that is used for the characterization and the optimization tuning of the cm-TX (downlink - Figure V-31) and the cm-RX (uplink - Figure V-33) circuit boards. The first goal is to regulate and optimize both the Variable Attenuator and the AGC in order to achieve optimal values identified in previous section V.B.1. The second goal is to analyze the cm-RX-TX system board in terms of the EVM degradation compared to the RoF block.

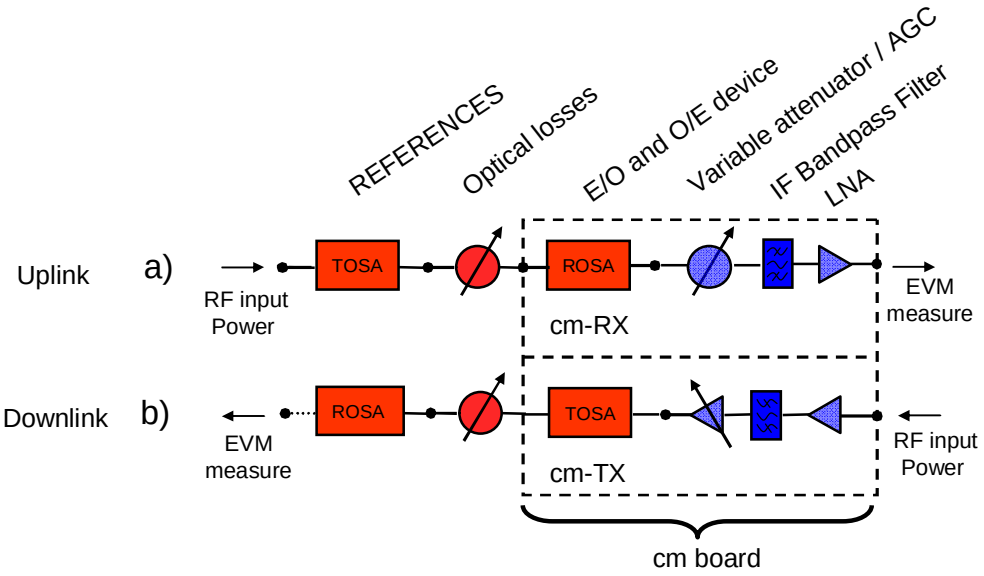

Figure V-43 – Block diagram representing the cm-wave system board experimental test setup for both cm blocks individually: a) uplink using the ULM TOSA as the reference; b) downlink using the Finisar ROSA as the reference.

The cm-TX and the cm-RX were characterized and optimized separately:
cm-TX block – presented in Figure V-43 b). This cm-TX includes a TOSA and cm-board. A second Finisar ROSA, previously characterized, is used as a reference detector to probe the opto-microwave signal generated by this cm-TX block and to fully characterize it. The procedure is to determine the overall gain and deduce the TOSA input power since we know the gain of each block. Then the TOSA input power can be regulated by adjusting the AGC.
cm-RX block – presented in Figure V-43 a). This cm-RX includes a ROSA and cm-board. A second ULM TOSA, previously characterized, is used as a reference light source to generate the opto-microwave signal into this cm-RX block and to fully characterize it. The cm-TX output power (mm-RX input) is regulated by adjusting the Variable Attenuator.

Considering the proposed free space distance scenarios (1 and 10 m) the input power range on the cm-TX block varies from -42 dBm to -22 dBm (see Table V.6). The EVM results are presented in Figure V-44 as a function of the input RF power. Figure V-44 a) shows the uplink (ULM TOSA reference followed by the cm-RX) results for two different optical losses of 10 and 15 dB. The input RF power is applied directly to the ULM TOSA reference. Two curves are traced for each optical loss showing the comparison between RoF only and the cm board connected to the RoF link. An increase of the noise level is expected due to all the electronic devices. That assumption appears on the EVM measurement with an increase in low input RF power, typically around 3 % more when 10 dB optical losses are used. It is, however, an increase of 7-8 % when 15 dB optical losses are used. Figure V-44 b) shows the downlink (cm-TX followed by the Finisar ROSA reference) results for both 10 and 15 dB optical losses where the input power is applied at the input of the cm-TX board. The input RF power varies from -42 to -22 dBm (equivalent 1 and 10 meters conditions) as previously. Indeed, we started at -50 dBm which represents a distance higher than 10 meters.

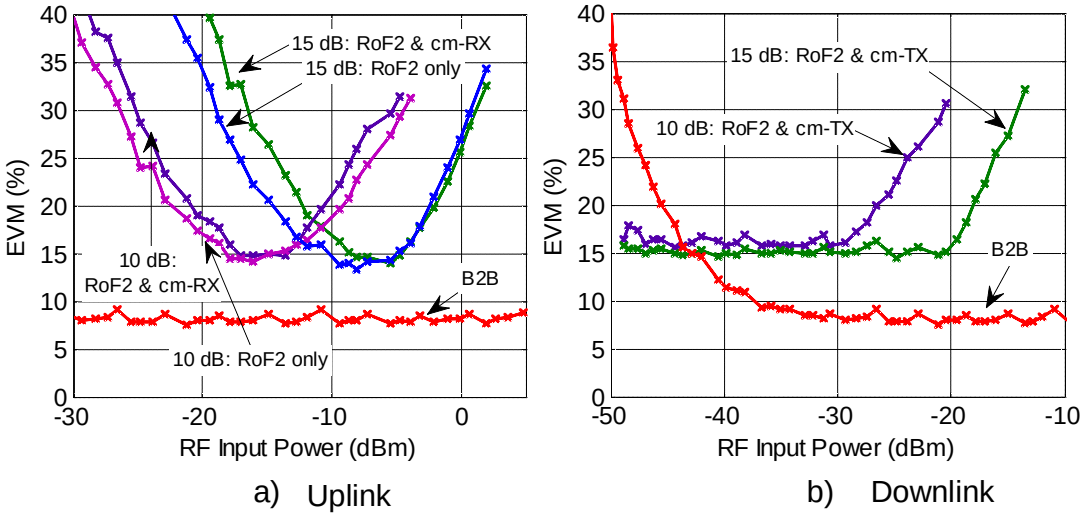

Figure V-44 – EVM curve as a function of the input RF power comparing the EVM degradation when the cm board is integrated (RoF2 & cm-TX/RX) or not (RoF2 only) with both 10 and 15 dB optical losses: a) Uplink; b) Downlink

Here, as expected, the EVM shape is flat for low input power because of the compensation performed by the AGC on the RF power feeding the TOSA. For high input power we reach the ROSA saturation limit where 15 dB optical losses are required to fix the input power to -20 dBm corresponding to 1 meter distance. The back-to-Back measurement basically shows the limitation of the Oscilloscope for low input power where the EVM increases in power lower than -30 dBm. Since the input power delivered from the test bench setup into the oscilloscope is usually higher than -30 dBm to probe the real conditions for the demonstrator (-23 dBm at the ROSA output and -26 dBm at the cm-TX board output - Table V.7), the B2B is kept within the 8 % region.

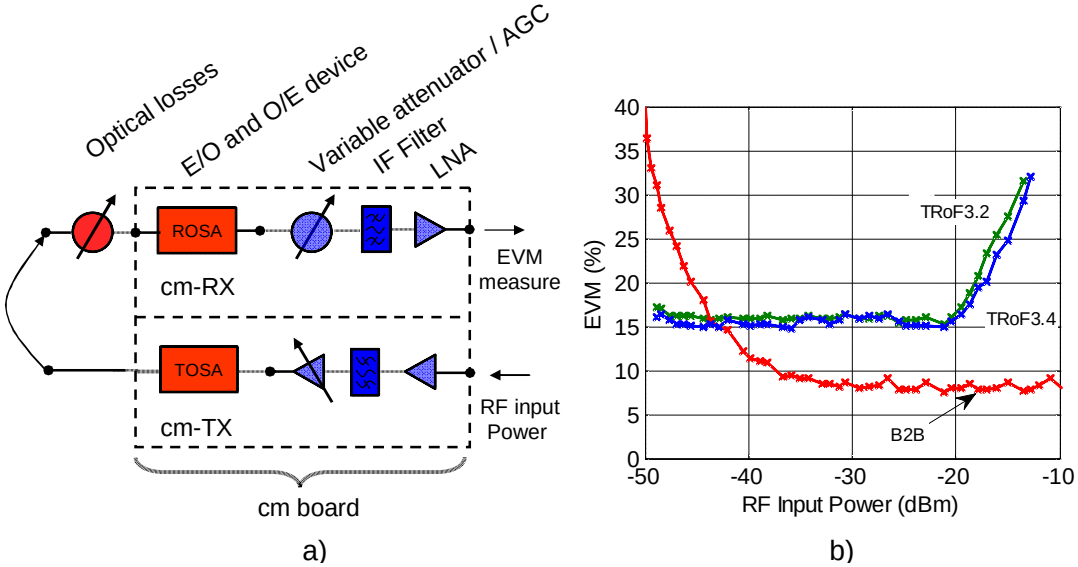

Figure V-45 – Both cm TX and RX board calibration: a) block diagram representing the cm-wave circuit board experimental test setup for both cm blocks at the same time; b) EVM as a function of the input RF power for two complete TRoF without the mm circuit board.

Final measurement considers both downlink and uplink linked together see Figure V-45 a). It considers the cm-RX block, TOSA module, optical losses, ROSA module and cm-TX block. The Figure V-45 b) shows the EVM results for two different TRoFs. Indeed, the uplink side was directly connected to the downlink of each TRoF module. The EVM for both TRoF is around 16 % across the whole targeted input RF power range (-50 to -20 dBm). These results provide a good expectation for the final demonstrator result. Comparison between two TRoF3 samples (TRoF3.2 and TRoF3.4) shows that they all have similar characteristics (low variation).

V.C.2.2 The LO and power supply circuit boards

The Local Oscillator (LO) circuit board generates the signal used on the mm modules for the conversion frequency. The LO frequency is 13.82 GHz with ±0. 5ppm stability, which meets the specifications of the WirelessHD (±1. 5ppm). This was designed and assembled by IETR Nantes

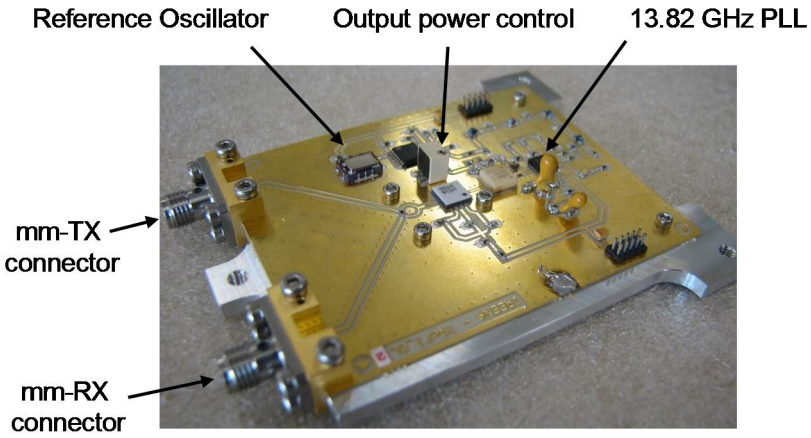

Figure V-46 – LO circuit board, from IETR ORIGIN partner.

Finally, the second channel of the unlicensed mm band, centered at 60.48 GHz, is then converted to an IF of:

$$IF = 60.48GHz - 4 \times 13.82GHz = 5.20GHz \quad \text{Equation Section 5} \qquad (5.1)$$

The power supply circuit board creates the different bias levels required by the TRoF, i.e. cm board, LO board, mm board and ROSA/ROSA. These levels are generated from a 48 V input voltage provided by the hybrid copper-fiber cables that feed the TRoF module (PoE). The RF power control regulation at the input of the TOSA and the output of the ROSA is made on this board by controlling the gain of the variable attenuator and the AGC.

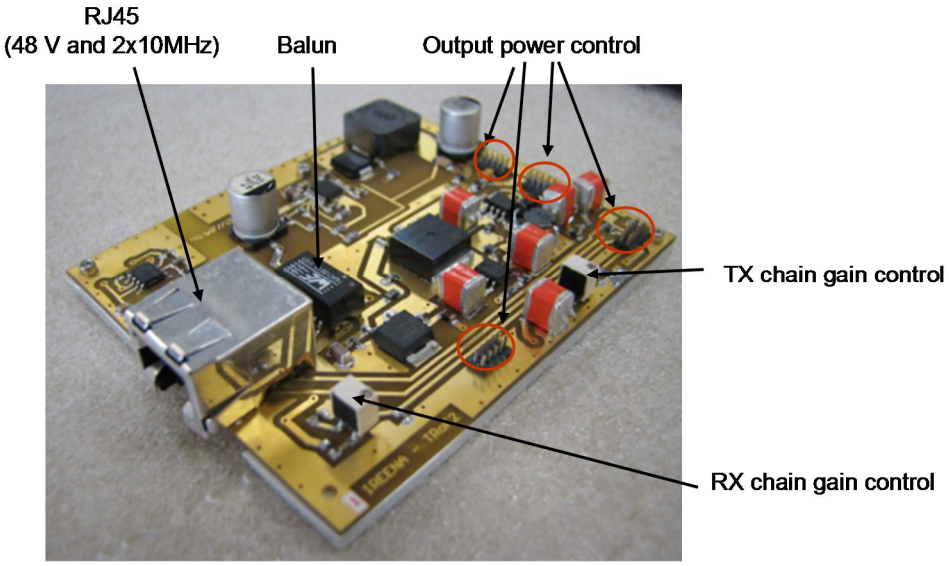

Figure V-47 – Power Supply circuit board, from IETR ORIGIN partner.

It also includes the switching interface which enables the management of the optical infrastructure by turning 'on' and 'off' the different cm circuit boards. This control is made by sending two monitoring signals to each TRoF through the copper quad of the hybrid cable: one quad for the TOSA; the second one for the ROSA. The implementation is characterized by the presence (turn on) or absence (turn off) of an RF carrier signal at 10 MHz.

V.C.2.3 The millimeter-wave circuit board

Each TRoF contains two millimeter-wave modules, one for the transmission (mm-TX block) and another one for the reception (mm-RX block). Their purpose is to capture the 60 GHz signals and down-convert it to the IF (mm-RX bock), and up-convert the IF signal to 60 GHz (mm-TX block). Figure V-48 shows the complete mm module including the electronics and the bias board supply. They were designed and assembled by Telecom Bretagne partner.

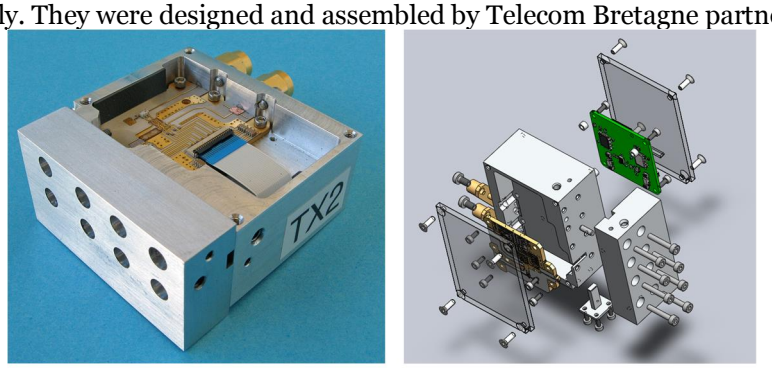

Figure V-48 – The millimeter –wave circuit module, from Télécom Bretagne ORIGIN partner.

The RF boards, fabricated on a Rogers RO4003 substrate, are assembled on a metal carrier and confined in an individual metal package with an mm power supply board installed. The total mm-TX block gain conversion was measured to be 3 dB, which corresponds to a 27 dB lower than expected. Improvements must be done for the future generations.

The last element is the horn antenna which was fabricated using metal coated foam with a permittivity close to the air. After machining, the foam is covered with silver paint to metalize the antenna walls (Figure V-49). This concept has performances nearly as good as commercial available metal horn antennas (about 0.1dB additional losses), while the cost is only about one tenth of the metal ones.

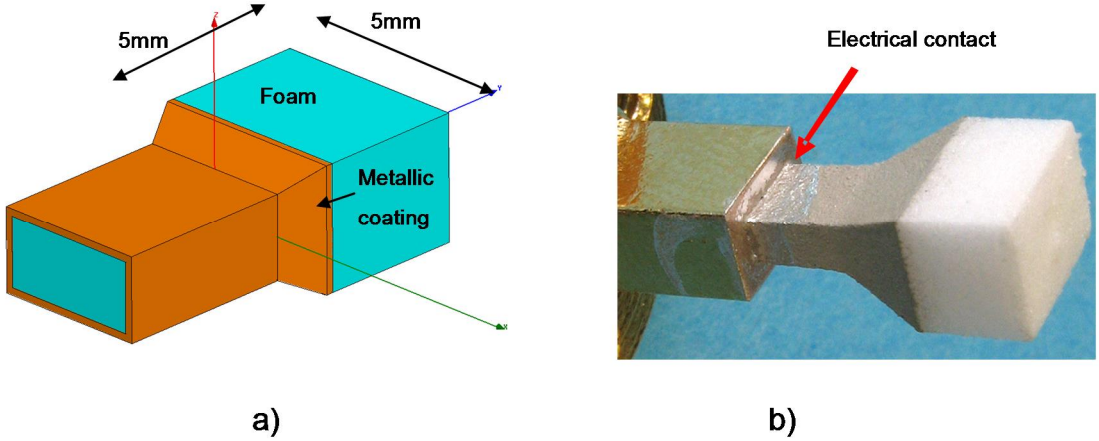

Figure V-49 –The horn antenna, from Télécom Bretagne: a) 3D schematic; b) photo.

The antenna gain is 10 dB with aperture angles of 43° in the E-plane and 57° for the H-plane. This technology is simple and low cost where different gain antennas were manufactured. This was done by Telecom Bretagne.

V.C.2.4 Final TRoF assembling

The final step is the integration of the mm modules into the RoF transducer, as depicted in Figure V-50. And now we are ready to perform a free-space point-to-point communication and measure the EVM degradation using a complete path.

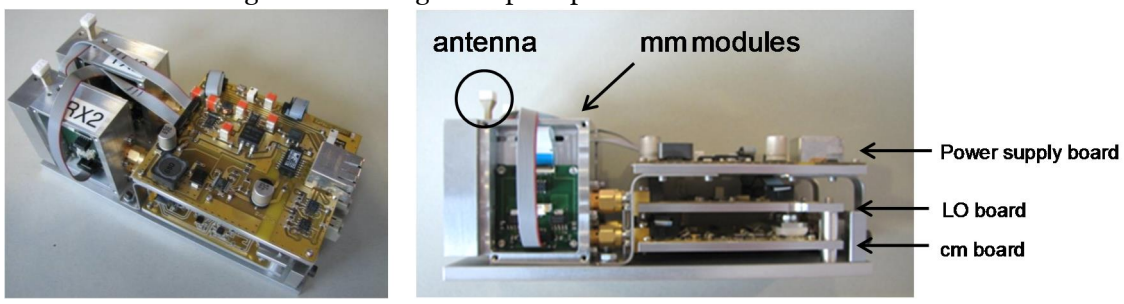

Figure V-50 –TRoF photograph.

The EVM calibration needs the integration of the 60 GHz signal transposition as depicted in Figure V-51. The EIRP was regulated by the variable attenuator to be +27.6 dBm (standard) close to real 60 GHz commercial devices (27 dBm). The free space communication distance was fixed to be the intermediate distance of our scenarios, 5m. After an optimization of the different parameters we achieved an EVM of 10.7 % on the B2B measurement with mm signal transposition (—24 dBm at the oscilloscope input).

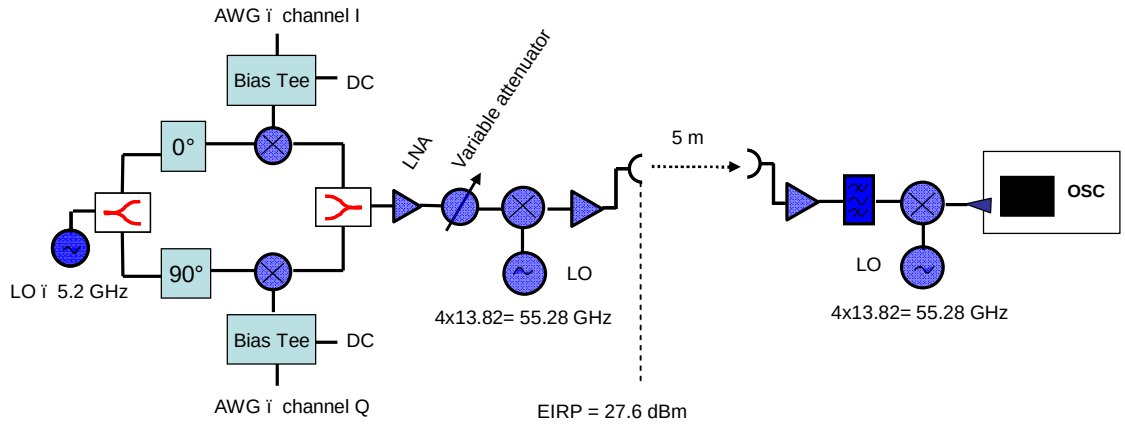

Figure V-51 – EVM bench setup integrating the 60 GHz transmission signal.

Figure V-52 shows the P2P architecture block diagram using two complete TRoFs with two free space communications.

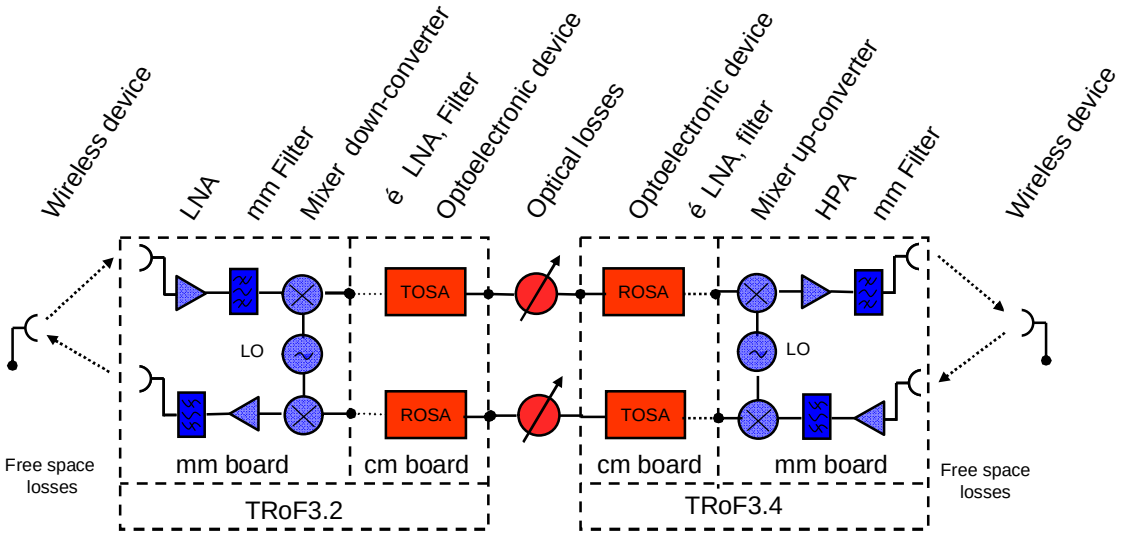

Figure V-52 – Bidirectional P2P block diagram using two TRoF modules.

A test system was mounted at ORANGE, Lannion (France) to test a point to point communication using two complete TRoFs. The EVM test setup was placed in two different rooms with no direct view. The two TRoFs were mounted with 12 dBi antennas. The first free space communication was from a distance of 5.2 meters between the EVM bench setup (signal generation) and the first TRoF3.2. The signal was then transmitted trough 2 meters of optical fiber (adding the15 dB optical losses) to a second room (TRoF3.4) and re-emitted with 3 meters of free space to the EVM receiver setup bench.

The initial cm board gain calibration was re-adjusted to compensate the mm module low gain (see V.C.2.3). The measured spectrum showed some parasitics at some frequencies which were shifting near the wanted signal. The EVM was measured continuously and the cm gain boards were optimized in live. The mm modules were optimized and we measured EVM down to 25 %, but still with an average of around 30 %.

We made a second test measurement by removing the mm-TX module of the second room (TRoF3.4) connecting it directly to the oscilloscope getting EVM stable of 17 %. Therefore, we can conclude that the mm-TX low gain is the main cause of the deterioration on the EVM measurement where the only solution was to increase the input power on the mm-TX module

from gain regulation on the cm boards. In this way we can compensate the mm-TX low gain. However, the constraint now is the saturation problems that are difficult to control.

Even so, a real-time transmission between two commercial (Gefen) WirelessHD devices was realized, as described in Figure V-53. An uncompressed 1080i video from a Blu-ray player was displayed on an HD screen validating the feasibility of the RoF architecture. Indeed, taking a simple 16:9 picture in 1080p coded with 24 bits per pixel (i.e. RGB color coded over 8 bits) at 60 Hz requires a data speed of

$$\begin{aligned} HD\ video\ data\ rates &= H_{pixels} \times V_{pixels} \times f_{refresh} \times D_{bits/pixel} \\ &= (16/9 \times 1080) \times 1080 \times 60 \times 24 \\ &= 2.986\ Gbit/s \end{aligned} \quad (5.2)$$

where,

- H_{pixels} is the number of vertical lines (horizontal resolution)
- V_{pixels} is the number of horizontal lines (vertical resolution)
- $f_{refresh}$ is the number of frames per second
- $D_{bits/pixel}$ is the number of bits coding per pixel

The WirelessHD devices from Gefen transmits an EIRP of 27 dBm and has a receiver sensitivity of —65 dBm. The emitted radio signals are centered in the second channel of the millimeter-wave band (see Figure II-1).

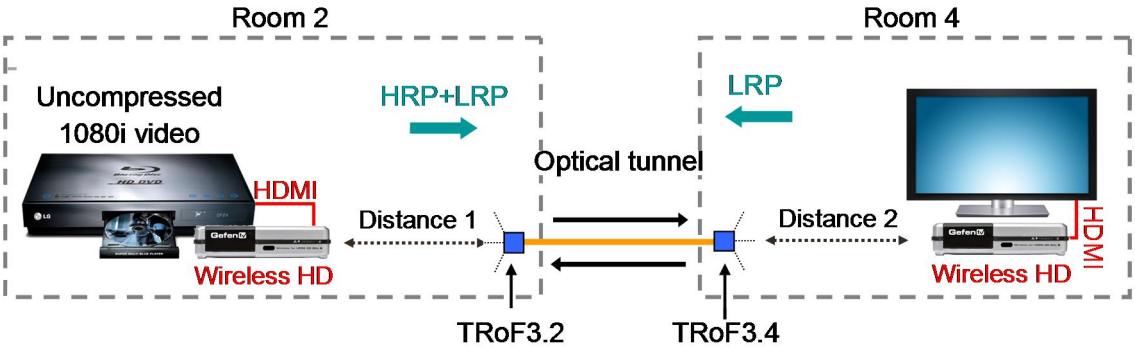

Figure V-53 – Real-time HD video transmission between two commercial WirelessHD devices from Gefen: P2P

The downlink channel, at high data rate for video transmission, is called High Rate Physical layer (HRP), whereas the uplink channel, at a low data rate for monitoring, is called Low Rate Physical layer (LRP), both represented in Figure V-53.

The Gefen WirelessHD products are characterized by an HRP with PHY data rate equal to 2.856 Gbit/s. The LRP with PHY data rate of 40 Mbit/s. The system was running smoothly even with measured EVM of 30 %, probably because of the error code correction which is intrinsic to the standard.

V.C.2.5 Synthesis

The four circuit boards were presented and integrated into the final RoF Transducer to be used on the system demonstration implementation. The cm-wave circuit board has shown good results in term of the EVM with 6 % of degradation (from the B2B reference) over the whole

input RF power range when 15 dB optical losses were used. Both LO and power supply circuit boards have shown good results in terms of IF operation signal generation, biasing condition platform and signal controlling. The mm-wave circuit board was presented with both transmission and reception modules including the mm antennas. The P2P link (optical tunnel) was implemented using two TRoFs which were composed by the implementation of the previous 4 circuit boards. We measured 14.3 % EVM degradation from the B2B using two free space communications with 3 and 5.2 meters. Complementary the transmission of a real HD movie transmission (using Gefen commercial modules) was demonstrated successfully at ~3 Gbit/s. We observed the limitation from the mm-TX modules due to failure in its gain (20 dB loss). However, a 16 % EVM was demonstrated for a two-hop scenario until the input of the mm-TX, which a successful achievement in terms of performances. The mm-TX modules added an extra 14 % to the EVM, achieving an overall 30 % EVM including the two hops. This proved to be compensated in the 3 Gbit/s transmission by the CRC implementation in the Gefen commercial modules.

V.C.3. Final MME demonstrator

Finally, this subsection implements the full architecture approach and signal controlling to achieve the final demonstrator with multi-room communication.

The MMO architecture uses multiple lasers simultaneously, which results in the high noise (RIN and shot noise) and the presence of the optical heterodyning interferences. This problem can be avoided with an optical access management by controlling the activation of each laser and photodetector on the different rooms. This is also avoided in the MME architecture. Two important characteristics come out along this optical access management, however, that can benefit both the MME and MMO architectures: minimization of the Electro-Magnetic-Fields (EMF) exposures by turning off the TRoF where they are not needed; minimization of the power consumption of the system by reducing the number of TRoF operation. A solution to optical management access consists of reading the MAC radio layer information which provides the communication parameters as the source and destination stations [113] [114]. Here Beamforming (BF) is a technique which can be introduced providing an optimized channel communication. The radio demodulation is necessary to recover information such as device activation information and the BF information. This implementation is not possible due to the fact that the IEEE 802.11ad radio chipsets are not available today. However, a solution is proposed to overcome it with a Graphic User Interface (GUI) and a 'Green Box' that allow a manual control of activated room by the user. The GUI gives the users the option to choose two rooms in their house for a P2P communication, for instances a broadcast of an HD movie. In the case of the Green Box, it generates the controlling signals responsible for the laser and photodiode activation. The unused lasers can be turned off removing the optical heterodyning detections (MMO case) and the unused photodiodes as well reducing the EMF radiations (reason for the 'Green' name attribution). The Green Box plays the role of the interface between the GUI and the RoF transducers: it receives the user information and creates the electrical signal for the TRoF activation. The final demonstrator is sketched in Figure V-54 here below.

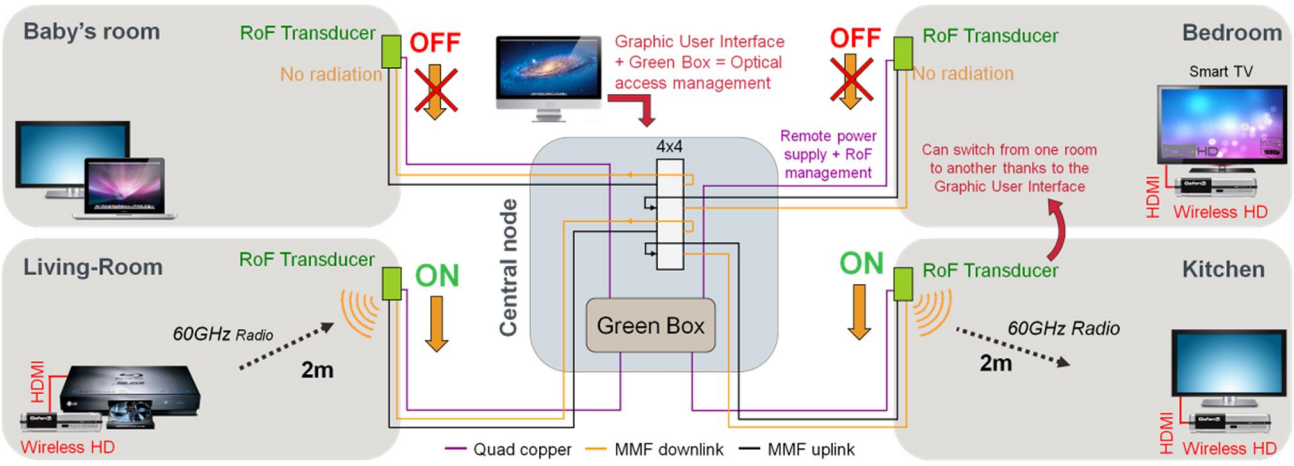

Figure V-54 – Real-time HD video transmission between two commercial WirelessHD devices from Gefen: MME

The final demonstrator pretended to recreate a real demonstration using an MME architecture between 2 rooms (capable up to 4 rooms). The GUI and the Green Box were part of the demonstration. The TRoFs were placed at 2 meters from the Gefen emitter and receptor with 12 dBi antennas in each module. The optical losses were reduced to 10 dB to compensate the mm-TX board low gain. The demonstration was a success with a transmission of an HD

movie even with certain restriction is terms of distance and the position (angle) of the TRoF compared to the Gefen. A high radiating coupling through the two antennas between the mm-TX and mm-RX modules was detected. An improvise isolation was placed between both antennas and a quality improvement was found.

Photo of the demonstrator are given here below, with the TRoF and hybrid cable installed in the walls.

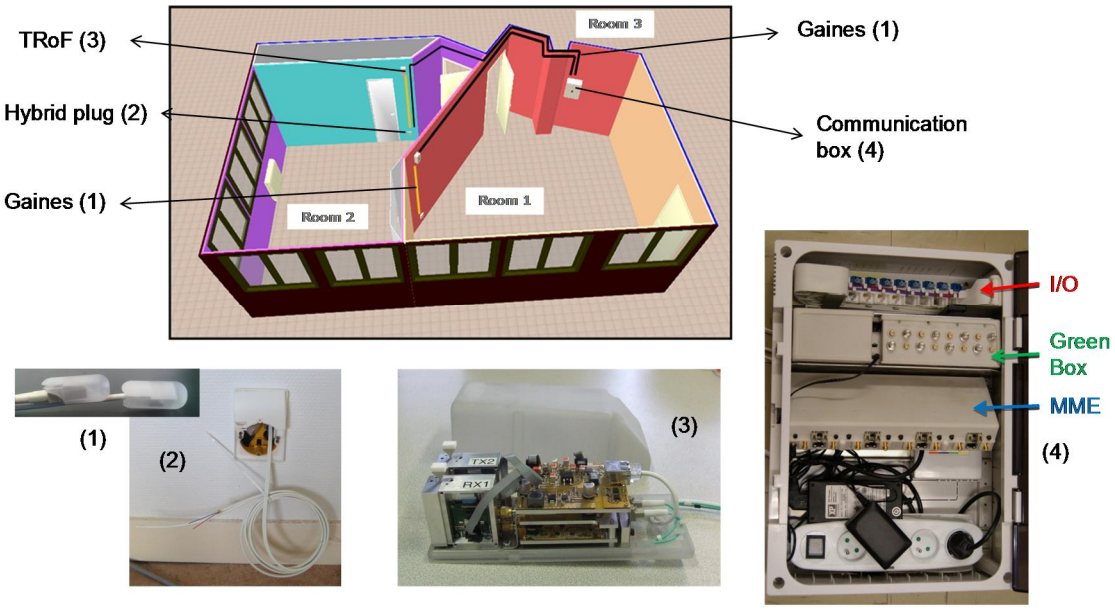

Figure V-55 – ORIGIN Final demonstrator

A video of the demonstrator can be found in [175].

V.D. Summary and Conclusion

In this chapter we have shown the development of the optoelectronic modules (ROSA and TOSA) from the single chip (VCSEL and HPT) to the packaged modules, and their integrated into the RoF transducer used in the ORIGIN system. Those modules are the final RoF generation and were successfully designed and fabricated through the development in both electrical and optical interconnections. The optical coupling using a ball lens technique shows a coupling efficiency of 60 and 40 % for the home-made TOSA and ROSA, respectively. The TOSA was fabricated using an 8 µm aperture diameter 10 Gbps ULM VCSEL at 850 nm. The ROSA was fabricated using a 10x10 µm² SiGe 2T-HPT with two 10 dB LNA associated. ULM TOSA and SiGe ROSA performances were measured showing 3 and 16 % EVM degradation compared to the B2B, respectively. Although, the promising results of the SiGe ROSA require further optimization. Perspectives are to use a 3T-HPT, to improve the -9 dB coupling efficiency and to improve the frequency flatness through an improved integration and matching with LNA ICs. This section also prepares the interconnection substrate for a further matching of the VCSEL, as will be discussed in Chapter VI.

The second section presented the link system power design for the final TRoF3 which considered the gain, noise and nonlinearities of each device of the system including: RoF, cm circuit boards, mm circuits boards and the antennas. The system architectures were taken into account with the optical tunnel (P2P) and the multipoint-to-multipoint (MME and MMO) architectures with special attention to the compatibility for both the Finisar ROSA (RoF2) and SiGe ROSA (RoF3). The critical points were identified and solutions proposed. The MMO architecture reveals to be an eventual future option with further development to be solved: multiple lasers working simultaneously create optical heterodyning interferences i.e. optical beating between the different laser optical wavelengths; furthermore as all lasers are simultaneously on, they might increase their RIN impact on the system and the shot noise induced by the sum of all DC optical powers on the photodetectors; Last, since we are using lasers with multimode operation, the optical splitter must be well balanced also. To overcome those problems the lasers operation could be controlled by the access to the media. The cm-board integrates two 14 dB LNA. The MME, MMO and P2P architectures are designed to provide a 37 dB gain. MME and MMO architectures prove to have similar noise figure down to 18 dB with only one LNA with the Finisar ROSA and up to 45 dB with the 2T-HPT ROSA.

The last section presented the integration of the TOSA and ROSA modules into the RoF Transducer (TRoF) for the final demonstrator. Performances were evaluated from each part of the system with special attention to the RoF module and cm circuit board power final experimental adjustments. Performances optimization was regulated in terms of the input RF power, bias condition and optical losses. The RoF1 revealed strong nonlinearities on both Finisar TOSA and ROSA modules. The evolution toward RoF2 implemented the home-made ULM TOSA module which solved the Finisar TOSA limitation on its linearities. Although, in order to improve the linearity of the remaining Finisar ROSA, 5-15 dB optical losses are required. The final RoF evolution (RoF3) implemented the home-made SiGe ROSA module and so improves the receiver nonlinearities. The first results were promising, but four main improvements must be considered: IC design, electrical matching network, 3T-HPT operation and finally the optical coupling efficiency. Therefore the TRoF3 was implemented using the RoF2.

Integration of the four circuit boards into the final RoF Transducer was presented. The cm-wave circuit board has shown good results in term of the EVM with a maximum of 7 %

degradation over the whole input RF power range. 15 dB optical losses were used to accomplish the power requirement and avoid eventual Finisar ROSA saturation. Both LO and power supply circuit boards were presented and integrated. The final module was the mm-wave circuit board for both transmission and reception path including the mm antennas. The complete TRoF3 was tested within the P2P link (optical tunnel) architecture, integrating the previous boards. We measured 14.3 % EVM degradation using two free space communications with 3 and 5.2 meters. The mm-TX module was found to be the weakness of the system for its low gain as a loss of 20 dB was found with respect to the gain expectation. However, a 16 % EVM was demonstrated for a two-hop scenario until the input of the mm-TX, which a successful achievement in terms of performances. The mm-TX modules added an extra 14 % to the EVM, achieving an overall 30 % EVM including the two hops. This proved to be compensated in the 3 Gbit/s transmission by the CRC implementation in the Gefen commercial modules.

The final step was the implementation of the MME architecture and signal controlling to achieve the final demonstrator with multi-room communication. The demonstration between the two rooms was successful using the home-made GUI and the Breen Box. A successful transmission of a real 2.8 Gbps HD movie using Gefen commercial modules was realized.

Chapter VI – **Optoelectronic Device Next Generation Developments**

From all the work presented in the last chapters, two main topics are identified to be limiting the link performances and to need further development for future RoF transducers: the system operating frequency limited by the optoelectronic device bandwidth and the optical packaging coupling efficiency. This chapter pretends to explore these two directions.

The first section intends to focus on the operating frequency considered until now of around 5 GHz, which revealed to be adjusted for 10 Gbps optoelectronic devices. Analogue VCSELs performance towards 20 GHz are considered through the modification of the layout in terms of optical aperture diameter and RF access lines together with the improved vertical stack of layers provided by Philips-ULM Photonics. From this study, we should be able to choose one device to be the candidate for the next of TOSA generation.

The second section covers the problematic of the optical coupling with a simulation of the ball lens technique and a proposition of a new optical coupling technique to improve the efficiency results in a collective and passive process. Both techniques are compared.

VI.A. Toward 20 GHz analogue VCSELs and beyond

The layout design of VCSEL devices is very important since it influences all the performances, including the frequency modulation and the transverse mode shape. We have performed two main improvements on the device layout: in the electrical interconnections with the goal to maintain the impedance up to the pads and to improve the thermal dissipation; in the lateral dimension through a variation of the optical aperture diameter with the goal to investigate the performance and the coupling efficiency as a function of the optical window size. The VCSELs were fabricated by Philips / ULM Photonics (see Chapter II, section II.B.1.6) where the technology is based on GaAs active material with epitaxial optimization in order to reach 20 Gbps applications.

We start to present the static characteristics of the device as a function of the optical aperture diameter by the LI curves where the different DC parameters are extracted. The following subsection presents the laser input impedance study with RF access transmission lines de-embedding using three one-port de-embedding methods. The next subsection presents the extracted laser opto-microwave gain and the frequency response behavior as a function of the device size. Both DC and RF responses lead to a trade-off between the different simulated performance that allow us to select a specific size of VCSEL that is completely characterized and that is developed further to be integrated into a TOSA including a matching network.

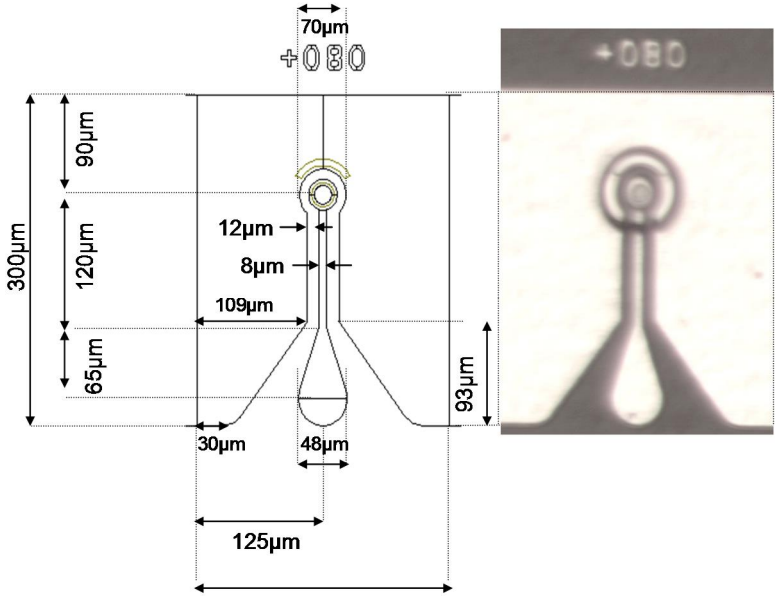

Figure VI-1 – 20 Gbps VCSEL layout structure (8 µm diameter size)

The representation of the 20 Gbps VCSELs is presented in Figure VI-1 including a photo on the right side. The layout modifications compared to the 10 Gbps ULM VCSEL are the RF access coplanar transmission lines and the diameter size of the optical aperture with a range of 2-20 µm. The metalized surface of the ground plane is also increased to improve the thermal radiative and conductive dissipation.

VI.A.1. Static performances as a function of the VCSEL size

The LI curves using the DC2PM (directly to the power meter) measurement configuration as a function of the aperture diameter is shown in Figure VI-2: smallest devices are gathered on

the left (2, 3, 4 and 5 µm diameters) and largest ones on the right (6, 8, 10, 12 and 20 µm diameters). The DC2PM technique, as described in previous chapters, allows to collect the total power emitted from the VCSEL. The bias current is intentionally limited on the smallest structures to avoid saturation (thermal roll-over) and consequently device damage. VCSEL devices with aperture diameter of 6, 8, 10 and 12 µm were biased up to 10 mA but did not achieve the maximum output power for VCSEL size above 8 µm.

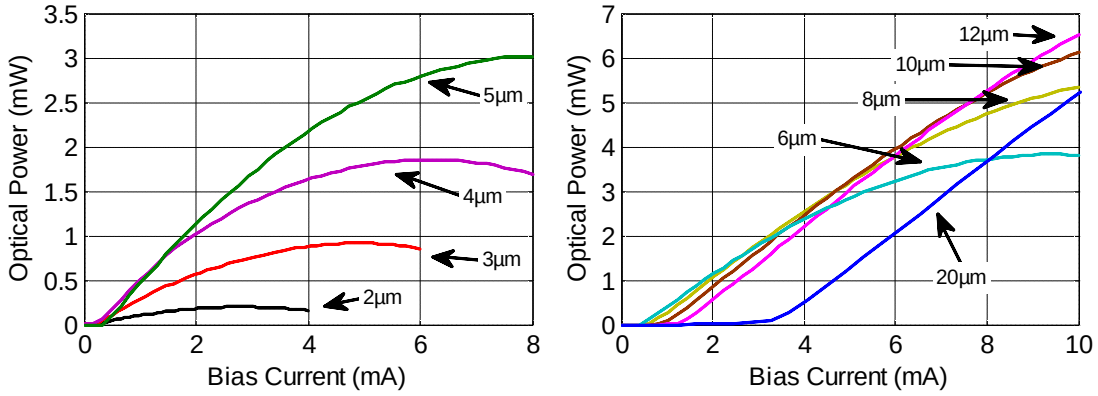

Figure VI-2 – Static characteristics presented as an LI curve (DC2PM) for different VCSEL optical aperture sizes: a) 2, 3, 4, 5 µm; b) 6, 8, 10, 12 and 20 µm.

The static parameters are then extracted and presented in Table VI.1 and compared to the 8 µm standard 10 Gbps die VCSEL (Chapter III). These parameters are the threshold current (I_{th}), threshold current density (J_{th}), threshold voltage (V_{th}), maximum optical output power (P_{max}), slope efficiency (S_{LD}), differential quantum efficiency (η_d) and differential resistance (R_d). The S_{LD}, η_d and R_d where computed at 50 % of the maximum optical output power.

Table VI.1 – Static VCSEL extracted parameters as a function of the diameter optical aperture diameter in a DC2PM measurement configuration

Size	I_{th}	J_{th}	V_{th}	P_{max} /(Bias)	S_{LD}*	η_d*	R_d*
Unity µm	µA	KA/cm^2	V	mW/(mA)	W/A	%	Ω
2	123	3.915	1.8	0.21/(2.78)	0.1	7	400
3	165	2.334	1.68	1/(4.78)	0.3	23	137
4	170	1.353	1.66	1.85/(6.2)	0.5	34	94
5	328	1.67	1.64	3/(8)	0.58	40	93
6	410	1.45	1.64	3.28/(9.4)	0.61	41.8	73
8* (standard)	610	1.214	1.55	>3.83/(10)	0.63	43.3	70
8	613	1.220	1.68	>5.35/(10)	0.63	43.3	73
10	817	1.040	1.65	>6.11/(10)	0.75	51	62
12	1225	1.083	1.66	>6.5/(10)	0.8	55	57
20	2858	0.910	1.66	>11.1/(20)	0.76	51.6	30

*at 50 % of maximum power

As expected the threshold current and the output power decrease as the VCSEL size decreases down to 123 µA and 0.21 mW for the smallest size, respectively. As the surface enlarges, more current is required to fulfill the lasing condition, up to I_{th}=2.858 mA at 20 µm of aperture diameter. This will have an important impact on the dynamic characteristics. The J_{th} is, however (Figure VI-3), stable around 1 kA/cm² except for the smallest size where it increases

up to 4 kA/cm² which can be explained by the high differential resistance and current leakage. The low differential resistance is shown to be inversely proportional to the area of the Ohmic contact.

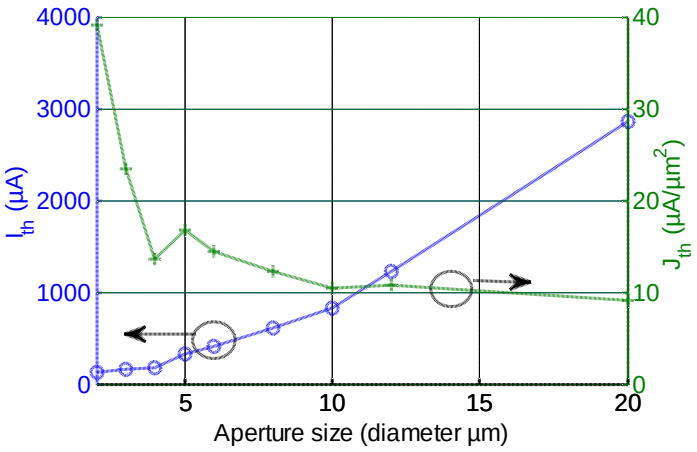

Figure VI-3 – Threshold current and threshold current density as a function of the VCSEL aperture size.

As the VCSEL size is reduced, the optical output power is lowered, resulting in a low slope efficiency, as depicted in Figure VI-4. This can be explained by the high cavity losses and/or the light divergence effect inducing a lower optical coupling to the power meter. At 2 µm aperture diameter the slope efficiency is 0.1 W/A at 50 % of the maximum output power. On the other side the slope efficiency is improved up to 0.8 W/A for 12 µm VCSEL, giving a differential quantum efficiency of 55 %.

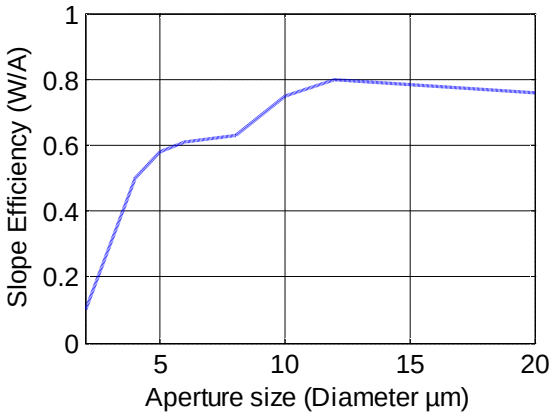

Figure VI-4 – Slope Efficiency as a function of the VCSEL optical aperture size.

At 20 µm aperture diameter VCSEL, the slope efficiency falls slightly which could be attributed to the current crowding. The 8 µm VCSEL is similar in performance to the standard 8 µm 10 Gbps VCSEL. However, the saturation is reduced in the modified version, which may be provided by the better thermal dissipation.

VI.A.2. De-embedding of RF access lines

On the same wafer of the fabricated modified VCSELs, open, short and thru lines were added using the same dimension sizes (Figure VI-5). These structures were designed and implemented in order to extract and understand the RF access transmission line influence on

the VCSEL input impedance. The VCSEL targeted for de-embedding study is the 8 µm optical aperture diameter.

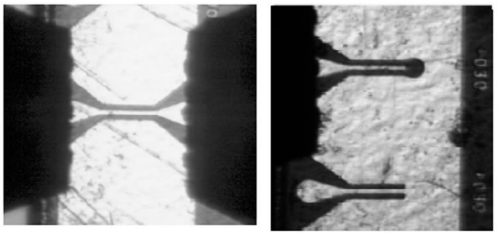

Figure VI-5 – Dummy test structures on probe test station (GSG - 100 µm pitch): Photos of thru, open and short lines

Three one-port de-embedding methods are based on the measurement of 'open' and 'short' lines reflections coefficient. Two methods [173] rely on the parasitic structure representation. The "open-short" (OS) configuration in Figure VI-6 a) as

$$y_{LD,OS} = \left[(y_M - y_{open})^{-1} - (z_{short}^{-1} - y_{open})^{-1} \right]^{-1} \quad \text{Equation Section 6} \qquad (6.1)$$

and the "short-open" (SO) configuration in Figure VI-6 b) given by

$$y_{LD,SO} = (y_M^{-1} - z_{short})^{-1} - (y_{open}^{-1} - z_{short})^{-1}. \qquad (6.2)$$

The last method, Figure VI-6 c), is based on the generic S-parameters representation and the assumption of the symmetry on the RF access line (SL), S11=S22 [174]. The reflection coefficient of the laser diode is given by

$$\Gamma_{LD} = \frac{A - \Gamma_M}{A^2 - A \cdot \Gamma_M - B} \qquad (6.3)$$

Where

$$A = \frac{\Gamma_{M,OPEN} + \Gamma_{M,SHORT}}{2 + \Gamma_{M,OPEN} - \Gamma_{M,SHORT}} \qquad (6.4)$$

$$B = (\Gamma_{M,OPEN} - A) \cdot (1 - A) \qquad (6.5)$$

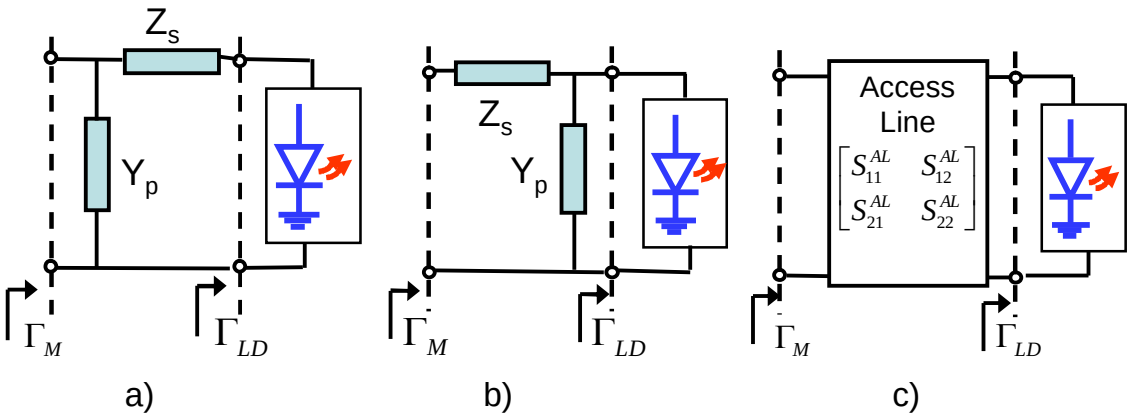

Figure VI-6 – One-Port De-embedding methods equivalent circuit: a) – Open-Short (OS); b) - Short-Open (SO); c) – Symmetrical Line (SL)

The final extracting results on the laser input reflection coefficient using the 3 de-embedding methods are presented in Figure VI-7. The symmetrical line method presents results with less dispersion at high frequency compared to the OS and SO methods. S11 of the 8 µm aperture diameter modified VCSEL presents very good results with reflection losses lower than —15 dB over the frequency range (impedance presented on the pad), presenting an improvement on the input impedance compared to the de-embedded result (input impedance at

the optical window). Comparing this measurement result with the 8 µm aperture diameter ULM standard we see an improvement of 10 dB at 10 GHz.

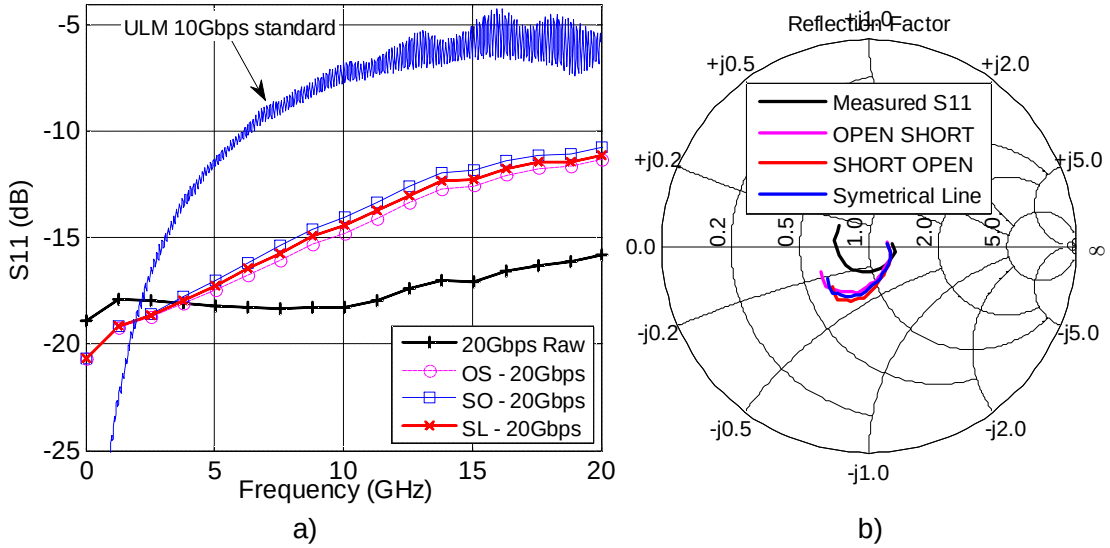

Figure VI-7 – 8 µm aperture diameter 20 Gbps VCSEL (8 mA) input reflection coefficient comparison between the three extraction methods: a) S11 magnitude compared to the measured 8 µm aperture diameter ULM 10 Gbps VCSEL (8 mA); b) Smith chart.

VI.A.3. Dynamic response as a function of the VCSEL size

The OM gain frequency responses are presented in Figure VI-8 for different aperture size diameters: smallest ones on the left; largest ones on the right. At 24 GHz we note the influence of the reference photodiode (see NFPD frequency response in Figure III-5) that can be seen as a bench setup limitation on the very high-speed frequency lasers. The extracted opto-microwave gain includes the losses due to the coupling coefficient of the VCSEL to the multimode lensed fiber. Thus, it differs even at low frequency from the DC slope efficiency, extracted from a measurement with the large detector of the power meter.

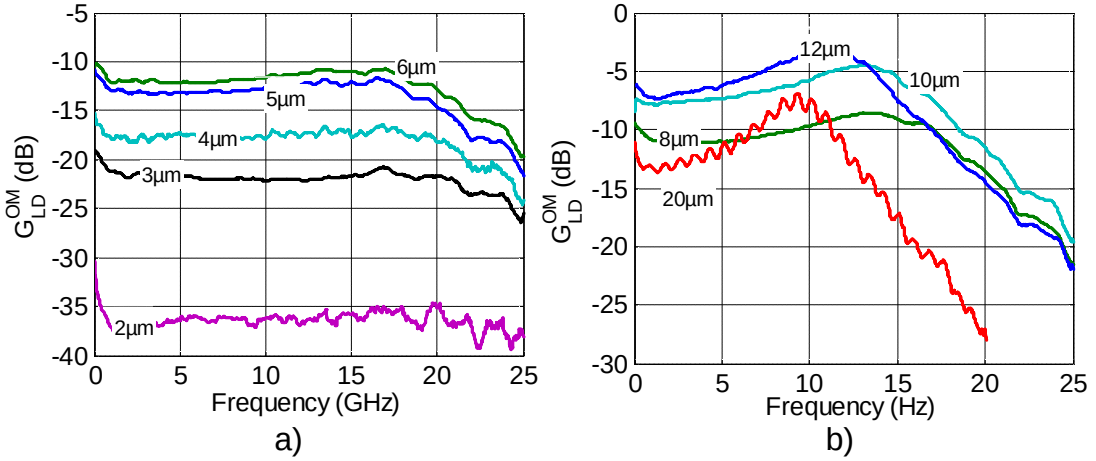

Figure VI-8 – VCSEL OM gain frequency response extraction (DC2OP) for different VCSEL aperture diameters and correspondent bias current in the linear region of the LI curve: a) 2, 3, 4, 5 µm; b) 6, 8, 10, 12 and 20 µm.

The dynamic characteristics are given in Table VI.2 for the different VCSEL diameter sizes in terms of the OM laser gain before resonance, extracted from the link measurement, and the cut-off frequency using the reference NFPD.

Table VI.2 – Dynamic VCSEL Parameters extracted using the reference NFPD (DC2OP)

Size	OM Gain*	I_{bias}	J_{bias}	f_{3dB}
µm	dB	mA	kA/cm^2	(GHz)
2	-36	2	15.9	>25
3	-21.8	2	7.07	>24.3
4	-18.1	3	5.97	23.7
5	-13.26	4	5.09	21.6
6	-12.08	5	4.42	21.29
8* (Standard)	-10.17	8	3.98	12.31
8	-10.8	8	3.98	20.2
10	-7.8	10	3.18	19.5
12	-7.3	10	2.21	17.2
20	-13.43	20	1.59	14.4

*including the optical probe optical coupling losses (alignment and insertion losses - 1 dB measured for the 8 µm diameter size)

The cut-off frequency, as expected, increases with the VCSEL size decrease (the active volume reduced). It reaches up to more than 25 GHz with a size of 2 µm aperture. However, the measurement may also be limited by the photodector, as its response is flat up to 25 GHz only. At such an aperture size, the VCSEL has very low opto-microwave gain, i.e. low slope efficiency. The OM gain increases with size, corresponding to the increase of the laser slope efficiency making this device less attractive. However, with a 20 µm aperture diameter VCSEL, the coupling efficiency is reduced because of the large difference between the emitted light spot and the fiber lens diameter. When we compare the 10 µm with 20 µm aperture size in terms of slope efficiency, they are equally which means that they should have the same OM gain. However 5.6 dB OM gain difference can be attributed to the increase coupling losses of the 20 µm size compared to the 10 µm aperture diameter. Therefore, adding the -1 dB OM gain of the optical losses founded on the 8 µm aperture diameter VCSEL (assumption that is the same for the 10 µm size VCSEL) we can estimate the total optical coupling losses of 6.6 dB corresponding to 47 % optical coupling efficiency for the largest VCSEL device. The cut-off frequency is reduced to 14 GHz for the larger aperture size. So a compromise between the size and the dynamic performances must be done depending on the targeted application (Figure VI-9).

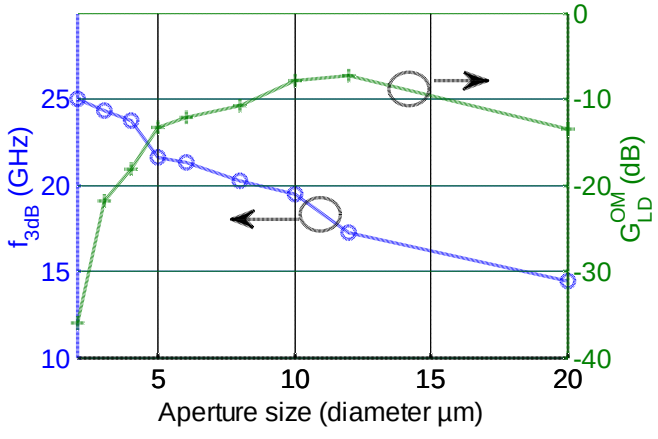

Figure VI-9 – Cut-off frequency (◦) and OM laser gain (+) as a function of the optical aperture size.

The smallest devices are very fast, but with low gain and induce tremendous challenges on the optical packaging and on the optical alignment precision. The largest devices facilitate the light coupling, providing higher gain, but increasing the consumption and decreasing the cut-off frequency. The VCSEL device bias condition is important also. It was demonstrated that operating at current densities below 10 kA/cm² ensures a viable device reliability and long-term stability based on industry certification specifications [176] [177]. In our case, only the smallest device (2 µm) does not fulfill this guideline.

VI.A.4. Synthesis

Static and RF characterizations were done as a function of the VCSEL optical aperture diameter in order to understand the VCSEL performances in terms of the layout size. A trade-off must be done between of speed, size and OM gain. The RF access transmission lines designed proved to be efficient, maintain the impedance up to the pad improving the reflection losses lower than -15 dB up to 20 GHz. For the future 20 GHz RoF applications and beyond, the VCSEL size diameter must be lower than 8 µm. The two smallest devices (2 and 3 µm) present a low slope efficiency (lower than 0.5 W/A) and high coupling losses revealing a very low OM gain. Therefore, only 3 device candidates: 4, 5 and 6 µm aperture diameters are eligible. Here the choice is between the fastest device and the one which has the highest coupling efficiency. The 4 µm aperture diameter is preferred for two main reasons: first its high-speed performance, with almost 24 GHz cut-off frequency; and its higher input reflection that could be optimized adding a passive reactive matching network. Therefore, the choice criteria were the fastest and with best potential performances after integration and optical coupling.

VI.A.5. Focused study on the 4 µm aperture diameter VCSEL

The VCSEL device with a diameter of 4 µm was chosen to be the next candidate for the future ORIGIN TOSA generation. The measurements include the static and RF characteristics and provide the noise behavior and nonlinearities (after extraction of the photodiode parameter extracted). Finally, we simulate the influence of a passive matching network at the device input feeding.

VI.A.5.1 Static Performances

Figure VI-10 a) shows the LIV curve and the slope efficiency as a function of the bias current of a VCSEL with 4 µm optical aperture diameter. The saturation is now around 4 mA with the

power up to 1.85 mW as seen in Figure VI-2. Comparing with standard 8 µm aperture diameter VCSEL, the power is half reduced as its aperture size. The slope efficiency as a function of the bias current has a maximum value of 0.55 W/A at bias current slightly above threshold. Increasing the bias current, SLD reduces progressively because of the thermal and divergence effects (Figure VI-10 b)).

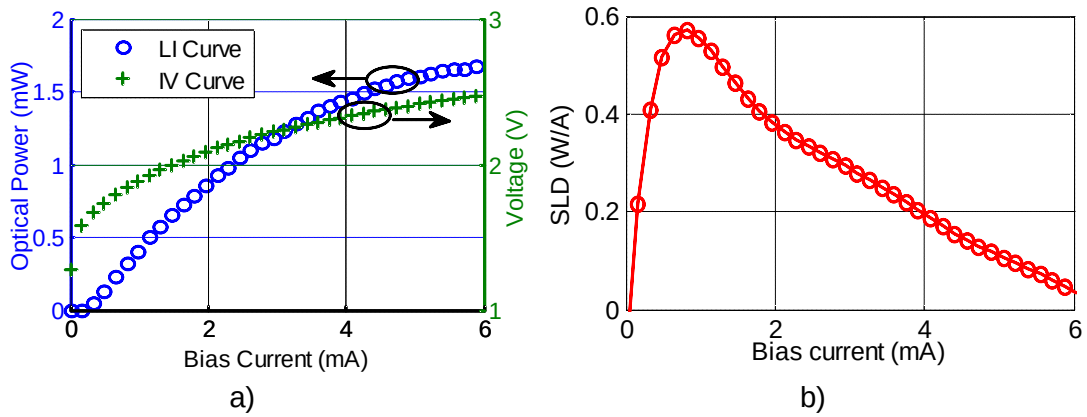

Figure VI-10 – Static characteristics of the 4 µm aperture diameter VCSEL using DC2OP measurement configuration: a) LIV Curves; b) Slope efficiency (S_{LD}) as a function of the bias current.

VI.A.5.2 Dynamic Small-Signal response

The laser OM gain (-18.1 dB) is 8 dB lower than the standard 8 µm aperture diameter ULM VCSEL (-10.1 dB), as depicted in Figure VI-11 a). These results can be explained by higher losses on the optical coupling, lower slope efficiency and higher input mismatch. A bias current increase reduces the OM Gain slope efficiency mainly by thermal effects. We detect a strong relaxation oscillation frequency effect on the frequency response at 1 mA and for higher bias current, the response is flat. A frequency bandwidth up to 24 GHz is achieved. The input reflection coefficient shown in Figure VI-11 b) is not near the Smith chart center, corresponding to the matching impedance.

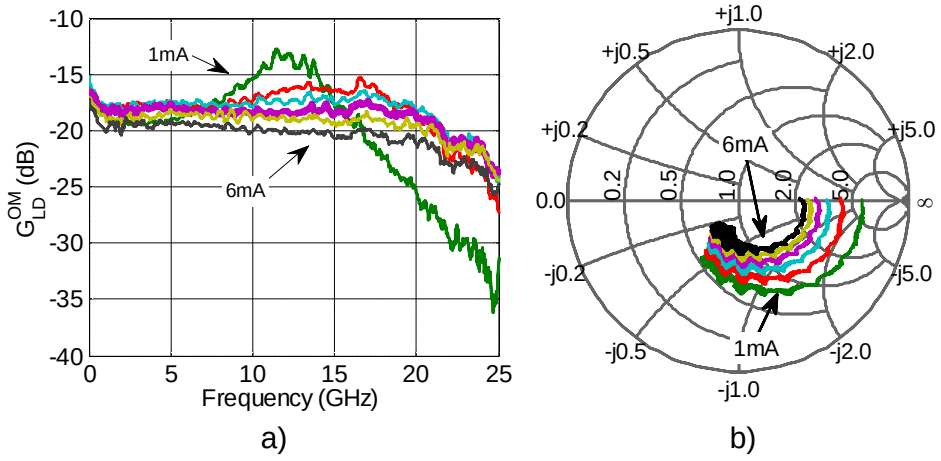

Figure VI-11 – Frequency response of the 4 µm aperture diameter VCSEL using NFPD as a reference photodiode: a) laser OM gain as a function of the frequency; b) Input reflection coefficient - S11 (for different bias currents: 1, 2, 3, 4, 5 and 6 mA)

VI.A.5.3 Noise Behavior

The RIN measurement for different bias currents is shown in Figure VI-12. For currents higher than 4 mA the RIN is lower than -140 dB/Hz at a frequency above 6 GHz, which can be interesting for analogue applications. At low frequency, oscillations on the noise curve increase from 1 mA to 2 mA and then reduce as we increase the bias current. This can be explained by the laser multimodes behavior as a function of the bias current. In any case we can predict that the best performances are achieved at a frequency above 6 GHz for 4 µm aperture, and 4 GHz for 8 µm aperture diameter standard 10 Gbps VCSEL.

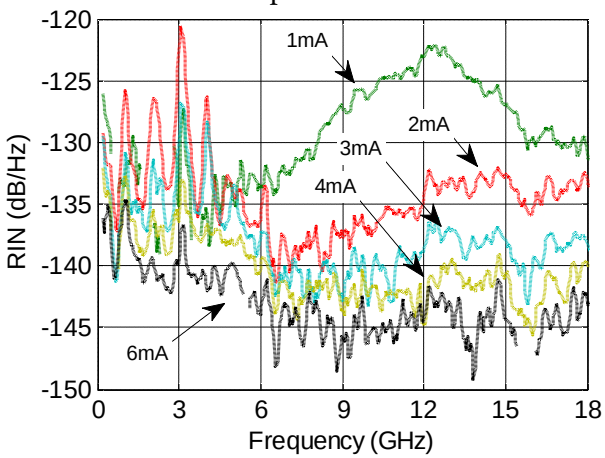

Figure VI-12 – 4 µm VCSEL RIN response as a function of the frequency for different bias currents: 1, 2, 3, 4 and 6 mA

VI.A.5.4 Dynamic Large-Signal Response - Nonlinearities

The Figure VI-13 a) gives the OM input compression gain power point measurement of the laser. The measurement was performed up to 20 GHz with a variable bias current from 1 mA to 3 mA. We can observe that the VCSEL can handle high power up to 11 dBm for bias currents higher than 3 mA and frequency higher than 7 GHz. Currents lower than 2 mA should be avoided on all frequency range as the relaxation oscillation frequency limits the device linearity. Operation frequency lower than 4 GHz should be avoided for bias current lower than 3 mA since the compression point is affected, probably related by the same reasons.

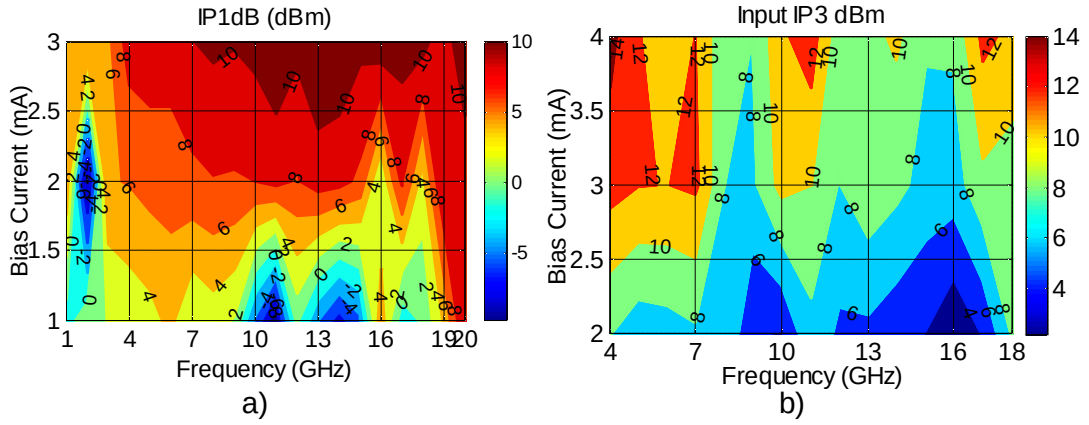

Figure VI-13 – VCSEL nonlinearities: a) Input gain compression as a function of the frequency for different bias currents; b) Input IP3 as a function of the frequency for different bias currents

The Figure VI-13 b) shows the input OM IP3 of the laser in the frequency range [4-18 GHz]. The bandwidth is defined by the specifications of the RF combiner of the test setup and the RF generator limits. A maximum OM IIP3 value up to 14 dBm was reached at 4 GHz with 4 mA. The IP3 results follow the P1dB shape: A bias current increase improves the input power point and the linearity, too.

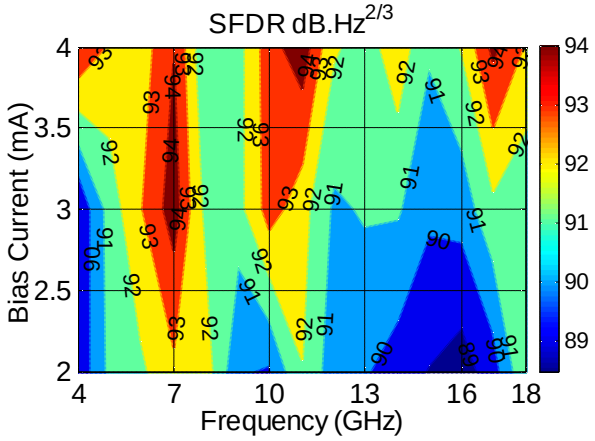

Figure VI-14 – VCSEL OM SFDR as a function of the frequency for different bias currents

The OM SFDR was computed and is presented in Figure VI-14 as a function of the bias current (2-4 mA) and the frequency (4-18 GHz). An increase of the bias current improves SFDR up to 94 dB.Hz$^{2/3}$. Compared to the standard 8 µm aperture diameter ULM 10 Gbps VCSEL (Figure III-18 and Figure III-20) the obtained IIP3, IP1dB and SFDR are 3 to 4 dB lower, but for frequencies higher and bias current much lower, which corresponds to lower consumption.

VI.A.5.5 Electrical interconnection matching

The difference between the VCSEL OM gain under 50 Ω and its available OM gain is given in Figure VI-15 as a function of the frequency. The 4 µm aperture diameter VCSEL is compared with other sizes: 2, 6, 8 µm. The 8 µm VCSEL is compared to the standard 10 Gbps. As we decrease the size we increase the improvement from available gain of the VCSEL input. This

curve shows that for a 2 µm VCSEL, one can improve the OM gain of the VCSEL by 4 dB up to 10 GHz with a matching network.

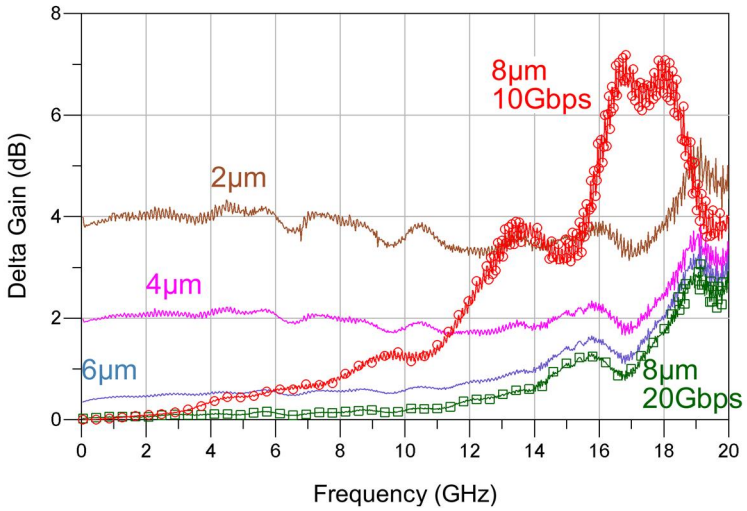

Figure VI-15 – Available improvement to the OM gain of the modified VCSELs as a function of the frequency for different aperture diameter (bias conditions given in Table VI.2). The standard 10Gbps VCSELs is also measured.

Comparing both devices of 8 µm we see clearly an improvement on the 20 Gbps modified VCSEL in terms of the input impedance at high frequency, which thus do not require any matching network to be improved. This is given mainly by the optimized stack layer by ULM Photonics and the access transmission line modification, as discussed previously. The 4 µm size VCSEL shows around 2 dB of available gain improvement, over the whole frequency range. We will try to achieve this gain improvement by using the pi interconnection structure, presented in Chapter V, section V.A.2. The matching network is designed with SMT components that are limited by their Self-Oscillation Frequency. Devices with an SFR of 15 GHz are selected. Therefore the center frequency is fixed to 10 GHz, corresponding to twice the previous operation frequency. A pi-network structure used in the simulation is: SMT1- 0.3 nH; SMT2 – 0.7 pF; SMT3 – 0.6 pH.

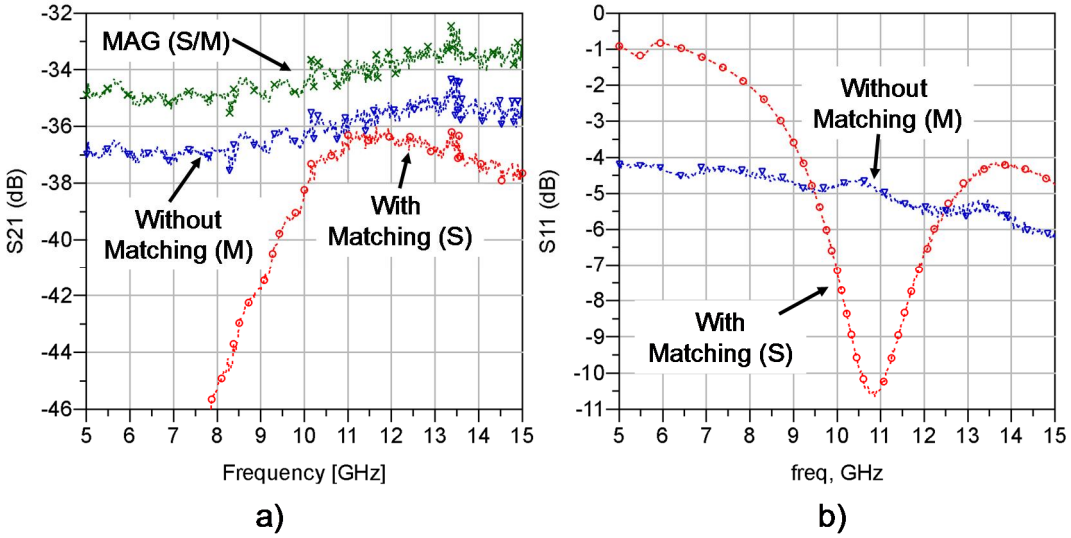

Figure VI-16 – Frequency response using the 4 µm aperture diameter VCSEL and the reference photodiode: a) Link gain Δ – raw measurement without matching network, ◦ - simulation with matching network., x – Maximum Available Gain (considering only the VCSEL port); b) Reflection coefficient with and without matching.

The results are presented in Figure VI-16 showing the matching network simulation compared to the raw 50 Ω measurement (without matching). Figure VI-16 a) compares the link gain, using the reference photodiode, for both configurations (with and without matching network) and presents the maximum available gain from the link with matching the VCSEL. The available gain shows a potential improvement by 2 dB compared to the raw VCSEL gain. However, the simulated matched structure fails to achieve this improvement. This is explained by the RF platform transmission lines and the SMT components losses. The wideband matching is difficult even using a π-network structure. Another difficulty is the inductor and the capacitor configuration which cannot be changed because of the biasing input. Although, the available gain proves that we can improve the VCSEL gain by 2 dB, another method must be used to achieve such a matching. For instance by using integrated matching circuits.

VI.A.5.6 Synthesis

Complete characterization was performed from the static to the nonlinearity performances on the 4 µm aperture diameter VCSEL. It presents a slope efficiency up to 0.3 W/A at 3 mA, that allows good dynamic performances such as OM gain with equal to -18.1 dB and a 3dB cut-off frequency of 24 GHz. Comparing to the state-of-the-art on 850 nm GaAs-based VCSELs we found modulation bandwidth equal to the fastest VCSEL [98] found in the literature with InGaAs-based quantum wells and aperture size of 8µm (bit rates up to 57 Gbit/s in B2B configuration with no effort for temperature control as well but with Anti-Reflection coated lens package to improve the coupling into the fiber). We though believe on the great potential of our 4 µm aperture diameter 850 nm VCSEL GaAs-based. Indeed, our results, clearly, could be improved applying better thermal dissipation and increasing the coupling efficiency. RIN measurement shows laser potential above 6 GHz with a noise lower than -140 dB/Hz for a bias current higher than 3 mA. In terms of laser nonlinearities, the opto-microwave input P1dB was measured up to 10 dBm and the opto-microwave input IP3 up to 14 dBm. From these results we

found an opto-microwave SFDR up to 94 dB.Hz$^{2/3}$. Regarding the input reflection coefficient, we proved that we can improve the VCSEL gain by 2 dB, but another method must be used to match this device, for instance by using integrated circuits.

The 4 μm aperture diameter VCSEL was proved to be an interesting candidate with a lot of potential of the 20 GHz analogue applications and 3 main directions for improvement can be pursued: better thermal dissipation management; increased coupling efficiency; electrical matching improvement.

VI.B. Optical coupling techniques for optoelectronic devices

The optical interface structure has two main challenges: to maximize the coupling efficiency and to improve the misalignment tolerance. Of course the cost and the time of production are important too. Typically, optical packaging techniques use an active alignment procedure where the optoelectronic device is turned on. It can be very precise (~1 μm) but with some constraints in terms of packaging time and the necessity to realize a test setup with contact connections to bias the device. Another method is the passive alignment technique (pick-and-place) where there is no need to turn on the optoelectronic device, but in this case all the physical dimensions and position must be known. The alignment precision is lower than the active method (~10 μm). The advantages are the realization time and eventually the collective production possible onto an entire wafer, but yet for large VCSEL, multimode and coupling efficiencies below 70 %.

An important parameter of the optical interface is the coupling efficiency, which requires simulation and optimization. The simulation of light propagation in arbitrary waveguide structures is the first step to understand the light transmission effect on those structures. The simulation not only gives a start point in evaluating the performances before the fabrication, but it also allows parameter optimization. Unfortunately, the simulation is performed in a quasi-ideal environment, so it is very difficult to take into account all parameters and effects. Another drawback is the simulation time, which imposes certain approximations. Therefore the effective implementation and characterization of the structure are included, when possible, to validate the simulation results.

We are interested to study and simulate two optical coupling techniques: the ball lens optical coupling technique (home-made TOSA and ROSA) and an innovative technique that we proposed based on the vertical optical waveguide. Both techniques can either couple the VCSEL or the photodetector to a MM fiber.

The first subsection presents the simulation method which is based on the Beam Propagation Method where the simulation criteria and limitation conditions are exposed. The second subsection will work out the ball lens technique developed by the ORIGIN partner INNOPTICS. It is simulated to couple a photodetector using different sizes, and is compared to data extracted from measurements.

The last subsection presents the proposed innovative technique that is patented [15]. It targets to couple a compact photodetector to a MM fiber or a MM fiber to a VCSEL using a passive and collective coupling method. Its capability to couple them to a SM fiber will not be discussed here.

VI.B.1. Beam Propagation Method

The performed simulations are based on the Beam Propagation Method (BPM) which approximates the exact wave equation for a monochromatic propagation to compute how light propagates on a certain medium. We used BeamPROP™ which is a simulation engine from RSoft Photonics Suite and which is based on advanced Finite-Difference BPM approach. This technique uses finite difference methods (FDM) to solve the well-known parabolic or paraxial

approximation of the Helmholtz equations. BPM has been one of the most popular approaches used in the modeling and simulation of electromagnetic wave propagation in guided-wave optoelectronics and fiber-optic devices [178]-[182].

VI.B.1.1 Basic principals

A simulation of the light wave propagation in an arbitrary medium can be done rigorously by solving Maxwell's equations. However, solving these equations analytically is particularly difficult. Finding the exact analytical solutions for wave propagation in waveguide structures can be done only for a limited number of simple structures such as step-index slab waveguides and fibers. For more sophisticated structures, which cannot be solved analytically, numerical treatments may be feasible where a simplification of Maxwell's equation is needed to have an efficient and fast solution. One simplification is to use the well-known simplified version of Maxwell's equations with certain assumptions - the Helmholtz equations.

With assumptions that we are using a homogeneous medium, lossless dielectric medium, linear medium, isotropic medium and $e^{j\omega t}$ time dependence, the Maxwell's equations are given, in terms of the electric field E and magnetic field H, by:

$$\nabla \times E = -j\omega\mu_0 \frac{\partial \vec{H}}{\partial t} \tag{6.6}$$

$$\nabla \times \vec{H} = j\omega\varepsilon_0 n^2 \frac{\partial \vec{E}}{\partial t} \tag{6.7}$$

and

$$\nabla \cdot \left(n^2 E\right) = 0 \tag{6.8}$$

$$\nabla \cdot H = 0 \tag{6.9}$$

with ε_0 and μ_0 being the permittivity and permeability of the vacuum, respectively. The n=n(x, y, z) is the refractive index of the medium.

By taking the curl of Eq. (6.6) and using Eq. (6.7), we obtain the vectorial wave equation for the electric field, or the magnetic field, as follows:

$$\vec{\nabla} \times \left[\vec{\nabla} \times \vec{E}\right] - n^2 k^2 \vec{E} = 0 \tag{6.10}$$

where $k = \omega\sqrt{\varepsilon_0\mu_0}$ is the wave number in free-space. By using the identity given by

$$\vec{\nabla} \times \left[\vec{\nabla} \times \vec{f}\right] = \vec{\nabla}\left(\vec{\nabla} \cdot \vec{f}\right) - \vec{\nabla}^2 \cdot \vec{f} \tag{6.11}$$

The Eq. (6.10) can be written by

$$\vec{\nabla}^2 \cdot \vec{E} + n^2 k^2 \vec{E} = \vec{\nabla}\left(\vec{\nabla} \cdot \vec{E}\right) \tag{6.12}$$

If we consider the transverse component ($_t$) of the electrical field we can write

$$\vec{\nabla}_t^2 \cdot \vec{E}_t + n^2 k^2 \vec{E}_t = \vec{\nabla}_t \left(\vec{\nabla}_t \cdot \vec{E}_t + \frac{\partial \vec{E}_z}{\partial z}\right) \tag{6.13}$$

Furthermore, using Eq. (6.8)

$$\vec{\nabla}_t \cdot \left(n^2 \vec{E}_t\right) + \frac{\partial n^2}{\partial z} \vec{E}_z + n^2 \frac{\partial \vec{E}_z}{\partial z} = 0 \tag{6.14}$$

If the refractive index varies slowly along z, then the $\left(\partial n^2/\partial z\right)\vec{E}_z$ may be neglected.

Thus from Eq. (6.14) we obtain the equation for uniform (or z-invariant) structures as follows:

$$\frac{\partial \vec{E}_z}{\partial z} \approx -\frac{1}{n^2}\vec{\nabla}_t \cdot \left(n^2 \vec{E}_t\right) \tag{6.15}$$

And finally by substituting Eq. (6.15) into Eq. (6.13), we obtain the vectorial Helmholtz equation based on the transverse electrical field:

$$\vec{\nabla}_t^2 \cdot \vec{E}_t + n^2 k^2 \vec{E}_t = \vec{\nabla}_t \left(\vec{\nabla}_t \cdot \vec{E}_t - \frac{1}{n^2}\vec{\nabla}_t \cdot \left(n^2 \vec{E}_t\right)\right) \tag{6.16}$$

If we assume the restrictions of a scalar field (i.e. neglecting polarization effects) and paraxiality (i.e. propagation restricted to a narrow range of angles), the wave Eq. (6.16) for monochromatic waves can be written by the scalar Helmholtz equation [178]:

$$\frac{\partial^2 \phi}{\partial x^2} + \frac{\partial^2 \phi}{\partial y^2} + \frac{\partial^2 \phi}{\partial z^2} + k^2 n(x,y,z)^2 \phi = 0 \tag{6.17}$$

Where the scalar electric field is written as $E(x,y,z,t) = \phi(x,y,z)e^{j\omega t}$.The geometry of the problem is given by the refractive index distribution given by n(x, y, z).

After some mathematical rearrangements we can find the basic BPM equation representing a parabolic partial differential equation that is integrated forward in z using the finite-difference approach (FD-BPM) [178].

VI.B.1.2 Method Limitations

The assumptions made on the previous BPM approach lead to 3 main limitations which were developed on the BeamPROP simulator given by:

- Removing paraxiality: the paraxiality restriction on the BPM was relaxed on BeamPROP through the use of extensions that have been referred to as wide-angle BPM [178] [186]-[189].The essential idea behind this approach is to reduce the paraxial limitations by incorporating the effect of the $\partial^2 u/\partial z^2$ term that was neglected in the derivation of the basic BPM.
- Including polarization: the BeamPROP includes Polarization effects by recognizing that the electric field E is a vector, and starting the derivation from the vector wave equation rather than the scalar Helmholtz equation [178] [190] [191].
- Handling Reflections: the BPM approach described previously can not account for backward reflections since the one-way wave equation on which it is based does not admit both positive and negative traveling waves. BeamPROP has a bidirectional BPM algorithm as described in [178] [192] which considers coupled forward and backward traveling waves, and can account for reflection phenomenon, including resonant effects as found in grating structures.

VI.B.1.3 Optical coupling simulation conditions

Our goal is to simulate a simple coupling efficiency between a MMF fiber and various coupling structures. The shape and the dimensions of the coupling structure are to be optimized to maximize the power transmitted from the fiber to the optoelectronic device (HPT photodetector) or on the other way round from the VCSEL to the fiber.

BeamPROP Simulation conditions are:

Since the BeamPROP solves for the electromagnetic fields within a given structure within a computational domain on a spatial grid, it is important to define this grid properly to ensure correct results. It is critical to perform a convergence study on the X, Y and Z grid sizes to optimize the tradeoff between speed and accuracy. To perform this convergence study, we used the scanning capabilities of MOST, RSoft's scanning and optimization tool. The scan results show, as expected, that as the grid size decrease the results converge to a particular solution. The grid size for X, Y and z was chosen to be 0.125 μm providing a good compromise between convergence and simulation time.

Another parameter defined was the boundary conditions which defines how the field behaves at the boundaries of the selected domain. By default, we used the option Full Transparent Boundary Conditions (TBC). This type of boundary is designed to let radiation pass through the boundary without reflection back into the simulation domain.

BeamPROP includes many options that control how polarization is handled, including scalar calculations, TE, TM, quasi-TE, quasi-TM, semi-vector, and full-vector options. To get the most accurate results we decided to use the full vectorial method which recognizes that the electric field E is a vector, and starting the derivation from the vector wave equation rather than the scalar Helmholtz equation. On the polarization field side, we used TE which determines the polarization of the major component used in the beam propagation calculation (E_x).

The definition of the launch field is another important parameter which defines the initial condition for the simulation. The launch field can be seen as the input excitation mainly characterized by the desired field profile. The goal is to provide the fiber modes coming out of the 50 μm core MMF. Therefore two options were targeted: use the fundamental mode and another using all the modes of the fiber, equally distributed, to study the multimode behavior. The input field is a superposition of all fiber (3D) modes supported by the input component with equal power in each mode and a random phase for each mode.

Monitoring and analysis of simulation results are the last consideration on the simulation settings setup. Since we want to analyze the optical power in a particular region, pathways monitors definition is needed BeamPROP calculates the steady-state optical field throughout an entire design file. It is frequently useful to analyze this field in standard physical quantities such as the optical power in a particular region of the circuit or the power traveling in a particular mode. Pathway monitors are what makes these types of measurements possible. Results are given as a function of the propagation direction Z and are measured along a pathway. Monitors can be used to measure the power in the propagating field via overlap integrals or power integrals, measure the phase of a propagating field relative to a test field, and measure other output such as spot size. We used the option 'partial power' which computes the power in the simulated field via a power integral at the current Z position. The width/height and shape of the integration area can be set manually by the settings which we define to be a 10x10 μm^2, 20x20 μm^2 and 30x30 μm^2 (same as the HPT shape). It computes the total power traveling within the coupling structure.

The default fiber parameters are given in Table VI.3 as extracted from typical the manufacturing companies.

Table VI.3 – Fiber intrinsic parameters

FIBER	MMF	SMF
Core (μm)	50	9
Cladding (μm)	125	125
n_{core}	1.491	1.4700
$n_{cladding}$	1.481	1.4664
Δn (%)	1	0.36
NA (°)	0.2 (11.5)	0.14 (8.5)
Att. (dB/Km)	<2.5	<0.7

The polymer used for the taper simulation is SU-8 with refractive index of 1.584 at 850 nm [193]. This polymer was selected to its transparency at 850 nm wavelength, with low optical losses (0.6 dB/cm) and its thermal conductivity (0.3*1e-6 W/ (μm*K)). SU-8 is a well known material, commonly used in laser coupling [194]-[201].

VI.B.2. Ball lens coupling technique

The ball lens coupling technique developed by the project partner INNOPTICS was presented in Chapter V on the subsection V.A.1 where the mechanical receptacle structure is shown in Figure V-2. To simplify we decide to simulate only the ROSA module optical coupling from the MM fiber to the photodetector. The Figure VI-17 shows the correspondent light path within the mechanical receptacle where the light goes from the MM fiber, on the bottom, to the ball lens and the substrate until reaches the detector at the top. The air gaps are considered and the distance between the MM fiber (ferrule) and the ball lens is optimized.

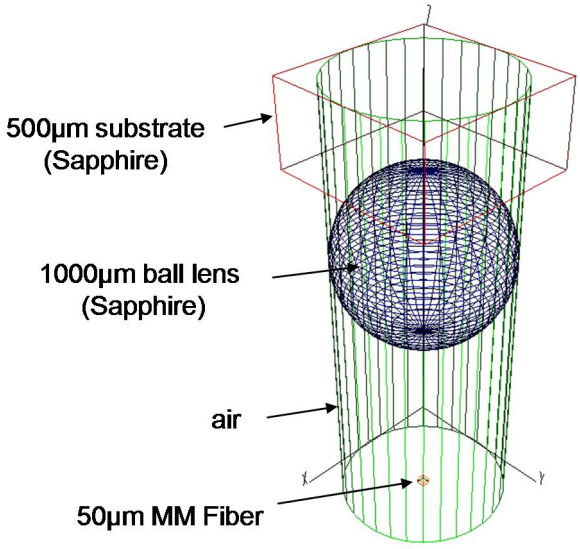

Figure VI-17 – Light path of the ROSA module using the ball lens coupling technique

At the top we consider 3 detector window sizes as discussed previously with 10x10 μm², 20x20 μm² and 30x30 μm² areas.

The Figure VI-18 shows the coupling efficiency of the ball lens coupling method as a function of the distance between the ball and the MMF for different detector sizes (using the fundamental mode). A distance of 1160 µm was implemented on the mechanical receptacle by INNOPTICS. This distance provides an efficiency of 40 % when using an HPT size of 10x10 µm², according to our simulations, which are thus in good correlation with measurements in Chapter V, section V.A.2.2.

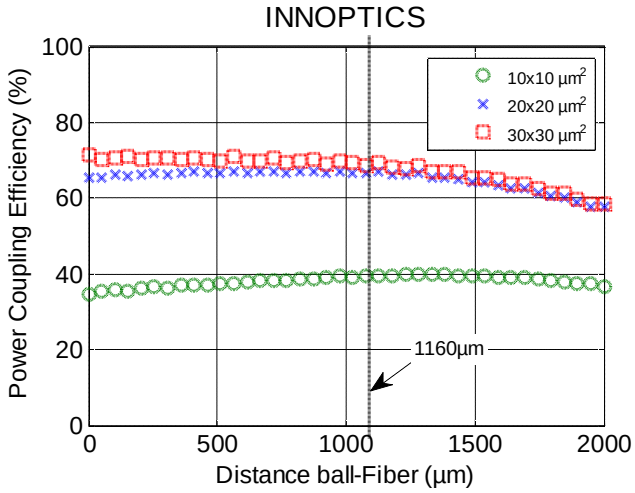

Figure VI-18 – INNOPTICS coupling technique: simulation in terms of power coupling efficiency on the 3 photodetector sizes (10x10, 20x20 and 30x30 µm²)

The 20x20 µm² size simulation has a coupling efficiency of 67 % at 1160 µm distance providing a 4.5 dB improvement in the coupling power efficiency as compared to 10x10 µm² device. For the 30x30 µm² the results are slightly the same as the 20x20 µm² with a 68 % coupling efficiency at 1160 µm distance. The variations between the 10, 20 and 30 squared HPT in terms of coupling efficiency allow us to conclude that for an eventual future solution using this packaging technique and the same laser source (same optical beam condition), the best HPT size is of 20x20 µm². The drawback when using this HPT size comes from its frequency response gain at 5 GHz, which is 3.5 dB lower than the 10 µm squared HPT. The coupling efficiency improvement compared to the 10x10 µm² HPT is of a factor of 1.675, thus 4.48 dB at the electrical output. Therefore, the overall gain in the coupling efficiency appears partially wasted even if still positive.

VI.B.3. Collective and passive optical coupling technique

Contrary to the mechanical receptacle ball lens technique, we propose an intermediate optical coupling structure to enable low optical losses and good tolerance to misalignment where there is no need to turn on the device. This structure is based on polymer (SU-8 for instances) which can be collectively produced by photolithography over an entire wafer. Passive coupling alignment is the target between optoelectronic devices such as VCSELs or phototodetectors and the optical fiber (MM/SM) or other optical waveguides. This structure comprises a tapered waveguide consisting of a transparent material with a refractive index higher than the air (and close to the one of the fiber) allowing to couple the light between the VCSEL surface (or the photodetector) and the optical fiber. This structure also includes an anchoring system that allows to maintain the waveguide in position and to leave an open space for the electrical connections to the VCSEL or the photodetector. The originality of the structure

is to dispose of materials / air interfaces in the light path to guide and reduce the opening of the output optical beam that theoretically allows better coupling angle performance.

The coupling structure is presented in Figure VI-19 where three main parts can be found:
The vertical taper waveguide 12 assures the optical coupling between the optoelectronic devices 3 and the fiber core 2.
The anchoring system 15 of the coupling structure.
The holder arms 152 supporting the waveguide 12 to anchoring system 15.

As the element 2 is an optical fiber, the coupling structure 1 can be completed by a fiber supporting and alignment structure 17.

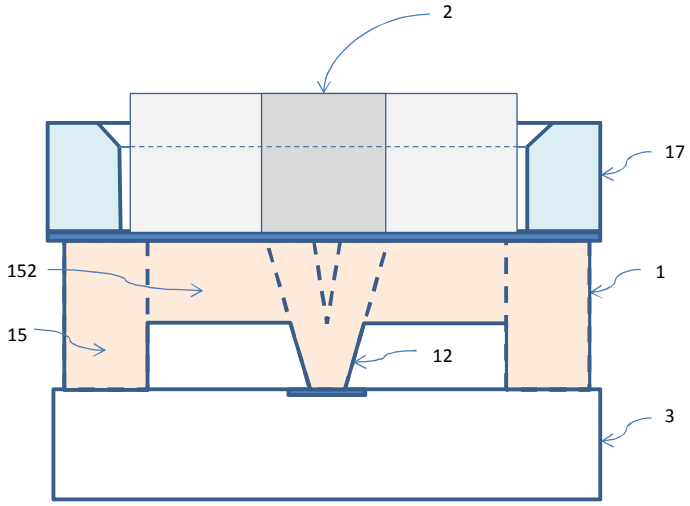

Figure VI-19 – Schematic structure of the system coupling: – profile view

The mechanical receptacle based on the ball lens gives us a reference coupling efficiency of 40 % on the ROSA module when a SiGe HPT is used with 10 µm squared size. In the case of the TOSA module the reference is 60 % when 8 µm aperture diameter GaAs VCSEL was used. For all the results achieved on the TOSA side, we can say that the challenging here goes for the optical coupling on the photodetector side (ROSA).

The coupling structure is acting as an optical waveguide taper using a polymer with variable sizes and shapes depending on the optoelectronic device size and light properties. Two different configurations are considered in the following: Optical coupling between a VCSEL with 8 µm optical aperture diameter and a MMF with 50 µm core size; Optical coupling between the MMF with 50 µm core size and a photodetector (HPT) with 10 µm squared optical window. The complete coupling system could be designed collectively on the substrate of the optoelectronic devices, allowing an integrated and packaged system (Figure VI-20). Coupling to a single mode fiber with 9 µm core diameter size is a direction of further work.

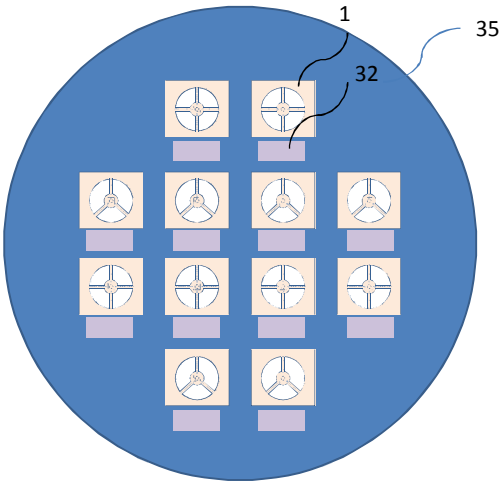

Figure VI-20 – Illustration a collective production of the coupling structure on VCSEL 2D array.

The Figure VI-20 shows the electrical interconnection illustration on wafer with an array of VCSELs. The coupling structure 1 and the anchoring system 15 will not superpose the electrical contact, zone 32, of the optoelectronic device to package. The electrodes are outside the anchoring zone by electrical contact stretching (transmission lines and pads) or by anchoring structure optimization as represented in the illustration.

VI.B.3.1 Coupling simulation for a 10x10 µm² detector and a MM fiber

We focus, in this section, on the simulation and optimization of the coupling structures between a 10x10 µm² detector and a MMF. Intuitively, we consider a truncated conic shape with a circular or squared cross section as sketched in Figure VI-21.

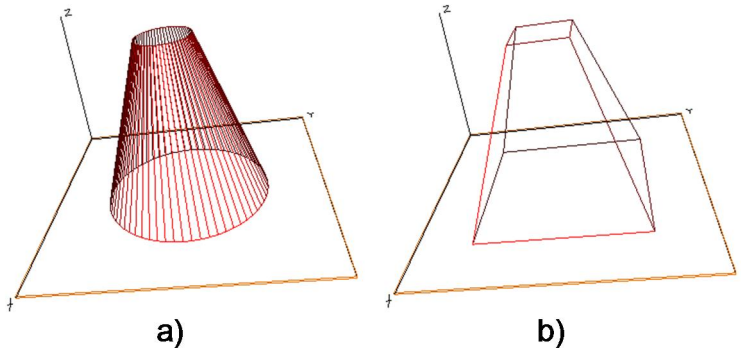

Figure VI-21 – BeamPROP waveguide taper design: Taper shape: a) Circular taper; b) Squared shape

The monitor created, so that the coupling can be measured, is a 10x10 µm² window which defines a squared cross-section within which the optical power is computed. This value tries to approach the real 10x10 µm² squared HPT which is our focus here. The results are shown in Figure VI-22, it can be seen that the total power being guided in the waveguide is about 22 % of the incident power at the waveguide input (Z=0) and increases to 79 % at Z=20 µm.

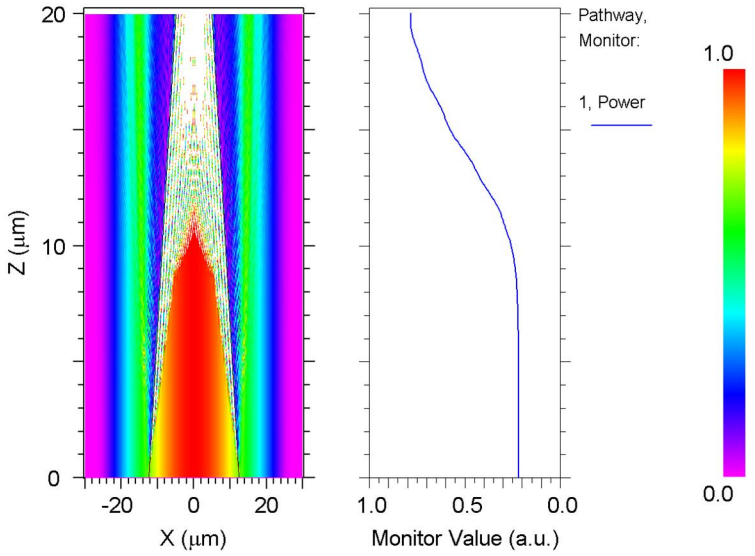

Figure VI-22 – Example of the propagation field during simulation as a function of the length (Z=20 µm)

The conic shape should provide us a robust coupling on the alignment rate efficiency. Two considerations were made in terms of the output shape: Figure VI-21 a) - circular to match with the optical fiber; Figure VI-21 b) - squared shape to match with the HPT shape. The cone base is in contact with the core of the fiber. The truncated side of the cone is in contact with the detector. We consider a fixed dimension for it of 10 µm size, while we vary the dimensions of the base and the cone height. Figure VI-23 shows the simulation results on the power coupling efficiency using circular section with the base width varying from 10 to 35 µm and with the length from 20 to 35 µm. The simulation dimension ranges were adapted to the process technology available.

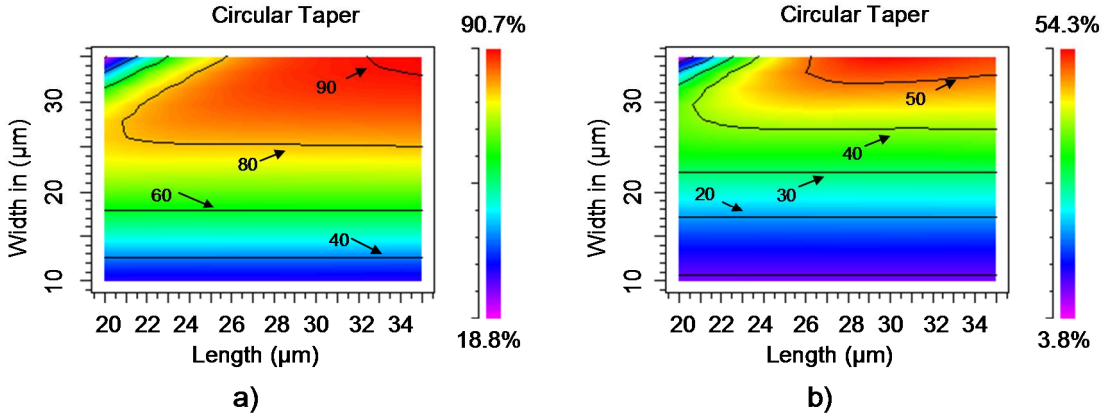

Figure VI-23 – Waveguide simulation as a function of the cone base width and length using circular taper shape: a) fundamental mode simulation; b) multimode simulation (all modes)

Figure VI-23 a) shows the simulation results considering only the fundamental mode of the fiber. The coupling efficiency could range above 90 %, and is above the 80% for a large range of values. One specific set includes a height and width of 25 µm each. Figure VI-23 b) shows the results where all modes of the fiber are distributed equally. The coupling efficiency is lower and goes up to 54.3 %. It is above 40 % with a width of 30 µm and height of 25 µm, e.g.

The results using the squared taper shape are presented in Figure VI-24 using the fundamental mode a) and the multimode operation b). The results are slightly better in both cases.

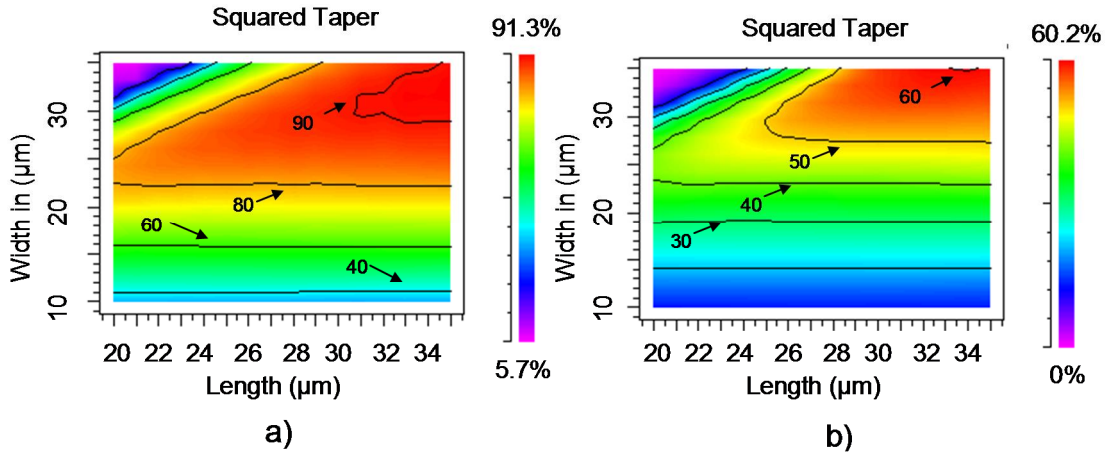

Figure VI-24 – Waveguide simulation as a function of the cone base width and the length using squared taper shape: a) fundamental mode simulation; b) multimode simulation (all modes)

From those results we decided to choose the length of 25 µm and base width of 25 µm (width_in) to simulate the fiber-waveguide misalignment coupling. Those values were chosen considering the process technology possibilities. The results are presented in Figure VI-25 for both shapes and launch field types (fundamental mode or all modes equally distributed) shifting the MMF position from —40 µm to +40 µm to the nominal position. The squared taper shows, as expected, better results on the fundamental mode with 83 % as compared to 79 % with circular shape exactly positioned in the middle where the fiber is completely aligned with the taper. The shape of the simulation curve using all the modes, shows that most of the modes propagate in the border of the 50 µm fiber core.

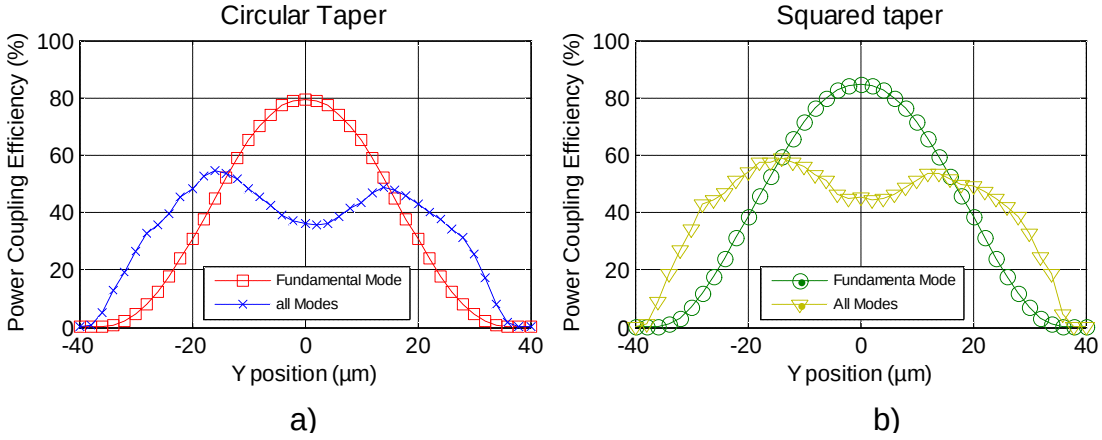

Figure VI-25 – Fiber to Waveguide alignment simulation as a function of the y fiber position: a) circular taper shape; b) squared taper shape (base width and length equal to 25 µm)

These results indicate a tolerance to misalignment up to ± 20 µm in all injection conditions, thus ensuring the technique to be passive.

VI.B.3.2 Coupling simulation for a 8 µm diameter VCSEL and SM/MM fiber

This section focuses on the coupling of a high speed 8 µm aperture diameter VCSEL to a SM or MM fiber. The first step was to recreate the VCSEL output modes which correspond to the divergence angle of the beam. To simplify our work we simulate only the fundamental mode represented by 8 µm-diameter Gaussian beam with a 25° divergence ($1/e^2$) given by a typical VCSEL, as depicted in Figure VI-26. This option was implemented by a launch field Gaussian type, corresponding to an input Gaussian field as:

$$f(x,y) = e^{\left(-x^2/a^2\right)} \cdot e^{\left(-y^2/b^2\right)} \tag{6.18}$$

where a=w/2, b=h/2, and w and h are the 1/e width/height of the Gaussian function which are set to 1.45 µm. These dimensions were optimized to recreate the 25° of divergence ($1/e^2$). By default, the Gaussian field is launched from the waist, but an offset of 10 µm was introduced, as depicted in Figure VI-26 a). The last 2 µm were implemented with a gold (au) ring with 8 µm diameter, which pretended to recreate the VCSEL output interface, as depicted in Figure II-13. The Figure VI-26 b) represents the transverse field at Z=10 µm corresponding to the VCSEL output fundamental mode with 8 µm aperture diameter.

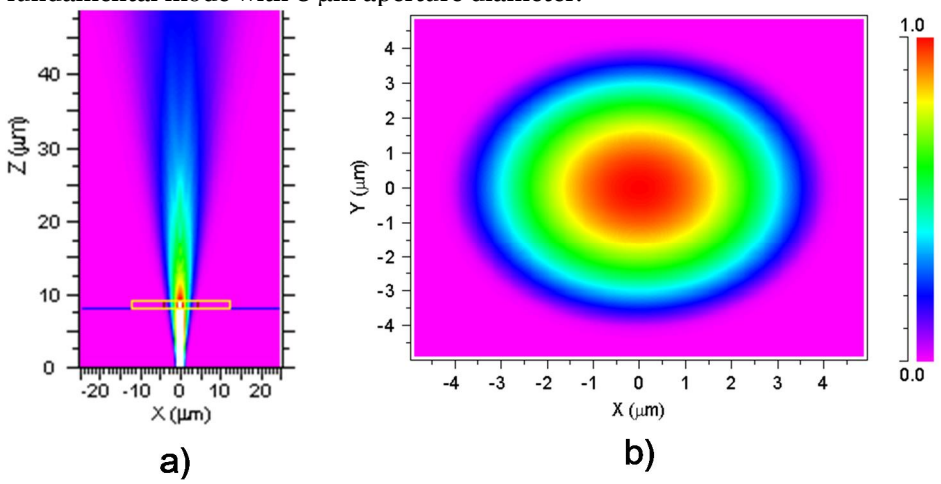

Figure VI-26 – Output VCSEL fundamental transverse mode simulation (8 µm aperture diameter and divergence of 25°): a) lateral view; b) top view (Z=10 µm)

With some trigonometric equations, we can demonstrate that 86 % of the beam intensity emitted from the VCSEL surface is injected in the MMF if it is placed at 45 µm from the surface, as depicted in Figure VI-27.

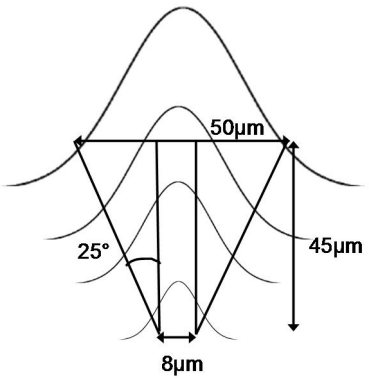

Figure VI-27 – Output Gaussian beam propagation width 25° divergence

The optical power emitted by a VCSEL was measured on wafer using a lens optical probe positioned at approximately 50 µm from the surface. We measured 79 % coupling efficiency, which is quite close to the simulated value. The mode shape measured given in Figure III-27 was imported into the simulator to compare with the mode created by the simulation. Figure VI-28 shows the measurement (VCSEL mapping) compared to the simulation, both were done at 50 µm height (Z) from the VCSEL surface.

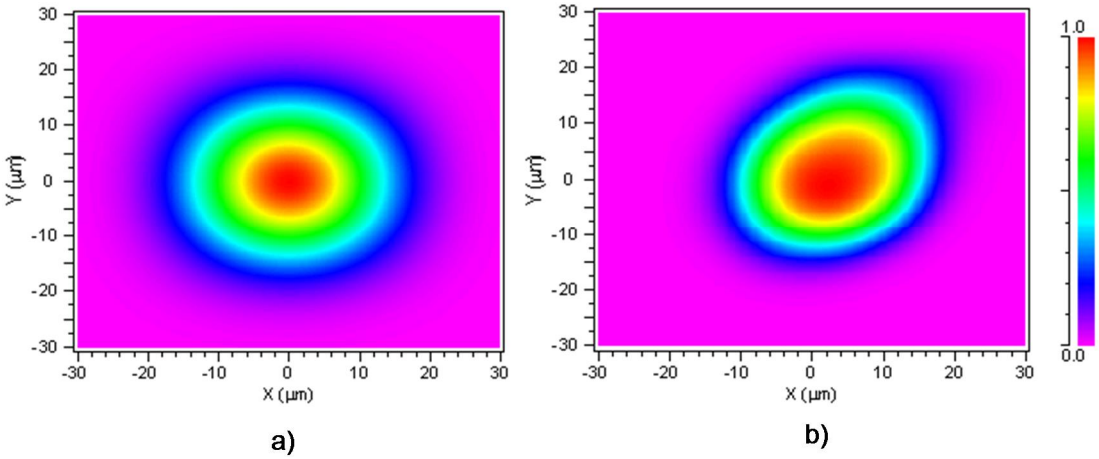

Figure VI-28 – Output VCSEL transverse mode: a) Simulation at Z=60 µm (10+50 µm); b) Measurement at Z=50 µm height (see Chapter III section III.A.7)

It shows good agreement between them with slight difference in the VCSEL beam shape, the measurement shape is more elliptical. This measurement results can be imported into the simulator providing more accurate simulation results (further work).

The waveguide structure, connecting the output VCSEL surface to the MMF input, used for simulation was a simple cylinder with 10 µm-diameter using the SU-8 polymer.

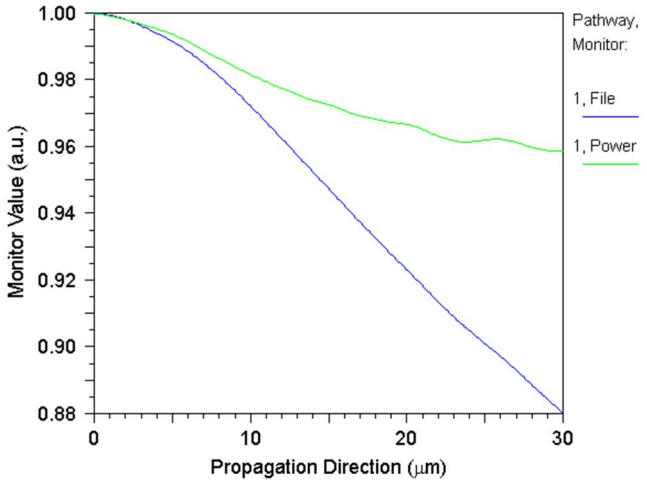

Figure VI-29 – Power coupling simulation results as a function of the propagation direction length (Z)

Figure VI-29 shows the total power being guided inside the waveguide. At 30 µm of the cylinder surface, about 96% is founded from what was launched. In addition, at the same distance (Z=30 µm) about 88 % of the optical field is in the waveguide fundamental mode. Along the propagation, the fundamental mode diverges and higher propagation modes are

excited which explains the difference between the simulated total power and the fundamental mode.

VI.B.4. Synthesis

We developed a novel optical coupling structure, under patent, to collectively and passively, couple small and high speed optoelectronic devices (VCSEL and HPT) to a MM fiber. SM fibers were also partially considered.

A simulator based on the DF-BPM method was presented using commercial software (BeamPROP). The method was explained and its limitation indicated the solutions proposed by the software. Our goal here was to simulate the coupling efficiency in a fast and accurate way. The method allowed us to simulate the ball lens optical coupling technique developed by the partner INNOPTICS used to package Philips ULM VCSEL in the previous chapters. The result presents a 40 % coupling efficiency between the MM fiber and the 10 µm squared photodetector which are in good agreement with measured optical losses on the SiGe ROSA. This validates the simulation approach.

This section, thus proposed our novel vertical optical waveguide structure, to increase the optical coupling efficiency of such small optoelectronic devices and to provide a passive and collective coupling over an entire wafer. The vertical optical waveguide is supported by an anchoring system and is patent pending. The simulation shows 83 % coupling efficiency between the MMF and 10 µm squared detector using a taper waveguide of SU-8 material with a length of 25 µm, base width (fiber side) of 25 µm and truncated case width (detector side) of 10 µm. The alignment simulation shows 50 % coupling efficiency dropping for ± 20 µm lateral displacement.

The VCSEL to MM fiber have shown even higher optical coupling efficiency with values in excess to 88 % compared to a 60 % value using the ball lens technique.

VI.C. Summary and Conclusion

This chapter presented the evolution on the optoelectronic devices exploring two directions: the laser diode performance improvement as a function of the layout; the optical coupling techniques.

The modifications on the VCSEL were done in terms of access RF transmission lines and on the optical aperture diameter from 2 µm up to 20 µm. Comparing the 8 µm aperture diameter ULM standard 10 Gbps VCSEL and the new 20 Gbps version with same size, the cut-off frequency goes from 12.3 GHz to 20.5 GHz which reveals the intrinsic technology improvement made by Philips-ULM Photonics. Clearly a trade-off between the speed and OM gain must be done taking into account the device size. The smallest devices are very fast but with low gain. Moreover, they are more difficult to be coupled which can be a challenge where the optical alignment precision becomes extremely important. On the other hand, larger devices facilitate the light coupling, providing higher link gain, but increase the consumption and decrease the modulation speed. The VCSEL choice to be integrated in the next generation TOSA was set on the 4 µm aperture diameter VCSEL because of its measured 24 GHz bandwidth and its good linearity and its prediction for further enhancement in its thermal dissipation, better optical coupling and mismatching improvement. Measured on wafer, it shows a cut-off frequency of 24 GHz and an OM gain of —18.1 dB (i.e. slope efficiency of 0.13 W/A). Complementary, interesting performances were found on the RIN (<-140 dB/Hz) and on the nonlinearities: input $P1dB_{OM}$ up to 10 dBm; input $IP3_{OM}$ up to 14 dBm and an $SFDR_{OM}$ of 94 dB.$Hz^{2/3}$. The best performances were found with biasing higher than 3 mA and modulation frequency higher than 6 GHz.

The second direction to take into account is the optical device packaging where two techniques were simulated: the ball lens technique used in the home-made TOSA and ROSA; and a new collective and passive optical coupling technique. The ball lens technique simulations took into account the following parameters: 500 µm sapphire substrate, a diameter of the Sapphire ball lens and a free space between the ball and the ferrule of 1000 µm each. Simulation agrees with the optimum distance of 1160 µm to be used between the ball lens and the ferrule in terms of the optical coupling efficiency. The simulation using the 10 µm squared detector shows a coupling efficiency of 40 % for this distance which fits with the real measurement. Using the 20 µm and 30 µm squared detectors we got around 68 % coupling. These results reveal that the 20 µm squared HPT could be a good compromise, using this ball lens technique, in terms of coupling efficiency and OM gain at 5 GHz.

A new solution for the optical packaging was proposed based on a collective and passive optical coupling through a vertical waveguide. The core of the solution is an optical waveguide in a taper shape to provide the best coupling. The optical waveguides are integrated on an anchoring platform which holds the taper and provides the passive alignment plus the contact to the fiber. This structure is patent pending. Our simulation focused on the taper size and shape study considering an HPT device of 10 µm square layout. The simulation does not only take into account the fundamental mode propagated in the multimode fiber (MMF) but also its multimode behavior considering all the modes equally distributed. Neither one nor the other represents a real case, but it gives the range of what can be expected on the coupling efficiency. The squared taper shape, using the same size dimensions study, gives a slightly better result compared to the circular taper either from the fundamental simulation (83 %) or from the multimode simulation (60 %). From the results where we varied the cone base width and the height, with the truncated base width fixed at 10 µm we decided to choose 25 µm for both

dimensions providing an average of 80 % optimum coupling efficiency on the fundamental mode. Misalignment tolerance was then simulated and evaluated to be of up to ± 20 μm at half the power, for both fundamental mode injection and all mode equilibrated excitation.

The simulation of coupling efficiency between the VCSEL and the optical waveguide was considered too. Such structure was also studied and optimized to couple an 8 μm aperture diameter VCSEL to a multimode fiber. Its height should be 30 μm with a cylinder shape of 10 μm in width. The structure thus reaches a coupling efficiency as high as 96 %. Therefore, here we have proposed an innovate low cost passive and collective optical coupling technique which the simulation reveals interesting in terms of coupling efficiency on small optoelectronic devices.

Chapter VII - **Conclusions and Perspectives**

1) Conclusions:

In this final chapter, the final conclusions and perspectives of this PhD work are enlightened. First we start with an overview of the main conclusion of each developed chapter. Second, the main contributions of this work are synthesized. And, finally few directions are presented in terms of perspectives.

Chapter II

Chapter II presented the evolution of the broadband wireless network toward the multiGbit/s communications. It explored the different technologies used in our days with special interest in the 60 GHz band frequency wireless communication technology. The 60 GHz Wi-Fi technology based on the IEEE 802.11ad answer the question of the multiGbit/s short range communication (indoor) with an issue of limited coverage due to the air and walls absorption. This issue (single room communication) is proposed in the ORIGIN project to be overcome by the Radio-over-Fiber (RoF) technology allowing the multi-room network communication. Both 60 GHz wireless and RoF technologies, got a particular interest since they are the core of the ORIGIN project introduced here. The ORIGIN project intended to explore both technologies to provide multiGbit/s indoor communication with multi-room communication based on domestic cloud approach. The goal was to develop a complete system based on RoF transducers and multipoint-to-multipoint architecture. The RoF technology was presented by fundamental principles and state-of-the-art with focus on multimode 10 Gbps optoelectronic device technologies operating at 850 nm: VCSEL and HPT. The reason of the choice was the compromise between the performances and flexibility in terms of integration and packaging resulting in a low cost solution. This choice affected directly the transducer approach which was decided to be based on the intermediate frequency operation. Three RoF transducers generations with the main differences in the optoelectronic devices were presented: the first uses pure commercial devices, the second a hybrid solution between commercial and home-made devices and the last implements both home-made devices. The point-to-point (optical tunneling) and multipoint-to-multipoint architectures were presented and compared exposing its advantages and disadvantages. This chapter introduced the multiGbit/s domestic cloud problematic with its corresponding state-of-the-art.

Chapter III

Chapter III presented the die performance measurements on both VCSEL and HPT technologies. The experimental bench setups were developed and implemented for both E/O

and O/E devices, and its corresponding reference (NFPD and ULM TOSA), covering main characteristics: static performances, dynamic small-signal response, noise behavior and nonlinearities. The system performance metrics with Error-Vector-Magnitude was considered as well. The RoF performance characterization of the link made by the standard multimode 10 Gbps 850 nm VCSEL die with 8 µm aperture diameter and the reference commercial New Focus Photodiode were presented. Two important parameters that strongly influence the link performances are the coupling efficiency and the thermal dissipation. The performance characterization allowed us to optimize the VCSEL bias current and frequency operation (8-10 mA and frequency around 4 GHz). The link was measured with an SFDR of 99 dB.Hz$^{2/3}$, a minimum EVM degradation from back-to-back setup of 1 %, and a power dynamic range of 35 dB at an EVM degradation of 20 %. This link characterization led us to the importance of individual optoelectronic block performances extraction. In the case of 850 nm SiGe HPT characterization, two layout structures were characterized in order to choose the candidate to be integrated into a packaged module: 10x10 µm^2 and 30x30 µm^2 optical windows. The characterization was made using a ULM 10 Gbps TOSA module as a reference. A compromise between size and performances had to be made: small structures are faster devices but with low coupling efficiency. The main focus here is the opto-microwave frequency response at 5 GHz, dictating the smallest structure choice with 7 dB higher gain than the 30x30 µm^2 with a value of 1.45 A/W responsivity in DC and 0.034 A/W at 5 GHz (including optical losses to a MM fiber). Both VCSEL and HPT dies were characterized in a link configuration.

Chapter IV

Chapter IV presented the definition and simulation of opto-microwave figures of merit covering the three main analog characteristics: frequency response, noise and the nonlinearities. Indeed, we proposed a definition of the opto-microwave figures of merit which allowed the individual optoelectronic devices representation as an equivalent electrical two-port network. Optical Microwave Gain (G_{OM}), Optical Microwave Noise Figure (NF_{OM}), Optical Microwave compression Point ($P1dB_{OM}$), Optical Microwave Third-Order Intercept Point ($IIP3_{OM}$), Optical Microwave Spurious-free dynamic range ($SFDR_{OM}$) and finally Opto-microwave Error Vector Magnitude (EVM_{OM}) definition were presented for each individual device. Each block of the RoF system was considered in a flexible opto-microwave behavioral model implemented on a microwave RF electrical simulator. The model was successfully implemented, simulated and validated, with measurement comparisons, using different RoF system configuration. The model allowed, not only to simulate the full RoF system and identify the critical point, but also to help to extract system parameters for each individual components from the EVM measurements.

Chapter V

Chapter V presented the implementation of the VCSEL and SiGe 2T-HPT die into ROSA and TOSA modules to target their final integration into the ORIGIN demonstrator. Both VCSEL and HPT die were integrated and packaged into module with the development in terms of electrical and optical interconnections. The optical packaging was based on a ball lens technique. The electrical connections were developed as well using a transparent substrate. RF transmission lines were designed for both VCSEL and 2T-HPT dies and the chip die integration was developed by thermo-compression technique. Active IC and passive reactive electrical matching network were also considered. The optical coupling using the ball lens technique shows a

coupling efficiency of 60 % and 35 % for the home-made TOSA and ROSA, respectively. Good results were found in terms of thermal dissipation for the VCSEL. EVM performances were measured showing 3 % and 16 % EVM degradation compared to the B2B, respectively for the VCSEL TOSA and the 2T-HPT ROSA. Although, the SiGe ROSA shows first promising results, it requires further optimization especially on the optical coupling efficiency and on the base connection to move from 2T-HPT to a 3T-HPT configuration. The power link budget study to design the complete system was presented. The system architectures were taken into account with the optical tunnel (P2P) and the multipoint-to-multipoint (MME and MMO) architectures with special attention to the compatibility for both Finisar ROSA (RoF2 configuration) and SiGe ROSA (RoF3 configuration). The critical points were identified and solutions proposed. The MMO architecture reveals to be an eventual future option with further questions to answer: optical beating and saturation. The final demonstrator was finally implemented using a communication between 2 rooms based on an optical Multipoint-to-Multipoint architecture with electrical multiplexing (MME) using a 4x4 multiplexing central node and a signal controlling device implementation. A 16 % EVM was demonstrated for a two-hop scenario until the input of the mm-TX, which is a successful achievement in terms of performances. The mm-TX modules added an extra 14 % to the EVM, achieving an overall 30 % EVM including the two hops. This proved to be compensated in the 3 Gbit/s transmission by the CRC implementation in the Gefen commercial modules.

The demonstration between the two rooms was successful using the home-made GUI and the Green Box by a real HD video communication using two 60 GHz wireless commercial modules with data rate of 3 Gbps.

Chapter VI

The final Chapter VI explored two future RoF transducers evolutions: the system operating frequency limited by the optoelectronic devices and the optical packaging coupling efficiency. Analogue VCSELs performances toward 20 GHz IF were considered through the modification of the layout in terms of optical aperture diameter and RF access lines together with the improved vertical layers stack from ULM Photonics. Comparing the 8 µm aperture diameter ULM standard 10 Gbps VCSEL and the new 20 Gbps version with same size the cut-off frequency goes from 12.3 GHz to 20.5 GHz. The cut-off frequency of the modified VCSELs varies from 14 GHz to more than 25 GHz with the size of the VCSEL. Clearly a trade-off between the speed and OM gain must be done taking into account the device size. The smallest devices are very fast but have low gain and are more difficult to be coupled which can be a challenge where the optical alignment precision becomes extremely important. On the other hand, larger devices facilitate the light coupling, providing higher link gain, but increase the consumption and decrease the modulation speed. The VCSEL with aperture diameter of 4 µm was chosen and performances characterized. Its bias condition and frequency operation were optimized. It shows a cut off frequency of 24 GHz and an OM gain of —18.1 dB i.e. responsivity of 0.13 W/A. Complementary, interesting performances were found on the noise (<-140 dB/Hz) and on the nonlinearities: input $P1dB_{OM}$ up to 10 dBm; input $IP3_{OM}$ up to 14 dBm and an $SFDR_{OM}$ of 94 $dB.Hz^{2/3}$. The best performances were found with biasing higher than 3 mA and modulation frequency higher than 6 GHz. The second direction was the optical packaging of optoelectronic devices where two techniques were simulated: the ball lens technique, used in the home-made TOSA and ROSA; and a new collective and passive optical coupling technique. The new proposed solution for the optical packaging is based on a collective and passive optical coupling

through a vertical waveguide. The optical waveguides are integrated on an anchoring platform which holds the taper and provides the passive alignment plus the contact to the fiber. This proposed technique in patent pending. From the results where we varied the cone base width and the height, with the truncated base width fixed at 10 µm we decide to choose 25 µm for both dimensions providing an 80 % optimum coupling efficiency to a 10 µm detector. This a 6 dB OM gain improvement compared to the ball lens technique used on SiGe HPT. Misalignment tolerance was then simulated and evaluated to be of up to ± 20 µm at half the power. The simulation of coupling efficiency between the VCSEL and the optical waveguide was considered too. Such structure was also studied and optimized to couple an 8 µm aperture diameter VCSEL to a multimode fiber. Its height should be 30 µm with a cylinder shape of 10 µm in width. The structure thus reaches a coupling efficiency as high as 96 %. Therefore, here we have proposed an innovate low cost passive and collective optical coupling technique which the simulation revealed interesting in terms of coupling efficiency on small optoelectronic devices.

2) Novelty of the work:

The overview of this work is defined within the title: Technological development and system integration of VCSELs and SiGe HPT receivers for 60 GHz low cost Radio-over-Fiber applications.

The main contributions of this work are presented as the following topics:

- Optoelectronic experimental setups development and implementation: it covered the static performances, dynamic small-signal response, noise behavior and nonlinearities. System performance metrics were implemented too, based on OFDM signal according to the existing 60 GHz wireless standards.
- Die performances optimization study: the measurement was successfully performed, resulting in optimizing on the bias condition, structure layout and frequency operation, especially for RoF applications.
- Extension of Opto-microwave figures of merit: definition of the Optical Microwave Gain (G_{OM}), Optical Microwave Noise Figure (NF_{OM}), Optical Microwave compression Point ($P1dB_{OM}$), Optical Microwave Third-Order Intercept Point ($IIP3_{OM}$), Optical Microwave Spurious-free dynamic range ($SFDR_{OM}$) and finally Opto-microwave Error Vector Magnitude (EVM_{OM}) of each individual device.
- Novel Opto-microwave behavioral model: implementation into a microwave RF electrical simulator. Based on an equivalent electrical two-port network it allows the simulation, extraction and design of the RoF devices and system opto-microwave figures of merit.
- System power budget design and link optimization in terms of gain, noise and nonlinearities. This work allows to study the different optical link configurations with different sources and detectors. It was made in an original and simple way as a direct application of the OM figures.
- First time that a 2T-HPT was introduced in a RoF system and its EVM characterized.
- Next generation developments solutions
- A contribution was given on the improvement of VCSEL speeds, through their bandwidth towards 25 GHz VCSEL with ULM Photonics, their matching and their thermal dissipation, altogether with the concern of monitoring their RoF performances.

- An innovative optical coupling technique was proposed that is expected to lower the tradeoff between size, i.e. speed performance, and coupling efficiency, thus between performances and cost.

3) Perspectives:

The perspectives of this work are presented on the following two main topics.

First the RoF module developments:

The TOSA and ROSA modules evolution: the transducer technology based on the IF of 5 GHz is given by the low cost optoelectronic devices. One direction to take is to increase this frequency which means using faster optoelectronic devices, ideally operating in the wireless center frequency to provide a direct transmission in order to make a simpler and compact system. In terms of optoelectronic device the speed is inversely proportional to the size. Small die structures for the VCSEL and the HPT will increase its frequency response. We present VCSELs with cut-off frequency up to more than 25 GHz for small structures (<4 μm). HPT structure with size lower than 10x10 μm^2 could be studied with even different technology modification to achieve higher frequencies too. Such small structures (VCSEL and HPT) are faster, but characterized by a low OM gain mainly due to low coupling efficiencies (not only however). Therefore the TOSA/ROSA module implementation plays an even bigger role: the active IC further development and integration is an option in order to design and implement a Power Amplifier (PA) on the VCSEL input and LNA on the HPT output. Using the same SiGe technology an integrated matching network could be used to optimize the reflection losses between the active IC and optoelectronic device on both sides. Moving from 2T-HPT toward 3T-HPT will be important as well. During this thesis an HBT was integrated with a VCSEL using the emitter connector into the VCSEL cathode. The results of this configuration need to be explored in future work. The optical interconnection is an important task to develop for such small structures where the ball lens technique proves to be insufficient. The development of our new coupling technique is a solution which can solve this problem.

Modeling further improvement: A better nonlinear equation would be needed instead of the hyperbolic tangent. Also the implementation of the test board effects in the model could be usefull.

Second, in terms of the system integration and development:

Further development with special attention on the mm-TX and mm-RX modules: the mm-TX module was found to be the critical block with gain 27 dB lower than what was expected. Therefore, the improvement must be taken into account of its performances and further integration too. We could envisage a further integration into SiGe technology. This activity is actually on going.

The antennas coupling between both mm-TX and mm-RX modules are another point to be improved which will influence the system performance. In fact, the location of the transducer in relation to the wireless emitter/receptor had a great impact on system performance. The improvement can be in the antenna design or on the transducer location.

Optical access management could be the solution to implement the M2M architecture with automatic radiation exposure control.

Further developments are needed, taking advantages of previous VCSEL improvements, to transmit the four 2 GHz channel of the 60 GHz standards.

The RoF architecture must also move to the integration of multiple services including 1 Gbps Ethernet, RTV phone, satellite TV and 2.4/5 GHz Wi-Fi signals over the same hybrid cable.

Finally, our theoretical work on the novel proposed vertical waveguide based optical coupling technique is currently under a maturation project development for industrial transfer and licensing.

Appendix

A.1 – Link OM beahvioral Model

Figure A.1-1 shows the Opto-microwave behavioral model of the complete RoF link in the Microwave simulator enviorament (ADS). Two links are represented where the first on the top represents the ULM die VCSEL and the reference the photodetector (New Focus PD). As we can see a 36 dB Low Noise Amplifier[7] (NF=3dB) is used at the end of the link to avoid the oscilloscope sensitivity (see section III.A.6). The second one replaces the NFPD by the Finisar ROSA integrating a TIA, which removes the need of the LNA in the measurement bench setup and simulation.

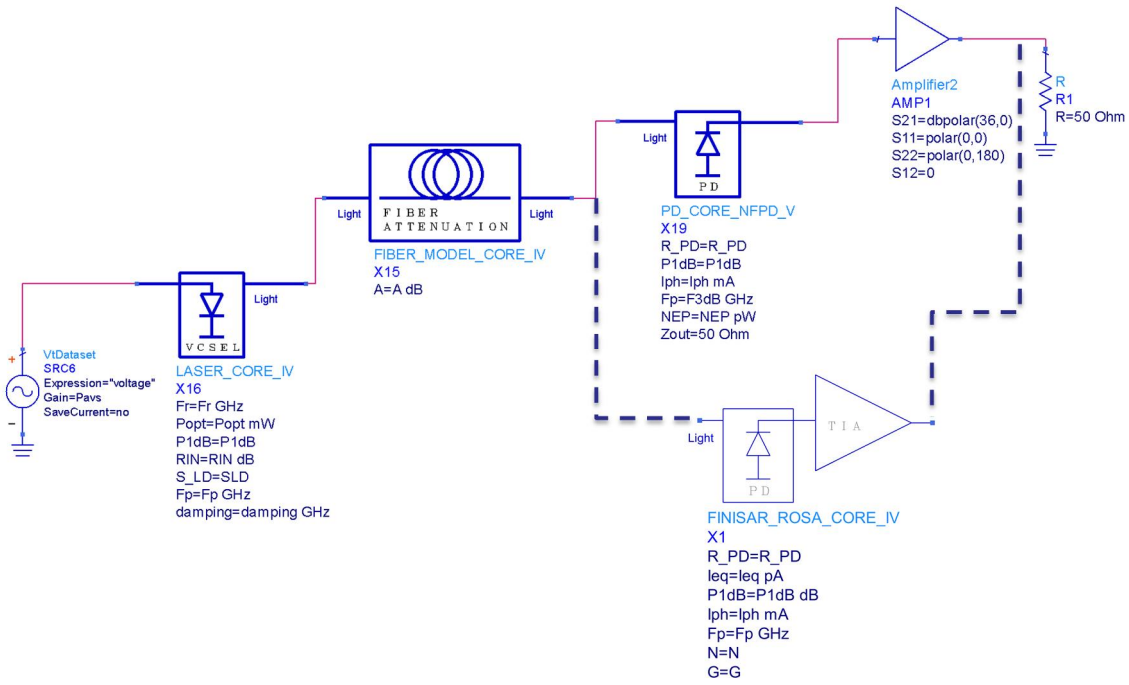

Figure A.1-1 - Radio-over-Fiber transceiver modules

The signal generator is real data measured in the Back-to-Back configuration, because we intend to approximate the simulation to the real measurement. Indeed the good agreement in the fit was only possible with this method since the noise contribution of the AWG and

[7] MITEQ - AFS4-02000800-30-22P-4

oscilloscope can not be neglected (6% at IF=3 GHz). The simulator engine performed was Circuit Envelope since it adds physical analog/RF performances to system simulation with digitally modulated signals. It combines time- and frequency domain representation which allows a fast and complete analysis of complex signals. The output signal is simulated in 50 Ω load impedance and extracted to a datafile to be, afterwords, imported into Matlab enviorement. The signal demodulation and EVM computation is performaed on Matlab.

A.1.1– Laser OM beahvioral Model

The laser behavior mode is presented in the Figure A.1-2 which is divided in 3 blocks: Noise voltage source (V_Noise), 1-Port S-parameter file (S1P) and the symbolically defined device (SDD3P).

The SDD block implements the Figure IV-10 introducing the hyperbolic tangent (Eq. (4.40)) to implement the OM gain and the nonlinearities ($P1dB_{OM}$ and $IP3_{OM}$). It introduces also adds the frequency response of the laser Eq. (2.14) in H[2]. The OM laser noise factor identified in Chapter IV (Eq. (4.11)) is introduced by the rms noise voltage including the noise frequency response given by Eq. (4.41). The reflection coefficient measurement (S11) was implemented by the S1P block.

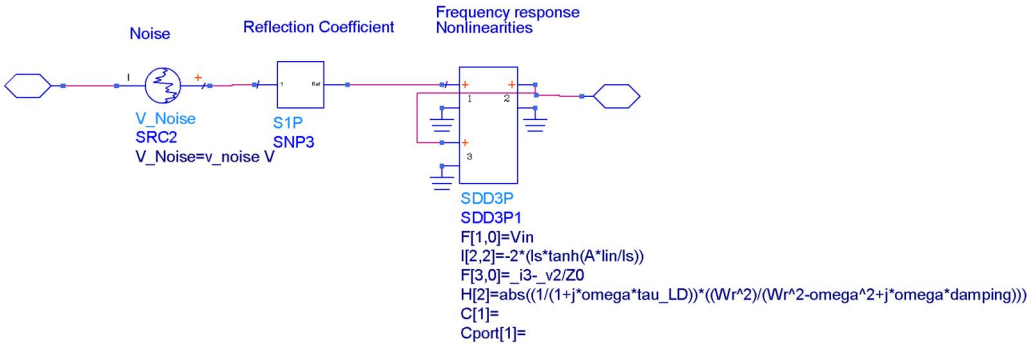

Figure A.1-2 – Laser OM behavioral model implementation

A.1.2– Photodiode OM beahvioral Model

The photodiodeOM behavioral model is presented in Figure A.1-3 where we identified exactly the same concept of the laser OM model. We neglect the photodiode output reflection coefficient since we were using commercial photodetector with 50 Ω matched output. As we can see in H[2] parameter the frequency response of the PD is a simple low pass filter (25GHz 3dB cutoff frequency for the NFPD).

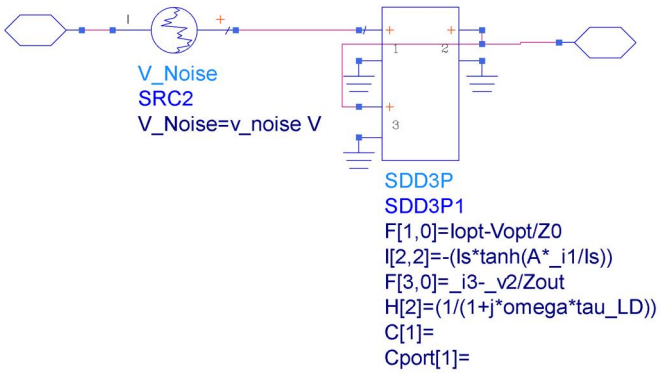

Figure A.1-3 – Photodiode OM behavioral model implementation

A.1.3– Fiber OM beahvioral Model

Finally the optical fiber OM beahvioral model is presented in Figure A.1-4. We can see that the nether noise and nonlinearities are implemented. Input and output perfectly 50 Ω matched SDD where the OM equivalence is implemented.

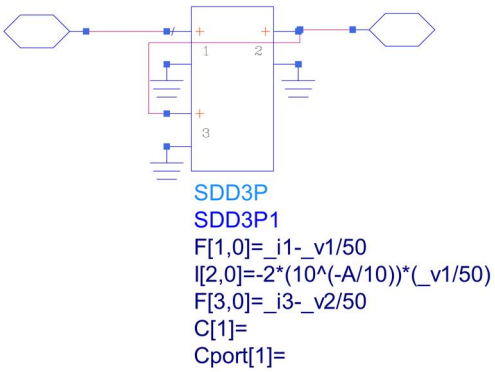

Figure A.1-4 – Fiber OM behavioral model implementation

A.1.4– Finisar ROSA OM beahvioral Model

Figure A.1-4 shows the OM behavioral model implemented for the Finisar ROSA which includes the TIA. The photodiode model in the left is exactly the same approach in A.1.3. The TIA is implemented by a current-controlled voltage source (CCVS) adding the transimpedance gain (V/A) with 50 Ω output impedance. The TIA SDD block implements the frequency response by a variable order (N) low pass filter.

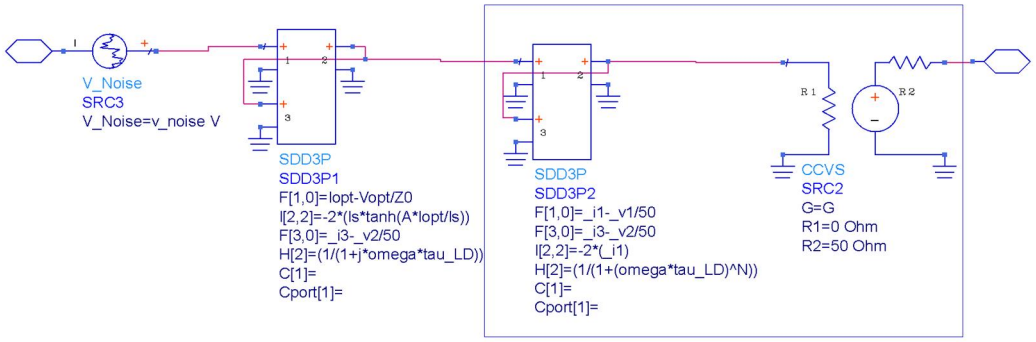

Figure A.1-4 – Finisar ROSA OM behavioral model implementation

Personal scientific publications and patent

International conferences with proceedings

[1] M.D. Rosales, J. Schiellein, C. Viana, J.-L. Polleux, C. Algani, « Full Area Emitter SiGe Phototransistor for Opto-Microwave Circuit Applications », 9th IEEE International Conference on Group IV Photonics, GFP 2012

[2] C. Viana, J.-L Polleux, C. Algani, "VCSEL Characterizations At The Circuit- And System-Levels For Low-Cost RoF Applications", 13th Edition of Mediterranean Microwave Symposium, Leban, 2013

[3] Jean-Luc Polleux, Carlos Viana, "Radio-Over-Fibre Techniques within Home Networks. Focus on VCSELs and Photoreceivers (SiGe HPT and Commercial ROSA)", Workshop at European Microwave Week, Nuremberg, 2013

[4] Lukas W. Snyman, Kingsley A. Ogudo, Jean-Luc Polleux , Carlos Viana and Sebastian Wahl, "High Intensity 100 nW 5 GHz Silicon Avalanche LED using graded junction and carrier momentum engineering», Optical Interconnects XIV, SPIES OPTO'14

[5] Lukas W. Snyman, Kingsley A. Ogudo, Jean-Luc Polleux , Carlos Viana and Sebastian Wahl, "10-40 GHz on- chip micro optical links with all integrated Si Av LED optical sources, waveguides and SiGe detectors", Optical Interconnects XIV, SPIES OPTO'14

[6] C. Viana , Z.G. Tegegne, M. Rosales, J.L. Polleux, C. Algani, V.Lecocq, C.Lyszyk, S.Denet, "A hybrid photo-receiver module based on a two-terminals SiGe Heterojunction Photo-Transistor for low cost 60GHz Radio-over-Fiber Applications", ECOC, Cannes, France 2014 (submitted)

[7] Kingsley Ogudo. A, Lukas W. Snyman, Jean-Luc Polleux, Carlos Viana, Zerihun Tegegne, Diethelm Schmieder, "Towards 10 – 40 GHz on-chip micro-optical links with all integrated Si Av LED optical sources, Si N based waveguides and Si-Ge detector technology", In proceeding of SPIE Vol. 8991, 899108, San Francisco California, USA, 2014

[8] Lukas W. Snyman, Jean-Luc Polleux, Kingsley A. Ogudo, Carlos Viana, Sebastian Wahl, "High Intensity 100 nW 5 GHz Silicon Avalanche LED utilizing carrier energy and momentum engineering", In proceeding of SPIE Vol. 8990 89900L-1 Silicon Photonics IX, 2014

National conferences with proceedings

[9] Julien Schiellein, Carlos Viana, Jean-Luc Polleux, Catherine Algani, Thomas Merlet, « Réalisation et modélisation comportementale d'un oscillateur photoinjecté pour applications d'antennes à balayage électronique », 17èmes Journées Nationales Microondes 18-19-20, Brest, 2011

[10] Carlos Viana, Jean-Luc Polleux et Catherine Algani, « VCSEL 850nm à ligne d'acces coplanaire et 15 GHz de bande passante », Journées Nationales d'Optique Guidée, Lyon, 2012

[11] Y. Paugam, J. Guillory, A. Pizzinat, B. Charbonnier, O. Bouffant, N. Evanno, D. Le Coq, Carlos Viana, Jean-Luc Polleux, M. Rosales, C. Algani, S. Faci, K. Chikha, A.L. Billabert, D. Bourreau, G. Guevel, C. Kärnfelt, M. Ney, M. Brunet, G. Lirzin, E. Tanguy, A. Chousseaud,

H.W. Li, C. Canepa, G. Gougeon, J. Poinen, C. Sun, V. Lecocq et S. Denet., « Liaison sans fils à 60 GHz et réseaux domestique Multi-gigabit/s basé sur une infrastructure Radio-sur-Fibre bas coût », 18èmes Journées Nationales Microondes, Paris, 2013

[12] Carlos VIANA, Jean-Luc POLLEUX, Catherine ALGANI, « Caractéristiques optique-microonde en bruit et en non linéarité de VCSEL 850nm multimodes pour des applications Radio-sur-Fibre », 18èmes Journées Nationales Microondes, Paris, 2013

Communications

[13] Carlos Viana, Jean-Luc Polleux, J. Guillory, M. Rosales, C. Algani, S. Faci, A. Pizzinat, K. Chikha, B. Charbonnier, O. Bouffant, D. Le Coq, N. Evanno, A.L. Billabert, D. Bourreau, G. Guevel, Y. Paugam, C. Kärnfelt, M. Ney, M. Brunet, G. Lirzin, E. Tanguy, A. Chousseaud, H.W. Li, C. Canepa, G. Gougeon, J. Poinen, C. Sun, V. Lecocq and S. Denet., « VCSEL performance analysis in an intermediate-frequency 60 GHz Radio-over-Fiber application » 5th European VCSEL Day, Berlin, 2012

[14] J.-L. Polleux et C. Viana, « VCSEL 850nm pour les applications RoF 60GHz à bande intermédiaire », Journée du club optique-microonde, Paris, 2013

Patent

[15] Inventors : Jean-Luc Polleux and Carlos Viana, «Structure de couplage optique collective passive de composants optiques et opto-électroniques», Application number: 1450962, Submission number: 1000226986, Date of Patent: 7 February 2014

References

[16] IEEE 802.11ad, May 2010, www.ieee802.org/11
[17] Press release by WiGig. “WiGig Taipei Summit Grand Debut - reveals the blueprint and market opportunities”, consulted in June 2012, http://www.digitimes.com/supply_chain_window/story.asp?datepublish=2012/06/14&pages=PR&seq=203
[18] International Telecommunication Union, Press Release, Geneva, 27 February, 2013, available in: www.itu.int
[19] IEEE 802.11TM Wireless Local Area Networks, http://www.ieee802.org/11/
[20] IEEE standards Association, "AMENDMENTS IN IEEE 802.11ad™ ENABLE MULTI-GIGABIT DATA THROUGHPUT AND GROUNDBREAKING IMPROVEMENTS IN CAPACITY", press release available in: standards.ieee.org/news/2013/802.11ad.html
[21] T. Seki, K. Hiraga, K. Nishimori, K. Nishikawa, and K. Uehara, “High Speed Parallel Data Transmission and Power Transmission Technology for Wireless Repeater System”, 5th European Conference on Antennas and Propagation (EUCAP), Italy, 2011
[22] S.-B. Lee, S. Choudhury, A. Khoshnevis, S. Xu, S. Lu, “Downlink MIMO with Frequency-Domain Packet Scheduling for 3GPP LTE”, IEEE INFOCOM, Rio de Janeiro, 2009
[23] G. T. A. El Sanousi, “A WIMAX MIMO Network Architecture Exploiting Spatial Diversity of Multiple Antenna Sites”, Second International Conference on Advances in Mesh Networks, Athens, 2009
[24] H. Sari, G Karam, I Jeanclaude, “Transmission Techniques for Digital Terrestrial TV Broadcasting”, IEEE Communication Magazine, Volume 33, No. 2, pp. 100–109, 1995
[25] First Report and Order in the Matter of Revision of Part 15 of the Commission’s Rules Regarding Ultra-Wideband Transmission Systems. ET Docket 98-153, Federal Communications Commission, FCC 02-48, April 22, 2002
[26] W. Zhuang, X. Shen, and Q. Bi, "Ultra-wideband wireless communications," Wireless Communications and Mobile Computing, Volume 3, pp. 663-685, 2003.
[27] R. J. Fontana, "Recent system applications of short-pulse ultra-wideband (UWB) technology," IEEE Transactions on Microwave Theory and Technology, Volume 52, No. 9, pp. 2087-2104, 2004.
[28] M. Jazayerifar, B. Cabon, and J. A. Salehi, “Transmission of Multi-Band OFDM and Impulse Radio Ultra-Wideband Signals Over Single Mode Fiber”, Journal of Lightwave Technology, Volume 26, No. 15, 2008
[29] High Rate 60 GHz PHY, Mac and HDMI PAL, Standard ECMA-387, December 2008
[30] Part 15.3: Wireless MAC and PHY Layer Specifications for High Rate Wireless Personal Area Networks (WPANs): Amendment 2: Millimeterwave based Alternative Physical Layer Extension, IEEE P802.15.3c/D13 July 2009.
[31] Wireless Gigabit Alliance (WiGig), http://wirelessgigabitalliance.org
[32] Su Khiong Yong and Chia-Chin Chong. An Overview of Multigigabit Wireless through Millimeter Wave Technology: Potentials and Technical Challenges. EURASIP Journal on Wireless Communications and Networking, vol. 2007, article ID 78907, pp. 1–10, 2007.
[33] IEEE 802.11ad pre-Standard. IEEE P802.11 Wireless LANs, PHY/MAC Complete Proposal Specification. IEEE 802.11-10/0433r0, May 2010. http://www.ieee802.org/11/.
[34] F. Brunet, S. Roblot, I. Siaud, E. Conil, M.F. Wong and M. Bellec. Impact and Acceptance of 60 GHz systems. Internal White Paper, Orange Labs, November 2010.

[35] J.J. O'Reilly, P.M. Lane, M.H. Capstick, H.M. Salgado, "Wireless connection using mm-waves and fibre", The X International Symposium on Subscriber Loops and Services, Proceedings, 1993
[36] IEEE 802.11ad, May 2010, www.ieee802.org/11
[37] A. Miller, M. Ebrahimzadeh, D. M. Finlayson, "Semiconductor quantum optoelectronics: from quantum physics to smart devices", John Wiley & Sons, Inc, 1998
[38] T.E. Sale, "Vertical cavity surface emitting lasers"– John Wiley & Sons Inc, 1995.
[39] T. Numai, "Fundamentals of Semiconductor Lasers",Springer, New York, 2004
[40] G. Agrawal, Fiber-Optic Communication Systems, John Wiley & Sons, New York, 2002
[41] Yu, Siu Fung, "Analysis and Design of Vertical Cavity Surface Emitting Lasers", John Wiley&Sons, 2003
[42] Gerd Keiser, "Optical fiber communications", McGraw-Hill, 1991
[43] K. Iga, "Vertical-cavity surface-emitting laser: its conception and evolution", Japanese Journal of Applied Physics, Volume 47, No. 1, 2008.
[44] F. Hopfer, A. Mutig, G. Fiol, M. Kuntz, V. Shchukin, N.N. Ledentsov, D. Bimberg, S.S. Mikhrin, I.L. Krestnikov, D.A. Livshits, A.R. Kovsh, and C. Bornholdt, "20 Gb/s 85°C error free operation of VCSEL based on sub-monolayer deposition of quantum dots", 20th IEEE International Semiconductor Laser Conference, pp. 119–120, 2006
[45] K.L. Lear, A. Mar, K.D. Choquette, S.P. Kilcoyne, R.P. Jr. Schneider, and K.M Geib, "High-frequency modulation of oxide-confined vertical cavity surface emitting lasers", Electronics Letters, 32, pp. 457–457, 1996,
[46] G. Dang, W.S. Hobson, L.M.F. Chirovsky, J. Lopata, M. Tayahi, S.N.G. Chu, F. Ren, and S.J. Pearton, "High-speed modulation of 850-nm intracavity contacted shallow implant-apertured Vertical-Cavity Surface-Emitting lasers", IEEE Photonics Technology Letters, Volume 13, pp. 924–926, 2001
[47] G. Shtengel, H. Temkin, P. Brusenbach, T. Uchida, M. Kim, C. Parsons, W. E. Quinn, and S. E. Swirhun, "High-speed vertical-cavity surface emitting lasers", IEEE Photonics Technology Letters, Volume 5, pp. 1359–1362, 1993
[48] B. J. Thibeault, K. Bertilsson, E. R. Hegblom, E. Strzelecka, P. D. Floyd, R. Naone, and L. A. Coldren, 'High speed characteristics of low optical loss oxide apertured vertical cavity lasers", IEEE Photonics Technology Letters, Volume 9, pp. 11–13, 1997
[49] T. Tanigawa, T. Onishi, T. Nagaix, and T. Ueda, "High-speed 850 nm AlGaAs/GaAs vertical cavity surface emitting lasers with low parasitic capacitance fabricated using BCB planarization technique", Lasers and Electro-Optics Conference, Volume 2, pp. 1381–1383, 2005
[50] Y. Satuby, and M. Orenstein, "Limits of the modulation response of a single-mode proton implanted VCSEL", IEEE Photonics Technology Letters, Volume 10, pp. 760–762, 1998
[51] K. L. Lear, V. M. Hietala, H. Q. Hou, M. Ochiai, J. J. Banas, B.E. Hammons, J. C. Zopler, and S. P. Kilcoyne, "Small and large signal modulation of 850 nm oxide-confined Vertical-Cavity Surface-Emitting Lasers", Summaries of Papers Presented at the Conference on Lasers and Electro-Optics (CLEO '97), Volume 15, pp. 69–74, 1997
[52] A. K. Dutta, K. Kosaka, K. Kurihara, Y. Sugimasa and K. Kasahara, "High-speed VCSEL of modulation bandwidth over 7.0 GHz and its application to 100 m PCF datalink", IEEE Journal Lightwave Technology, Volume 16, pp. 870–875, 1998
[53] T. S. Kim, A. J. Danner, D. M. Grasso, E. W. Young, and K. D. Choquette, "Single fundamental mode photonic crystal vertical cavity surface emitting laser with 9 GHz bandwidth", Electronics Letters, Volume 40, pp. 1340–1341, 2004
[54] A. N. Al-Omari, G. P. Carey, S. Hallstein, J. P. Watson, G. Dang and K. L. Lear, "Low thermal resistance, high speed, top emitting 980 nm VCSELs", IEEE Photonics. Technology Letters, Volume 18, pp. 1225–1227, 2006
[55] N. Suzuki, H. Hatakeyama, K. Yashiki, K. Fukatsu, K. Tokutome, T. Akagawa, T. Anan, and M. Tsuji, "High-speed InGaAs VCSELs", Lasers and Electro-Optics 19th Annual Meeting, 2006
[56] A. N. Al-Omari, and K.L. Lear, "Polyimide-planarized Vertical-Cavity Surface Emitting Lasers with 17.0 GHz bandwidth", IEEE Photonics Technology Letters, Volume 16, pp. 969–971, 2004
[57] A. N. Al-Omari, and K.L. Lear, 'VCSELs with a self-aligned contact and copper-plated heatsink', IEEE Photonics Technology Letters, Volume 17, pp. 1767–1769, 2005
[58] A. Al-Omari and K.L. Lear, "Low current density, inverted polarity, high speed, top emitting 850 nm VCSELs", IET Optoelectronics, Volume 1, pp. 221-225, 2007.

[59] Chen Chen, Zhaobing Tian, K.D. Choquette, and D.V. Plant, “25-Gb/s direct modulation of implant confined holey Vertical-Cavity Surface-Emitting Lasers”, IEEE Photonics Technology Letters, Volume 22, Issue 7, pp.465–467, 2010.
[60] Chen Ji, Jingyi Wang, D. Soderstrom, and L. Giovane, “20-Gb/s 850-nm oxide VCSEL operating at 25°c - 70°c”, IEEE Photonics Technology Letters, Volume 22, Issue 10, pp.670 –672, 2010.
[61] M. S. Alias, S. Shaari, P. O. Leisher, K. D. Choquette, “Highly confined and continuous single-mode operation of self-align photonic crystal oxide VCSEL”, Applied Physics B: Lasers and Optics, Volume 100, Number 3, pp. 453-459, 2010
[62] Y. Ding, W. J. Fan, D. W. Xu, C. Z. Tong, Y. Liu, L. J. Zhao, "Low threshold current density, low resistance oxide-confined VCSEL fabricated by a dielectric-free approach", Applied Physics B: Lasers and Optics, Volume 98, Issue 4, pp. 773-778, 2010
[63] H. Hatakeyama, T. Akagawa, K. Fukatsu, N. Suzuki, K. Tokutome, K. Yashiki, T. Anan and M. Tsuji, “25 Gbit/s 100 °C operation of highly reliable InGaAs/GaAsP-VCSELs”, Electronics Letters, Volume 45, Issue 1, pp. 45–46, 2009.
[64] K. Yashiki, N. Suzuki, K. Fukatsu, T. Anan, H. Hatakeyama, and M. Tsuji, “1.1 μm-range tunnel junction VCSELs with 27-Ghz relaxation oscillation frequency”, Conference In Optical Fiber Communication and the National Fiber Optic Engineers Conference, pages 1 –3, 2007.
[65] Y.-C. Chang, C.S. Wang, and L.A. Coldren, “High-efficiency, high-speed VCSELs with 35 Gbit/s error-free operation”, Electronics Letters, Volume 43, Issue 19, pp. 1022 –1023, 2007.
[66] P. Westbergh, J.S. Gustavsson, B. K. andgel, A. Haglund, A. Larsson, A. Mutig, A. Nadtochiy, D. Bimberg, and A. Joel, “40 Gbit/s error-free operation of oxide-confined 850 nm VCSEL”, Electronics Letters, Volume 46, pp.1014–1016, 2010.
[67] P. Westbergh, J.S. Gustavsson, A. Haglund, M. Skold, A. Joel, and A. Larsson, “High-speed, low-current-density 850 nm VCSELs”, IEEE Journal of Selected Topics in Quantum Electronics, Volume 15, Issue 3, pp. 694–703, 2009.
[68] P. Westbergh, J.S. Gustavsson, A. Haglund, A. Larsson, F. Hopfer, G. Fiol, D. Bimberg, and A. Joel, “32 Gbit/s multimode fiber transmission using high-speed, low current density 850 nm VCSEL”, Electronics Letters, Volume 45, Issue 7, pp.366–368, 2009.
[69] P. Westbergh, J.S. Gustavsson, A. Haglund, H. Sunnerud, and A. Larsson, “Large aperture 850 nm VCSELs operating at bit rates up to 25 Gbit/s”, Electronics Letters, Volume 44, Issue 15, pp.907 –908, 2008.
[70] S.A. Blokhin, J.A. Lott, A. Mutig, G. Fiol, N.N. Ledentsov, M.V. Maximov, A.M. Nadtochiy, V.A. Shchukin, and D. Bimberg, “Oxide-confined 850 nm VCSELs operating at bit rates up to 40 Gbit/s”, Electronics Letters, Volume 45, Issue 10, pp.501–503, 2009.
[71] M. S. Alias, P. O. Leisher, K. D. Choquette, and S. Shaari, “High efficiency 850 nm vertical-cavity surface-emitting laser using fan-pad metallization and trench patterning”, 33rd IEEE/CPMT International In Electronic Manufacturing Technology Symposium (IEMT), pages 1 –4, 2008
[72] K. Fukatsu, K. Shiba, Y. Suzuki, N. Suzuki, T. Anan, H. Hatakeyama, K. Yashiki and M. Tsuji, “30 Gb/s over 100-m MMFs using 1.1μm range VCSELs and photodiodes”, IEEE Photonics Technology Letters, Volume 20, Issue 11, pp.909–911, 2008.
[73] Y.C. Chang, C.S. Wang, L.A. Johansson and L.A. Coldren, “High-efficiency, high-speed VCSELs with deep oxidation layers”, Electronics Letters, Volume 42, Issue 22, pp. 1281–1282, 2006.
[74] Y.-C. Chang, C.S. Wang and L.A. Coldren, “Small-dimension power-efficient high-speed vertical-cavity surface-emitting lasers, Electronics Letters, Volume 43, Issue 7, pp.396 –397, 2007
[75] J. A. Lott, N. N. Ledentsov, V. A. Shchukin, A. Mutig, S. A. Blokhin, A. M. Nadtochiy, G. Fiol, and D. Bimberg, “850 nm VCSELs for up to 40 Gbit/s short reach data links”, Conference on Lasers and Electro-Optics (CLEO) and Quantum Electronics and Laser Science Conference (QELS), pages 1–2, 2010.
[76] H. Hatakeyama, T. Anan, T. Akagawa, K. Fukatsu, N. Suzuki, K. Tokutome and M. Tsuji, “Highly reliable high-speed 1.1 μm-range VCSELs with InGaAs/GaAsP-MQWs”, IEEE Journal of Quantum Electronics, Volume 46, Issue 6, pp.890–897, 2010
[77] P. Westbergh, J.S. Gustavsson, B. Kogel, A. Haglund, A. Larsson, and A. Joel, “Speed enhancement of VCSELs by photon lifetime reduction”, Electronics Letters, Volume 46, Issue 13, pp. 938 –940, 2010.

[78] M.S. Alias, S.M. Mitani, M.F. Maulud, and H.A. Hasbi, “High speed vertical-cavity laser for local area network communication”, Asia-Pacific Conference on Applied Electromagnetics, APACE, pp. 1–5, 2007
[79] Z. Tian, C. Chen, K.D. Choquette, and V. David, “Plant. 30 Gb/s direct modulation of holey VCSELs with thermoelectric cooling”, Conference In Lasers and Electro-Optics (CLEO) and Quantum Electronics and Laser Science Conference (QELS), pages 1 –2, 2010.
[80] P.O. Leisher, A.J. Danner, J.J. Raftery, D. Siriani, and K.D. Choquette, “Loss and index guiding in single-mode proton-implanted holey vertical-cavity surface-emitting lasers”, IEEE Jounal of Quantum Electronics, Volume 42, Issue 10, pp. 1091 –1096, 2006.
[81] C. Jung, R. Jager, M. Grabherr, P. Schnitzer, R. Michalzik, B. Weigl, S. Muller, and K.J. Ebeling, “4.8 mw single-mode oxide confined top-surface emitting vertical-cavity laser diodes”, Electronics Letters, Volume 33, pp.1790 –1791, 1997.
[82] R. Jager, M. Grabherr, C. Jung, R. Michalzik, G. Reiner, B. Weigl, and K.J. Ebeling, “57 % wallplug efficiency oxide-confined 850 nm wavelength GaAs VCSELs”, Electronics Letters, Volume 33, pp.330 –331, 1997.
[83] R.A. Morgan, G.D. Guth, M.W. Focht, M.T. Asom, K. Kojima, L.E. Rogers, and S.E. Callis, “Transverse mode control of vertical-cavity top-surface-emitting lasers”, IEEE Photonics Technology Letters, Volume 5, Issue 4, pp. 374 –377, 1993.
[84] E.W. Young, K.D. Choquette, S.L. Chuang, K.M. Geib, A.J. Fischer, and A.A. Allerman, “Single-transverse-mode vertical-cavity lasers under continuous and pulsed operation”, IEEE Photonics Technology Letters, Volume 13, Issue 9, pp. 927 –929, 2001.
[85] H. Martinsson, J.A. Vukusic, M. Grabberr, R. Michalzik, R. Jager, K.J. Ebeling, and A. Larsson, “Transverse mode selection in large-area oxide-confined vertical-cavity surface-emitting lasers using a shallow surface relief”, IEEE Photonics Technology Letters, Volume 11, Issue 12, pp. 1536 –1538, December 1999.
[86] D.L. Huffaker, L.A. Graham, H. Deng, and D.G. Deppe, “Sub-40 μA continuous-wave lasing in an oxidized vertical-cavity surface-emitting laser with dielectric mirrors”, IEEE Photonics Technology Letters, Volume 8, Issue 8, pp.974 –976, 1996.
[87] M. Miller, M. Grabherr, R. King, R. Jager, R. Michalzik, and K.J. Ebeling, “Improved output performance of high-power VCSELs”, IEEE Journal of Selected Topics in Quantum Electronics, Volume 7, Issue 2, pp. 210 –216, 2001.
[88] Chao-Kun Lin, A. Tandon, K. Djordjev, S.W. Corzine, and M.R.T. Tan, “High-speed 985 nm bottom-emitting VCSEL arrays for chip-to-chip parallel optical interconnects”, IEEE Journal of Selected Topics in Quantum Electronics, Volume 13, Issue 5, pp. 1332 –1339, 2007.
[89] C.J. Chang-Hasnain, J.P. Harbison, G. Hasnain, A.C. Von Lehmen, L.T. Florez, and N.G. Stoffel, “Dynamic, polarization, and transverse mode characteristics of vertical cavity surface emitting lasers”, IEEE Journal of Quantum Electronics, Volume 27, Issue 6, pp. 1402 –1409, 1991.
[90] R.S. Geels, S.W. Corzine, and L.A. Coldren, “InGaAs vertical-cavity surface-emitting lasers”, IEEE Journal of Quantum Electronics, Volume 27, Issue 6, pp. 1359 –1367, June 1991
[91] M.H. MacDougal, P.D. Dapkus, V. Pudikov, Hanmin Zhao, and Gye Mo Yang, “Ultralow threshold current vertical-cavity surface-emitting lasers with alas oxide-gaas distributed bragg reflectors”, IEEE Photonics Technology Letters, Volume 7, Issue 3, pp. 229 –231, 1995.
[92] H. Martinsson, J.A. Vukusic, and A. Larsson, “Size dependence of single-mode power for mode-stabilized oxide confined VCSELs”, Conference on Lasers and Electro-Optics (CLEO 2000), page 169, 2000.
[93] S.-H. Chung and N. Balkan, “Micro-cavity surface emitting gunn laser”, IEE Proceedings - Optoelectronics, Volume 153, Issue 2, pp. 84 – 86, 2006.
[94] Yu-Chia Chang and L.A. Coldren, “Efficient, high-data-rate, tapered oxide-aperture vertical-cavity surface-emitting lasers”,IEEE Journal of Selected Topics in Quantum Electronics, Volume 15, Issue 3, pp. 704 –715, 2009.
[95] Y. Ou, J.S. Gustavsson, P. Westbergh, A. Haglund, A. Larsson, and A. Joel, “Impedance characteristics and parasitic speed limitations of high-speed 850-nm VCSELs, IEEE Photonics Technology Letters, Volume 21, Issue 24, pp. 1840 –1842, 2009.
[96] T. Anan, N. Suzuki, K. Yashiki, K. Fukatsu, H. Hatakeyama, T. Akagawa, K. Tokutome, and M. Tsuji, “High-speed 1.1- μm range InGaAs VCSELs” presented at the OFC, San Diego, CA, 2008
[97] D. M. Kuchta, C. L. Schow, A. V. Rylyakov, J. E. Proesel, F. E. Doany, C. Baks, B. H. Hamel-Bissell, C. Kocot, L. Graham, R. Johnson, G. Landry, E. Shaw, A. MacInnes, and J. Tatum,

"A 56.1 Gb/s NRZ modulated 850 nm VCSEL-based optical link", Proc. Optical Fiber Communication Conference, USA, 2013.
[98] P. Westbergh, E.P. Haglund, E. Haglund, R. Safaisini, J.S. Gustavsson and A. Larsson, "High-speed 850 nm VCSELs operating error free up to 57 Gbit/s", Electronics Letters, Volume 49, Issue 16, 2013
[99] J.-L. Polleux, "Contribution à l'étude et à la modélisation de phototransistors bipolaires à hétérojonction SiGe/Si pour les applications opto-microondes.", PhD Thesis, CNAM, Paris, Oct. 2001.
[100] J.-L. Polleux et al. "Optimization of InP-InGaAs HPT gain: design of an opto-microwave monolithic amplifier", IEEE Transactions on Microwave Theory and Techniques, Volume 52, Issue 3, 2004
[101] J.-L. Polleux, F. Moutier, A.L. Billabert, C. Rumelhard, E. Sönmez, H. Schumacher, "A Strained SiGe layer Heterojunction Bipolar Phototransistor for Short-Range Opto-Microwave Applications", in IEEE International Topical Meeting on Microwave Photonics, MWP2003, Budapest, Hungary, September 2003.
[102] J.-L. Polleux, F. Moutier, A.L. Billabert, C. Rumelhard, E. Sönmez, H. Schumacher, "An Heterojunction SiGe/Si Phototransistor for Opto-Microwave Applications: Modeling and first Experimental Results", GAAS Conference of the European Microwave Week 2003, pp.231-234, Munich, Germany, 2003.
[103] J.-L. Polleux and C. Rumelhard, "Optical absorption coefficient determination and physical modeling of strained SiGe/Si photodetectors", IEEE EDMO 2000 Proc., Glasgow, Scotland, pp. 167-172, 2000.
[104] J.-L Polleux, C. Rumelhard, "Optical absorption coefficient determination and physical modelling of strained SiGe/Si photodetectors", 8th IEEE International Symposium on High Performance Electron Devices for Microwave and Optoelectronic Applications, Glasgow, 2000
[105] Z. Pei et al., "SiGe/Si multi-quantum-well phototransistor for near-infrared operation", Physica E 16, Elsevier, pp.554-557, 2003.
[106] M. Egels et al., ''Design of an optically frequency or phase-controlled oscillator for hybrid fiber-radio LAN at 5.2GHz", Microwave and optical technology letters, Volume 45 n°2, page 104-107, April 2005
[107] T. Yin et al., "Low-cost, High Efficiency and High-Speed SiGe Phototransistors in Commercial BiCMOS", IEEE Photonics Technology Letters, Vol.18, N°1, January 2006.
[108] G. Meinhardt, J. Kraft, B. Löffler, H. Enichlmair, G. Röhrer, E. Wachmann, M. Schrems, R. Swoboda, C. Seidl, H. Zimmermann, "High-speed blue-, red-, and infrared-sensitive photodiode integrated in a 0.35 μm SiGe:C-BiCMOS process", IEDM Tech. Dig., pp. 821-824, 2005
[109] Yong Zhang, Cheng Li, Song-Yan Chen, Hong-Kai Lai and Jun-Yong Kang, "Numerical analysis of SiGe heterojunction bipolar phototransistor based on virtual substrate", in Solid-State Electronics, Vol.52, Iss.11, pp. 1782-1790, Nov. 2008.
[110] K.S. Lai; J.C. Huang; K.Y.J. Hsu, "Design and Properties of Phototransistor Photodetector in Standard 0.35- μm SiGe BiCMOS Technology", in IEEE Transactions on Electron Devices, Vol.55, Iss.3, pp. 774 – 781, 2008
[111] O. Qasaimeh, Z. Ma, P. Bhattacharya and E.T. Croke, "Monolithically Integrated Multichannel SiGe/Si p-i-n–HBT Photoreceiver Arrays", in IEEE Journal of Lightwave Technology, Vol. 18, No. 11, pp.1548-1553, Nov. 2000
[112] G. Liu, A. Trasser, and H. Schumacher, "33–43 GHz and 66–86 GHz VCO With High Output Power in an 80 GHz SiGe HBT Technology", in IEEE Microwave And Wireless Components Letters, Vol. 20, No. 10, pp.557-559, Oct. 2010
[113] Joffray Guillory, "Radio over Fiber for the future Home Area Networks", PhD thesis, ESYCOM-le Cnam join with France Telecom R&D – Orange Labs, Paris, 2012
[114] J. Guillory, S. Meyer, I. Siaud, A.M. Ulmer-Moll, B. Charbonnier, A. Pizzinat and C. Algani, "Radio-over-Fiber architectures, Future Multigigabit Wireless Systems in the Home Area Network", IEEE Vehicular Technology Magazine (VTM), Volume 5, Issue 3, pp. 30-38. 2010.
[115] Julien Schiellein, "Etude de Phototransistors bipolaires à hétérojonction InP/InGaAs pour applications d'oscillateurs photo-injectés trés faible bruit de phase", PhD Thesis, ESYCOM (ESIEE-Paris and Le Cnam) join with Thales Air system, Paris, 2012
[116] J. Schiellein, M. Rosales, J.-L. Polleux, F. Duport, C. Algani, C. Rumelhard, T. Merlet, N. Zerounian, M. Riet, J. Godin, A. Scavennec, "Experimental influence of the base load effect

on SiGe/Si and InGaAs/InP HPTs", International Topical Meeting on Microwave Photonics, 2009.
[117] New Focus™ (Newport Corporation), http://www.newport.com/
[118] NFPD, http://www.newport.com/15-and-25-GHz-Photodetectors/918055/1033/info.aspx
[119] Philips Technologie GmbH U-L-M Photonics, http://www.ulm-photonics.com/
[120] M. Grabherr, D. Wiedenmann, R. King, R. Jager, B. Schneider, "Speed it up to 10 Gb/s and flip chip it: VCSELs today", White paper, Philips Technologie GmbH U-L-M photonics, 2002
[121] M. Grabherr, S. Intemann, R. Jager, R. King, R. Michalzik, H. Roscher, D. Wiedenmann, "Comparison of approaches to 850 nm 2-D VCSEL arrays", White paper, Philips Technologie GmbH U-L-M photonics, 2003
[122] M. Grabherr, S. Intemann, C. Wimmer, L. R. Borowski, R. King, D. Wiedenmann, R. Jager, "120 Gbps VCSEL arrays: fabrication and quality aspects", White paper, Philips Technologie GmbH U-L-M photonics, 2010
[123] M. Grabherr, S. Intemann, S. Wabra, P. Gerlach, M. Riedl, R. King, "25 Gbps and beyond: VCSEL development at Philips", White paper, Philips Technologie GmbH U-L-M photonics, 2013
[124] M. D. Rosales, F. Duport, J. Schiellein, J.-L. Polleux, C. Algani, C. Rumelhard, "Opto-microwave experimental mapping of SiGe/Si phototransistors at 850nm", International Journal of Microwave and Wireless Technologies, Volume 1, Issue 06, pp 469-473, 2009
[125] C. Carlsson, H. Martinsson, R. Schatz, J. Halonen, and A. Larsson, "Analog modulation properties of oxide confined VCSELs at microwave frequencies", Journal of Lightwave Technology, Volume 20, Issue 9, pp. 1740, 2002
[126] P. Westbergh, J.S. Gustavsson, A. Haglund, M. Skold, A. Joel, and A. Larsson, "High-speed, low-current-density 850 nm VCSELs", IEEE Journal of Selected Topics in Quantum Electronics, Volume 15, No.3, 694 –703, 2009
[127] A. Valle, L. Pesquera, "Relative Intensity Noise of Multitransverse-Mode Vertical-Cavity Surface-Emitting Lasers", IEEE Photonics Technology Letters, Volume 13, Issue 4, 2001
[128] L.-G. Zei, S. Ebers, J.-R. Kropp, K. Petermann, "Noise performance of multimode VCSELs", Journal of Lightwave Technology, Volume 19, Issue 6, 2001
[129] A. Valle, L. Pesquera, "Theoretical Calculation of Relative Intensity Noise of Multimode Vertical-Cavity surface-Emitting Lasers", IEEE Journal of Quantum Electronics, Volume 40, No.6, 2004
[130] J. Poette, P. Besnard, L. Bramerie, J.-C. Simon, "Highly-sensitive measurement technique of relative intensity noise and laser characterization", Proceedings. SPIE 6603, Noise and Fluctuations in Photonics, Quantum Optics, and Communications, 2007
[131] C. J. O'Brien, M. L. Majewski, A. D. Rakic, "A critical comparison of high-speed VCSEL characterization techniques", Journal of Lightwave Technology, Volume 25, Issue 2, 2007
[132] A. Quirce, A. Valle, C. Gimenez, L. Pesquera, "Intensity Noise Characteristics of Multimode VCSELs", Journal of Lightwave Technology, Volume 29 , Issue 7, 2011
[133] Agilent Technologies,"Lightwave signal analyzers measure relative intensity noise," Product Note 71400-1, 2000.
[134] "Noise Figure Measurement Accuracy – The Y-Factor Method", Agilent Technologies Application Note 57-2, 2010
[135] S. Belkin, "Spectrum Analyzer Noise De-Embedding for Accurate Measurements", High Frequency Design, April 2005.
[136] "The Y Factor Technique for Noise Figure Measurements", Rohde & Schwarz Application Note 1MA178_0E, 2012
[137] MITEQ, 'Microwave Information Transmission Equipment', http://www.miteq.com/
[138] M. Sauer, A. Kobyakov, and J. George. "Radio Over Fiber for Pico cellular Network Architectures" Journal of Lightwave Technology. Volume 25, No.11. pp. 3301-3320, 2007
[139] M.D. Rosales, PhD Thesis on SiGe HPT, ESIEE-Paris, in Progress.
[140] A. Bdeoui, "Etude des éléments d'une liaison optique en microonde", PhD Thesis, le CNAM, Paris, 2006
[141] C. Rumelhard, C. Algani, A.-L. Billabert, 'Microwave Photonics Links' Components and Circuits, John Wiley & Sons, ISBN 978-1-84821-226-8, 2011
[142] J. Liu, "Practical behavioral modeling technique of power amplifiers based on load pull measurements", PhD Thesis, http://scholarcommons.usf.edu/etd/743, 2005

[143] C. Rapp, "Effects of HPA-nonlinearity on a 4-DPSK/OFDM signal for a digital sound broadcasting system", Proceedings of the Second European conference on satellite Communications, Belgium, 1991.
[144] Adel A.M. Saleh, “Frequency-Independant and Frequency-Dependant Nonlinear Models of TWT Amplifiers”, IEEE Transactions on Communications, Volume com-29, Issue 11, 1981.
[145] A. Ghobani and M. Sheikhan, “The effects of solid state power amplifier (SSPA) nonlinearities on M-PSK and M-QAM signal transmission,” Sixth International Conference on Digital Processing of Signals in Communications, pp. 193–197, UK, 1991
[146] S.A. Billings, S. Y. Fakhouri, "Nonlinear system identification using Hammerstein model", International Journal of Systems science, Volume 10, Issue 5, pp.567-578, 2007
[147] D. Bauer, B. Ninness, "Asymptotic properties of least squares estimates of Hamerstein-Wiener models", International journal of control, Vol.75, No.1, pp. 34-51, 2002
[148] L. Ding, G. Tong Zhou, R. Morgan, “A Robust Digital Baseband Predistorter Constructed Using Memory Polynomials”, IEEE Transactions on Communications, Volume 52, Issue, pp. 159-165, 2004
[149] M. Schetzen, “The Volterra and Wiener Theories of Nonlinear Systems”, New York: Wiley 1980
[150] H. M. Salgado and J. J. O’Reilly, “Volterra series of distortion in semiconductor lasers”, IEE Proceedings- J Optoelectronics, Volume 138, Issue 6, 1991
[151] D. Coelho, J.M.B. OLiveira, L.M. Pessoa, J.C.S. Castro, H.M. Salgado, "Experimental and theoretical performance assessment of WiFi-over-fiber using low cost directly modulated VCSELs”, ICTON 2012 - 14th International Conference on Transparent Optical Networks, UK, 2012.
[152] C. H. Cox III., G. E. Betts, and L. M. Johnson, “An analytic and experimental comparison of direct and external modulation in analog fiber-optic links”, MTT, Volume 38, Issue 5, pp. 501–509, 1990
[153] C.H. Cox, “Gain and noise figure in analogue fiber-optic links”, IEE Proceedings Journal Optoelectronics, Volume 139, Issue: 4, 1992
[154] C.H. Cox, E.I. Ackerman, G.E. Betts, “Relationship between gain and noise figure of an optical analog link”, IEEE MTT-S International Microwave Symposium Digest, Volume 3, 1996
[155] C. H. Cox III, E. I. Ackerman, G. E. Betts, J. L. Prince, “Techniques and Performance of Intensity- Modulation Direct-Detection Analog Optical Links”, IEEE Transactions on Microwave Theory and Techniques, Volume 45, No.8, pp. 1375-1383, 1997
[156] E. I. Ackerman, C. H. Cox III, “State of the art in analog fiber-optic link technology”, ISSSE 98. 1998 URSI International Symposium on Signals, Systems and Electronics, 1998
[157] E.I Ackerman. C. Cox III, G. Betts, H. Roussell, F. O'Donnell, K. Ray, “Input impedance conditions for minimizing the noise figure of an analog optical link”, IEEE Transactions on Microwave Theory and Techniques, Volume 46, Issue 12, 1998
[158] E. I. Ackerman, “The effective gains and noise figures of individual components in an analog photonic link”, International Topical Meeting on Microwave Photonics, Budapest, pp. 369-372, 2003
[159] C. H. Cox III, E. I. Ackerman, G. E. Betts, J. L. Prince, “Limits on the Performance of RF-Over-Fiber Links and Their Impact on Device design”, IEEE Transactions on Microwave Theory and Techniques, Volume 54, No.2, pp. 906-920, 2006
[160] E.I. Ackerman, W.K. Burns, G. Betts, J.X. Chen, J.L. Prince, M.D. Regan, H.V. Roussell, C.H. Cox III, “RF-over-fiber links with very low noise figure”, Journal of Lightwave Technology, Volume 26, No; 15, 2008
[161] H.A. Haus, "Noise Figure Definition Valid From RF to Optical Frequencies, IEEE Journal Selected Topics in Quantum Electronics, Volume 6, pp.240-247, 2000.
[162] D.M. Baney, P. Gallion, R.S. Tucker, “Theory and Measurement techniques for the noise figure of optical amplifiers”, Optical fibre Technology 6, 122-154, 2000, pp.122-154.
[163] R.S. Tucker, D.M. Baney, "Optical Noise Figure: Theory and Measurements", Optical Fiber Communication Conference, Volume 3, pp. W11-1-3, 2001
[164] I. Frigyes, B.G. Habermajaer, A. Molnar, A. Seeds, F. Som, “Noise and loss characteristics of microwave direct modulated optical links”, 27th European Microwave Conference, Volume 1, 1997
[165] A. Bdeoui, A.-L. Billabert, J.-L. Polleux, C. Algani and C. Rumelhard, “Definition of Both Opto-microwave S-parameters and Noise Figures for the Elements of an IMDD Microwave Photonic Link”, 12th Microcoll, Budapest, 14-16, 2007

[166] G. Baudoin, 'Radiocommunications Numérique', 2nd éd., Dunod, Paris, 2002
[167] "Molecular Technology GmbH",www.mt-berlin.com
[168] M. Kang, S. Park, K. Kim, S.-M. Han, J. Lim, K. Choi and D. Ahn, "A New Extraction Method for the Characteristic Impedance and Effective Dielectric Constant of Transmission Line with DGS", IEEE International Symposium on Radio-Frequency Integration Technology, 2009
[169] J. Grzyb and G. Tröster, "S Matrix versus ABCD Chain Matrix Formulation in Probe-tip Calibrations", Signal Propagation on Interconnects, 6th IEEE Workshop on. Proceedings, 2002
[170] TDK Electronics Europe GmbH available in www.tdk-components.de/
[171] AVX corporation available in http://www.avx.com/
[172] R.A Shafik, S. Rahman and R. Islam, "On the Extended Relationships Among EVM, BER and SNR as Performance Metrics", International Conference on Electrical and Computer Engineering, 2006
[173] L. F. Tiemeijer, R. J. Havens, "A Calibrated Lumped-Element De-Embedding Technique for on-wafer RF Characterization of High-Quality Inductors High-speed Transistors", IEEE Transactions on Electron Devices, Volume 50, No. 3, 2003
[174] H. Xu et E. Kasper, "A De-embedding Procedure for One-port Active mm-Wave Devices", 10th Topical Meeting on Silicon Monolithic Integrated Circuits in RF Systems, pp. 37-40, 2010
[175] ORIGIN project available in https://www.youtube.com/watch?v=XZcIUNFLk40
[176] "European researchers demonstrate reliability of IQE grown VCSEL devices at 40 Gbit/s", http://www.iqep.com/news-2011/nov_10_11.asp
[177] Vertical Integrated systems, Press Releases, "Technology breakthrough: 40G VCSEL", 2009, http://www.v-i-systems.com/presse_e/detail.php?nr=147&rubric=Presse_en&
[178] BeamPROP™ User Guide, RSoft Inc., 200 Executive Blvd, Ossining, NY 10562.
[179] M. D. Feit and J. A. Fleck, Jr., "Computation of mode properties in optical fiber waveguides by a propagating beam method", Applied Optics, Volume 19, No.7, pp. 1154-1163, 1980.
[180] P. Danielsen, "Two-dimensional propagating beam analysis of an electro optic waveguide modulator", IEEE Journal Quantum Electronics, Volume 20, pp. 1093-1097, Sept. 1984.
[181] A. Neyer, W. Mevenkamp, L. Thylen, and B. Lagerstrom, "A beam propagation method analysis of active and passive waveguide crossings", IEEE Journal Lightwave Technology., Volume 3, pp. 635-642, Mar. 1985.
[182] L. Thylen, E. M. Wright, G. I. Stegeman, C. T. Seaton, and J. V. Moloney, "Beam-propagation method analysis of a nonlinear directional coupler", Optics. Letters, Volume 11, No.11, pp. 739-741, 1986.
[183] M.D. Feit and J.A. Fleck, "Light propagation in graded-index optical fibers", Applied Optics. 17, 3990, 1978.
[184] D. Yevick and B. Hermansson, "Efficient beam propagation techniques", Journal Quantum Electronics. 26, 109 (1990).
[185] R. Scarmozzino and R.M. Osgood, Jr., "Comparison of finite-difference and Fourier-transform solutions of the parabolic wave equation with emphasis on integrated-optics applications", Journal Optoelectronics Society of America. A 8, 724, 1991.
[186] D. Yevick and M. Glasner, "Analysis of forward wide-angle light propagation in semiconductor rib waveguides and integrated-optic structures", Electronics Letters. 25, 1611, 1989.
[187] G.R. Hadley, "Wide-angle beam propagation using Pade approximant operators", Optics Letters 17, 1426, (1992);
[188] G.R. Hadley, "Multistep method for wide-angle beam propagation", Optics Letters 17, 1743, 1992.
[189] H.J.W.M. Hoekstra, G.J.M. Krijnen, and P.V. Lambeck, "New formulations of the beam propagation method based on the slowly varying envelope approximation", Optics Communications, 97, 301, 1993.
[190] R. Clauberg and P. Von Allmen, "Vectorial beam propagation method for integrated optics", Electronics Letters. 27, 654, 991.
[191] W.P. Huang and C.L. Xu, "Simulation of three-dimensional optical waveguides by a full-vector beam propagation method", Journal Quantum Electronics 29, 2639, 1993.
[192] H. Rao, R. Scarmozzino, and R.M. Osgood, Jr., "A bidirectional beam propagation method for multiple dielectric interfaces", Photonics Technology Letters. 11, 830, 1999.

[193] MicroChem Corp., 90 Oak St. Newton, MA 02464, www.microchem.com
[194] A. Borreman, S. Musa, A.A.M. Kok, M. B. J. Diemeer and A. Driessen, “Fabrication of Polymeric Multimode Waveguides and Devices in SU-8 Photoresist Using Selective Polymerization”, Proceedings Symposium IEEE/LEOS Benelux Chapter, 2002, Amsterdam
[195] K. B. Mogensen, J. El-Ali, A. Wolff, and J. P. Kutter, “Integration of polymer waveguides for optical detection in micro fabricated chemical analysis systems”, Applied Optics, Volume 42, No.19, 2003
[196] C. Choi, L. Lin, Y. Liu, J. Choi, L. Wang, D. Haas, J. Magera, and R. T. Chen, “Flexible Optical Waveguide Film Fabrications and Optoelectronic Devices Integration for Fully Embedded Board-Level Optical Interconnects”, Journal of Lightwave Technology, Volume 22, No.9, 2004
[197] B. L. S. Pong, R. Pamnidigantham, and C S Premachandran, “Prototype Development for Chip-Chip Interconnection by Multimode Waveguide”, Electronics Packaging Technology Conference, Singapore, 2005
[198] Y.-M. Chen, C.-L. Yang, Y.-L. Cheng, H.-H. Chen, Y.-C. Chen, Y. Chu, T.-E. Hsieh, “10Gbps Multi-Mode Waveguide for Optical Interconnect”, Electronic Components and Technology Conference, 2005
[199] M. Diemeer, L. Hilderink, R. Dekker, and A. Driessen, “Low-Cost and Low-Loss Multimode Waveguides of Photodefinable Epoxy”, IEEE Photonics Technology Letters, VOLUME 18, NO.15, AUGUST, 2006
[200] M. Nordström, D. A. Zauner, A. Boisen, and J. Hübner, “Single-Mode Waveguides With SU-8 Polymer Core and Cladding for MOEMS Applications”, Journal Of Lightwave Technology, Volume 25, No.5, 2007
[201] A. Ghannam, C. Viallon, D. Bourrier, T. Parra, “Dielectric Microwave Characterization of the SU-8 Thick Resin Used in an Above IC Process”, Proceedings of the 39th European Microwave Conference (EuMA), Rome, 2009

Résumé

R.1 - Résumé general

Les technologies de communication sans fil sont devenues indispensables dans la vie de chacun ses dernières années. Elles offrent des services croissants innovants et une mobilité accrue, de la communication mobile aux réseaux locaux. Cette thèse s'inscrit dans le cadre du projet français FUI8-ORIGIN qui vise à développer les performances des réseaux domestiques en apportant des solutions sans multi-Gigabits faiblement radiatives, économes et pérennes. La solution ORIGIN est caractérisée par l'action complémentaire de deux technologies: les communications sans fil 60 GHz, avec notamment la création récente en Janvier 2013 de la nouvelle norme WiFi 60GHz, et la mise en place d'une infrastructure Radio-sur-Fibre (RoF) afin d'étendre la propagation de ses signaux radio fortement atténués par l'atmosphère et les murs, au sein de l'ensemble de la maison.

Le projet a une visée pré-compétitive et doit se doter d'un véritable prototype à l'échelle 1:1. Il couvrira ainsi 4 pièces d'une maison standard. Basé sur des transducteurs RoF et une architecture multipoint à multipoint pour couvrir les différentes pièces d'une maison, il doit mettre en jeu des dispositifs bas couts et performants permettant la transmission des signaux 60GHz eu travers de la liaison optique à dégradation minimale, respectant les contraintes de la norme.

Cette thèse porte sur le développement des composants et modules optoélectroniques bas couts, permettant d'assurer ces contraintes. Le travail implique de couvrir de la puce semi-conducteur au modules et jusqu'au système intégré dans le démonstrateur.

Le choix de la source LASER et du photodétecteur est très important car il impose l'architecture de transducteur RoF. Notre choix s'est porté sur dispositifs multimode à 850nm (GaAs VCSEL et SiGe HPT) qui sont compatibles avec les normalisations existantes des réseaux fibres dans la maison, et permettent des contraintes relâchées sur le couplage optique qui garantissent l'accès à des solutions bas cout. En termes de performances, ces dispositifs sont

limités à quelques dizaines de Gigahertz en bande passante, ce qui nécessite d'envisager une architecture à fréquence intermédiaire (IF).

Les puces sélectionnées sont caractérisées de manière précise en développant des bancs de mesures adaptées aux applications analogiques RoF. Des substrats d'interconnexions sont développés pour permettre le couplage optique et l'interconnexion électrique des puces et ainsi la création de modules de type Transmitter Optical Sub-Assemblies (TOSA) ou Receiver Optical Sub-Assemblies (ROSA). Ce développement est poussé de façon à intégrer de façon hybride des étages d'amplification en aval et amont des composants optiques, ainsi que des étages d'adaptations passifs. Les questions de couplage optique ont été traitées par une technique de couplage classique en utilisant d'abord une lentille sphérique.

Les performances RoF ont été évaluées et comparées en termes de réponse en fréquence, de bruit et de non-linéarités. Nous avons poursuivi l'approche actuelle des grandeurs optique-microondes, telles que le gain et le facteur de bruit, et l'avons étendu aux non-linéarités en définissant les points de compression à 1dB optique-microondes (IP1dB,OM et OP1dB,OM), les points d'interception d'ordre trois optique-microondes (IIP3OM et OIP3OM), et la grandeur système d'erreur vectorielle d'amplitude optique-microonde (EVMOM), qui chacune permette d'isoler et caractériser la performance individuelle des composants optiques ou opto-électroniques pris individuellement.

Ces grandeurs sont présentées puis exploitées dans un développement de modèle comportemental, permettant à la fois l'extraction des performances individuelles des composants et le design de l'ensemble du système.

Un dimensionnement complet de l'infrastructure Radio-sur-Fibre pour le démonstrateur est ensuite mené, intégrant et dimensionnant le bilan de liaison global à partir modules et cartes réalisés et développés par les partenaires du projet. Le module transmetteur Radio-sur-Fibre (TRoF) est ainsi conçu, assemblé et testé. Les performances du module ont été mesurées et simulées à chaque étape de la procédure d'intégration. Le démonstrateur final basé sur l'architecture multipoint-à-multipoint a été réalisée à l'aide d'un nœud central optoélectronique pour la répartition du signal et d'une Green Box permettant le contrôle de l'allumage des différentes pièces, et ainsi la rationalisation du rayonnement et de la consommation du système. Une transmission bidirectionnelle en temps réel entre deux dispositifs de WirelessHD commerciaux à ~3 Gbit/s a été démontrée.

Dans une dernière section de cette thèse, des directions pour améliorer les lasers à cavité émettant par la surface (VCSEL) et les phototransistors SiGe sont explorées. Des VCSEL analogiques avec une bande passante de plus de 25 GHz sont développés avec la société Philips ULM Photonics et mesurés. Notre action s'est concentrée sur les dimensions latérales de la structure, en bénéficiant des améliorations des couches verticale de la part de ULM Photonics. Outre les dimensions du VCSEL propre, ce travail a aussi visé l'amélioration des lignes d'accès pour permettre à la fois une meilleure dissipation thermique et une meilleure adaptation réactive du VCSEL à son électronique amont. Une nouvelle technologie de couplage optique collective et passive est enfin proposée. Originale et brevetée à l'occasion de ce travail, elle permet le couplage optique vertical à la fibre optique multimode et monomode de dispositifs optoélectroniques de petites tailles, inférieurs à 10µm, ainsi permettant simultanément de réduire les pertes de couplage, d'augmenter la fréquence de fonctionnement des composants couplés en réduisant leur dimensions, et de réduire le cout et le temps de réalisation du couplage.

R.2 - Introduction generale

Ce chapitre d'introduction générale a pour but de donner une vue générale des motivations des travaux de cette thèse, d'exposer le sujet et d'en décrire les objectifs.

R.2.1 - Contexte

La technologie sans fil à MultiGbit/s pour les réseaux local domestique (HAN) est un développement actuel qui fera partie du futur de chacun. Le développement de nouveaux services et de technologies sans fil innovantes nous mène vers de plus en plus de débits pour atteindre le besoin et la capacité du Gigabit par seconde. Les services à haute définition (HD) deviennent la réalité de nos jours et un exemple où le multiGbit/s est déjà nécessaire. Filaire par le câble HDMI il devient sans fils avec les normes et produits commerciaux WirelessHD. Une approche de cloud domestique doit être considérée dans ces évolutions avec l'accès à l'ensemble des services et appareils sans fil dans n'importe quel endroit dans la maison en même temps de manière ubiquitaire.

Cependant, le classique et le plus populaire Wi-Fi (Wireless-Fidelity) basé sur la norme IEEE 802.11, en utilisant la bande de fréquence centimétrique, permet des débits jusqu'à 600 Mbit/s. Une solution consiste en l'utilisation d'ondes dans la bande millimétrique, de 57GHz à 66GHz. Différentes normes dans cette bande ont été déjà élaborées, dont plus récemment en Janvier 2013, la technologie Wi-Fi IEEE 802.11ad, qui permet d'obtenir des débits de données jusqu'à 7 Gbit/s [16]. A cette bande de fréquences, l'absorption par l'oxygène est élevée, ce qui se traduit par une portée de communication, courte, de quelques mètres seulement (~10m). Cette caractéristique est très intéressante pour les réseaux domestiques en termes de sécurité de donnée, car le signal ne traverse pas les murs, reste ainsi limité généralement à une pièce et garantit ainsi de ne pas être reçu à l'extérieur du bâtiment restant ainsi confidentiel. Néanmoins, en raison de cette couverture restreinte, un réseau supplémentaire est nécessaire pour distribuer le signal haut débit à l'ensemble des pièces de la maison. Ici, l'inclusion de la technologie Radio-sur-Fibre semble très prometteuse, afin de proposer une solution bas cout, performantes et pérenne car capable de s'adapter aux évolutions futures de la technologie, le câble n'ayant intrinsèquement que peu de limitation de bande passante.

Le défi porte ici sur les dispositifs optoélectroniques de terminaison où des performances élevées et de faibles coûts sont des exigences fondamentales.

Sur une prospective d'intérêt du marché, notre proposition de connexion Wi-Fi 60 GHz au travers d'un réseau sans fil domestique multiGbit/s à infrastructure optique (RoF) est considéré comme l'une des solutions d'avenir pour l'habitat. En 2016, plus de 40% du marché total Wi-Fi devrait utiliser la bande de fréquence de 60 GHz, d'après une analyse proposée en juin 2012, [17]. Même si un retard d'un an a décalé la publication de la norme de Janvier 2012 à Janvier 2013, le développement des infrastructures RoF pour ce besoin est considéré comme essentiel dans les quelques années à venir.

R.2.2 - Objectifs de la thèse

Ce sujet de thèse est proposé dans le cadre d'un projet national consacré au développement de l'optoélectronique et de la photonique dans le domaine de l'infrastructure RoF pour des communications sans fil à 60 GHz. Le nom du projet est ORIGIN - Optical Radio Infrastructure

for Gbit/s Indoor Network. Le principal objectif de notre travail est le développement technologique des transducteurs RoF à bas coût pour le réseau domestique sans fil à des débits de données élevés (10 Gbit/s) et la participation à l'ensemble de la conception du système. Comme nous pouvons le voir dans la figure ci-dessous, un transducteur RoF générique composé de modules simples nous aident à définir nos objectifs de travail.

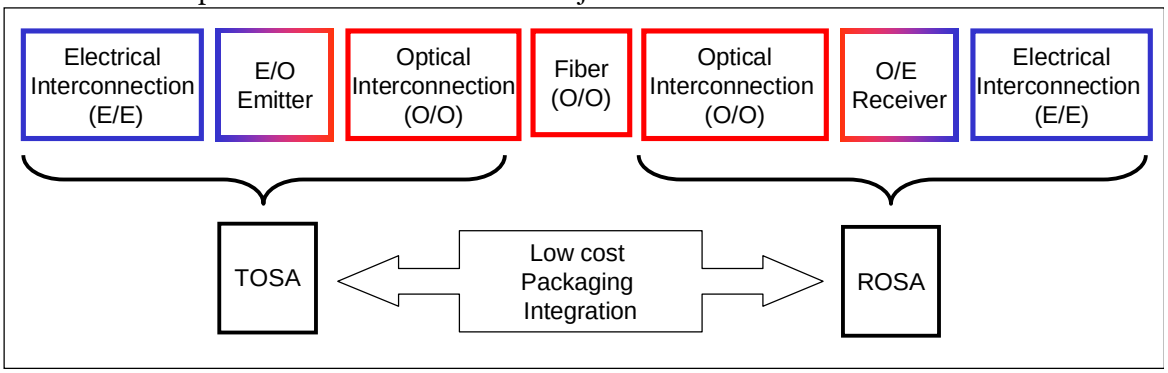

Modules transducteur Radio-sur-Fibre

Le cœur du transducteur RoF est composé de dispositifs actifs pour l'émetteur électrique-optique (E/O), et pour le récepteur optique-électrique (O/E). Les objectifs de ce travail de thèse sur ces modules sont les suivants:

- La caractérisation d'émetteur E/O et l'optimisation des performances. Des VCSEL GaAs multimode 850 nm sont considérés pour leur faible coût et leurs bonnes performances. Quelques degrés de liberté dans leur optimisation de design (*layout)* nous ont été permis, en termes de diamètre d'ouverture de la fenêtre optique et d'accès électriques. Leurs résultats de mesure seront introduits dans un modèle comportemental que nous avons développé pour inclure leurs réponses en fréquence, leurs non-linéarités et leur comportement en bruit.
- Caractérisation du récepteur O/E et optimisation des performances. Trois photodétecteurs sont considérés : Une photodiode de laboratoire New Focus de type PiN InGaAs, utilisée comme référence pour la caradctérisation des émetteurs E/O; un photorécepteur Finisar avec amplificateur trans-impédance intégré (TIA); et enfin un module photorécepteur basé sur des phototransistors bipolaires à hétérojonction (HPT) SiGe développé dans notre laboratoire. Ce dernier sera étudié en fonction de ses dimensions latérales, de sa configuration technologique et de ses conditions de polarisation et de connexions.

Les deux dispositifs, E/O et O/E, ont un impact important sur les performances de la liaison optique. Un outil de simulation est exploité pour prendre en compte l'influence individuelle de chacun de ces composants sur la liaison globale. Un modèle comportemental compatible avec des simulateurs conventionnels de système microondes (dans notre cas ADS Agilent) sera développé simultanément avec une nouvelle définition des grandeurs Optique-microondes. Ce modèle est utile de comprendre l'impact individuel de chaque dispositif sur les mesures de la liaison de système. Le développement du banc de mesures sera pris en compte pour obtenir des données précises en termes de caractéristiques statiques, dynamiques, non-linéaires et de bruit. Toutes ces données seront utilisées pour la modélisation comportementale de chaque dispositif. Des mesures système (EVM) seront effectuées et pourront valider les simulations système réalisées. Les modèles se montreront même capables de permettre d'extraire et d'affiner les paramètres individuels de chaque dispositif.

Le développement des interfaces électriques sera considéré pour l'intégration des puces et sera optimisé en termes de performances de transmission et réflexions en fonction de la fréquence. Des réseaux d'adaptation réactifs passifs seront développés pour réduire les pertes de réflexion et d'améliorer le gain du système et le rapport signal à bruit. Des circuits intégrés (IC) SiGe sont conçus pour alimenter les VCSEL en amont de la liaison par un amplificateur de puissance (PA) d'amplifier le signal reçu en aval de celle-ci par un amplificateur à faible bruit (LNA). Ces circuits sont conçus et intégrés.

L'interface optique, qui permet le couplage de la lumière entre l'émetteur E/O et la fibre, entre la fibre et le détecteur O/E, sera sur deux fronts : une solution à base de réceptacle mécanique portant une lentille sphérique; une solution à guide d'onde optique en polymère de type taper. La conception et la simulation des structures de guide d'ondes optiques seront considérées comme la méthode d'intégration.

Le Packaging et l'intégration des dispositifs optoélectroniques multimodes sont les prochains suivants: de la simple puce VCSEL jusqu'au module TOSA; de la puce HPT jusqu'au module ROSA. Là encore, des caractérisations et simulations seront effectuées pour chaque dispositif, avec notamment la comparaison des performances entre la puce et le résultat de sa mise en boitier. La dernière étape est l'intégration de ces modules dans le transducteur RoF (TRoF) qui sera utilisé dans le système de communication sans fil multi-Gigabit. L'intégration et la caractérisation des performances du système à l'échelle d'une maison de quatre pièces sont les objectifs finaux afin d'implémenter un démonstrateur à taille réelle.

R.3 - RoF dans le réseau sans fils domestique : le Project ORIGIN

Ce chapitre II présente l'état de l'art et la problématique des systèmes des communications sans fil à multiGbit/s dans le contexte des réseaux domestiques (HAN). Le contexte du projet d'ORIGIN y est présenté. Il fournit également un état de l'art, particulièrement sur les VCSEL de manière générale, et sur les phototransistors bipolaires à hétérojonction (HPT) SiGe/Si de manière particulière, car ces éléments constituent le cadre principal de notre travail au sein du projet avec l'objectif de mettre en place des solutions optoélectroniques faible coût.

L'évolution du réseau sans fil à large bande vers les communications multiGbit/s est étudiée, démontrant un intérêt particulier pour les technologies de communication sans fil à 60 GHz, avec les normes ECMA-387, IEEE802.15.3c et dernièrement la norme Wi-Fi 60 GHz, IEEE 802.11ad. Cette dernière norme est porteuse d'un développement important. Elle répond à la question d'un réseau local de communication courte distance (indoor) à multiGbit/s. Néanmoins la bande de fréquence s'accompagne d'une question de la limitation de portée en raison de l'absorption de l'air et des murs. Une solution à cette question (communication limité à une seule pièce) est proposée par le projet ORIGIN pour étendre la couverture radio par le biais d'une architecture RoF permettant ainsi la communication entre plusieurs pièces (figure ci-dessous).

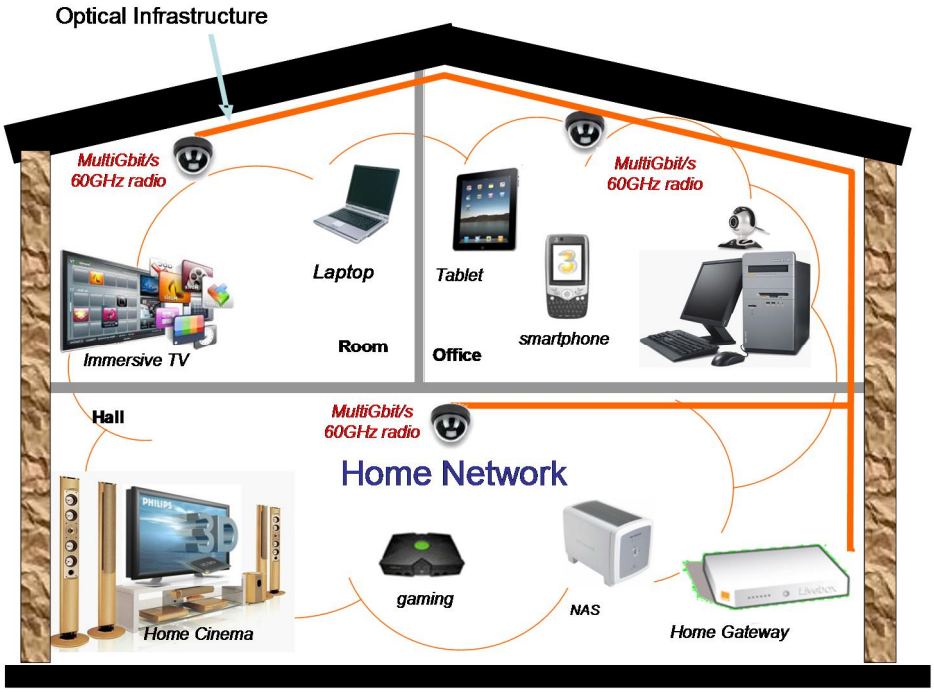

Illustration du concept du projet ORIGIN

Le projet ORIGIN propose d'explorer les deux technologies pour fournir une communication indoor à multiGbit/s et multi-pièces permettant ainsi l'approche de cloud domestique. L'objectif est de développer un système complet basé sur des transducteurs RoF et sur une architecture multipoint-à-multipoint. La technologie RoF y est présentée par les principes fondamentaux et l'état de l'art concentré en les technologies de dispositifs optoélectroniques multimode fonctionnant à 850 nm pour des applications 10 Gbps: VCSEL et HPT. La raison de ce choix tient dans le compromis entre performances et flexibilité en termes d'intégration et couplage optique pour obtenir une solution bas coût.

Ce choix oblige à l'utilisation d'une fréquence intermédiaire dans le module trasnducteur Radio-sur-Fibre (TRoF). Trois générations de transducteurs TRoF sont prévus dans la stratégie du projet ORIGIN : la première utilise des dispositifs commerciaux purs; la seconde, une solution hybride entre dispositifs commerciaux et dispositifs développés en laboratoire ; et la troisième vise à exploiter l'ensemble des développements technologiques, à la fois sur l'émetteur optique VCSEL et le récepteur optique SiGe. L'architecture point-à-point (tunnel optique) qui est une étape à la validation du système et l'architecture multipoint-à-multipoint cible sont présentées.

Le concept d'architecture d'ORIGIN est considéré en explorant l'architecture multipoint à multipoint optique avec soit un multiplexage électrique (MME) ou le multiplexage optique (MMO). Les solutions MME et MMO sont comparées en termes d'avantages et d'inconvénients.

R.4 - Caractérisation de puce E/O et O/E

Ce chapitre III traite de la caractérisation sous pointes des VCSEL et HPT sous formes de puces. Il intègre le montage minutieux des bancs de mesures adaptés aux applications RoF. Un photodétecteur de référence (pour le cas VCSEL), qui a une réponse en fréquence très plate et un comportement linéaire, est utilisé pour extraire les performances du laser. Une caractérisation complète de différents liens optiques est menée en termes de performances

statiques, réponse fréquentielle, de comportement en bruit et de non-linéarités comme le Spurious Free Dynamic Range (SFDR). Les performances EVM du système dans le contexte des normes de 60 GHz, sont également considérés. Chaque banc de mesure est présenté ainsi que les procédures de calibration attenantes et la prise en compte de la précision de mesure, pour le banc de mesure de RIN.

Les bancs de mesures ont permis la caractérisation notamment de VCSEL 10Gbps fournis par Philips ULM Photonics mesurés au travers d'une photodiode de laboratoire NewFocus, utilisée comme référence, de très grande linéarité et de fréquence à 3dB supérieure à 25GHz. Le banc sous pointe est décrit dans la figure ci-dessous :

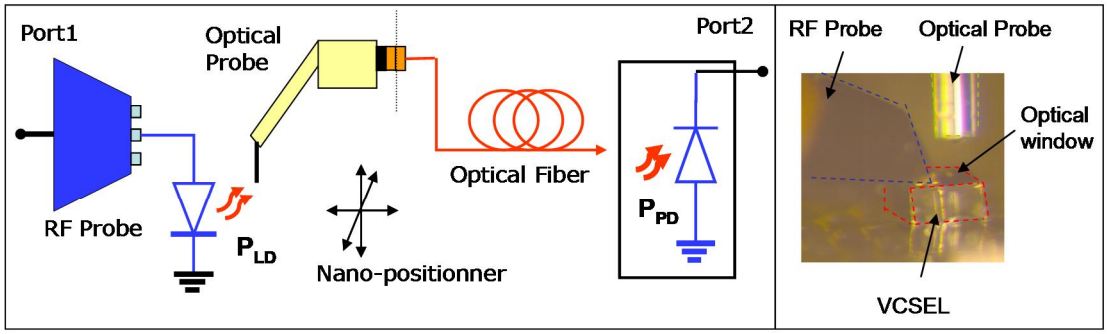

Banc de mesure sous pointes pour la puce VCSEL: a) schématique avec un 850 nm GaAs based VCSEL et la photodiode référence; b) photo du couplage en RF et optique sur le VCSEL.

Les VCSEL Philips ULM Photonics 10Gbps fonctionnent à 850 nm avec une fenêtre optique de 8 µm de diamètre. Deux paramètres importants qui influent fortement les performances de liaison sont le taux de couplage optique et la dissipation thermique du VCSEL. La puissance optique maximale rencontrée est de 3,8mW avec une responsivité de 0,52A/W, en considérant un couplage optique d'environ 100%. Le VCSEL présente un spectre optique caractéristique d'un comportement multimode transverse. La déviation du spectre de longueur d'onde pour la puce nue sous pointes en l'absence de dissipateur thermique est 0,5 nm/mA, indiquant un échauffement de la puce à 91°C pour un courant de 10mA et une température ambiante de 20°C.

Les mesures dynamiques ont démontrées une bande passante de 12,3GHz à 10mA, une déviation du spectre de longueur d'onde de 0,5 nm/mA, un MCEF de 5,995 GHz/√mA et un RIN inférieur à -140 dB/Hz de 1GHZ à 6GHz pour des courants de polarisation supérieurs à 8mA. Les mesures réalisées ont également permis d'optimiser le courant de polarisation du VCSEL (8 à 10mA) et de sélectionner sa fréquence de fonctionnement optimale (autour de 4 GHz) pour l'application Radio-sur-Fibre visée. La liaison RoF élémentaire (VCSEL + photodiode NewFocus) a été mesurée avec un IP1dB de 15dBm, un IP3 de 12dBm, un SFDR de 99 dB.Hz2/3 à 5GHz, pour un courant de polarisation 10mA. Un minimum de dégradation EVM par rapport à la mesure Back-to-Back de 1 % est obtenu avec une dynamique de puissance de 35 dB pour une dégradation de l'EVM de moins de 20 %, correspondant à la transmission d'un canal de 2GHz en norme IEEE802.15.3C mode HSI transposé à la fréquence intermédiaire de 5GHz.

Dans le cas de la caractérisation de HPT SiGe 850 nm (figure ci-dessous), deux structures ont été caractérisées afin de sélectionner la structure qui sera intégrée et couplée dans un

module packagé de type ROSA pour le démonstrateur. Il s'agit de phototransistors SiGe de fenêtres optiques de 10x10 µm2 et de 30x30 µm2, dont l'émetteur la base et le collecteur sont tous soumis à l'éclairement du signal optique. Un module TOSA équipé en interne d'un VCSEL 10 Gbps précédemment testé a été utilisé comme référence.

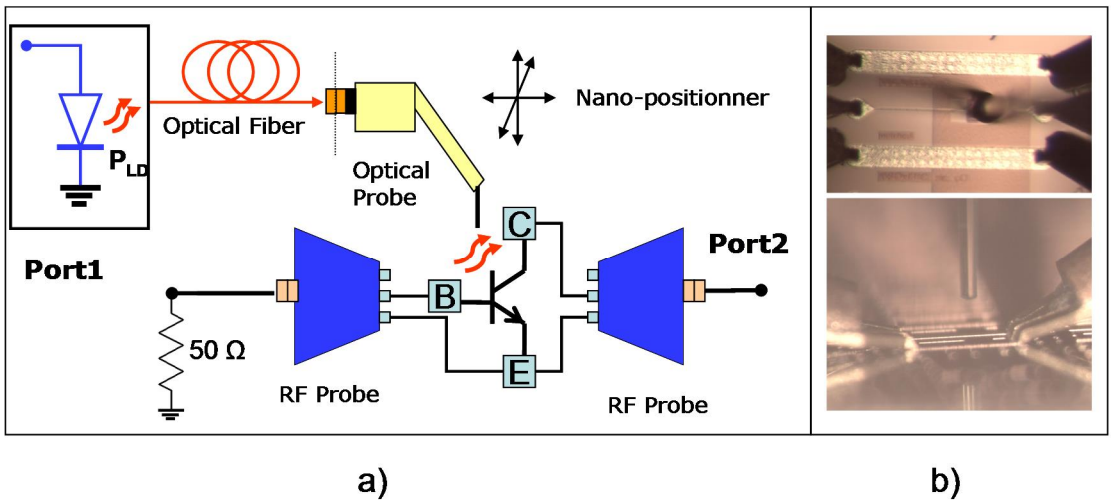

Banc de mesure sous pointes pour la puce HPT: a) schématique avec un HPT et la référence 850 nm TOSA; b) photo du couplage en RF et optique sur le HPT.

Il est démontré qu'un compromis entre la taille et les performances doit être fait. Les petites structures sont des dispositifs plus rapides mais avec présentent un taux de couplage optique plus faible. Afin de pouvoir être intégrée par la suite dans le démonstrateur ORIGIN, et par souci de disponibilité, une solution de HPT, dite 2T-HPT, sans connexion de la base est sélectionnée. Le projet ORIGIN fixe la fréquence intermédiaire à 5GHz. A cette fréquence, il apparait que la structure de 10x10µm² présente un gain de 7 dB plus élevé que le 30x30 µm2 avec une responsivité de 1,45 A/W en DC et de 0,034 A/W à 5 GHz (pertes de couplage optique à la sonde optique multimode inclues).

R.5 - Design de la liaison Radio-sur-Fibre

Ce chapitre IV porte sur le dimensionnement de liaisons Radio-sur-Fibre au sens général et la mise en place des outils nécessaires. L'accent est porté sur la bonne description de l'impact des performances individuelles des composants optoélectroniques et optiques sur le système complet.

La modélisation de dispositifs optoélectroniques pour les applications Radio-sur-Fibre nécessite la définition de grandeurs optique-microondes. Celles-ci sont présentées et élargie à l'ensemble des grandeurs non-linéaires et systèmes appropriées. Un modèle comportemental est également développé en utilisant l'outil Symbolically Defined Device (SDD) du logiciel ADS, pour permettre une analyse plus complète.

Les grandeurs optique-microondes développées couvrent les trois caractéristiques analogiques principales: la réponse en fréquence, le bruit et les non-linéarités. Ces grandeurs sont définies en s'appuyant sur une représentation individuelle de chaque composant, microonde, optique ou optoélectronique. La notion de puissance équivalente optique-microonde et la notion de puissance de bruit optique-microondes équivalentes, en tout point

d'une liaison, est rappelée. Elle permet ainsi une représentation en quadripôle électrique équivalent sur lesquels l'ensemble des notions microondes peuvent s'appliquer. Les notions de gain optique-microonde (GOM), facteur de bruit optique-microondes (NFOM) sont rappelées. Les définitions de point de compression optique-microonde (P1dBOM), point d'interception d'ordre trois optique-microonde (IP3OM), plage dynamique sans parasite optique-microonde (SFDROM) et enfin vecteur d'erreur d'amplitude optique-microonde (EVMOM) sont été présentés. Elles sont notamment appliquées aux VCSEL et aux photorécepteurs étudiés.

Chaque bloc du système RoF est ensuite considéré dans un modèle comportemental optique-microonde flexible, mis en œuvre sur le logiciel de simulation circuit et système électriques (Agilent ADS). Le modèle a été exécuté avec succès. Les simulations sont validées par comparaison aux mesures, ceci dans différentes configurations et différentes combinaisons de composants RoF. Le modèle a permis, non seulement de simuler le système RoF complet et identifier les points critiques, mais s'est montré capable de permettre l'extraction fine des paramètres individuels de chacun des composants, notamment à partir des mesures uniques d'EVM. Une illustration de ce modèle et des caractéristiques qui l'alimentent est fournie sur la figure ci-dessous :

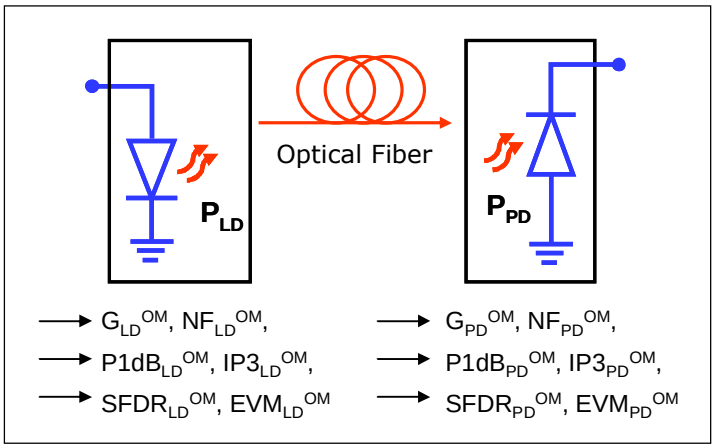

Illustration du modèle de chaque block RoF avec les grandeurs Opto-microonde correspondantes.

R.6 - Démonstrateur Final

Le chapitre V est consacré au dimensionnement et à la réalisation du démonstrateur final développé dans le projet ORIGIN.

La première partie porte sur le développement des modules packagés (TOSA et ROSA), avec le développement d'un substrat d'interconnexion transparent, Verre ou Saphir, pour la réalisation du couplage optique et des prises de connexions électriques. Les puces de VCSEL et des puces de 2T-HPT SiGe sont montés sur celui-ci. Le couplage optique est réalisé à l'aide d'une lentille sphérique d'un millimètre de diamètre montée dans une ferrule mécanique. Cette solution présente un coefficient de couplage de 60% pour les VCSEL 10Gbps de Philips ULM Photonics et de 35% pour le 2T-HPT de 10µm. Les lignes d'accès et de transmission sont optimisées. De bons résultats ont été trouvés en termes de dissipation thermique pour le VCSEL

avec une dérive spectrale réduite de 0,237 nm/mA et une température maximale de puce de 47,1°C seulement à 10mA de courant de polarisation.

Des réseaux d'adaptation, réactifs et passifs, sont préparés. Quoique non performants dans leur réalisation première, la bonne confrontation des simulations aux mesures lors d'un retro-engineering nous permettent de disposer d'un outil fiable pour de prochaines réalisations, notamment conduites au chapitre suivant. Des circuits intégrés SiGe sont également associés au 2T-HPT de façon à construire un module ROSA SiGe complet de gain suffisant. Les performances du module TOSA complète (basé sur le VCSEL ULM) et du module ROSA (basé sur le HPT SiGe), sont comparés aux performances des puces qui ont été mesuré dans le chapitre III. Les modules TOSA présentent de très bonnes performances EVM, avec une dégradation maximale de 3 % par rapport à la mesure EVM back-to-back. Les modules ROSA ont caractérisés. Ils présentent une de dégradation d'EVM de 16 %. Il s'agit d'une première au niveau international. Quoiqu'importante, il s'agit d'un résultat encourageant qui bénéficiera certainement des évolutions d'un 2T-HPT vers un 3T-HPT, d'une amélioration du couplage optique et d'un meilleur respect de la largeur de bande du canal par une intégration plus poussée du réseau d'adaptation.

La deuxième partie s'attache au dimensionnement des transducteurs TRoF en termes de budget de puissance sous deux configurations distinctes : l'une comprenant un ROSA commercial Finisar (configuration RoF2), l'autre comprenant le module à base de 2T-HPT SiGe en tant que ROSA (configuration RoF3). Le système est dimensionné pour atteindre la performance requise pour la transmission de signaux 802.15.3c, à savoir une PIRE de 20dBm maximum de réémission (c'est-à-dire 7dB en dessous des maximum autorisés), un canal de 2GHz centré autour de 60,48GHz (canal n°2) et une variation de la portée entre 1m et 5m pour chaque pièce. Le point fixe de la puissance d'entrée du VCSEL est sélectionné sur la base des données expérimentales. Cette puissance est de -4,6dBm. La réalisation de ce budget de liaison est mené grâce aux formules de compositions des gains optique-microondes (multiplication des gains) et des facteurs de bruit optique-microondes (formule de Friis vérifiée). L'architecture élémentaire point-à-point, dite tunnel optique, (P2P) et les architectures multipoint-à-multipoint (MME et MMO) sont traitées. Les points critiques sont identifiés et des solutions proposées. L'architecture de MMO se révèle être une option très intéressante pour le futur mais relève quelques questions à résoudre: celui du battement optique entre les lasers et celui de la saturation de la puissance optique reçue par les photodétecteurs. L'architecture MME est privilégiée pour le démonstrateur.

La dernière partie présente le système complet, tel qu'il est intégré dans le démonstrateur final. Il comprend la carte centimétrique, la carte de l'oscillateur local, la carte d'alimentation et la carte millimétrique. Chacune de ces parties, fabriquée et assemblée par les différents partenaires du projet ORIGIN, y est décrite. Les résultats expérimentaux principaux y sont donnés. Il ressort un bon respect de l'ensemble des contraintes de dimensionnement, hormis un défaut du module de transmission 60GHz qui présente un défaut de 20dB de gain par rapport aux spécifications.

La liaison de communication point-à-point avec deux transducteurs est cependant une réussite. Après optimisation et réglage des cartes, une transmission de données réelles Wireless HDMI multiGbit/s 3Gbps est effectuée avec succès. La dernière étape comprend la notion de communication multipoint-à-multipoint en utilisant le nœud central et la gestion des signaux

d'alimentation par la Green Box, responsable de la distribution du signal et la rationalisation de la consommation et du rayonnement.

Le démonstrateur final est finalement mis en œuvre (voir figure ci-dessous) en utilisant une communication entre deux chambres à partir d'une architecture multipoint-à-multipoint optique par multiplexage électrique (MME) à l'aide d'un nœud central de multiplexage 4x4 et un signal de commande pour les transducteurs. Un EVM de 16 % a été démontrée pour un scénario à deux chambres jusqu'à l'entrée du block mm-TX, qui représente une réalisation réussie en termes de performances. Les modules mm-TX, qui présentent un défaut de 20dB de gain, ajoutent un supplément de 14 % pour l'EVM, amenant à l'obtention d'un EVM globale de 30 %, comprenant les deux sauts (hop) et les défauts du banc de tests.

Les erreurs induites par cet EVM se sont avérées être compensée dans la transmission haut débit (~3 Gbit/s) par l'application de la correction d'erreur implémenté dans les modules commerciaux Gefen, proposant ainsi une intégration réelle réussie.

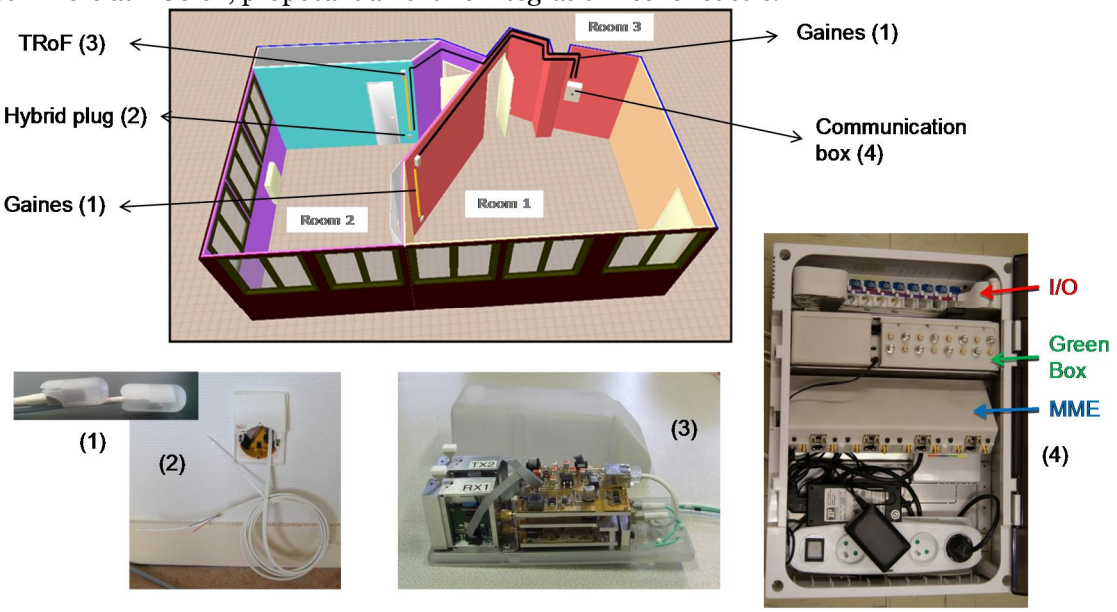

Démonstrateur final du projet ORIGIN organisé à France Telecom (Lannion)

R.7 - Développements des dispositifs optoélectronique pour la prochaine génération

Le chapitre VI présente les développements menés pour préparer les évolutions futures des transducteurs RoF. Deux orientations sont pointées: l'augmentation intrinsèque de la fréquence de fonctionnement des composants et l'amélioration du taux de couplage optique pour de petites structures.

Notre contribution sur l'augmentation de performances des VCSEL dits analogiques, portent la montée en fréquence au-delà de 20 GHz grâce à la modification de leur dessin de masques (voir figure ci-dessous), en termes de diamètre d'ouverture de la fenêtre optique, et de l'amélioration de leurs lignes d'accès RF, conjointement aux optimisations de couches verticales menées par Philips ULM Photonics.

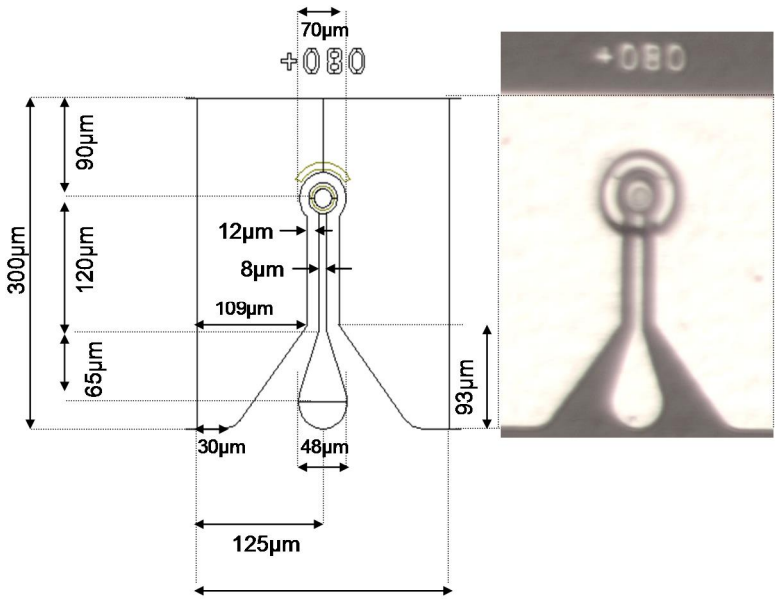

Layout de structure VCSEL à 20 Gbps (8 µm de diamètre)

Une bande passante de 20,5 GHz est démontrée pour un VCSEL de 8µm de diamètre. Elle varie de 14 GHz à plus de 25 GHz pour un diamètre d'ouverture optique entre 20 µm et 2 µm. Un compromis entre bande passante et gain optique-microonde doit être alors réalisé, en considérant que la réduction de taille augmente la fréquence de coupure, mais augmente la divergence du faisceau et rends donc plus difficile le couplage optique, réduisant ainsi le gain optique-microonde résultant. D'un autre côté, les dispositifs de plus grandes tailles facilitent le couplage de la lumière, donne un gain plus élevé à la liaison, mais augmentent la consommation et diminuent la fréquence de modulation. Le VCSEL à diamètre d'ouverture de 4 µm a été sélectionné et caractérisé de manière plus complète. Il montre une fréquence de coupure de 24 GHz, un gain optique-microonde de -18,1 dB, ce qui correspond à une responsivité de 0.13 W/A par couplage à une fibre optique lentillée multimode de 28µm de waist à 50µm de distance. Des performances intéressantes ont été trouvées en terme de bruit avec un niveau inférieur à -140 dB/Hz sur toute la plage de fréquence pour 6mA de courant de polarisation, et en terme de non-linéarité avec un IP1dBOM de +10 dBm un IIP3OM de +14 dBm et un SFDROM de 94 dB.Hz2/3, pour 4mA de courant de polarisation. Ces niveaux sont comparables à ceux des VCSEL ULM Photonics standard 10Gbps malgré la réduction de dimension par un facteur 2 sur le diamètre (4 sur la surface). Les meilleures performances ont été obtenues pour des courants de polarisation supérieurs à 3 mA (mesure réalisées jusque 4mA) et une fréquence de modulation supérieure à 6 GHz.

L'impact d'un réseau d'adaptation réactif a été exploré, démontrant un potentiel d'accroissement du gain de 4dB. Sa réalisation apparait cependant délicate par les pertes induites par ses composants. Une intégration monolithique s'avère nécessaire.

Notre contribution sur l'amélioration du taux de couplage optique permet de coupler des structures de plus petites tailles et donc intrinsèquement plus rapide. Cela concerne les VCSEL précédemment étudiés, mais aussi les phototransistors SiGe étudiés dans une autre thèse. Une nouvelle technique de couplage optique est proposée. Elle s'appuie sur une structure de guidage optique vertical, à base de structure polymère, pour confiner la lumière dans la transition entre le composant optique et la fibre. Cette technique fait l'objet du dépôt d'un brevet. Les simulations exploitées pour son dimensionnement sont appliquées dans un premier temps à la

technique à base de lentilles saphirs sphériques exploitée au chapitre V. Une bonne correspondance à la mesure est obtenue dans différentes configurations et valide notre approche. La nouvelle solution proposée (figure ci-dessous) est basée sur un couplage optique collectif et passif. Les guides d'onde optique verticaux sont intégrés sur une plateforme d'ancrage qui maintient le cône et fournit l'alignement passif en plus du contact à la fibre.

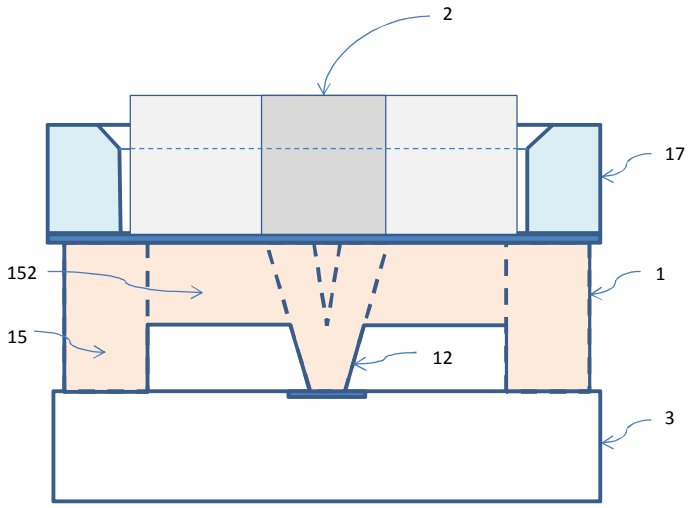

Système de couplage optique proposé

Des analyses de variation de dimensions, pour une largeur de base tronquée fixée à 10 µm indique un dimensionnement optimal et compact pour un grand diamètre de 25 µm et une hauteur de cône de 25µm. Ce dimensionnement permet le couplage d'une fibre multimode à un détecteur de 10 µm de côté avec un coefficient de couplage optimal de 80 %. Ceci correspond une amélioration de 6 dB sur le gain OM par rapport à la technique de la lentille sphérique utilisée sur le SiGe HPT. L'analyse de tolérance sur l'alignement a été simulée et évaluée à ± 20 µm à la moitié de la puissance.

La simulation de taux du couplage entre un VCSEL de 8µm d'ouverture optique et une fibre optique multimode a été évaluée également. Une structure cylindrique de guide de 10µm de large et 30µm de hauteur permet d'obtenir un coefficient de couplage aussi élevée que 96 %.

Ces résultats de simulation, confortés par une validation préliminaire du simulateur et des modèles, permettent d'envisager des améliorations notables sur les modules ROSA et TOSA en garantissant une réduction du cout et du temps d'alignement. Ils font l'objet d'un dépôt de brevet et d'un projet de maturation financé par la SATT IdFInnov.

R.8 - Conclusions et Perspectives

Ce dernier chapitre résume les travaux et fournit des conclusions générales. Il présente, également, la contribution principale de ce travail et les perspectives adressée pour les orientations futures.

En termes d'avancée et de nouveauté, les principales contributions de ce travail sont :

- La mise en place et le développement et implémentation de bancs de mesure avancés pour les composants et applications optique-microondes au sein du laboratoire : la mesure du RIN est réalisée de manière simple et fiable, les nonlinéarités sont mesurées et extraites séparément pour chaque composant, des

mesures systèmes sont traitées par le biais de la mesure d'EVM sur la base des spécifications et normes 60GHz.

- Une extension de grandeur optique-microondes a été apportée amenant à un jeu complet d'outils pour la caractérisation individuelle des composants. Les formules de composition classiques des microondes sont respectées : gain optique-microonde(G_{OM}), facteur de bruit optique-microondes (NF_{OM}), point de compression optique-microonde entrée et sortie ($P1dB_{OM}$), point d'interception d'ordre trois optique-microonde entrée et sortie ($IP3_{OM}$), plage dynamique sans parasite optique-microonde ($SFDR_{OM}$) et enfin vecteur d'erreur en amplitude optique-microonde (EVM_{OM}).
- Des modèles comportementaux sont mises en place exploitant ces grandeurs optique-microondes. Ils sont exploités pour mieux comprendre l'impact des performances de chaque composant, mais permet aussi une extraction fine des paramètres à partir des mesures EVM.
- Un système RoF de distribution de signaux 60GHz dans la maison est démontré en démonstrateur taille réelle pour la première fois au niveau international à partir de VCSEL.
- Pour la première fois au niveau international, un HPT SiGe, sous configuration 2T-HPT, a été intégré dans une liaison RoF large-bande. Il présente une dégradation d'EVM de 16% sur un signal de type IEEE802.15.3c
- Des VCSEL analogiques, c'est-à-dire à haute performance optique-microonde en linéarité, bande passante et bruit, ont été développés avec des performances records : bande passante de 25GHz avec un $IP1dB_{OM}$ de +10dB et un $SFDR_{OM}$ de 94 $dB.Hz^{2/3}$.
- Une technique innovante de couplage optique passif et collectif a été proposée avec des taux de couplage proche de 96% entre un VCSEL de 8µm de diamètre et une fibre optique multimode, et proche de 80% pour un photodétecteur de 10µm de côté et une fibre multimode également. Ceci devrait réduire le compromis entre taille, donc performances fréquentielles, et taux de couplage, soit donc entre performances et coût.

Les perspectives de ce travail sont présentées sur les deux thèmes principaux suivants.

Dans un premier axe de perspectives, la poursuite du développement des composants opto-électroniques et modules RoF et l'amélioration de leurs performances peut se réalisé sur les six plans suivants:

- La technologie IF-RoF à une fréquence intermédiaire de 5 GHz est imposée par le projet pour rester compatible avec les dispositifs optoélectroniques bas coût existants dans le commerce (exemple des TOSA/ROSA Finisar). Cette valeur de IF limite la bande passante possible pour la transmission. Un seul canal parmi les quatre disponibles dans les standards 60GHz est transmis. Une direction à prendre est d'augmenter cette fréquence intermédiaire, ce qui signifie d'utiliser des dispositifs optoélectroniques plus rapide. Cette augmentation permettra de transmettre un nombre croissant de canaux. Idéalement il serait visé d'atteindre un

schéma RoF sans nécessité de fréquence intermédiaire, ce qui économiserait les étages de conversion et les non-linéarités et facteurs de bruit associés, qui restent les points critiques. En termes de dispositif optoélectronique, la vitesse est inversement proportionnelle à la taille. Réduire les dimensions des VCSEL et des HPT devraient permettre d'augmenter leur réponse en fréquence, au moins dans une certaine limite. Ces petites structures (VCSEL et HPT) sont plus rapides, mais caractérisées par un faible gain OM principalement en raison du faible taux de couplage (pas seulement toutefois).

- Des solutions résident également dans la mise en œuvre du packaging et des interconnexions électriques et optiques avancées. Celles-ci permettront une intégration plus poussée avec une maitrise des contraintes d'adaptation soit à l'amplificateur de puissance (PA) sur l'entrée de VCSEL soit à un LNA à la sortie du HPT. En utilisant la même technologie SiGe, les circuits actifs et les réseaux d'adaptation intégrés pourraient être utilisé pour optimiser les pertes de réflexion entre le circuit et le dispositif optoélectronique.
- Des solutions côté du phototransistor proprement dit sont également à envisager, notamment en réalisant le passage d'un 2T-HPT vers un 3T-HPT, avec l'objectif également de réduire le bruit et d'augmenter le gain du composant. .
- Au cours de cette thèse un HBT a été associé à un VCSEL en utilisant le connecteur d'émetteur dans la cathode du VCSEL. Les résultats de cette configuration doivent être explorés dans les travaux futurs.
- L'interconnexion optique est une tâche importante pour mettre au point de telles petites structures où la technique de la lentille sphérique se révèle insuffisant. Le développement de notre nouvelle technique de couplage est une solution qui permet de résoudre ce problème. Il doit être envisagé de la démontrer expérimentalement et de pousser ces performances pour la réduction des dimensions du composant opto-électronique.
- Amélioration de la modélisation comportementale: Une meilleure modélisation de la composante non linéaire des dispositifs opto-électroniques serait nécessaire au lieu de la tangente hyperbolique. Aussi la mise en œuvre des effets des cartes de test dans le modèle pourrait être utile.

Un deuxième axe de perspectives réside dans le développement du système et de l'architecture complète:

- L'intégration globale doit être poursuivie, pour rendre compact et plus intégré le système TRoF complet. Les modules MM-TX et MM-RX sont critiques. Le module mm-TX a été jugée le plus critique avec un gain de 27 dB inférieur à ce qui était prévu. Par conséquent, l'amélioration doit être prise en compte de ses performances et une plus grande intégration aussi. Nous pourrions envisager une poursuite d'intégration dans la technologie SiGe . Des briques de bases ont été initiées..
- Le couplage entre les deux antennes et les modules mm-TX et mm-RX est un autre point d'amélioration qui va influencer les performances du système. L'amélioration peut être dans la conception de l'antenne.
- La gestion de l'accès optique pourrait être une solution à mettre en œuvre dans l'architecture M2M avec contrôle automatique de l'exposition aux rayonnements.

- D'autres développements sont nécessaires, en tenant compte des avantages de l'amélioration de VCSEL présentés dans cette thèse, pour transmettre le quatre canaux de 2 GHz de la norme 60 GHz.
- L'architecture RoF doit également évoluer et se compléter de façon à intégrer plusieurs services, y compris la transmission 1 Gbps Ethernet, la téléphonie RTC, les signaux de télévision par satellite et les signaux Wi-Fi 2.4/5 GHz sur le même câble hybride.

Enfin, il est à noter que notre travail théorique sur la nouvelle technique de couplage optique que nous proposons fait l'objet d'un projet de maturation pour le transfert industriel et la valorisation. Un brevet a été déposé préalablement.

Abstract

This work is based on the frame of the French ORIGIN project and intended to explore the Home Area Network using the most recent Wi-Fi standard at 60 GHz with the goal to present a solution for the upcoming days where MultiGbit/s wireless communication will be required. The ORIGIN solution is characterized by the complementary action of two technologies: 60 GHz Wireless communication and Radio-over-Fiber (RoF) infrastructure. The project pretends to propose a real prototype based on RoF transducers and a Multipoint-to-Multipoint architecture to cover the entire house. This thesis covers from the single optoelectronic chip devices until the system implementation and the final demonstrator. The light source and the photodetector choice were very important since it dictated the RoF transducer architecture. Our choice was on 850 nm multimode devices (GaAs VCSEL and SiGe HPT) which allow relaxed constraints on the optical packaging and, therefore, low cost solutions. In terms of performances those devices are limited in a few tens of Gigahertz of bandwidth which was the reason for the intermediate frequency (IF) architecture. This thesis work addressed the electrical and optical interconnection of the optoelectronic chip devices. It explored the integration of hybrid amplification stages and passive networks within optoelectronic receivers and emitters. The optical packaging issues were addressed through a conventional coupling technique using a ball lens first. The die device performances were evaluated and compared with a packaged module in terms of frequency response, noise and nonlinearities. Since performances are usually measured as link performances we proposed a definition of the Opto-microwave figures of merit, such as Opto-microwave gain, noise, nonlinearities and EVM. They are presented and integrated into behavioral models, allowing both the individual performances extraction and system design. The integration of the RoF module in the system is the final part of this thesis. The performances were measured and simulated at each integration step. The final demonstrator based on the multipoint-to-multipoint architecture was implemented using an optoelectronic central node for the signal repartition and the Green Box for signal controlling. Real-time bidirectional transmission between two commercial WirelessHD devices at ~3 Gbit/s was validated. In a final section directions to improve VCSEL and SiGe HPT are explored. 25 GHz analogue VCSELs are explored with a focus on their dimensions, improved access and the potential of a suited matching approach. A novel collective and passive optical coupling technology is also proposed for both VCSEL and top illuminated detectors that couple smaller and faster devices.

Keywords: Radio-over-Fiber, VCSEL, HPT, Optical Interconections, Opto-Microwave Modelling, 60 GHz wireless comunication.

Résumé:

Cette thèse s'inscrit dans le cadre du projet français FUI8-ORIGIN qui vise à développer les performances des réseaux domestiques en apportant des solutions sans multi-Gigabits faiblement radiatives, économes et pérennes. La solution ORIGIN est caractérisée par l'action complémentaire de deux technologies: les communications sans fil 60 GHz et la mise en place d'une infrastructure Radio-sur-Fibre (RoF). Cette thèse porte sur le développement des composants et modules optoélectroniques (GaAs VCSEL et SiGe HPT) bas couts. Le travail implique de couvrir de la puce semi-conducteur au modules et jusqu'au système intégré dans le démonstrateur. Les puces sélectionnées sont caractérisées de manière précise en développant des bancs de mesures adaptées aux applications analogiques RoF. Des substrats d'interconnexions sont développés pour permettre le couplage optique et l'interconnexion électrique des puces et ainsi la création de modules. Ce développement est poussé de façon à intégrer de façon hybride des étages d'amplification en aval et amont des composants optiques, ainsi que des étages d'adaptations passifs. Les performances RoF ont été évaluées et comparées en termes de réponse en fréquence, de bruit et de nonlinéarités. Nous avons poursuivi l'approche actuelle des grandeurs optique-microondes qui chacune permette d'isoler et caractériser la performance individuelle des composants optiques ou optoélectroniques pris individuellement. Ces grandeurs sont présentées puis exploitées dans un développement de modèle comportemental, permettant à la fois l'extraction des performances individuelles des composants et le design de l'ensemble du système. Un dimensionnement complet de l'infrastructure RoF pour le démonstrateur est ensuite mené, intégrant et dimensionnant le bilan de liaison global à partir modules et cartes réalisés et développés par les partenaires du projet. Le module transmetteur Radio-sur-Fibre (TRoF) est ainsi conçu, assemblé et testé. Le démonstrateur final basé sur l'architecture multipoint-à-multipoint a été réalisée à l'aide d'un nœud central optoélectronique pour la répartition du signal et d'une Green Box permettant le contrôle de l'allumage des différentes pièces, et ainsi la rationalisation du rayonnement et de la consommation du système. Une transmission bidirectionnelle en temps réel entre deux dispositifs de WirelessHD commerciaux à ~3 Gbit/s a été démontrée. Dans une dernière section de cette thèse, des directions pour améliorer les lasers à cavité émettant par la surface (VCSEL) et les phototransistors SiGe sont explorées. Des VCSEL analogiques avec une bande passante de plus de 25 GHz sont développés avec la société Philips ULM Photonics et mesurés. Une nouvelle technologie de couplage optique collective et passive est enfin proposée.

Mots clés : Radio-sur-Fibre, VCSEL, HPT, Interconnexions optiques, Modélisation optique microonde, Communications sans fil 60 GHz.